

# **For Reference**

---

**NOT TO BE TAKEN FROM THIS ROOM**

Ex libris  
UNIVERSITATIS  
ALBERTAEENSIS











Digitized by the Internet Archive  
in 2019 with funding from  
University of Alberta Libraries

<https://archive.org/details/Fillipow1976>



T H E   U N I V E R S I T Y   O F   A L B E R T A

RELEASE FORM

NAME OF AUTHOR                      Larry John Filipow  
TITLE OF THESIS                      GAMMA-RAY COLLIMATOR DESIGN FOR CLINICAL  
   RADIOISOTOPE STUDIES  
DEGREE FOR WHICH THESIS WAS PRESENTED:   MASTER OF SCIENCE  
YEAR THIS DEGREE GRANTED:   1976

Permission is hereby granted to THE UNIVERSITY OF ALBERTA LIBRARY to reproduce single copies of this thesis and to lend or sell such copies for private, scholarly or scientific research purposes only.

The author reserves other publication rights, and neither the thesis nor extensive extracts from it may be printed or otherwise reproduced without the author's written permission.



THE UNIVERSITY OF ALBERTA

GAMMA-RAY COLLIMATOR DESIGN FOR CLINICAL RADIOISOTOPE STUDIES

by



LARRY JOHN FILIPOW

A THESIS

SUBMITTED TO THE FACULTY OF GRADUATE STUDIES AND RESEARCH IN

PARTIAL FULFILMENT OF THE REQUIREMENTS FOR THE DEGREE

OF MASTER OF SCIENCE

IN

PHYSICS

DEPARTMENT OF PHYSICS

EDMONTON, ALBERTA

SPRING, 1976



2-12

THE UNIVERSITY OF ALBERTA  
FACULTY OF GRADUATE STUDIES AND RESEARCH

The undersigned certify that they have read, and recommend to the Faculty of Graduate Studies and Research, for acceptance, a thesis entitled GAMMA-RAY COLLIMATOR DESIGN FOR CLINICAL RADIOISOTOPE STUDIES submitted by LARRY JOHN FILIPOW in partial fulfilment of the requirements for the degree of Master of SCIENCE.





TO MY FATHER ..... WHOSE PRIDE IN ME NEVER CEASED



## ABSTRACT

Characteristics of gamma-ray collimators used in clinical applications were studied with the specific aims of defining and of simplifying collimator design procedures.

This work involved both theoretical and experimental studies. A precision, mechanical scanning device was constructed and used in field response characteristics measurements for various collimators.

A modelling theory was developed to determine analytically the field response parameters for various collimator-source configurations. Response contours were then computer generated. Factors considered in this modelling process were: air path length attenuation; tissue path length attenuation; possible bone absorption, and possible collimator penetration.

The modelling algorithm developed in this work provided good facsimiles of measured field isoresponse contours. Thus, using this algorithm, collimator characteristics for various source-detector configurations can be reasonably determined before fabrication and experimental measurements are made.



## ACKNOWLEDGEMENTS

I would like very much to thank my supervisor, Dr. T.R. Overton, for the great amount of assistance he has provided me through the course of this work. He generously donated his wisdom and time through many enjoyable discussions and it has been a pleasure to do research with him.

I would like to thank Dr. R.E. Snyder, who helped me a great deal in many aspects of this work. It was he who originally introduced me to this field.

I wish to thank Dr. D. Menon for the time he spent checking the theory.

Finally, I would like to extend a warm thank you to the other people I had the pleasure of interacting with at the university. Through their friendship my stay here was very pleasant. Lest I forget someone, I'll mention no names.



## TABLE OF CONTENTS

CHAPTER		PAGE
1	INTRODUCTION	1
1.1	Introduction	1
1.2	Background	2
1.3	The Pulmonary Function Studies System (University of Alberta)	9
2	THEORETICAL CONSIDERATIONS IN COLLIMATOR DESIGN	12
2.1	Sensitivity	12
2.2	Spatial Resolution	16
2.3	Field Response	18
3	EXPERIMENTAL DESIGN	20
3.1	Instrumentation	20
3.1.1	Raster Scanner	20
3.1.2	Data Acquisition System	25
3.1.3	Data Analysis	26
3.2	Modelling	28
4	RESULTS AND DISCUSSION	34
4.1	Introduction	34
4.2	Details of Collimators Studied	37
4.3	Experimental Scans and Models	39
4.4	Comparison of Collimators	77
5	SUMMARY AND CONCLUSION	81





## TABLE OF CONTENTS

	PAGE
BIBLIOGRAPHY	83
APPENDIX	
A            THE PHYSICS OF THE LUNG	87
A.1      Mechanics of Respiration	87
A.1.1  Expansion and Contraction	87
A.1.2  Respiratory Pressure - The Lung Pump	91
A.1.3  Compliance and Work	91
A.1.4  Surface Tension and Elastic Recoil	94
A.2      Flow Dynamics	96
A.2.1  Volumes and Capacities	96
A.2.2  Rates and Flows	99
A.3      The Lung and Gas Exchange	103
A.3.1  The Pressures	103
A.3.2  Diffusion and the Alveolar Membrane	108
B            COLLIMATOR FIELD-OF-VIEW DERIVATIONS	110
B.1      Cylindrical Collimators	110
B.2      Rectangular Collimators	112
C            MATHEMATICS OF RAY TRACING	118
C.1      Cylindrical Straight Collimator	119
C.2      Cylindrical Tapered Collimators	124
C.2.1  Cylindrical Diverging Collimator	124
C.2.2  Cylindrical Converging Collimator	126
C.3      Straight Rectangular Collimator	126
C.4      Tapered Rectangular Collimators	130



# TABLE OF CONTENTS

APPENDIX		PAGE
D	SOLID ANGLE DERIVATIONS	133
E	COMPUTER PROGRAMS	136



# LIST OF FIGURES

FIGURE		PAGE
1	Schematic Summary of Imaging Techniques	4
2	Schematics of Various Gamma-Ray Collimators	6
3	Schematic of the Pulmonary Function Studies System	10
4	The Line Spread Function and Modulation Transfer Function	15
5	Photograph of Raster Scanner	21
6	Schematic Diagram of Raster Scanner	22
7	Electronics Layout of Raster Scanner Control	24
8	Raster Scan Segmenting Process	27
9	Solid Angle Weighting Factor	31
10	Schematics of Collimators Used	38
11	Cylindrical Collimators Single Response $^{133}\text{Xe}$ AIR	40
12	Cylindrical Collimators Sum Response $^{133}\text{Xe}$ AIR	41
13	Rectangular Collimators Single Response $^{133}\text{Xe}$ AIR	42
14	Rectangular Collimators Sum Response $^{133}\text{Xe}$ AIR	43
15	Figure 11 Simulation	44
16	Figure 12 Simulation	45
17	Figure 13 Simulation	46
18	Figure 14 Simulation	47
19	Cylindrical Collimators Single Response $^{133}\text{Xe}$ $\text{H}_2\text{O}$	48
20	Cylindrical Collimators Sum Response $^{133}\text{Xe}$ $\text{H}_2\text{O}$	49
21	Rectangular Collimators Single Response $^{133}\text{Xe}$ $\text{H}_2\text{O}$	50
22	Rectangular Collimators Sum Response $^{133}\text{Xe}$ $\text{H}_2\text{O}$	51
23	Figure 19 Simulation	52
24	Figure 20 Simulation	53



FIGURE		PAGE
25	Figure 21 Simulation	54
26	Figure 22 Simulation	55
27	Cylindrical Collimators Single Response $^{22}\text{Na}$ AIR	56
28	Cylindrical Collimators Sum Response $^{22}\text{Na}$ AIR	57
29	Rectangular Collimators Single Response $^{22}\text{Na}$ AIR	58
30	Rectangular Collimators Sum Response $^{22}\text{Na}$ AIR	59
31	Figure 27 Simulation	60
32	Figure 28 Simulation	61
33	Figure 29 Simulation	62
34	Figure 30 Simulation	63
35	Cylindrical Collimators Single Response $^{22}\text{Na}$ $\text{H}_2\text{O}$	64
36	Cylindrical Collimators Sum Response $^{22}\text{Na}$ $\text{H}_2\text{O}$	65
37	Rectangular Collimators Single Response $^{22}\text{Na}$ $\text{H}_2\text{O}$	66
38	Rectangular Collimators Sum Response $^{22}\text{Na}$ $\text{H}_2\text{O}$	67
39	Figure 35 Simulation	68
40	Figure 36 Simulation	69
41	Figure 37 Simulation	70
42	Figure 38 Simulation	71
43	Miniature Probe Responses	72
44	Positron Coincidence Responses - AIR	73
45	Positron Coincidence Responses - $\text{H}_2\text{O}$	74
46	Modelled Scan - One Rib Absorber	75
47	Modelled Scan - Two Rib Absorber	76
48	Basic Lung Anatomy	85
49	The Mechanics of Breathing	86





FIGURE		PAGE
50	Respiratory Pressures and Compliance Diagrams	88
51	Surface Tension of a Bubble	93
52	Nomenclature for Pulmonary Function	94
53	Volumes and Capacities of the Lungs	96
54	Flow-Pressure Relationship in the Lungs	100
55	Oxygen Partial Pressure Vs. Time in the Capillaries and Partial Pressures in Respiration	103
56	Collimator Fields-of-View	107
57	Crystal-Collimator Configuration for Field-of-View Determination	110
58	Field-of-View for Circular Crystal in a Rectangular Collimator	113
59	Collimator Penetration Configuration	116
60	Collimator Penetration Possibilities	119
61	Cylindrical Tapered Collimator Geometries	121
62	Rectangular Collimator Geometry	123
63	Rectangular Tapered Collimator Geometry	127
64	Geometries for Determining Solid Angle Factors	130



# LIST OF TABLES

TABLE		PAGE
1	Experimental Detector-Source Configurations	35-36
A-1	Elastic Properties of the Chest Wall and Lungs	93
A-2	Viscosity and Density of Respiratory Gases	97
A-3	Reynolds' Number in the Lung	97
A-4	Gaseous Composition of the Atmosphere	102
A-5	Partial Pressures of Respiratory Gases	102



## CHAPTER ONE

### 1.1 Introduction

Nuclear medicine is an area of medical practice where radioisotopes and radioactive materials are used for the purpose of aiding the diagnosis of disease. In this diagnostic process the radioactive materials introduced into the body are localized in specific organs or tissues and subsequently counted or imaged, in normal practice, using scintillation radiation detectors.

The static volume distribution of the radioactive material in a tissue delineates anatomic structure whereas changes in the distribution or in the quantity of radioactive material with time demonstrate organ or tissue function.

A scintillation detector as used in nuclear medicine is composed of several components, most of which are used in conventional gamma-ray spectrometry systems. These are: a scintillation crystal, a photomultiplier, amplifiers, an energy analyser and a scaler or rate meter. A critical component of a medical radiation detector system not usually found in a conventional spectrometry system is the gamma-ray collimator which governs, to a great extent, detector sensitivity and spatial resolution. Scintillation detector performance is dependent upon these two factors, and optimising performance therefore, amounts to maximizing detector sensitivity for a well defined field-of-view. This raises certain problems, however, since for reasons of patient safety, a minimal quantity of radiation must be used in diagnostic investigations. By demanding that the detector



simultaneously yield both high sensitivity and good spatial resolution, one is thus confronted with the problem of reconciling two conflicting parameters in the design considerations.

It was the purpose of the present work to study gamma-ray collimator characteristics with the specific aims of defining and of simplifying collimator design procedures for various clinical measurement situations.

The particular clinical situation that is considered in this thesis is the measurement of regional pulmonary function using an inert, diffusible radioactive gas ( $^{133}\text{Xe}$ ). The scintillation detector system used in these investigations of regional lung function was designed and constructed at this university ( 1 ). Straight cylindrical gamma-ray collimators were used in this instrument but the system was not optimal with respect to sensitivity or field-of-view.

The present work was thus directed to studies of gamma-ray collimator characteristics best suited to regional lung measurements. Specific aims of the optimization process were

- (i) to provide a well defined, non-overlapping field-of-view between detectors,
- (ii) to obtain maximum sensitivity for this field-of-view,
- (iii) to produce a uniform, or iso-sensitive counting field at a distance from the collimator face.

## 1.2 Background

Two principal types of scintillation detector systems are used in nuclear medicine; the counting system and the imaging system. Historically, the first application of a scintillation detector in medical diagnosis was as a counting system ( 2 ).





In terms of instrumentation, counting systems and imaging systems have much in common. However, the purpose of each is different; one is designed to efficiently measure the total quantity of radioactivity, the other to efficiently measure its distribution.

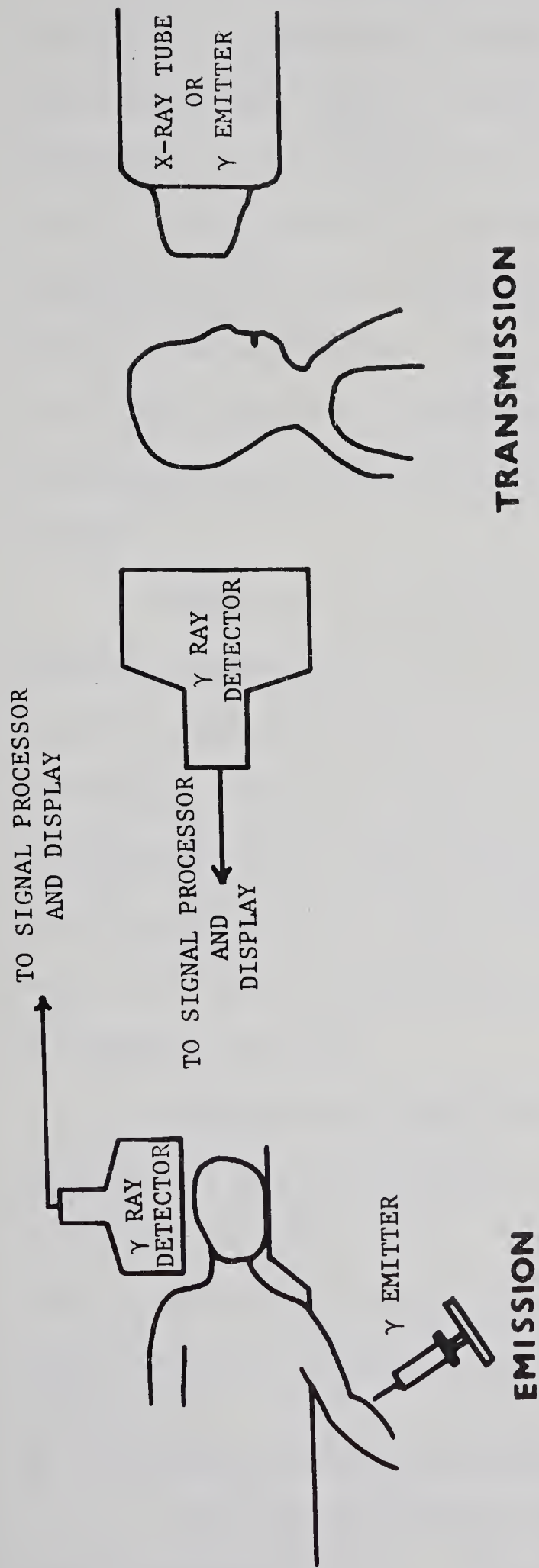
Counting systems are readily applicable to studies of dynamic organ function. As an example, a bolus (delta-function) type of tracer input can be applied to an organ or tissue, and measurements made of the time-rate of change of activity following this. In similar fashion, the uptake and clearance of a radio-labelled compound, which is localized by biochemical action, can be measured by such a system.

Imaging systems on the other hand are in a sense analogous to optical camera systems. Whereas the optical photo or image indicates the distribution and intensity of the different wavelengths of light photons emitted or reflected by the object, the gamma-ray camera system indicates the distribution and intensity of gamma photons emitted by the object.

Imaging systems have been developed based on gamma-ray emission (3-19), gamma-ray transmission (20-21), x-ray excitation fluorescence (22-24) and incoherent holographic (25-27) principles. A schematic summary of these techniques is shown in Figure 1.

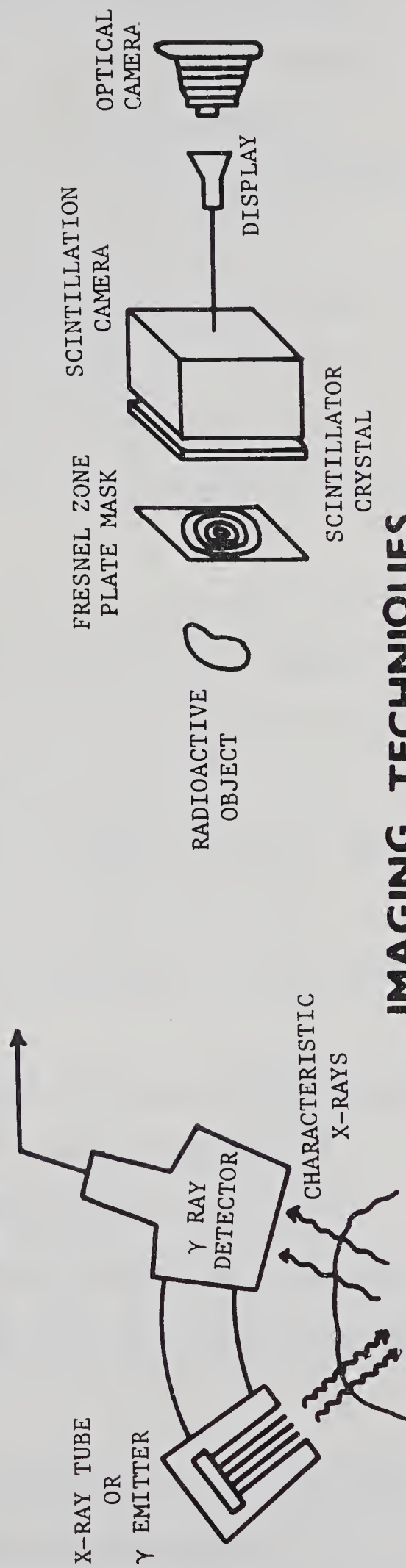
In an imaging system, the observed distributional variation in gamma-ray intensity results due to the fact that the radioactive material is biochemically accumulated in different concentrations by abnormal and surrounding healthy tissues. In disease situations an image thus contains "hot" spots (a high local concentration) or "cold" spots (a low local concentration) of radioactivity, depending on the type of tumour or lesion involved.





## INCOHERENT HOLOGRAPHIC

## FLUORESCENCE



## IMAGING TECHNIQUES

FIGURE 1



By a suitable choice of scintillation crystal size, good sensitivity, or detection efficiency, can be obtained for any given gamma-ray energy. However, in most medical applications, spatial resolution is also an important consideration and gamma-ray collimator design for any particular application is based upon a compromise between the conflicting requirements of high spatial resolution and high counting sensitivity. This necessary compromise in collimator design has resulted in a large variety of collimators in use, each being particularly advantageous when applied to a particular diagnostic problem.

Gamma-ray collimators function by providing access to the detector for gamma rays only from predetermined directions. Gamma rays from other directions are absorbed or greatly attenuated by the collimator. The most frequently used collimator material is lead - a consequence of its high density, high atomic number, relatively low cost and ease of fabrication. Tungsten ( 28 ), gold ( 29 ) and brass ( 30 ) have also been used as collimator materials, although not as frequently as lead.

Gamma-ray collimators are specified in terms of their physical parameters of spatial resolution, sensitivity, depth response, and penetration fraction ( 31 ). In the following review, the various types of collimators currently used in medical detection systems, and their particular advantages and disadvantages will be briefly discussed (Figure 2).

#### (A) Cylindrical Straight Bore Collimator

The first rectilinear scanning system built incorporated this type of collimator ( 32 ). It is inherently the most sensitive of collimators as it exposes the greatest crystal area to a point source





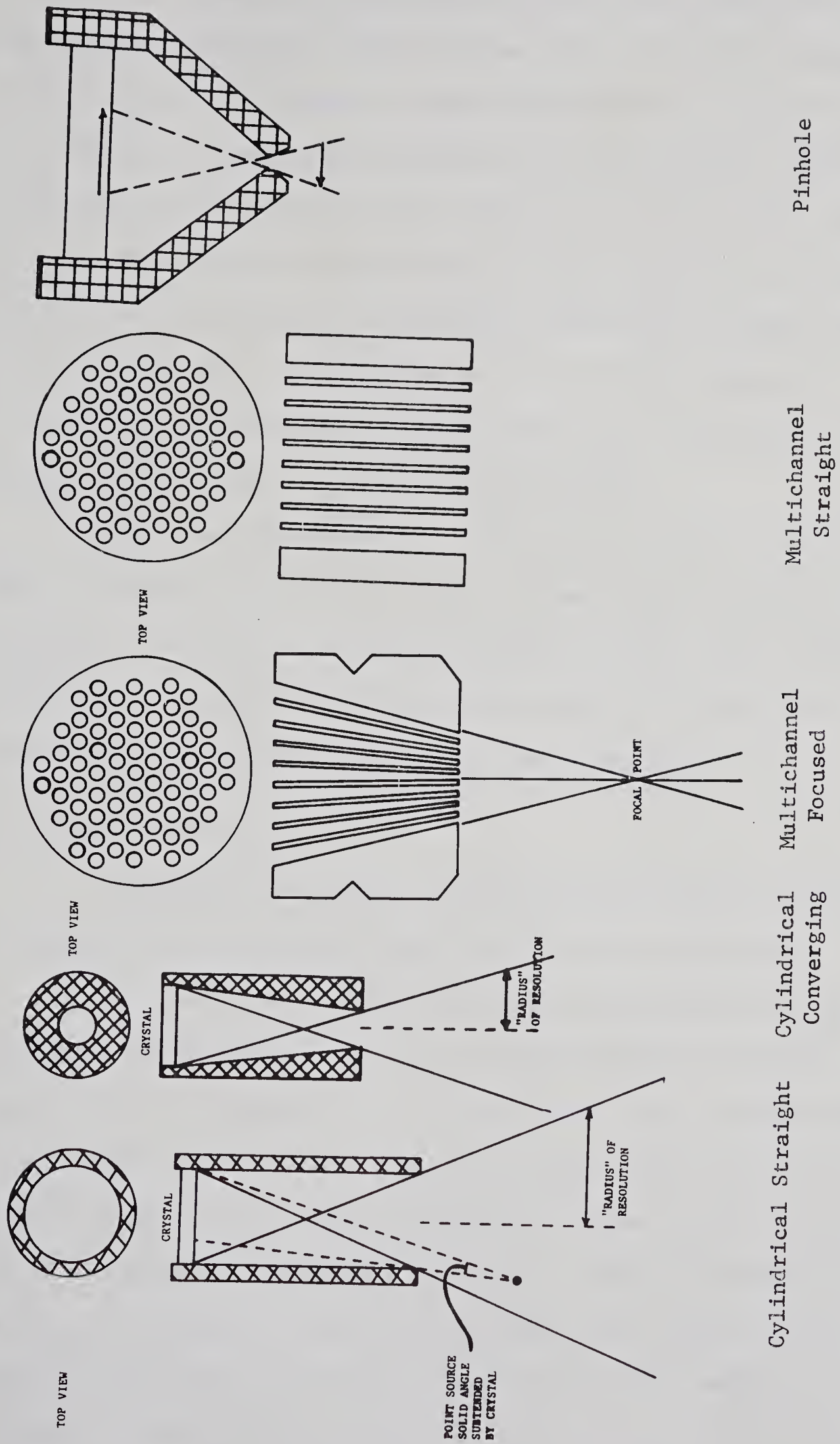


FIGURE 2





of radiation. However, the price paid for this high sensitivity is poor spatial resolution. This is because the solid angle subtended by the crystal at the source is large; consequently the points in the source from which gamma rays originate are poorly defined. These ever conflicting requirements of spatial resolution and sensitivity are better accommodated with a multichannel focused collimator which is discussed later. However, for situations where the principal purpose is to determine the gross distribution of total body radioactivity and to follow the distributional variation with time, the cylindrical straight bore collimator is still the best device.

Whole body measurements or measurements which involve large areas of the body such as the thoracic volume employ this type of collimator. By using two opposed collinear detectors with straight cylindrical collimators, a fairly uniform region of isosensitive response through the cross section of a patient can be obtained.

#### (B) Focused Collimators.

Included in this group are multichannel focused collimators and single channel conical or tapered cylindrical collimators.

The focused multichannel collimator generally gives the best combination of both high sensitivity and high spatial resolution. The reason is that approximately 50% of the crystal area is exposed through the collimator holes, thus increasing the sensitivity; the angle from which the gamma rays can reach the crystal, however, is much smaller than in the parallel single hole collimator. These collimators contain many holes or channels, which are both tapered and angled so that their combined geometrical projections meet at a focal point which is a fixed distance from the collimator face.



The single hole, tapered collimator ( 33 ) is a type of "focusing" collimator, but its characteristics of resolution and sensitivity are more related to the straight cylindrical hole collimator. It has better spatial resolution than the straight hole collimator because of its taper but it is not as sensitive. On the other hand, it is more sensitive than the multihole focusing collimator but does not resolve spatial changes of radiation as well.

#### (C) Parallel Multihole Collimator

This collimator consists of a lead block with 1,000, 4,000, 15,000 or more parallel cylindrical holes drilled into it. One of its main advantages is this relative ease of fabrication. These holes vary in diameter from collimator to collimator, making the septal thickness suitable for the energy that the collimator was designed. They are most frequently used with large crystal scintillation cameras (34). The spatial resolution of a parallel multihole collimator decreases steadily with distance from its face. Sensitivity is also maximal at the face of the collimator, so this collimator is well suited for the imaging of shallow-lying lesions and tumors. It is used primarily for low energy gamma photons because a parallel multihole collimator, if not properly designed, is susceptible to septal penetration from high energy radiation, resulting in poorly defined images.

#### (D) Pinhole Collimator

The pinhole collimator is the most analogous to an optical system - that of a pinhole camera. It was also one of the first collimators used for medical applications ( 35 ). The image is inverted, and depending on the distance of the source from the collimator, it may be enlarged or diminished in size, or at a particular



distance may be equal to the object size. Used primarily for viewing small organs, the pinhole collimator provides sensitivity approximately equal to that of a straight cylindrical hole collimator, and in addition gives improved resolution due to the "optical gain" effect of image enlargement.

#### (E) Rectangular Collimators

Each type of collimator considered to this point, whether single hole or multihole, straight or tapered, can have an analogous rectangular counterpart. Generally, the sensitivities and resolutions of these rectangular collimators are similar to the corresponding cylindrical collimators, the only real difference being in the field of view. Instead of a circular field of view from a cylindrical collimator, a "large rectangular" field of view is obtained.

### 1.3 The Pulmonary Function Studies System (University of Alberta)

The Pulmonary Function Studies System (PFSS) is a multi-detector counting system used to measure regional lung function using the radioactive gas  $^{133}\text{Xenon}$  ( 1 ). Certain basic physiological parameters of lung function can be measured and related to lung disease. (For a detailed explanation of these basic lung parameters, see Appendix A).

Each lung in the PFSS is viewed by 6 pairs of collinear detectors, one detector from each pair mounted anteriorly and the other mounted posteriorly (See Figure 3). It is the purpose of the present work to study collimator design with particular reference to this system and to develop a collimator which will simultaneously optimize sensitivity and uniformity of depth response and minimize field of view overlap between the detector pairs.





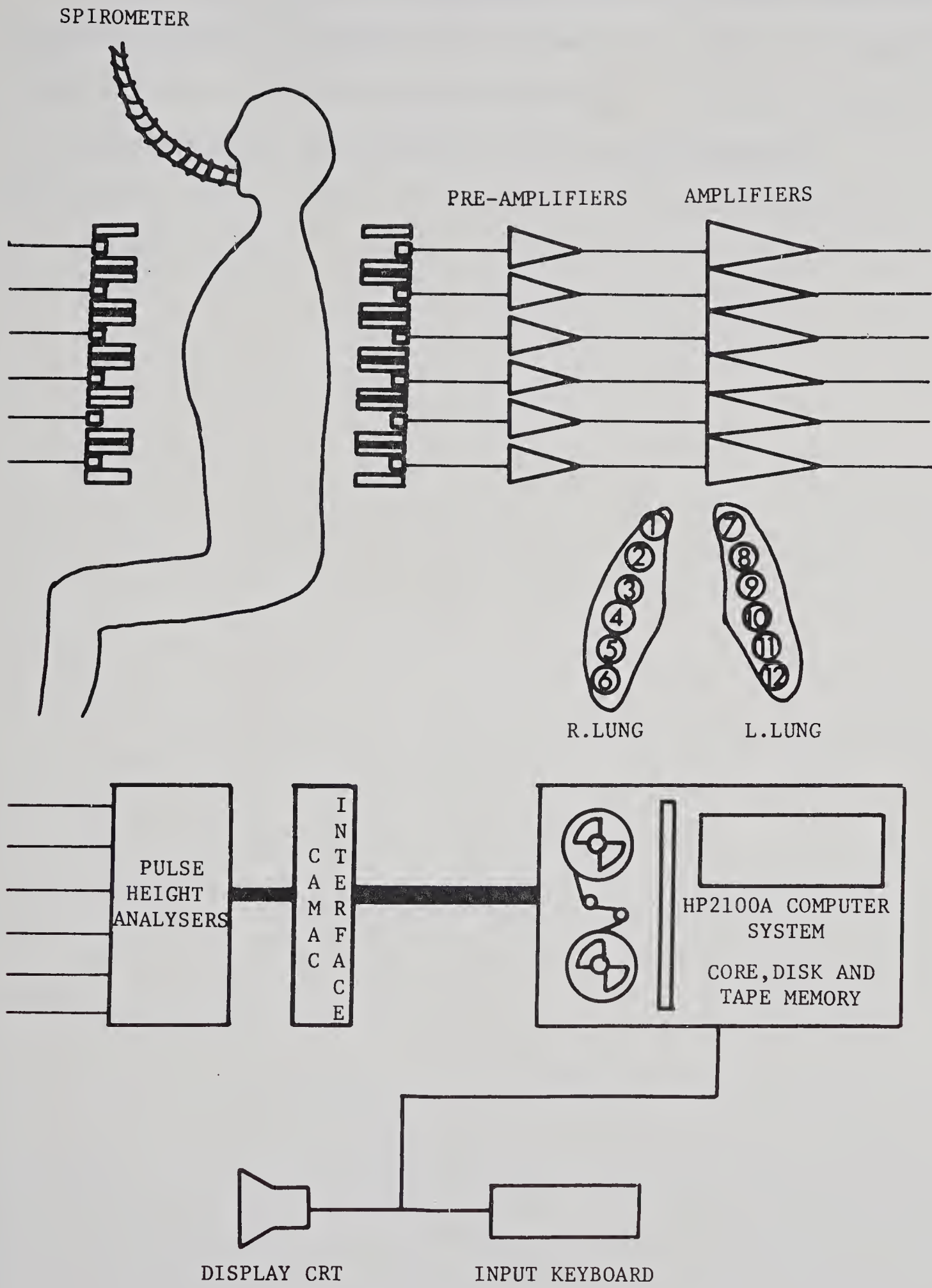


FIGURE 3





This work involves a combination of both theory and experiment. A modelling theory is developed and outlined, and a number of experimental studies are done. The theory is first discussed - theoretical aspects of collimator design, with reference to the various parameters (sensitivity, spatial resolution, etc.) are considered in detail in the following chapter.



## CHAPTER TWO

### THEORETICAL CONSIDERATIONS IN COLLIMATOR DESIGN

In any comparison between collimators, sensitivity, resolution, and field response need to be determined for each. To a large extent, these parameters can be obtained from geometrical considerations for the collimators. It is important to realize, however, that radiation scatter, penetration effects, and the uncertainty of a source distribution can considerably alter the effectiveness of a collimation system. This chapter deals with these factors and considers their individual effects on detector performance.

#### 2.1 Sensitivity

In any radionuclide detection system, the number of gamma-rays detected will always be less than the number emitted by the source, which can be distributed over any volume geometry. Since a detection system is made up of several components, one has to look at the influence of each of these separately. Following Mallard ( 36 ), we can define the fractional efficiency as:

$$\epsilon_i = \frac{\text{number of output events}}{\text{number of input events}}$$

for device  $i$ . It is obvious that the complete detection system has an overall efficiency equal to the product of all the component efficiencies:

$$\xi = \prod_i \epsilon_i \quad (2.1)$$



In clinical work, the source is generally distributed over a substantial volume, and thus the amount of radiation or activity that is viewed by the detector is usually difficult to determine analytically, if not impossible. It is therefore appropriate in sensitivity considerations to differentiate the source into infinitesimal point sources and then integrate the individual responses to each of these sources over the whole of the volume distribution.

If  $\rho_p$  is the number of gamma-ray photons emitted per unit time into a  $4\pi$  angular area by a point source and the exposed regions of the detector subtend a fractional solid angle  $\Omega$  at the source, then  $\rho_p\Omega$  is the number of photons incident on the detector per unit time. If the detection efficiency of the crystal-photomultiplier is  $\xi_D$ , then the counting rate will be:

$$C_I = \rho_p \Omega \xi_D \quad (2.2)$$

assuming that the other components of the counting system are ideal, and neglecting scatter and collimator penetration. If these latter two effects are included, then the practical counting rate will be larger than the ideal one. If  $C_S$  is defined as the count rate due to scattering alone and  $C_P$  as that due to penetration alone, then the true count rate,  $C_T$ , is given as:

$$C_T = C_I + C_S + C_P \quad (2.3)$$

The fractional increases in count rate due to scatter and penetration may be defined as:

$$f_S = C_S/C_I \quad f_P = C_P/C_I \quad (2.4)$$



Thus (2.3) may be rewritten:

$$C_T = \rho_P \Omega \xi_D (1 + f_S + f_P) \quad (2.5)$$

In (2.5), only  $\rho_P$  is directly dependent on the source, all other terms being concerned with the performance of the system. (Although  $f_S$ ,  $f_P$ ,  $\xi_D$  are obviously dependent on the energy of the photons, they are still governed by the type, thickness and material of the detector crystal and collimator). Thus the point source sensitivity ( $S_P$ ) of the system may be defined as

$$S_P = \Omega (1 + f_S + f_P) \xi_D \quad (2.6)$$

and

$$C_T = S_P \rho_P \quad (2.7)$$

It is found, however, that a line source of radioactivity is much more practical to fabricate and work with experimentally than a point source; it will also be shown that it yields more information.

If  $C_L$  is the measured count rate from a line source of radioactivity which emits  $\rho_L$  gamma-ray photons/unit length/unit time,

$$C_L = S_L \rho_L \quad (2.8)$$

and regarding the line source as an infinite number of point sources,

$$S_L = \int_y S_P dy \quad (2.9)$$

where  $S_L$  is the line sensitivity of the system. The graph of line sensitivity versus transverse displacement of the line source from the collimator axis is called a line spread function (LSF). (See Figure 4).





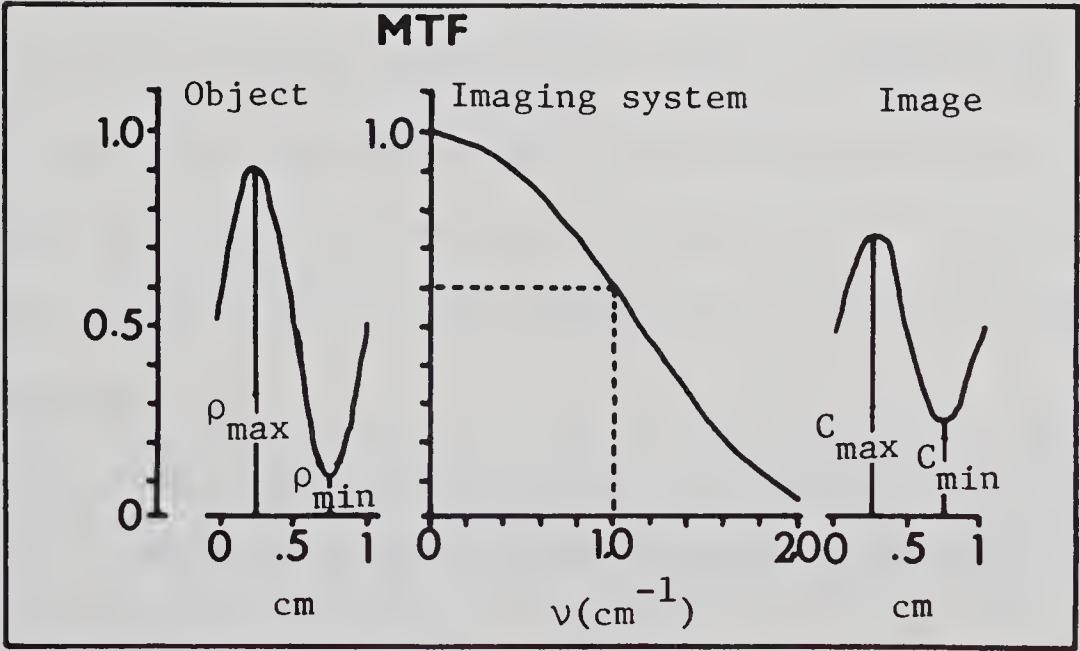
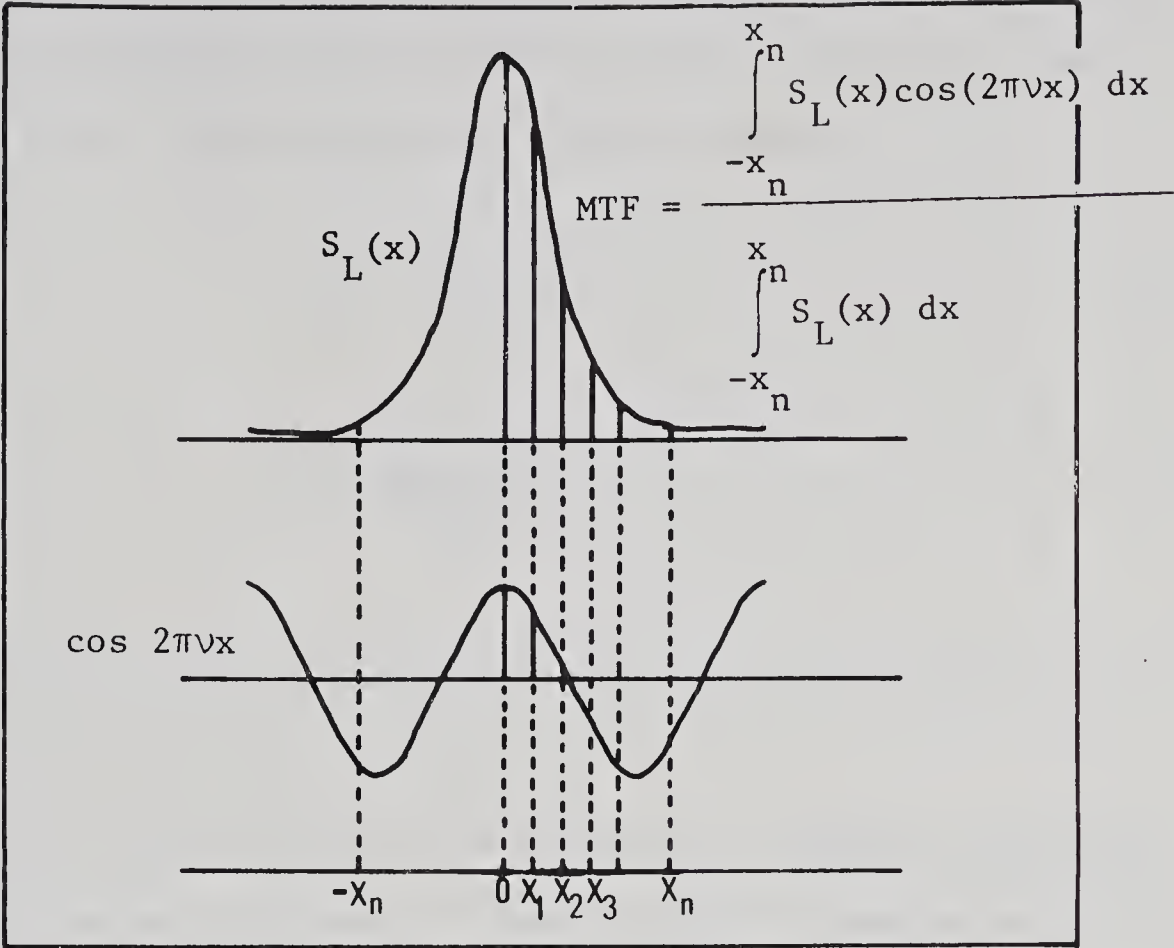


FIGURE 4



In order to obtain an LSF, the line source must be moved transversely across the field of view; it thus traces out a plane. In this way a plane source sensitivity can be obtained:

$$S_A = \frac{\int C_L dx}{\rho_L} \quad (2.10)$$

$$S_A = \frac{\iint C_P dxdy}{\rho_P} \quad (2.11)$$

Using (2.10), the plane sensitivity is therefore determined by the area enclosed by the LSF curve in Figure 4.

The plane sensitivity is valuable in comparing detection systems because the response to a plane source is independent of the distance from the detector, provided the field of view is uniformly covered by the source. This is because the increase in the area of the plane source in the field of view as the source - detector distance is increased is compensated by the decreased response to each of the infinitesimal point sources on the plane ( 37 ). Practically, however, scatter and penetration have an effect on the plane sensitivity but the variations with distance are slight compared with other source configurations. Attenuation of the gamma rays through the medium has also been neglected.

The LSF is also a valuable tool in defining the spatial resolution of a detection system. This parameter is discussed below.

## 2.2 Spatial Resolution

Spatial resolution is a measure of a system's ability to detect spatial changes of gamma-ray intensity from a radioactive source distribution. The optical analogue of resolution expresses the



minimum separation between two objects that can still be distinguishable as separate in the image.

It has become common practice to describe resolution by considering the response to sinusoidal distributions of radioactivity. In this way, any object or source distribution can be described by a set of spatial frequencies. A diffuse object with poor definition is thus described by a spectrum of low spatial frequencies while an object that has sharply defined edges requires in addition high frequency components to describe it. A mathematical analogue is found in Fourier series and transforms used to approximate edge and step functions.

Sources, or more meaningfully, source edges, can be regarded as alternating "activity amplitudes" with maximum activity  $\rho_{\max}$  and minimum activity  $\rho_{\min}$ . The source modulation is then defined as

$$m_S = \frac{\rho_{\max} - \rho_{\min}}{\rho_{\max} + \rho_{\min}} \quad (2.12)$$

The imaging system, in turn, produces an image of this modulation, which is called the image modulation:

$$m_I = \frac{C_{\max} - C_{\min}}{C_{\max} + C_{\min}} \quad (2.13)$$

where  $C_{\min}$  and  $C_{\max}$  are the minimum and maximum counting rates, respectively. The ability of the detection system in transferring the source modulation to an image modulation is represented by the modulation transfer function (MTF).

$$MTF = \frac{m_I}{m_S} \quad (2.14)$$



The source may be regarded as made up of numerous line elements and therefore the response of the detection system may be calculated by the convolution of each element with the LSF of the system. Thus, from (2.14):

$$\text{MTF}(\nu) = \frac{\int_{-x_0}^{+x_0} S_L(x) \cos(2\pi\nu x) dx}{\int_{-x_0}^{+x_0} S_L(x) dx} \quad (2.15)$$

Mallard (36)

It is evident from this consideration that the MTF is proportional to the Fourier transform of the LSF. The variable  $\nu$  is the spatial frequency parameter and has dimensions  $\text{length}^{-1}$  (See Figure 4).

Although the MTF is a valuable index of spatial resolution, in a detection system where resolution is not the prime criterion for design considerations, the MTF need not be taken into account. In single hole collimator counting systems resolution is degraded to provide for increased sensitivity. "Visualization" is not required and so the index of resolution refers mainly to the field of view. In the PFSS this determination of the field of view is an important consideration, since regional lung function is studied and overlap from adjacent regions will cause a "blurring" effect in the data analysis. The field of view is determined solely from collimator geometry, although edge penetration will increase the calculated values somewhat. Appendix B derives the configurations of the fields of view from cylindrical and rectangular collimators. It is shown that the field of view area increases as the square of the distance from the collimator face.

### 2.3 Field Response

The field response of a collimator system is valuable in determining both the spatial resolution and sensitivity of that system.







It is defined as the response of a detection system to a point source of radiation located anywhere in space. Practically, it is measured as the count rate of a system as a function of source point position. This parameter was measured for a variety of collimators and the results are presented in Chapter 4. Analytically, the field response,  $F(x,y,z)$ , is  $C_T$  from equation (2.5) measured over a source volume:

$$F(x,y,z) = \rho_p \Omega(x,y,z) \xi_D(x,y,z) [1 + f_s(x,y,z) + f_p(x,y,z)] \quad (2.16)$$

$F(x,y,z)$  is usually normalized to  $C_{T_{\max}}$ . If all points  $(x,y,z)$  that satisfy  $F(x,y,z) = \text{constant}$  are joined together, an isoresponse or isocount response line is formed. When several values of constants are used, isoresponse contours are generated. The depth of the field response contours indicates the sensitivity of the detection system as a function of distance; the broadness or width of the isoresponse lines indicates spatial resolution capabilities of the system. By comparing these isoresponse curves from different collimators, and collimator systems, both sensitivity and resolution can be optimized for particular purposes. The methods used to measure field response are considered in Chapter 3 - Experimental Design.



## CHAPTER THREE

### EXPERIMENTAL DESIGN

#### 3.1 Instrumentation

##### 3.1.1 Raster Scanner

In order to measure field response of the several collimators studied, a volume source distribution was needed. It was decided that the required source distribution could be most easily attained by integrating a point source of radiation over the appropriate volume. In practice, this integration is achieved by mechanically "scanning" the point source over the volume. Major design criteria for this scanner were the precision and accuracy required in source - detector positioning. Commercial scanning devices were initially considered for these studies, but none was available that could be modified to suit our requirements. The adaptation of a micro-manipulation device, such as is used in scanning microscopy, was then considered as a basis for our scanning unit. However, the available range of movement with these devices is generally limited to about 5.0 cm on a side, which was insufficient for our proposed measurements of about 25 cm a side (an approximation to the thorax dimensions).

The cost of these several commercial devices was also high, thus it was decided to undertake the design and construction of the raster scanner for this particular application. The mechanical arrangement in this design is shown in Figure 5.

Two Herst synchronous motors drive the source platform at a constant speed of 0.25 mm/sec in x or y directions (Figure 6 ).





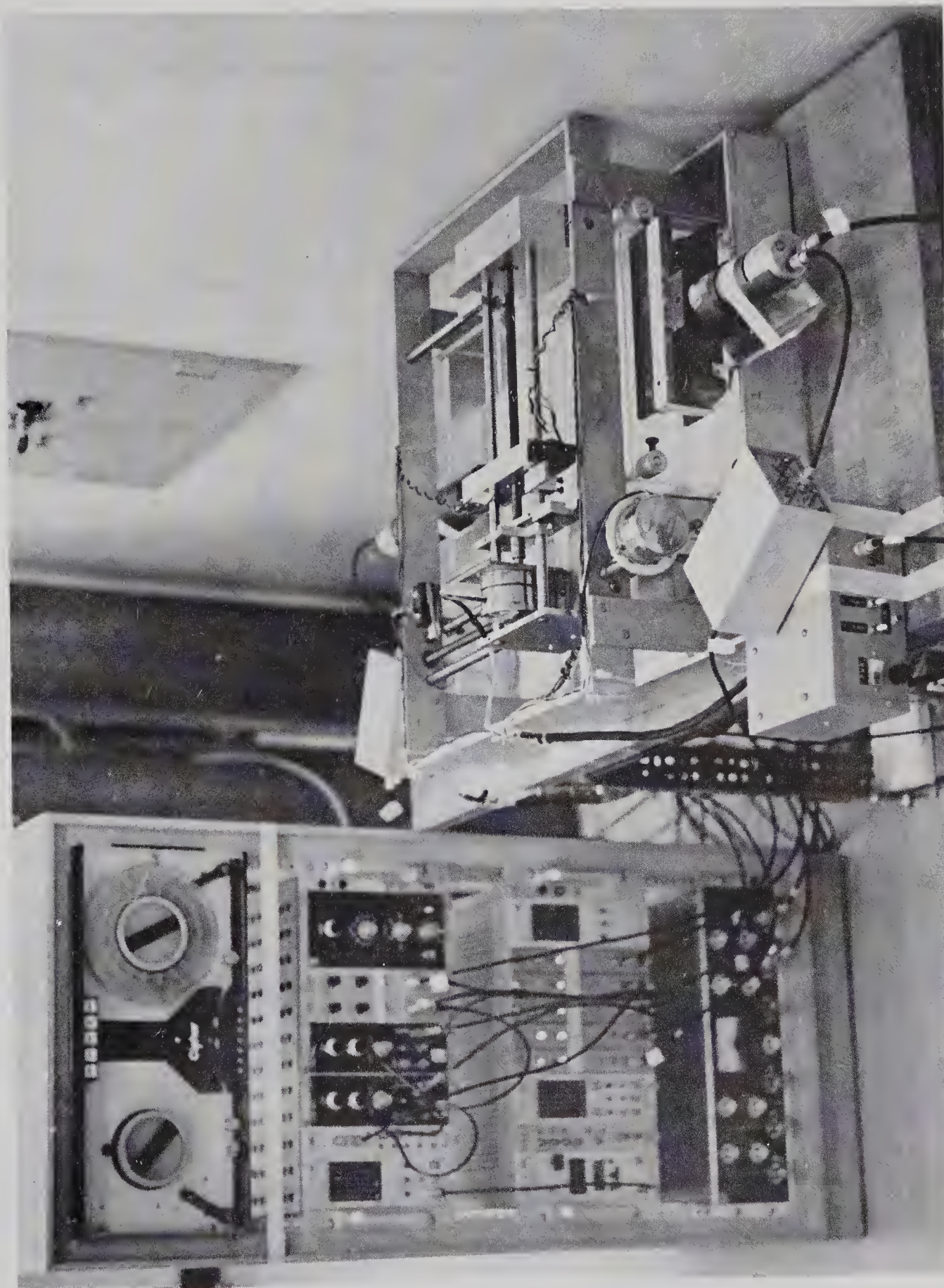


FIGURE 5



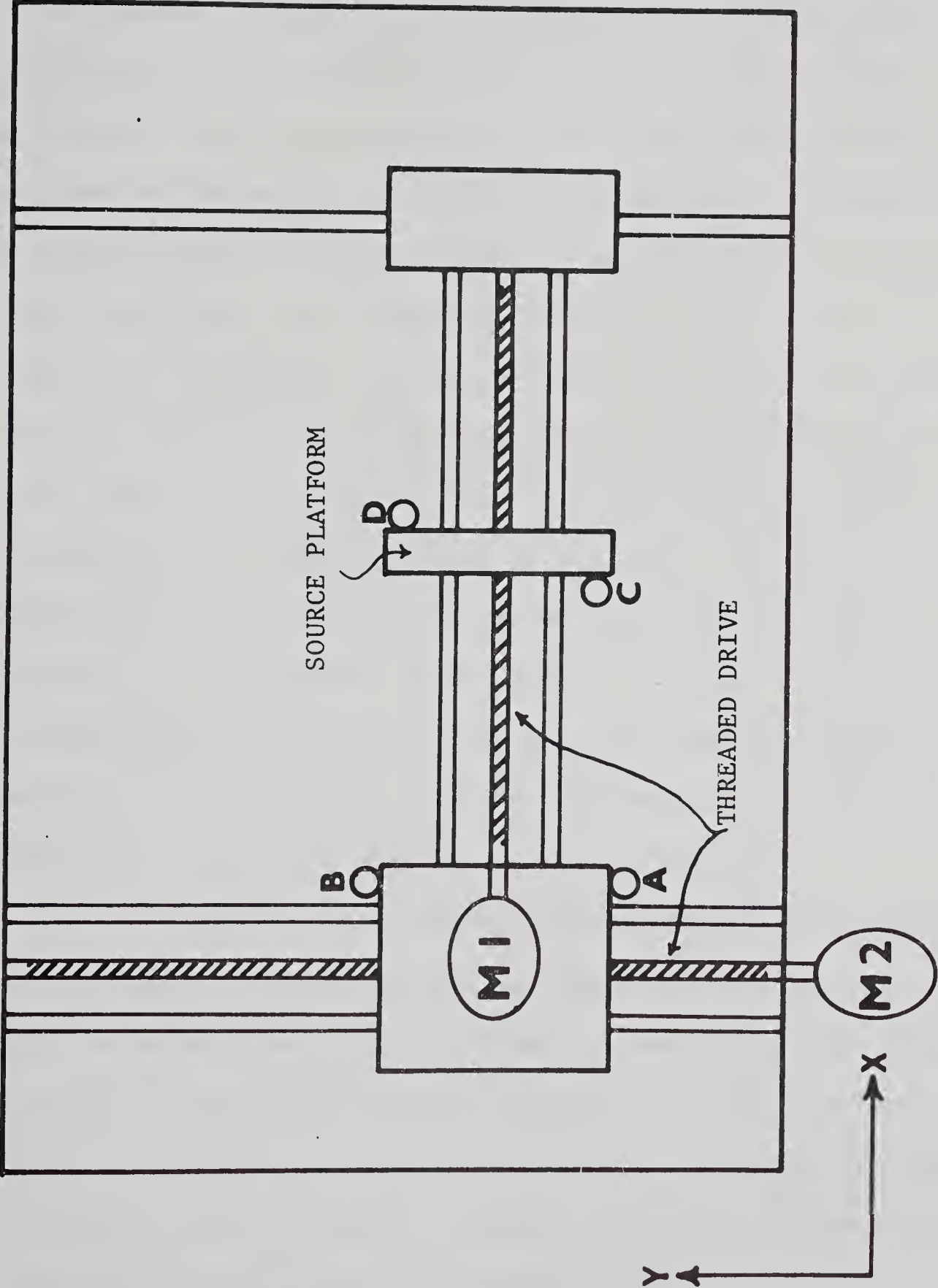


FIGURE 6

M1 , M2 → MOTORS  
A,B,C,D → MICROSWITCHES



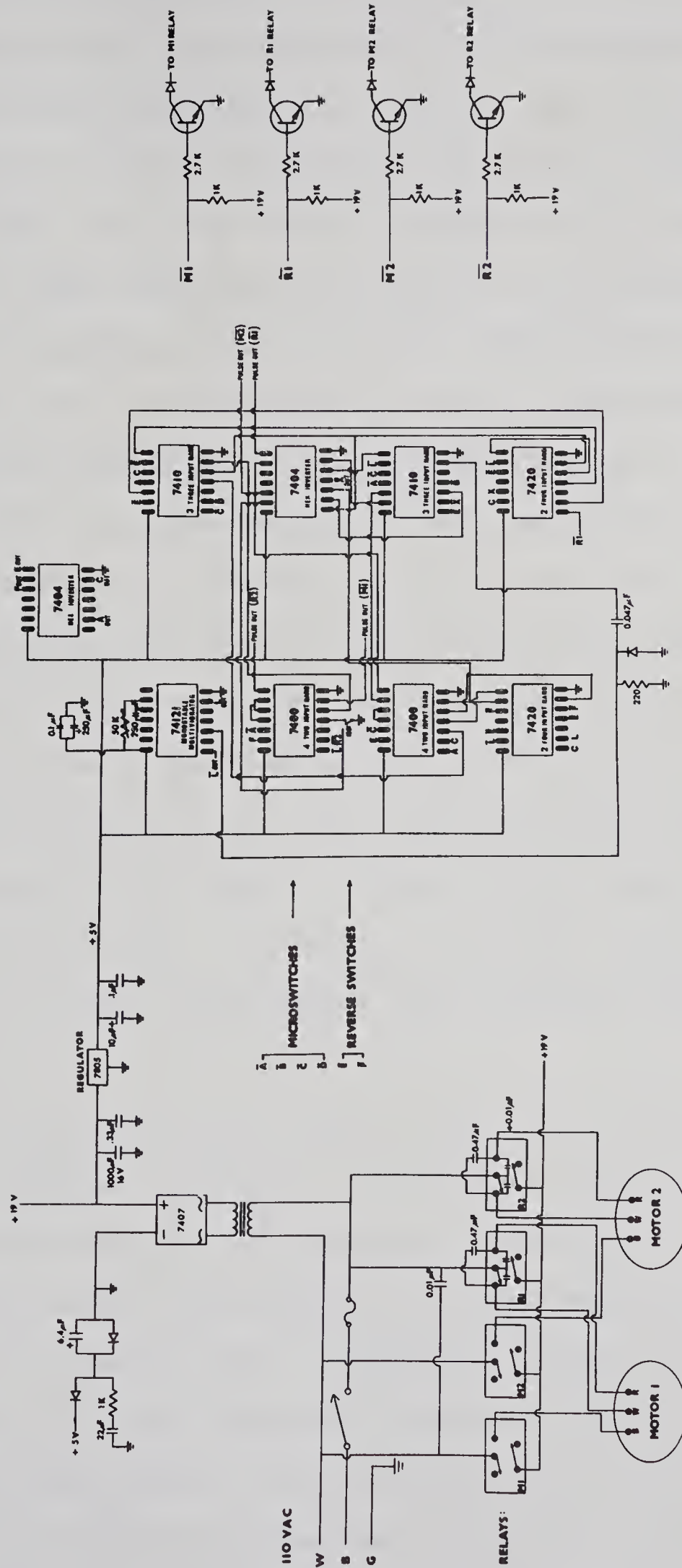


The maximum range of the scanner is 25 cm in the x direction and 26 cm in the y direction. The ranges can be varied within these maximum values by means of aluminum "stops" and microswitches.

An electronic logic device was designed to control the motion of the scanner (Figure 7). In operation, the scanning system is initialized with the source platform at (x,y) equal to (0,0). A pushbutton "start" provides power to the x motor which drives the platform to the end of the desired x scan length. A microswitch at this end-point provides a signal to stop the x-drive motor and start the y-drive motor for a preset time. This preset "on-time" of the y motor is controlled by means of a variable resistor and ranges between 40 nsec to 40 sec in duration. For the scans reported in this thesis the y motor was set to be driven for 10 seconds, during which time the platform and x motor assembly moved 2.5 mm. At the end of this preset time the y motor is shut off and the x motor started in reverse, bringing the platform back to the initial x value. At this point it is again stopped by a microswitch, and the y motor driven for another period of 10 seconds. One cycle of this system is completed after this latter 10 second period when the y motor is shut off.

In this way, the source platform traverses the area desired in a raster pattern. The scanning assembly stands at a height of about 15 cm with the collimator-crystal combinations mounted underneath the motor platform and the source suspended from the platform on a rigid rod. The source was positioned in the same plane as the detector longitudinal axis so that the (assumed) symmetrical response of the crystal could be used for calculation purposes.





I.C.'S ARE 7400 SERIES TTL NAND LOGIC  
TRANSISTORS SHOWN ARE 2N 3904  
DIODES SHOWN ARE 1N4006

FIGURE 7



### 3.1.2 Data Acquisition System

Each detector used was coupled to a pulse-shaping preamplifier. The pulse from the preamplifier was negative, 2  $\mu$ sec in length and nominally 10 mv in height for the 80 keV photopeak of  $^{133}\text{Xe}$ . The signal was then routed to an amplifier (HAMNER RC NA-11) and amplified to a 2-8 volt range (depending on the energy of the original incident gamma ray). It was then routed to a single channel analyser which was set to accept pulses corresponding to an energy range equal to that of the incident gamma rays. If the input pulse was in the correct energy "window" then a positive 10 volt pulse was provided to a scaler to record the event. Six 10 MHz scalers were linked in a "daisy chain" with a timer-scaler, and magnetic tape controller for a CIPHER seven track, write-only tape transport. The data on the scalers could thus be stored on magnetic tape after a preset data gathering period. After each record was written on the tape, the scalers were initialized and a new counting period was begun. A "record" on the tape was composed of a 42 digit BCD number. Each group of six digits comprised the count from one scaler, and therefore, each individual scaler could be identified.

At the end of each x-scan, by means of the microswitch on the source platform, a positive 5 volt pulse was sent to a "y position" scaler. By inspection of this scaler, the position of the source could be determined for any time interval, or for any particular data record. At the end of a complete scan, a microswitch provided a pulse to the appropriate scaler, thus "labelling" the termination of the scan. In the studies reported here, five scalers were used for data acquisition and coordinate position determination. The scalers in the "daisy chain" not in use were recorded on tape as having a zero count.





The data collection period was chosen to be 10 seconds, during which time the source moved 2.5 mm. At the end of the data acquisition period, the contents of the several scalers were written on tape and the scaling system reset. Each record was thus 10 seconds apart in time and 2.5 mm apart in space.

In these studies a normal scan of 20 cm by 23 cm required about 20 hours to complete and comprised some 7500 individual data records on tape. Data "blocking" could not be achieved with the magnetic tape unit available to this investigation, thus each scan occupied about 150 meters of tape. These data tapes were subsequently blocked and rewritten prior to processing using the IBM 360/67. Under normal circumstances about 20 individual scans were stored on one 180 meter tape reel.

### 3.1.3 Data Analysis

The data was read from tape and all records stored in core, each record being corrected for radioactive decay. A search was made for end-of-x-scan points by looking for two consecutive non-zero records from the particular scaler attached to the x-scan microswitch. By comparing x-scan lengths, artefacts due to line noise could be rejected, and the data then segmented into a number of one dimensional scans as detailed schematically in Figure 8 .

The maximum count in the scan matrix was then found and all records normalized to this value. This normalization procedure reduced the data from "count rate" to fractions of the maximum count rate. A plot file was then prepared by storing these fractions in a matrix array, the individual matrix elements corresponding one to one to an individual record in time and space. When the matrix was completed a





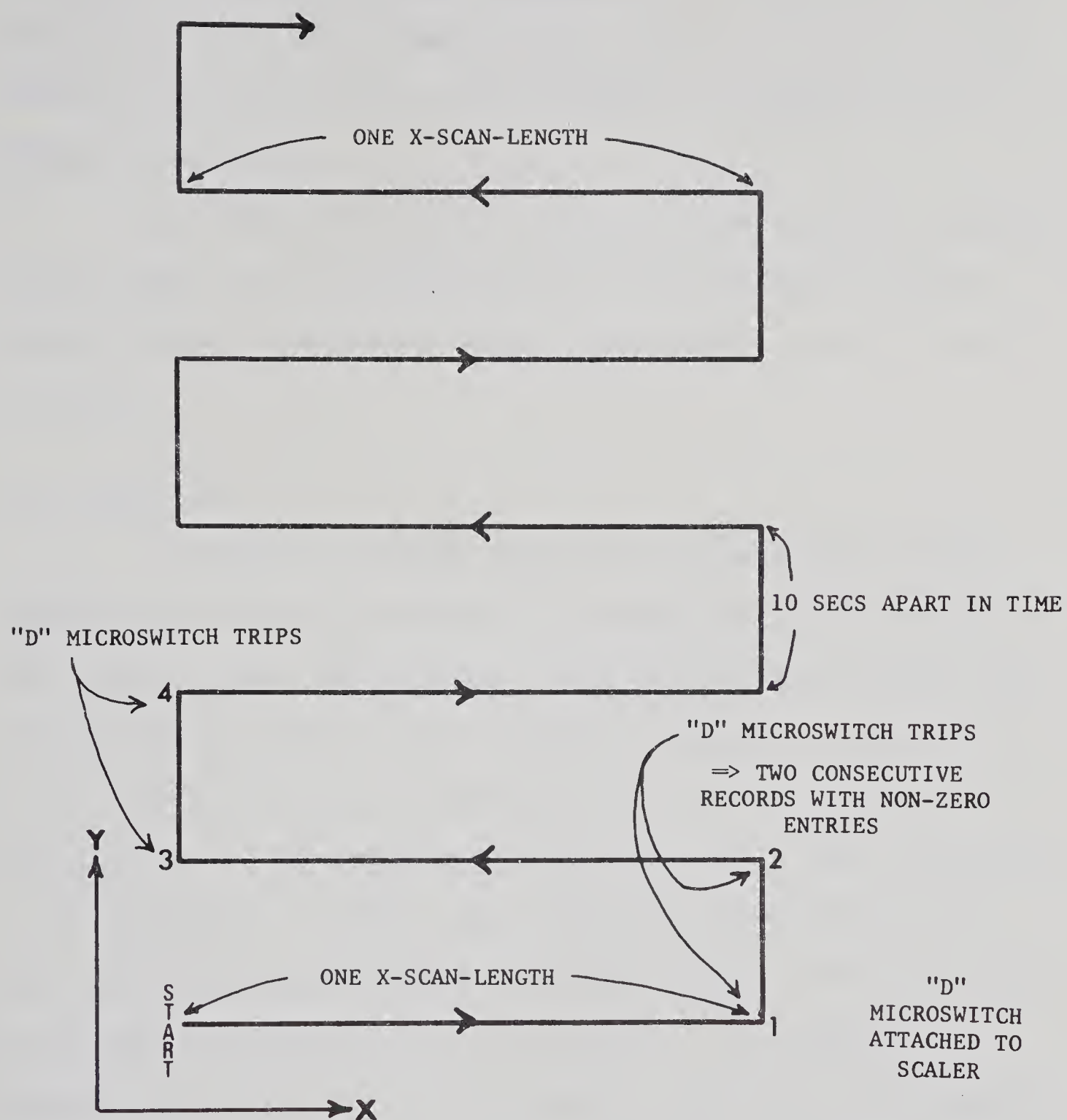


FIGURE 8



least-squares curve-fitting technique joined equal-valued records into an isocount response curve. This plot was stored into a final plot file and an isoresponse contour map drawn by a Calcomp plotter. The number of contours in this map and their values could be arbitrarily chosen by the operator and could be entered as parameters into the program via keyboard.

The interactive program (Appendix E) was written in Fortran IV and ran under the MTS operating system of the IBM 360/67 computer. Similar programs were used to analyse scans from one, two, or three detectors.

### 3.2 Modelling

In addition to making experimental measurements of field response for various source-detector configurations it was decided to also simulate these configurations and determine field response using the theoretical considerations discussed in Chapter 2. The purpose of this simulation was to determine the validity of the theoretical specifications of resolution and sensitivity, with a direct comparison to the experimental results. Also, using this "modelling" theory, lung configurations encountered by the PFSS detectors which could not be measured experimentally could be simulated. For example, rib absorbers were introduced into the modelled program and corresponding field responses calculated; this could not be done with the experimental scanning system. The approach taken in devising the modelling algorithm follows.

As discussed in Chapter 2, the simplest way to model a source distribution is to calculate point responses from a number of equally spaced points in the source volume and integrate these responses. With the raster scanner, a plane source response is measured. This plane is



parallel to the longitudinal axis of the cylindrical crystal. Making the approximation that the crystal response is circularly symmetric, the plane response can be rotated about the crystal axis and a three-dimensional volume response obtained. This method, however, assumes the source medium is homogeneous in absorption characteristics. In most clinical situations this is not true. For example in the lung (as viewed by the PFSS) the location from which a gamma-ray is emitted from the interior of an alveolus, and its direction, govern the amount of air and tissue absorber that it must pass through before reaching the detector. Part of this path might also lie through a rib.

A model is needed that accounts for these situations of absorber inhomogeneity. The approach taken was the use of a ray-tracing grid system. The source plane was broken up into an array of source points. The crystal face was also replaced by a grid system of points, lying in the  $z=0$  plane in normal 3-space. The collimators, absorber configurations (such as ribs), and tissue planes were described analytically. Each point on each grid had a unique set of cartesian rectangular coordinates assigned to it. The detector grid (DG) was used as the reference grid. From each point ( $P_D$ ) on the DG, lines were generated to all points ( $P_S$ ) on the source grid (SG). The equations of the lines were determined, and the various collimator, bone, and tissue attenuation distances, if any, calculated. The theory of this ray tracing method is detailed in Appendix C.

Besides considering attenuation of the gamma rays by bone and tissue, and also the attenuation due to possible collimator penetration, the solid angle factor for each detector-source point and each detector point-source point arrangement had also to be determined.





The calculation of these solid angles is detailed in Appendix D. The method used is that described by Gardner and Verghese ( 38 ) and consists of replacing the crystal disk by an equal area right polygon with total number of sides  $n$ , where  $n$  is even.

This solid angle,  $\Omega (s,R,\rho)$ , where  $s$  is the height of the source point above the crystal,  $R$  the radius of the crystal, and  $\rho$  the distance between the center of the crystal and the projection of the source point on the crystal plane, must be calculated for each source grid point. Let

$$\Omega_i \equiv \Omega (s,R,\rho) \quad (3.1)$$

for source point  $i$  with coordinates  $(x_S, y_S, z_S)$ .  $\Omega_i$  will be the solid angle subtended by the total crystal face from point  $i$ . However, the crystal will be broken up into an array, and therefore, each detector point must be considered separately. This is achieved by weighting all grid points, relative to each other, with respect to the solid angle. Since a solid angle depends on the area exposed and the distance from the subtended point, these were the criteria chosen to determine the weighting factors. For a detector point  $j$  and a source point  $i$  (Figure 9), the weighting factor becomes:

$$w_{ij} = \frac{\cos \theta_{ij}}{r_{ij}^2} \quad (3.2)$$

If the area of each square on the detector is identical, then the relative area exposed by each square will be directly proportional to the angle from the vertical that the ray  $ij$  makes. Hence the need for





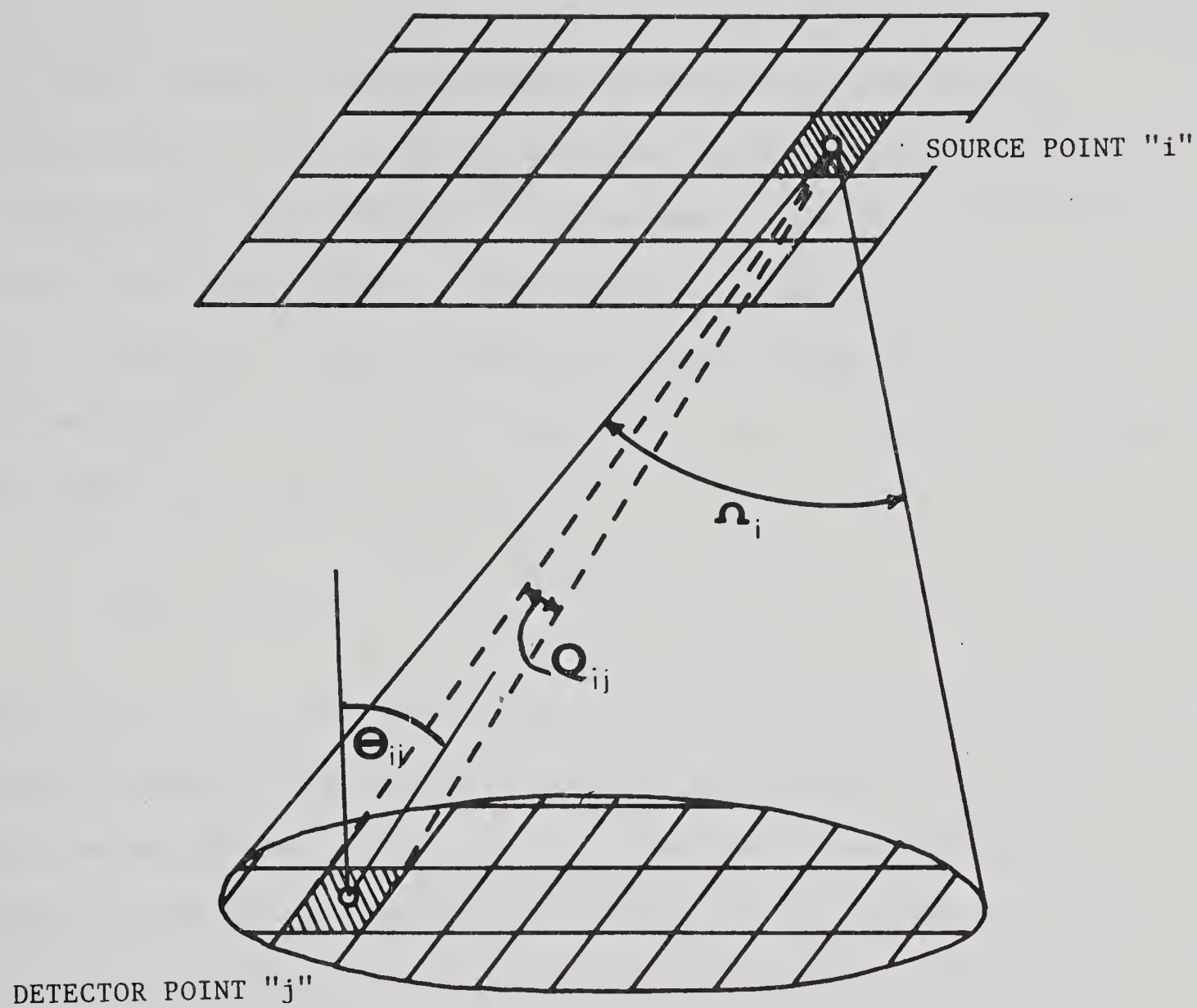


FIGURE 9



the cosine term in (3.2). Now, define

$$Q_{ij} = \frac{w_{ij}}{\sum_k w_{ik}} \Omega_i \quad (3.3)$$

$Q_{ij}$  is the assigned relative fraction of the total solid angle  $\Omega_i$  for the detector point  $j$ . In summarizing, if the source point  $i$  emits  $X_i$  gamma-rays per unit time into a  $4\pi$  geometry, then  $\Omega_i X_i$  gamma photons per unit time are incident on the crystal. The detector point  $j$  receives  $Q_{ij} X_i$  of these. Of course the beam is further attenuated by tissue, air, and possibly bone and collimator material. Thus the portion of activity from point  $i$  that point  $j$  detects is

$$A_{ij} = Q_{ij} X_i e^{-\mu_t t_{ij}} e^{-\mu_a a_{ij}} e^{-\mu_b b_{ij}} e^{-\mu_c c_{ij}} \quad (3.4)$$

where  $\mu_t$ ,  $\mu_a$ ,  $\mu_b$ ,  $\mu_c$  are the linear attenuation coefficients for tissue, air, bone, and collimator material respectively for a given gamma-ray energy and  $t_{ij}$ ,  $a_{ij}$ ,  $b_{ij}$ ,  $c_{ij}$  are the corresponding path lengths through these materials for the ray  $ij$ . By summing  $A_{ij}$  over either of its indices, interesting values are obtained.  $\sum_i A_{ij}$  is the total amount of radiation that reaches detector point  $j$ .  $\sum_j A_{ij}$  is the amount of activity that is detected by the total crystal from a source point  $i$ , and is equal to the field response parameter  $F(x,y,z)$  from equation (2.16). For a raster scanner simulation, the value  $\sum_j A_{ij}$  is stored in a location corresponding to source position  $i$  ( $x_s, y_s, z_s$ ) and after all rays have been traced, identical values are joined to form isocount response curves.



Most configurations scanned were also modelled, as described above; the algorithms used are described in Appendices C and D.

The results of both the experimental and modelling studies are presented in the next section.



## CHAPTER FOUR

### RESULTS AND DISCUSSION

#### 4.1 Introduction

Four types of collimators were studied: (1) straight cylindrical, (2) tapered cylindrical, (3) straight rectangular and (4) tapered rectangular.

A total of twenty-eight scans were done. Each collimator arrangement was assessed for a photon source in both air and water. The responses for both  $^{22}\text{Na}$  (551 keV) and  $^{133}\text{Xe}$  (80 keV) were determined. The experimental source-detector configurations studied are summarized in Table 1.

The experimental studies were carried out in parallel with theoretical simulations of the same source-detector geometries, employing the modelling theory developed earlier. These simulated isocount contours were compared with the experimental results in order to determine the range of applicability of the theoretical model. In this way, response curves from source-detector geometries that we were unable to duplicate experimentally could be obtained from the theoretical model.

The ray-tracing algorithm derived was general and allowed the study of several source-attenuator-collimator-crystal models. Both homogeneous and inhomogeneous distributions of radioactive source and attenuating media were evaluated. Source to tissue surface distance and tissue surface to collimator and crystal distance could be varied. The gamma ray energy considered was also varied as required for any one model but monoenergetic sources were assumed. Collimator type (e.g. cylindrical, conical, rectangular ) and construction material could also be changed as required.





TABLE 1 - Experimental Detector - Source Configurations

COLLIMATOR	SOURCE	ENERGY (keV)	MEDIUM	PAGE NO.
CC	$^{133}\text{Xe}$	80	AIR	40 , 41
CS	$^{133}\text{Xe}$	80	AIR	40 , 41
CD	$^{133}\text{Xe}$	80	AIR	40 , 41
R-0 <sup>o</sup>	$^{133}\text{Xe}$	80	AIR	42 , 43
R-30 <sup>o</sup>	$^{133}\text{Xe}$	80	AIR	42 , 43
R-45 <sup>o</sup>	$^{133}\text{Xe}$	80	AIR	42 , 43
R-60 <sup>o</sup>	$^{133}\text{Xe}$	80	AIR	42 , 43
CC	$^{133}\text{Xe}$	80	H <sub>2</sub> O	48 , 49
CS	$^{133}\text{Xe}$	80	H <sub>2</sub> O	48 , 49
CD	$^{133}\text{Xe}$	80	H <sub>2</sub> O	48 , 49
R-0 <sup>o</sup>	$^{133}\text{Xe}$	80	H <sub>2</sub> O	50 , 51
R-30 <sup>o</sup>	$^{133}\text{Xe}$	80	H <sub>2</sub> O	50 , 51
R-45 <sup>o</sup>	$^{133}\text{Xe}$	80	H <sub>2</sub> O	50 , 51
R-60 <sup>o</sup>	$^{133}\text{Xe}$	80	H <sub>2</sub> O	50 , 51
CC	$^{22}\text{Na}$	511	AIR	56 , 57
CS	$^{22}\text{Na}$	511	AIR	56 , 57
CD	$^{22}\text{Na}$	511	AIR	56 , 57
R-0 <sup>o</sup>	$^{22}\text{Na}$	511	AIR	58 , 59
R-30 <sup>o</sup>	$^{22}\text{Na}$	511	AIR	58 , 59
R-45 <sup>o</sup>	$^{22}\text{Na}$	511	AIR	58 , 59
R-60 <sup>o</sup>	$^{22}\text{Na}$	511	AIR	58 , 59
CC	$^{22}\text{Na}$	511	H <sub>2</sub> O	64 , 65
CS	$^{22}\text{Na}$	511	H <sub>2</sub> O	64 , 65
CD	$^{22}\text{Na}$	511	H <sub>2</sub> O	64 , 65



TABLE 1 - Continued.....

COLLIMATOR	SOURCE	ENERGY (keV)	MEDIUM	PAGE NO
R-0°	$^{22}\text{Na}$	511	H <sub>2</sub> O	66 , 67
R-30°	$^{22}\text{Na}$	511	H <sub>2</sub> O	66 , 67
R-45°	$^{22}\text{Na}$	511	H <sub>2</sub> O	66 , 67
R-60°	$^{22}\text{Na}$	511	H <sub>2</sub> O	66 , 67
Miniature	$^{133}\text{Xe}$	80	AIR	72
Miniature	$^{133}\text{Xe}$	80	H <sub>2</sub> O	72
Miniature	$^{133}\text{Xe}$	80	H <sub>2</sub> O + SKULL	72
Coincidence	$^{22}\text{Na}$	511	AIR	73
Coincidence	$^{22}\text{Na}$	511	H <sub>2</sub> O	74

Legend: CC - Cylindrical Converging

CS - Cylindrical Straight

CD - Cylindrical Diverging

R-0° - Rectangular - 0° Taper from Normal

R-30° - Rectangular - 30° Taper from Normal

R-45° - Rectangular - 45° Taper from Normal

R-60° - Rectangular - 60° Taper from Normal



## 4.2 Details of Collimators Studied

The straight cylindrical collimator was made of lead, 6 mm thick. The crystals used were 25.4 mm diameter, 12.7 mm thick NaI(Tl) (Harshaw Chemical Company), and were placed 7.6 cm back from the face of the collimators.

The tapered cylindrical collimator was machined from a stock brass cylinder, 6.35 cm in diameter. The inside diameters of this collimator were 3.175 cm and 1.905 cm respectively; the total length of the collimator was 7.6 cm and taper angle  $4.76^\circ$ . This collimator was used in both converging and diverging directions.

The rectangular collimator was fabricated from 0.635 cm cold-rolled steel plate, and its dimensions are shown in Figure 10. One side was designed to swivel around its end, permitting measurements to be made of a tapered rectangular collimator, with varying degrees of taper.

A miniature detector system, comprising a 0.6 cm diameter, 1.27 cm thick NaI(Tl) crystal was also studied. The crystal was recessed 9 cm from the face of a straight, cylindrical, stainless steel and lead collimator 1.27 cm internal diameter. In these particular studies, a Rhesus monkey skull was placed against the collimator face to simulate gamma-ray scattering effects in bone.

In addition to the single photon measurements, coincidence scans in both air and water were performed, without collimation, using a  $^{22}\text{Na}$  source.

In the modelling program, the crystal was always assumed to be a right cylinder, although two different sizes were used. One crystal



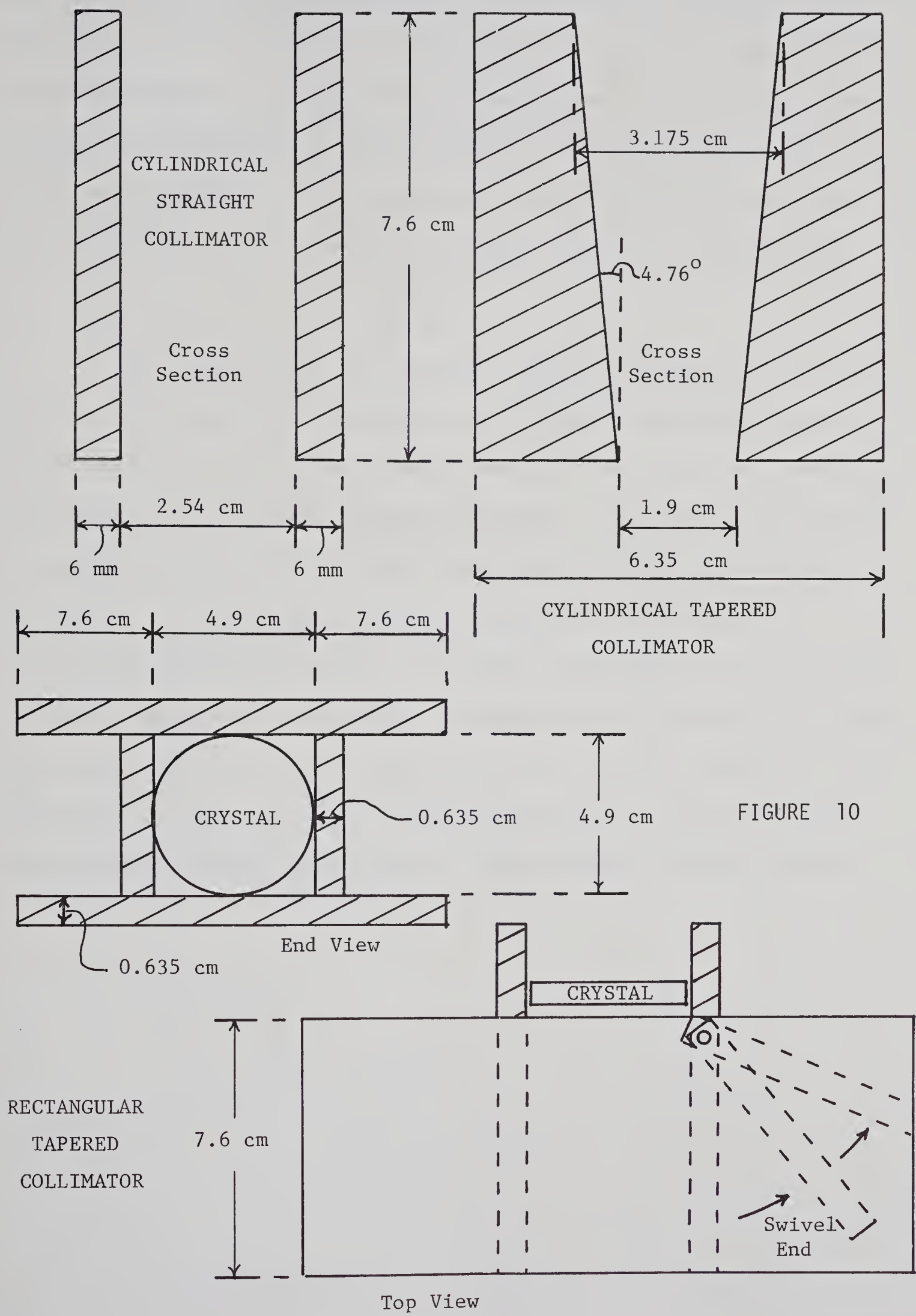


FIGURE 10





was taken to be 2.54 cm in diameter, 1.27 cm thick, of the type used in the PFSS; the other was 0.6 cm diameter, 1.27 cm thick as used in the miniature system for cerebral blood flow studies. The 2.54 cm diameter crystal was replaced by a square grid with points spaced at 2 mm for a total of 129 points. The source grid points were set at a spacing of 5 mm but the source array was made much larger, with 40 x 40 grid points.

#### 4.3 Experimental Scans and Models

The experimental and simulated scans are presented in Figures 11-47 . For a particular combination of source and attenuating medium, field responses for the cylindrical straight, converging and diverging collimators are presented in the same figure. Field responses for the rectangular collimators (straight and tapered) for the same source-attenuator combinations are presented immediately following the cylindrical results in order to facilitate comparisons. The simulated scans for particular experimental arrangements are presented following the experimental data. The jaggedness of the isocount contours in the experimental scans is due to random fluctuations in source activity. Scan numbers prefixed with an M are those produced from the computer.



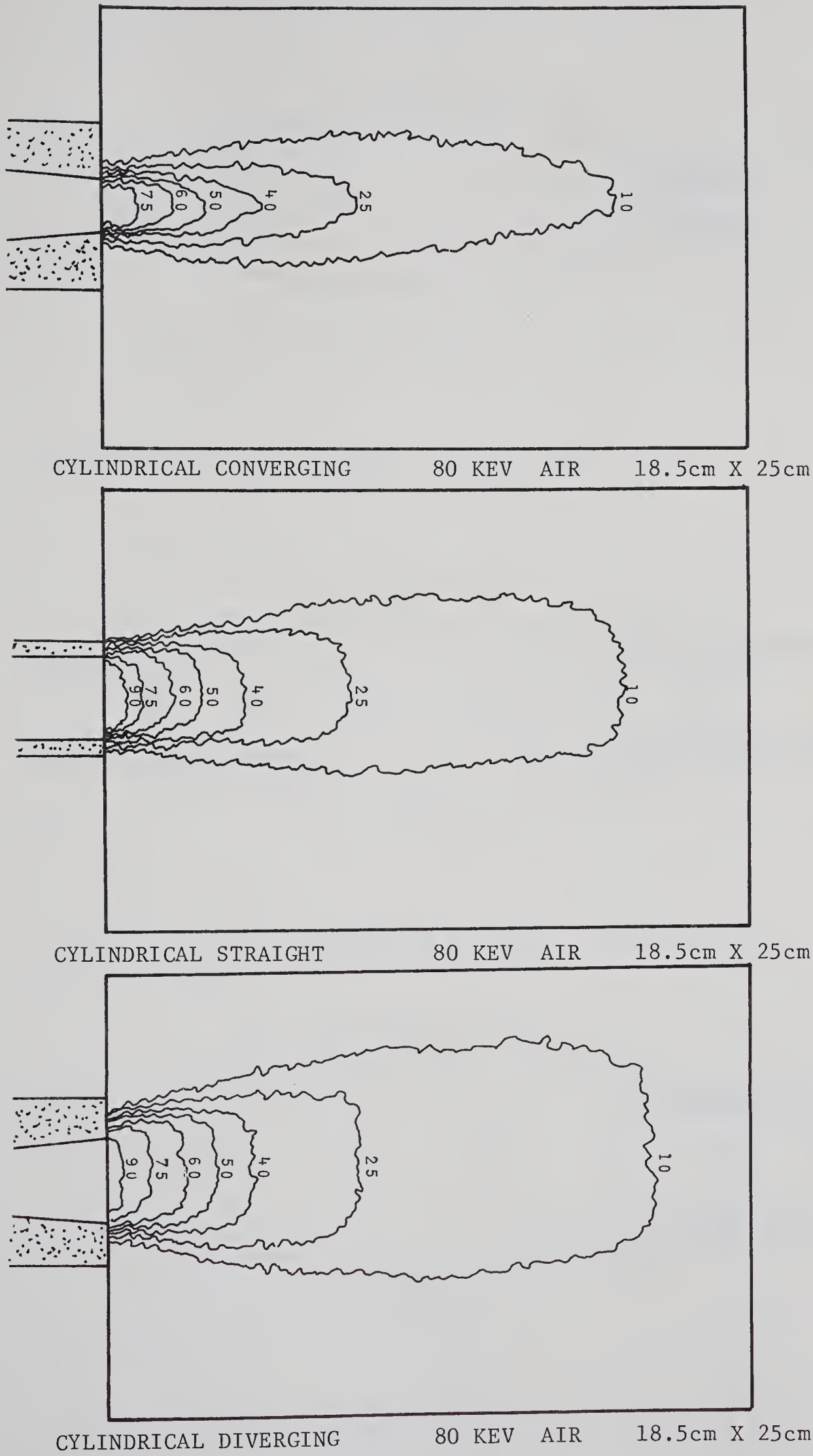
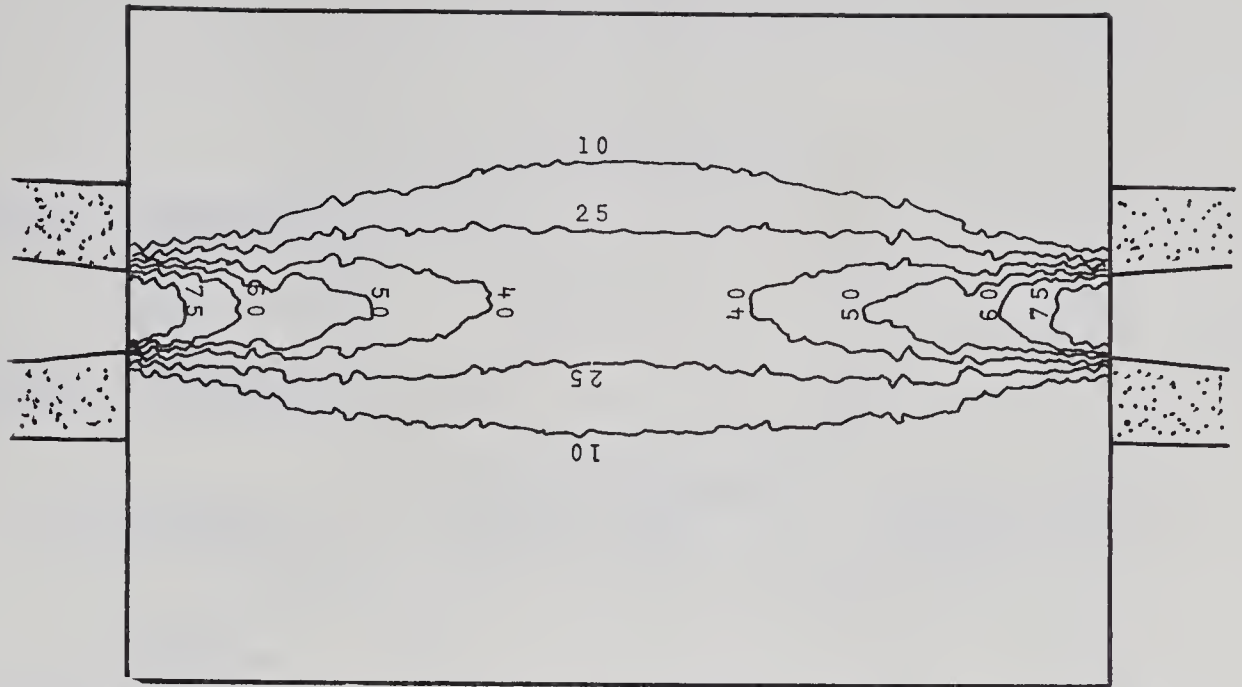
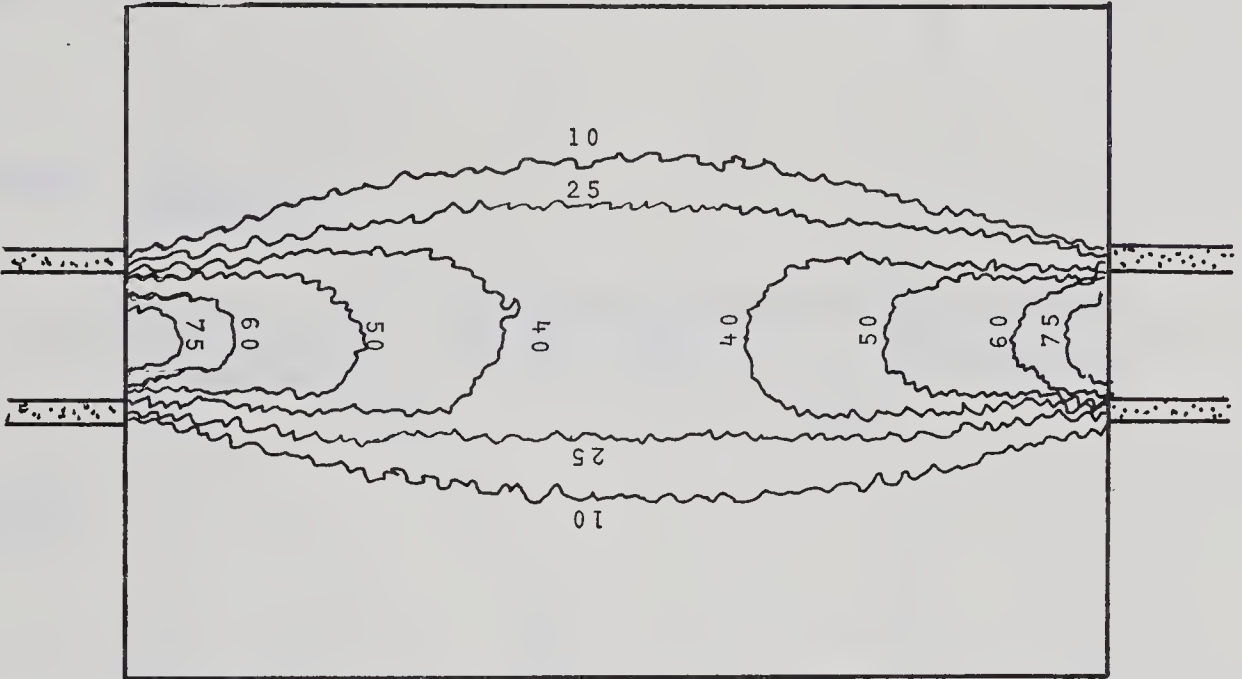


FIGURE 11

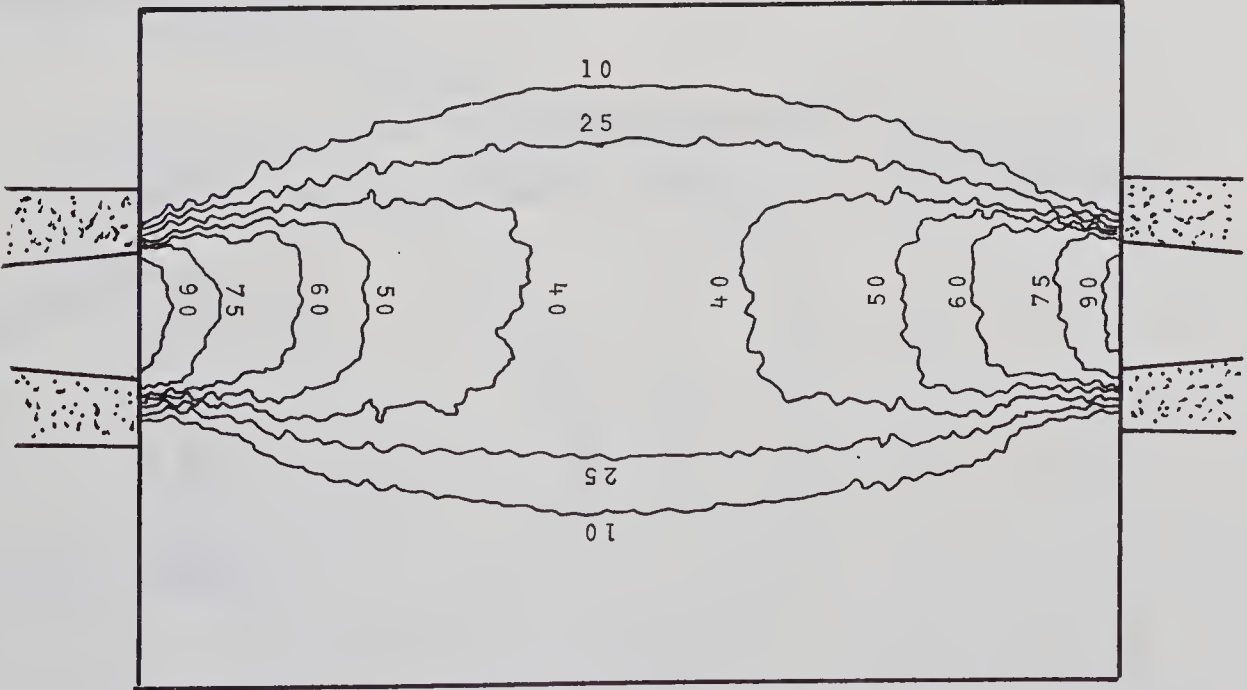




CYLINDRICAL CONVERGING-SUM 80 KEV AIR 18.5cm X 25cm



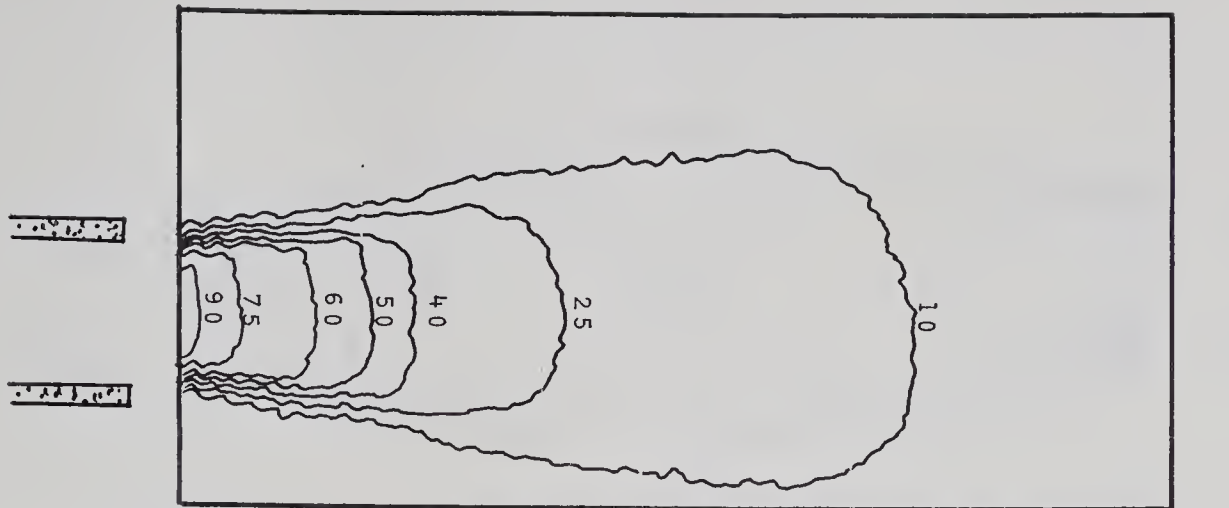
CYLINDRICAL STRAIGHT-SUM 80 KEV AIR 18.5cm X 25cm



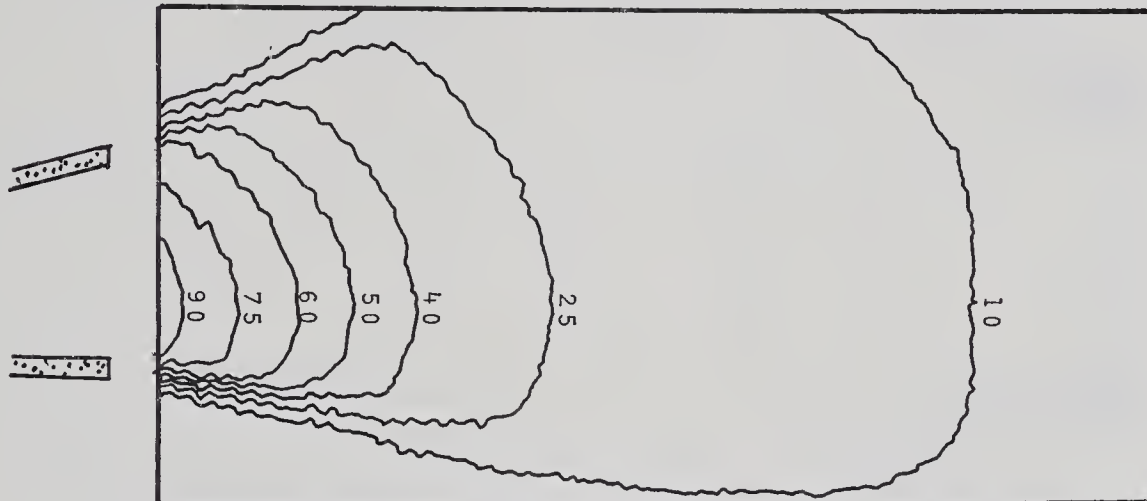
CYLINDRICAL DIVERGING-SUM 80 KEV AIR 18.5cm X 25cm

FIGURE 12

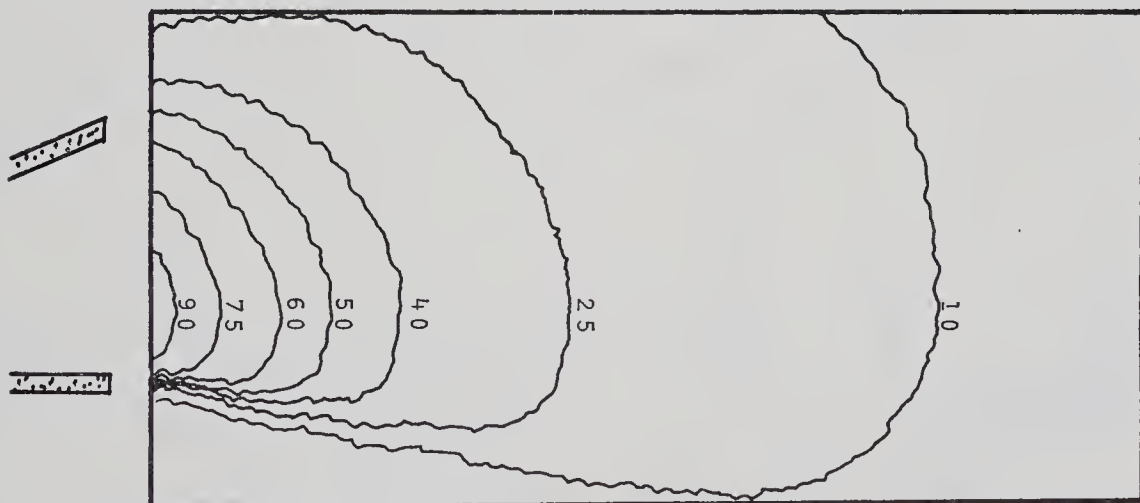




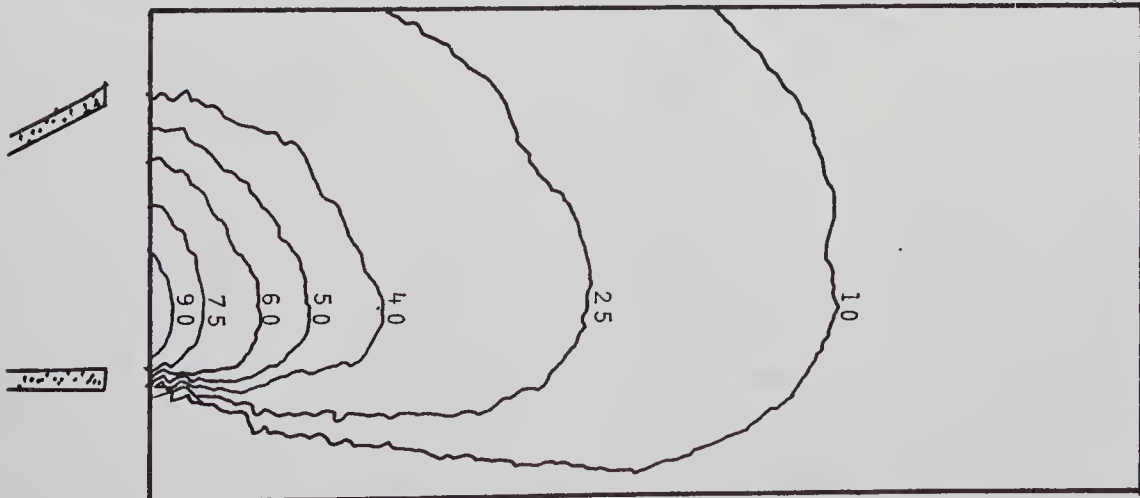
RECTANGULAR 0° 80 KEV AIR 24.1cm X 25cm



RECTANGULAR 30° 80 KEV AIR 24.1cm X 25cm



RECTANGULAR 45° 80 KEV AIR 24.1cm X 25cm

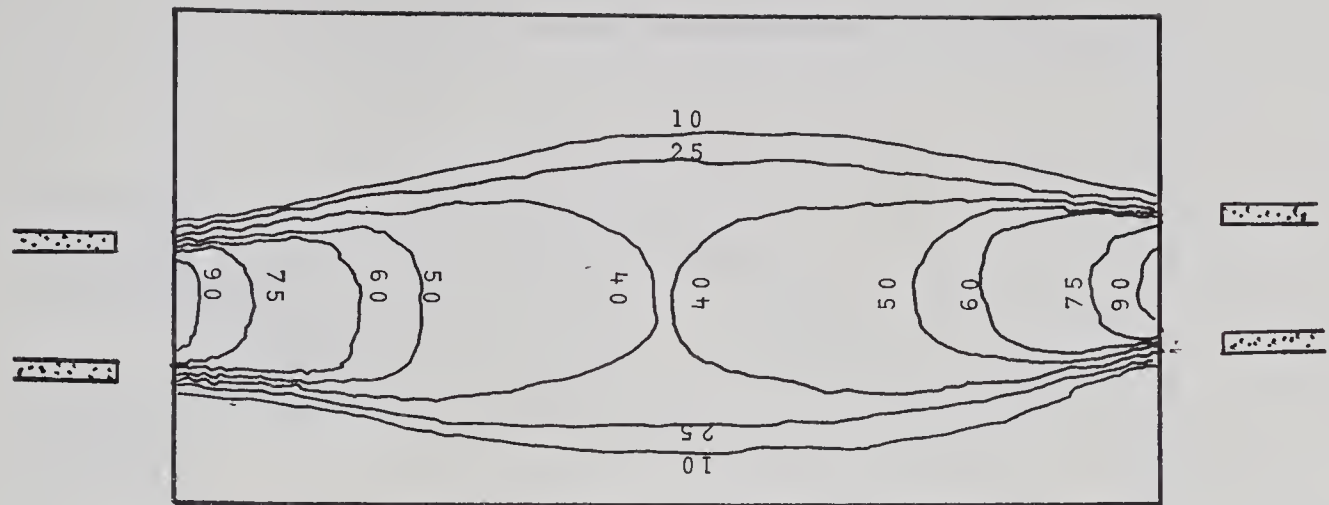


RECTANGULAR 60° 80 KEV AIR 24.1cm X 25cm

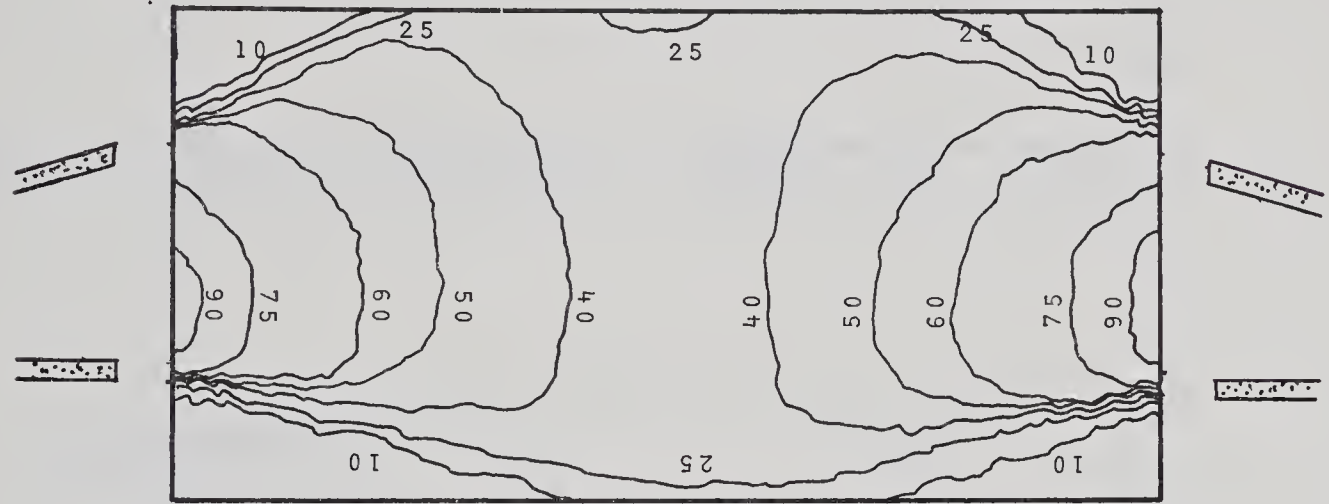
FIGURE 13



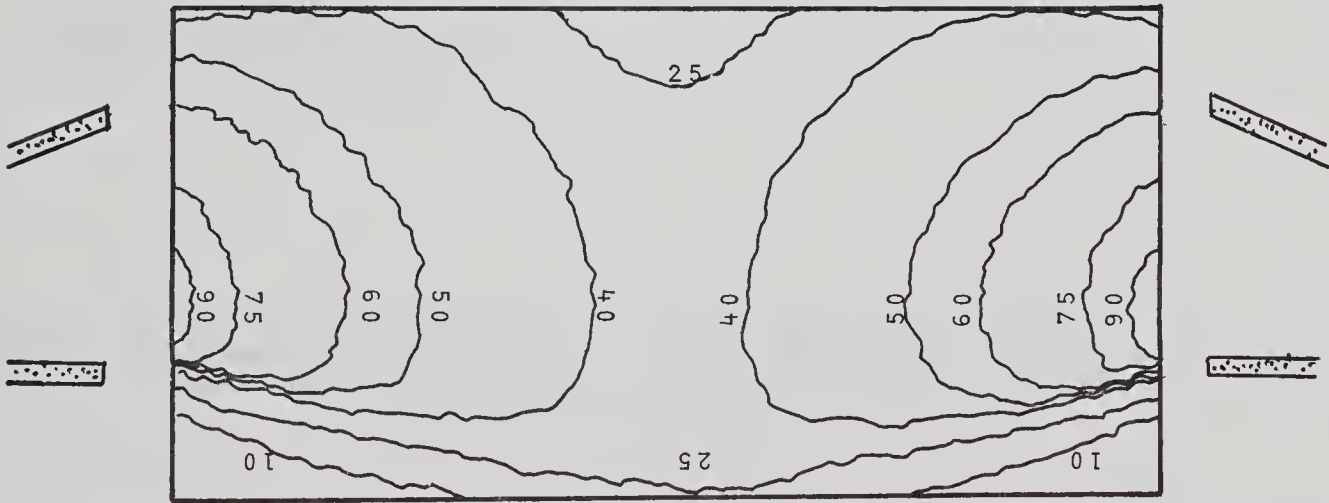




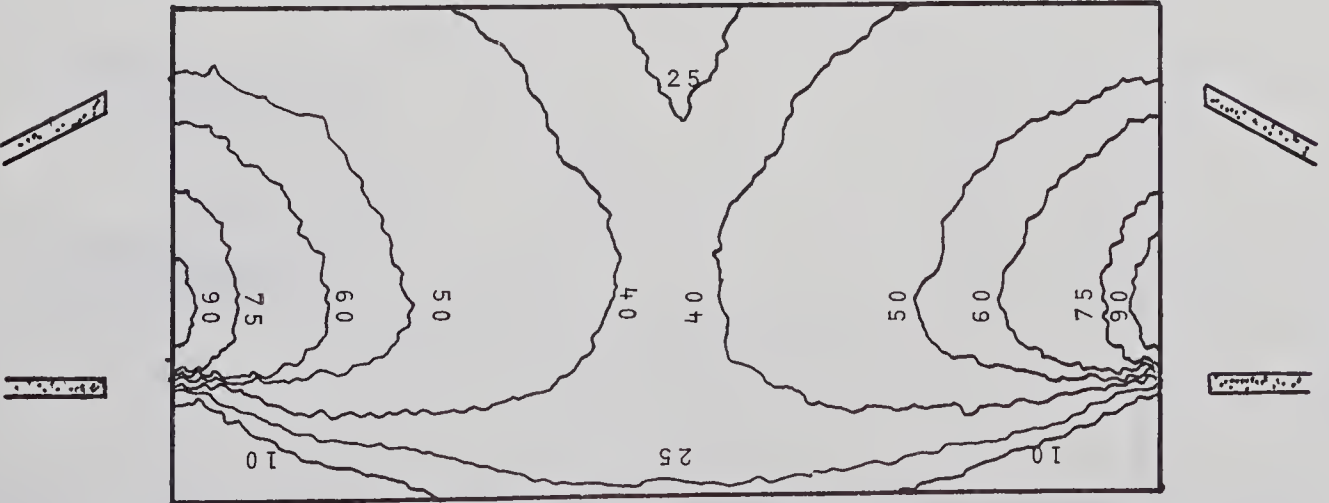
RECTANGULAR 0° - SUM      80 KEV AIR      24.1cm X 25cm



RECTANGULAR 30° - SUM      80 KEV AIR      24.1cm X 25cm



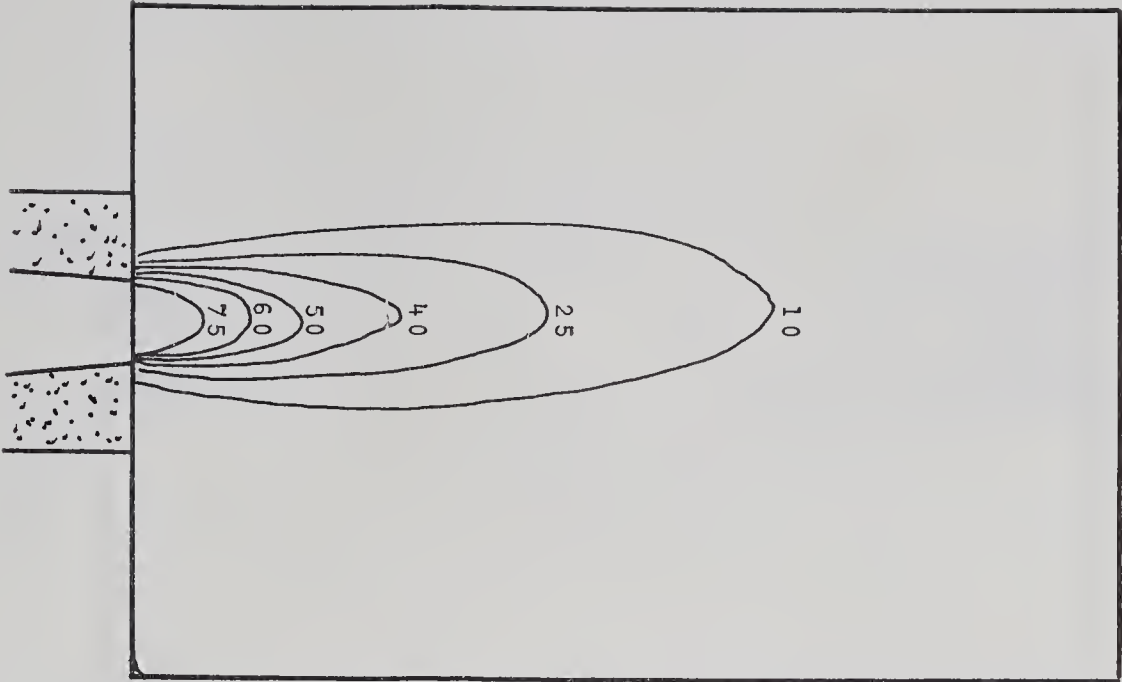
RECTANGULAR 45° - SUM      80 KEV AIR      24.1cm X 25cm



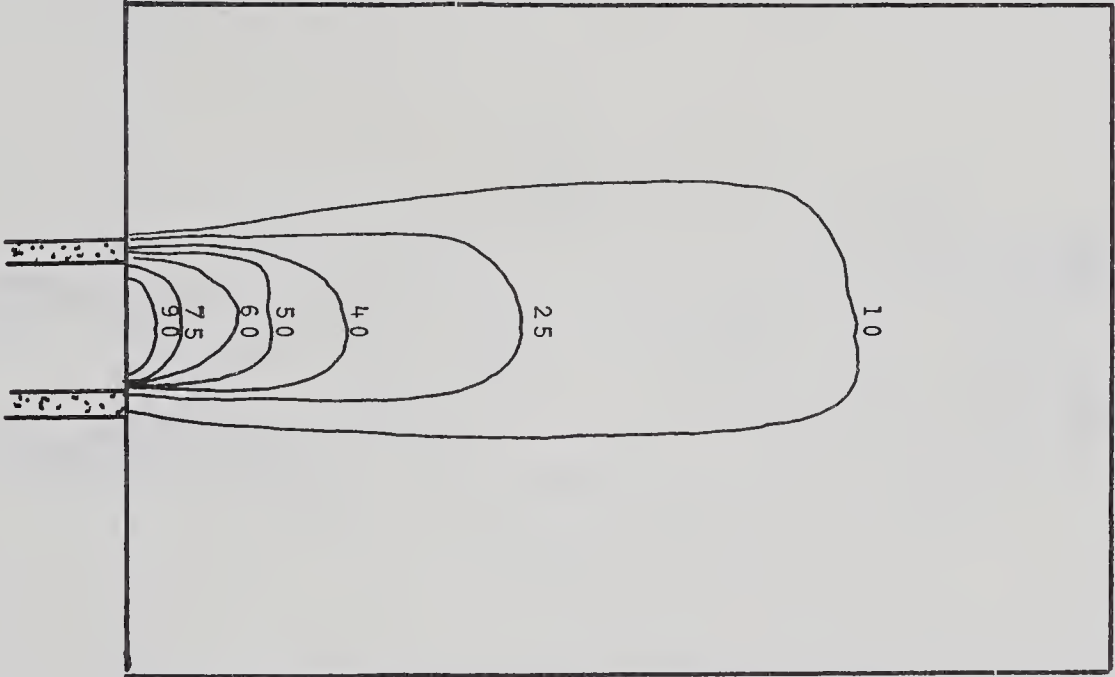
RECTANGULAR 60° - SUM      80 KEV AIR      24.1cm X 25cm

FIGURE 14

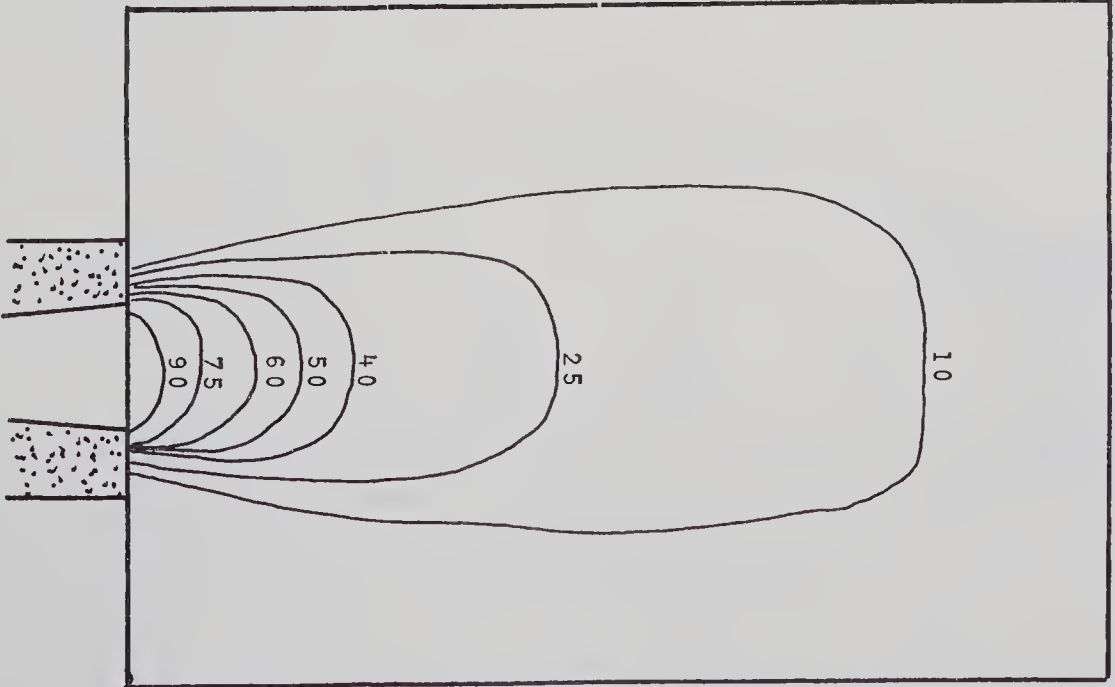




MODEL CYLINDRICAL CONVERGING 80 KEV AIR 18.5cm X 25cm



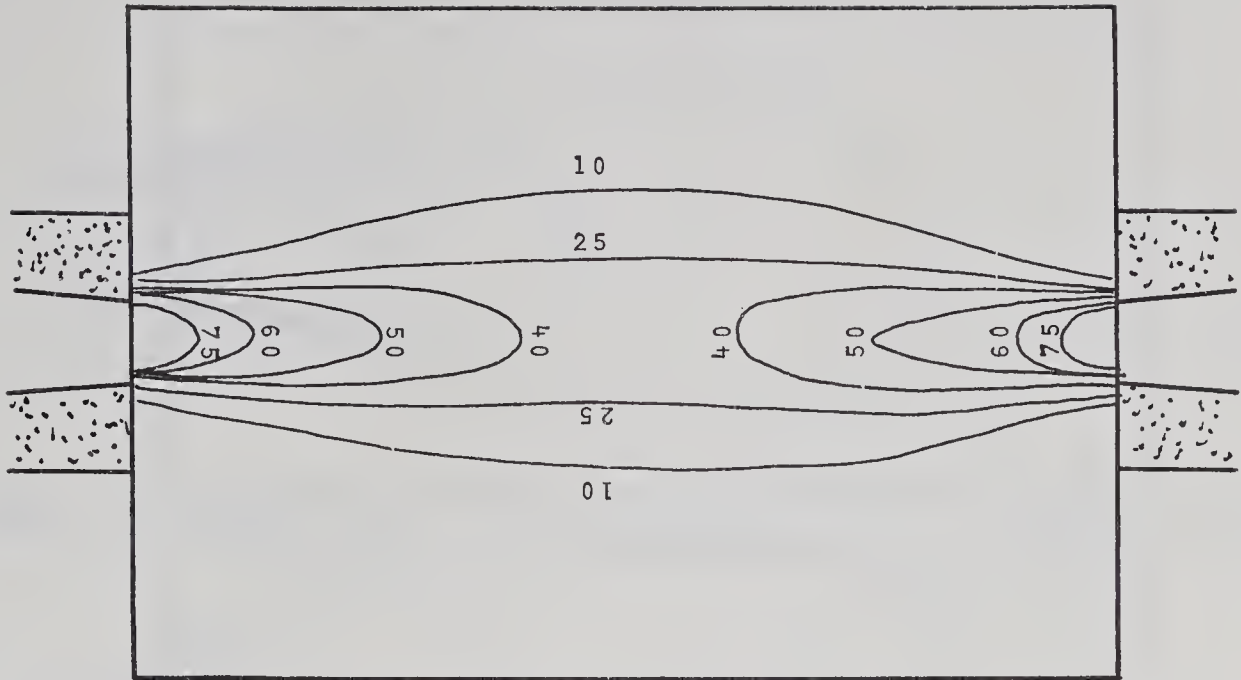
MODEL CYLINDRICAL STRAIGHT 80 KEV AIR 18.5cm X 25cm



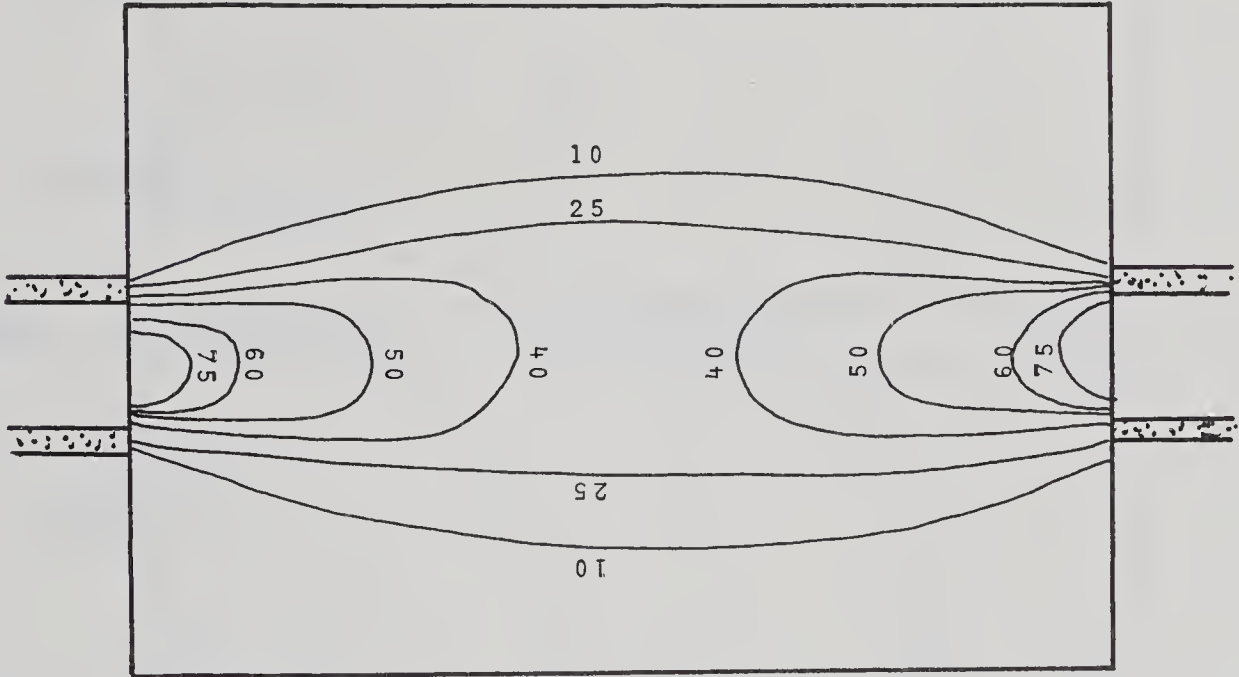
MODEL CYLINDRICAL DIVERGING 80 KEV AIR 18.5cm X 25cm

FIGURE 15

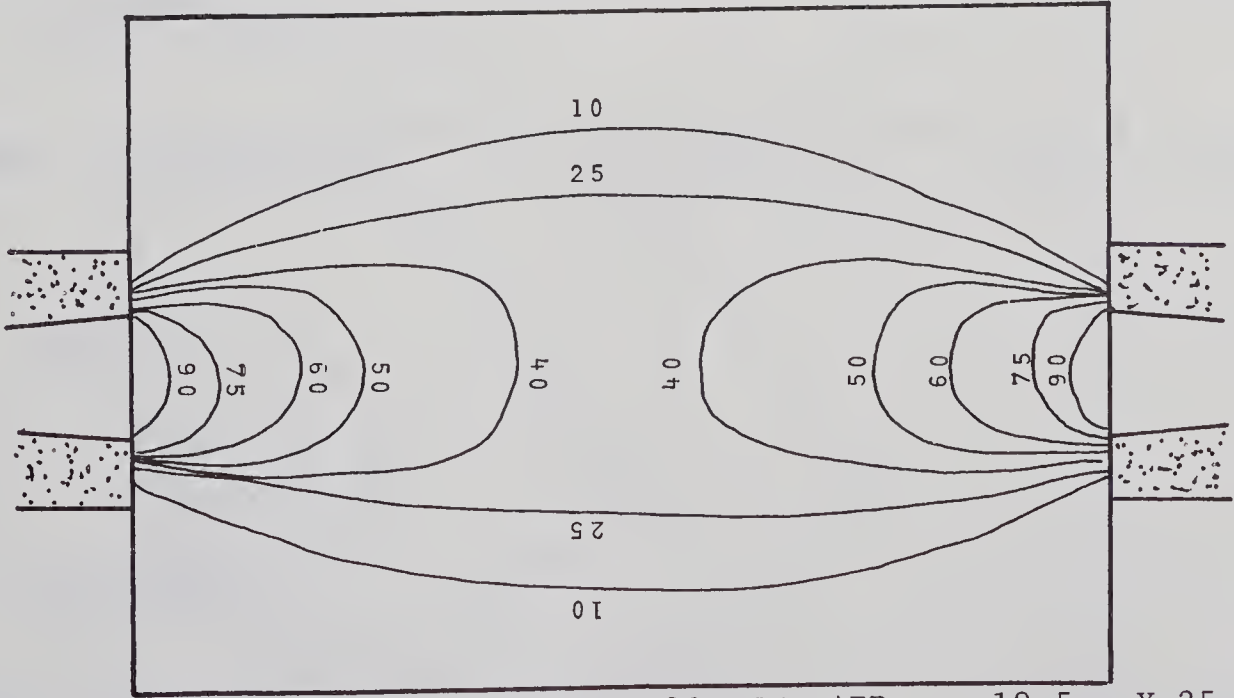




MODEL CYLINDRICAL CONVERGING-SUM 80 KEV AIR 18.5cm X 25cm



MODEL CYLINDRICAL STRAIGHT-SUM 80 KEV AIR 18.5cm X 25cm



MODEL CYLINDRICAL DIVERGING-SUM 80 KEV AIR 18.5cm X 25cm

FIGURE 16



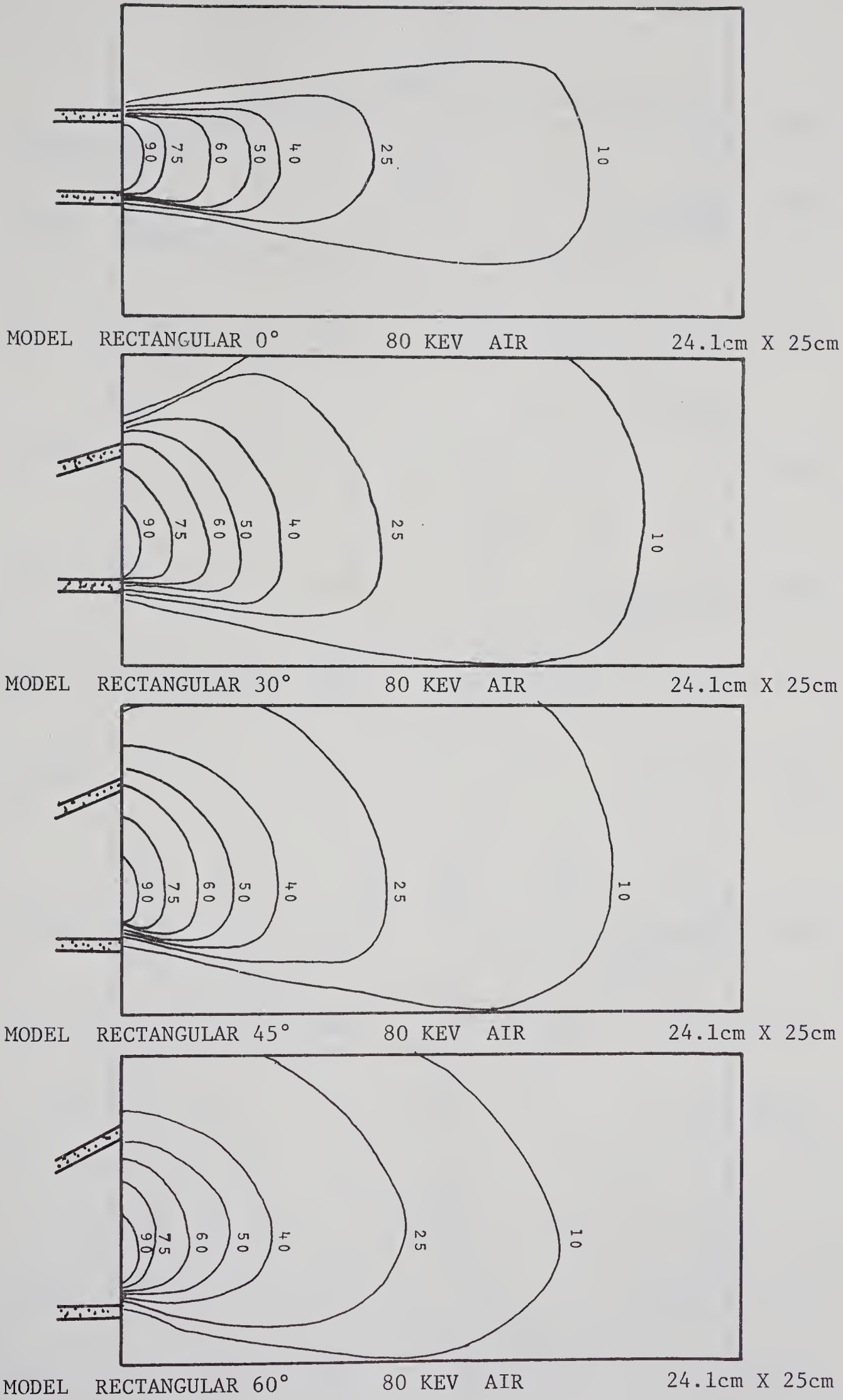


FIGURE 17





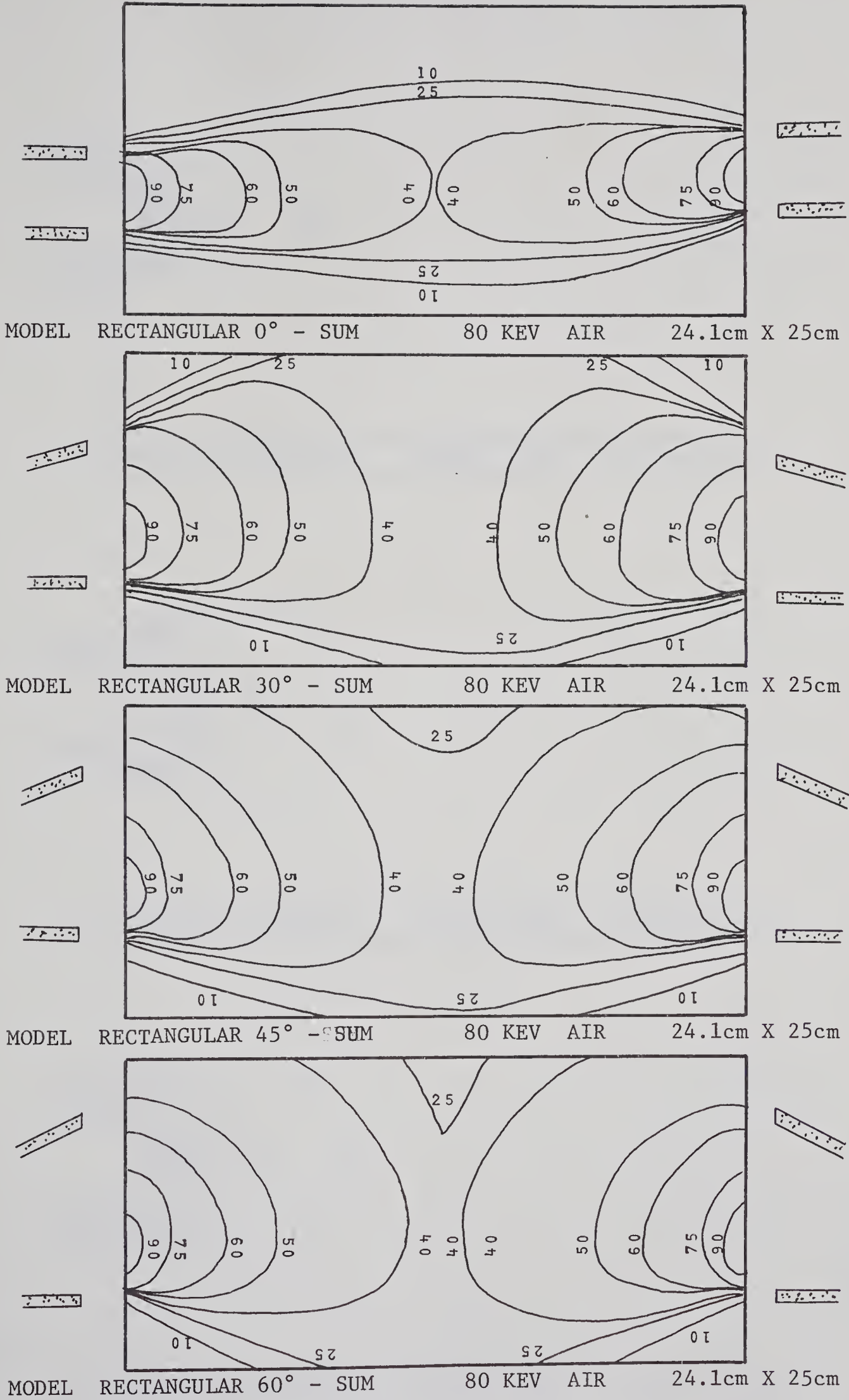


FIGURE 18



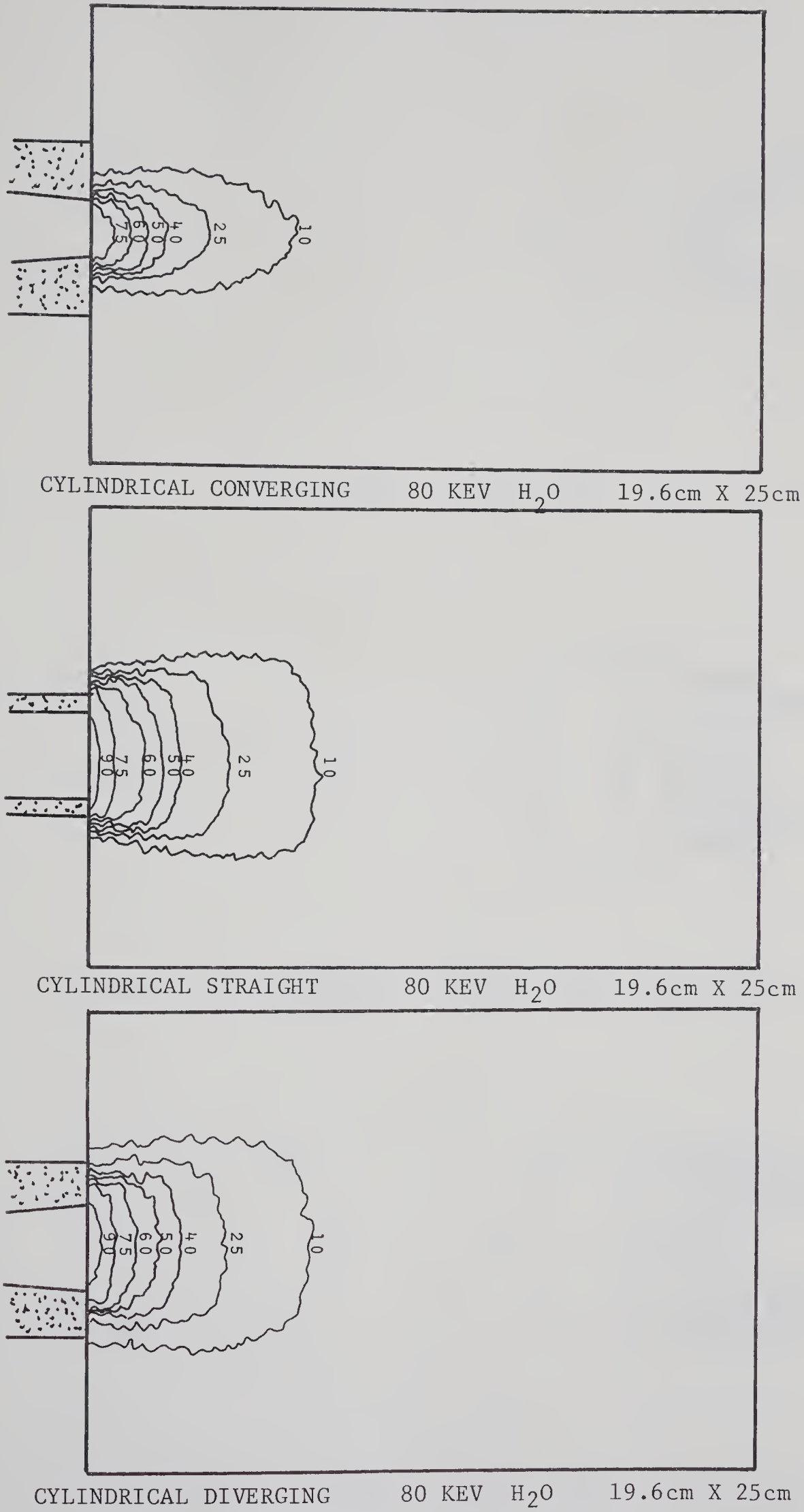


FIGURE 19



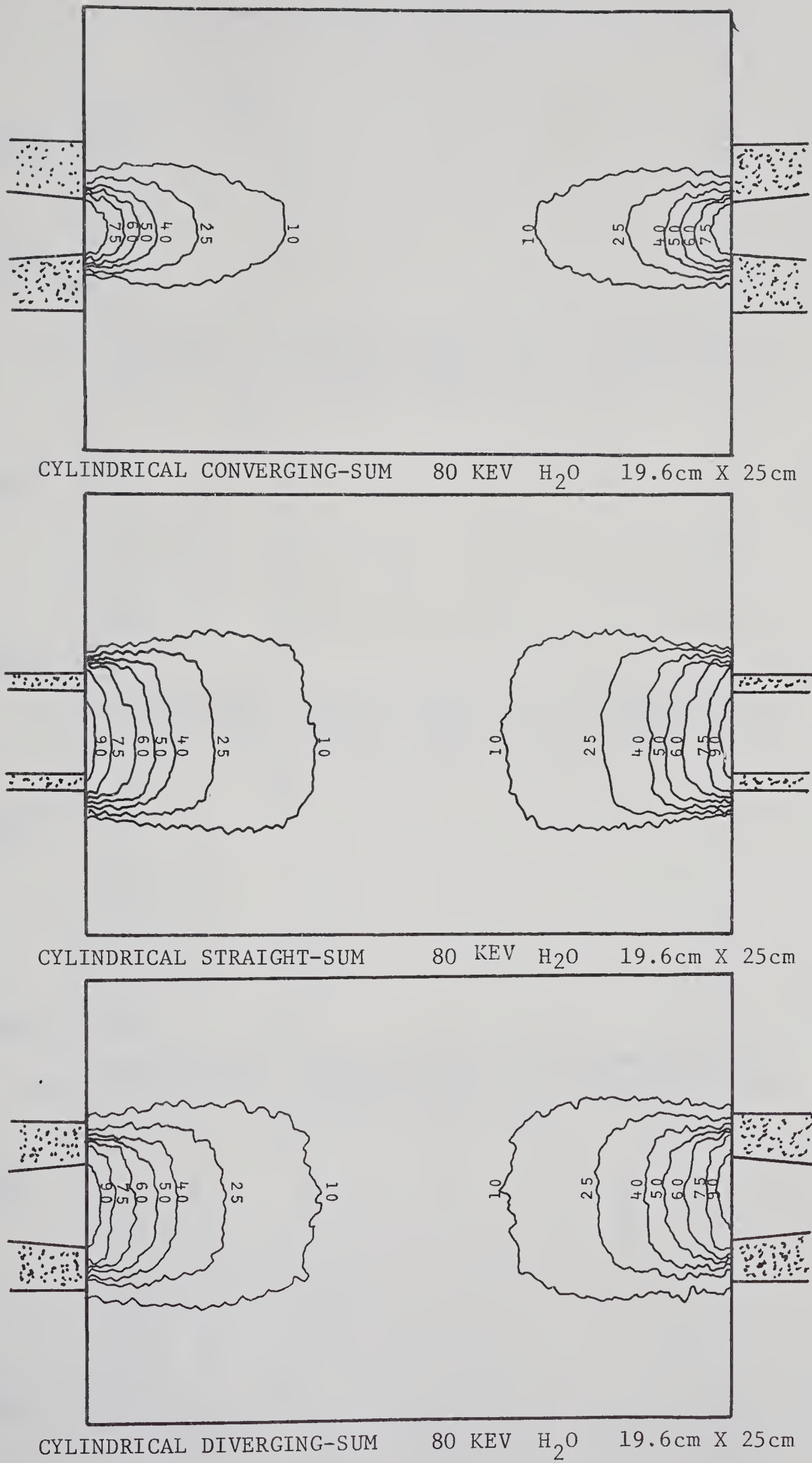


FIGURE 20



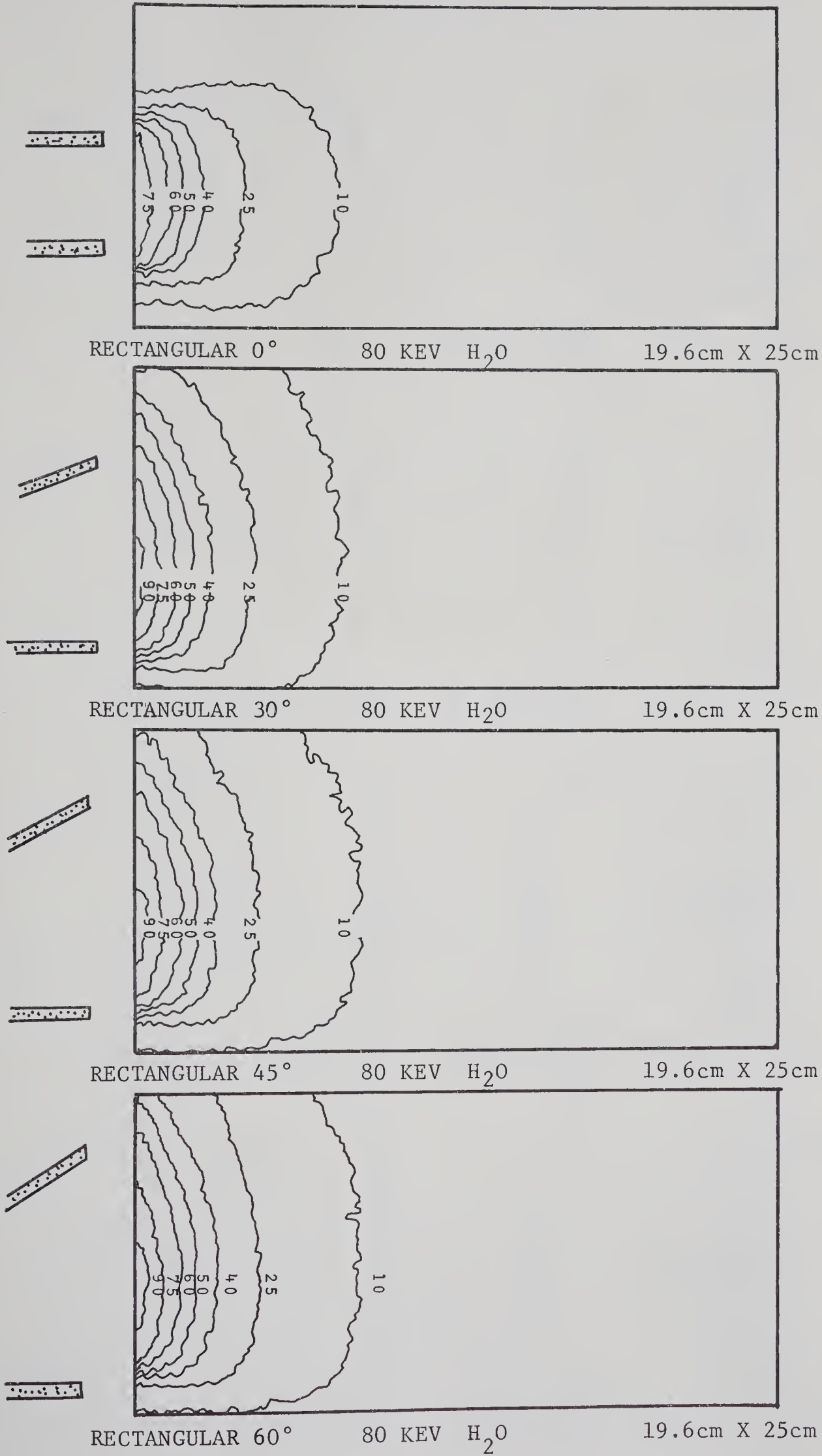


FIGURE 21





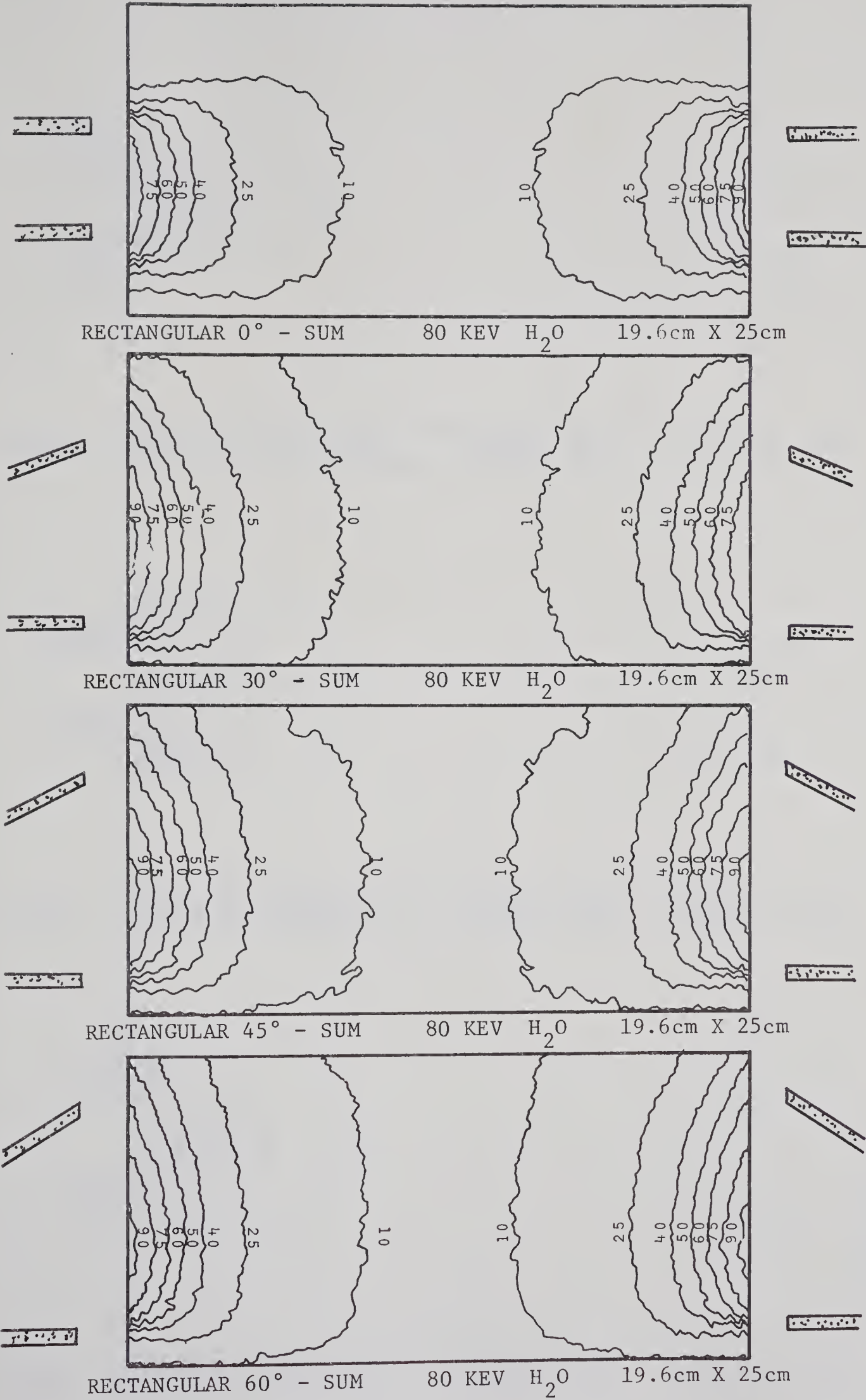
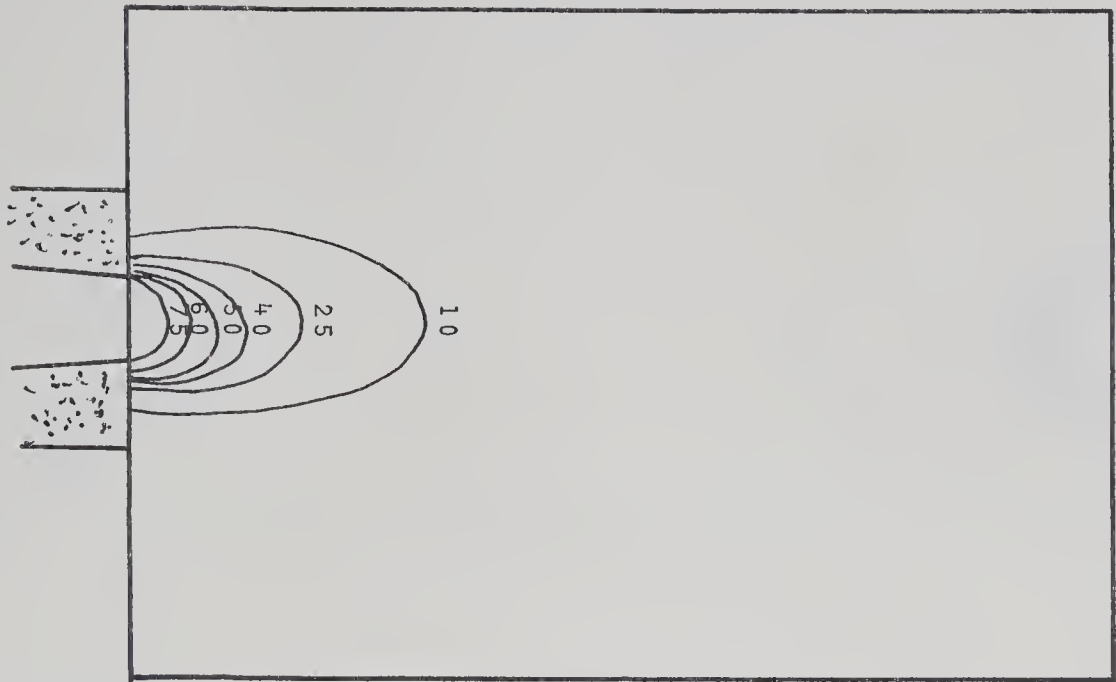
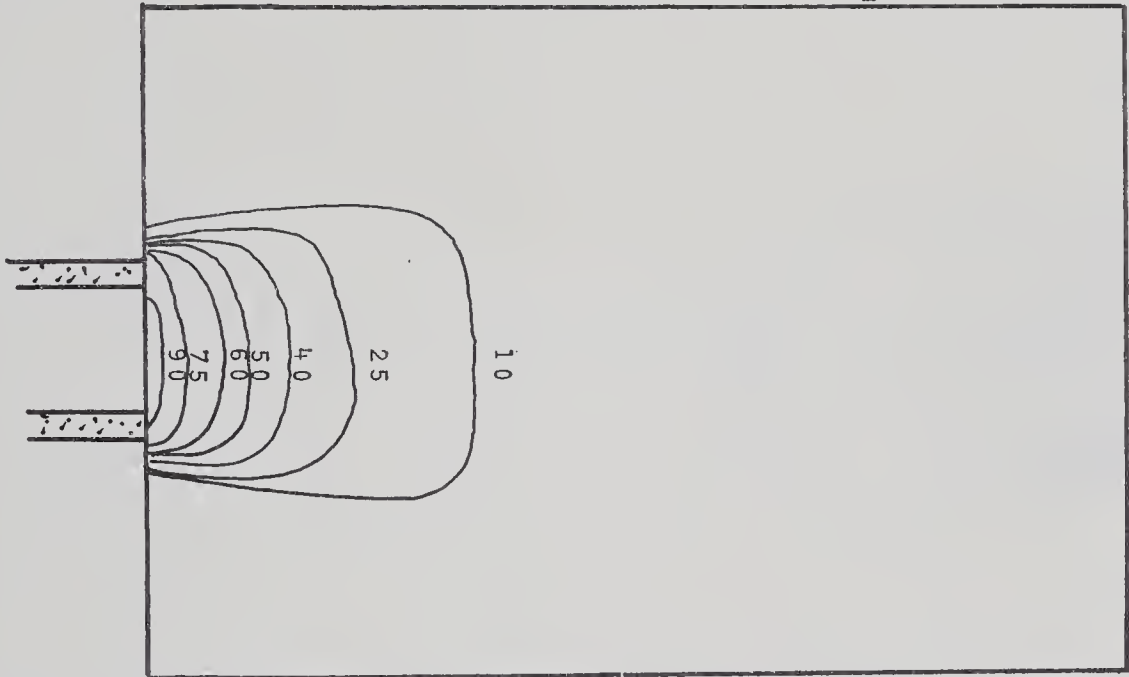


FIGURE 22

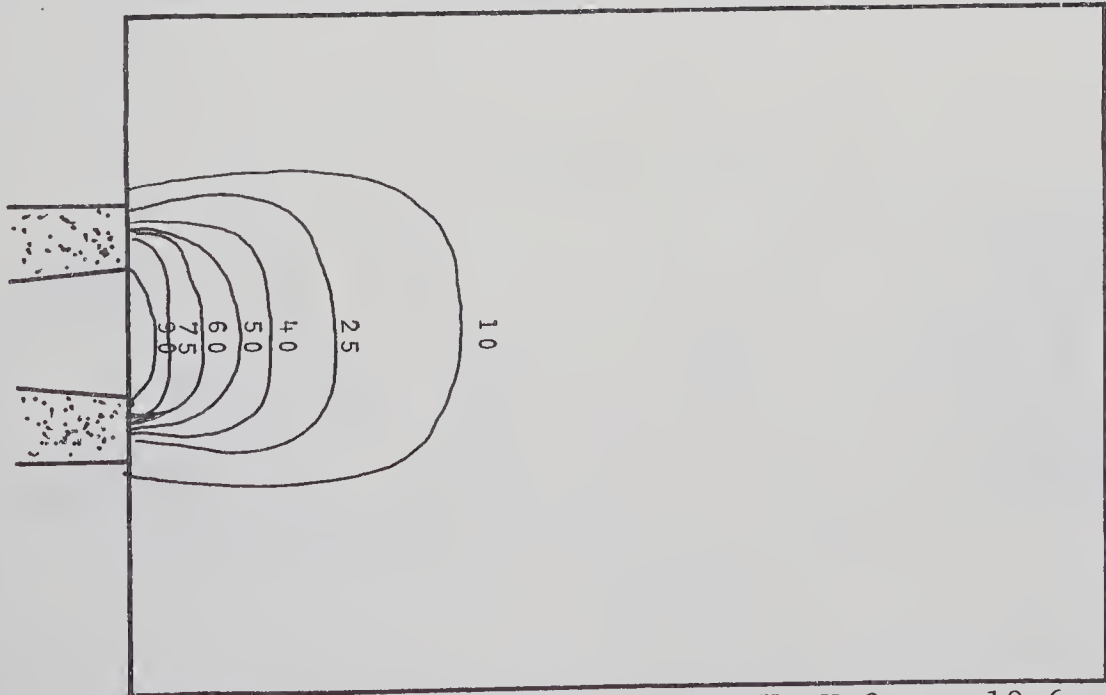




MODEL CYLINDRICAL CONVERGING 80 KEV H<sub>2</sub>O 19.6cm X 25cm



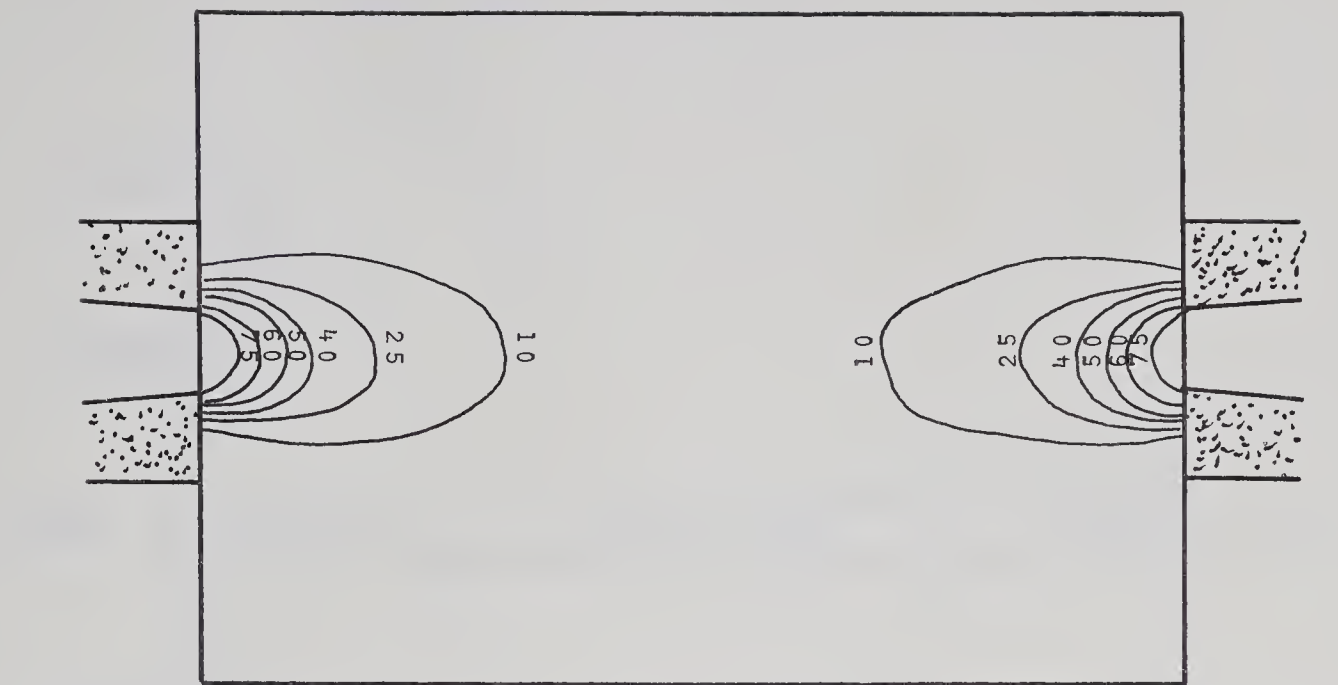
MODEL CYLINDRICAL STRAIGHT 80 KEV H<sub>2</sub>O 19.6cm X 25cm



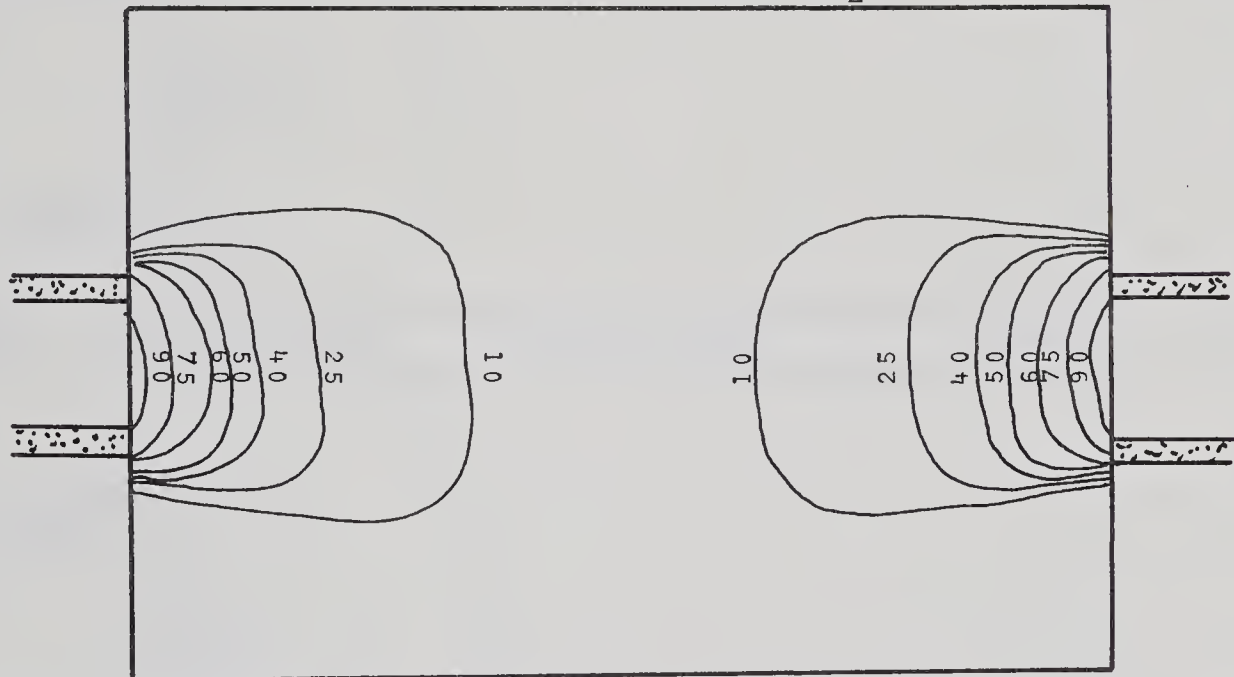
MODEL CYLINDRICAL DIVERGING 80 KEV H<sub>2</sub>O 19.6cm X 25cm

FIGURE 23

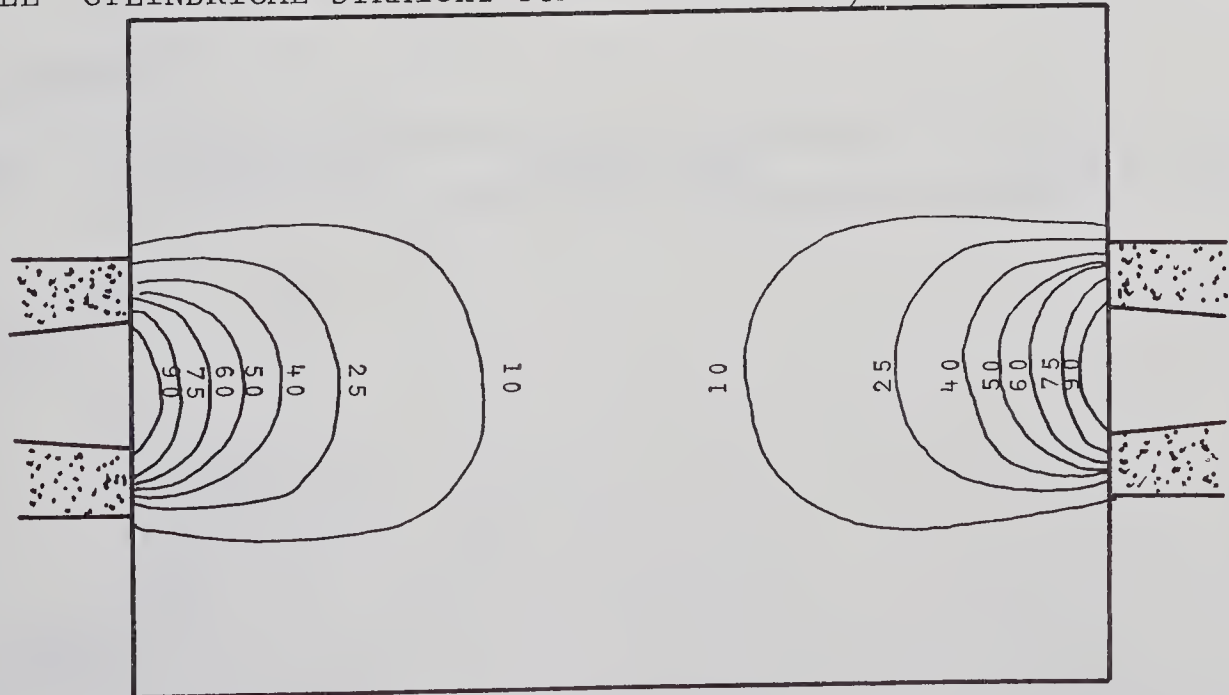




MODEL CYLINDRICAL CONVERGING-SUM 80 KEV H<sub>2</sub>O 19.6cm X 25cm



MODEL CYLINDRICAL STRAIGHT-SUM 80 KEV H<sub>2</sub>O 19.6cm X 25cm



MODEL CYLINDRICAL DIVERGING-SUM 80 KEV H<sub>2</sub>O 19.6cm X 25cm

FIGURE 24



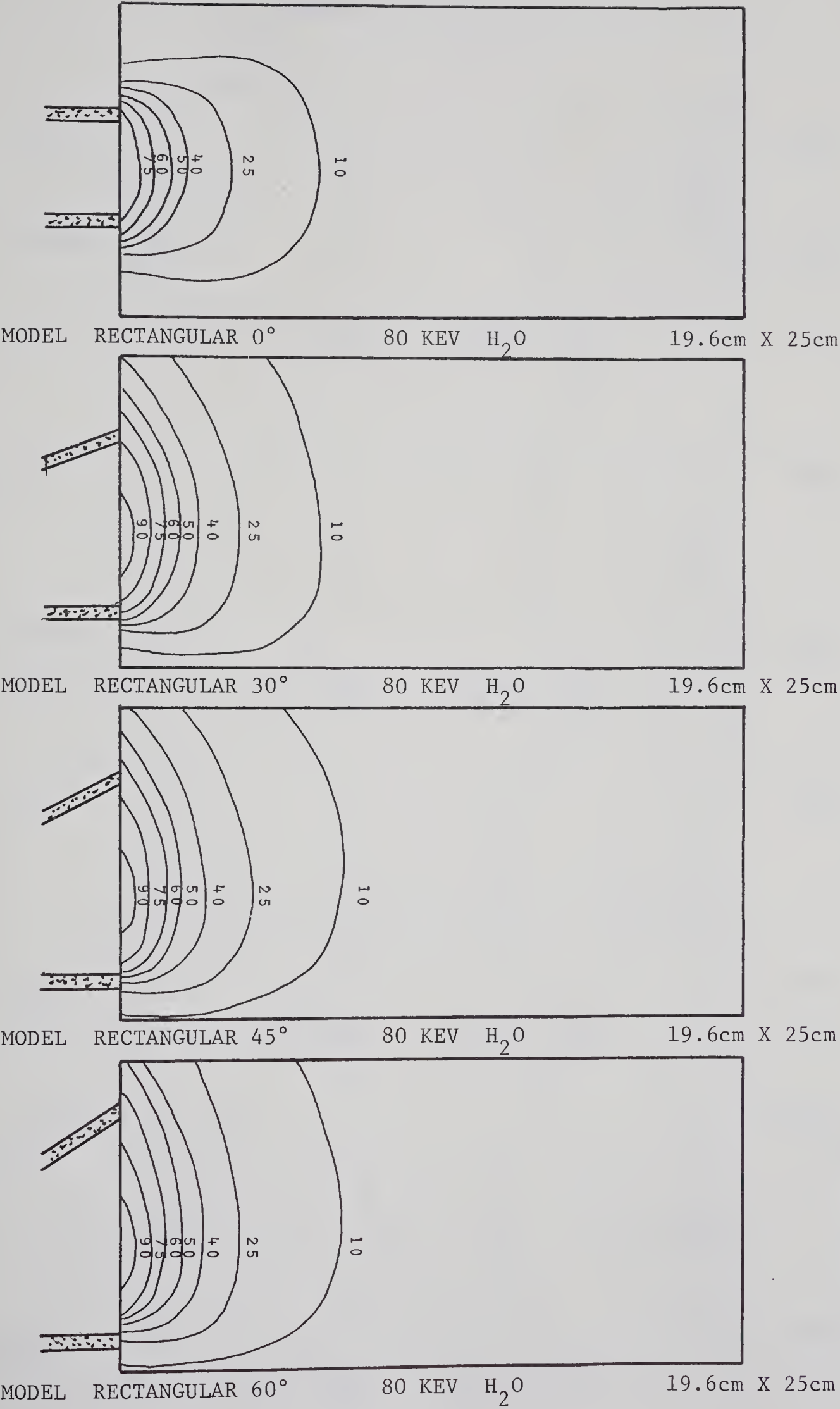
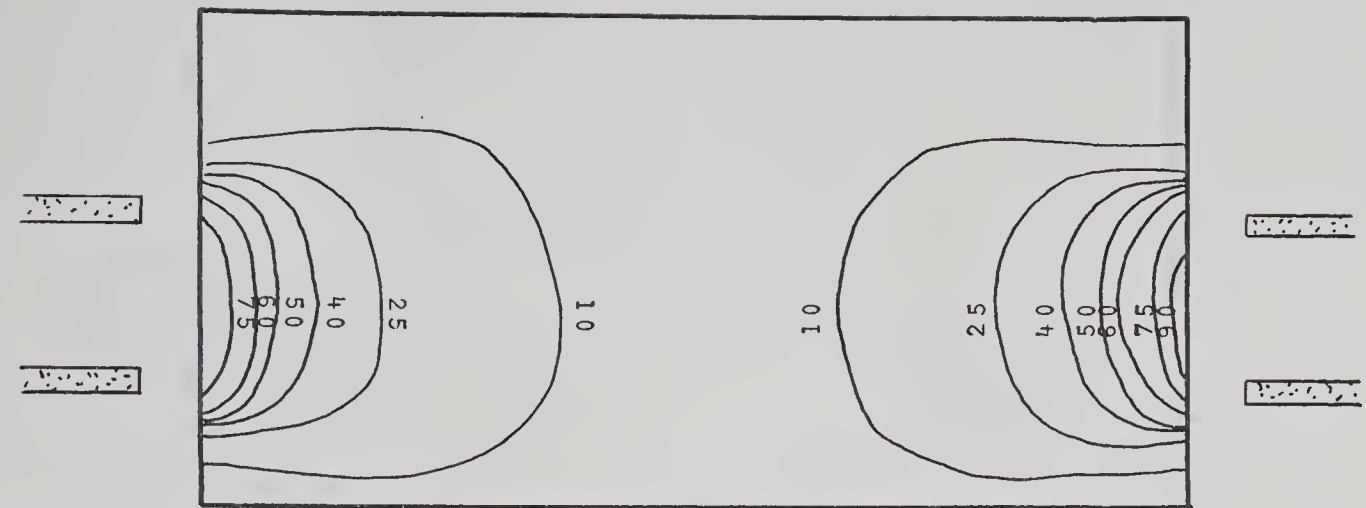


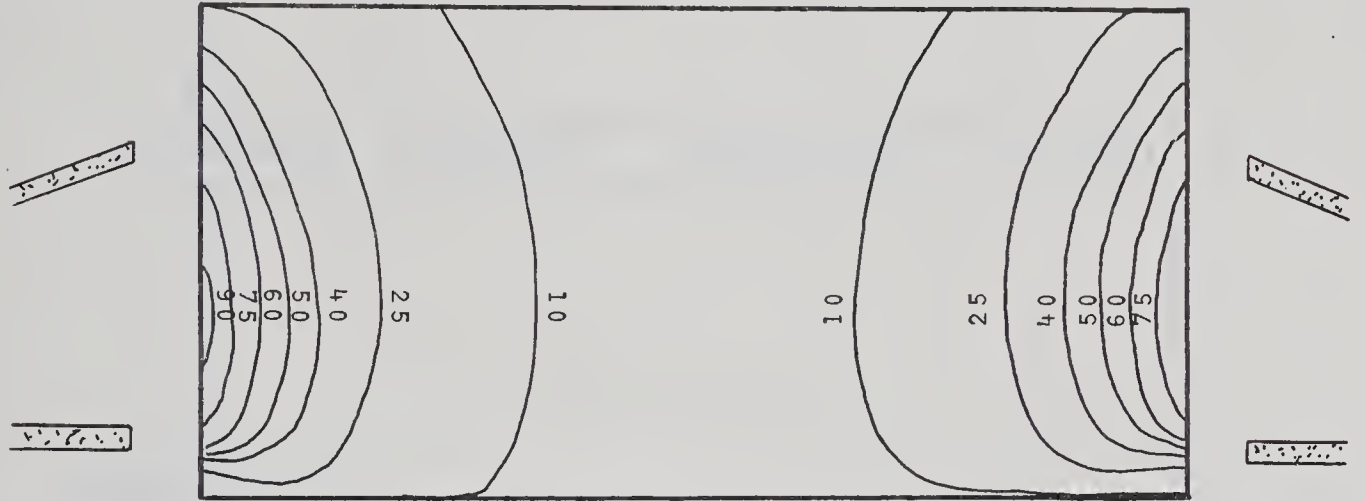
FIGURE 25



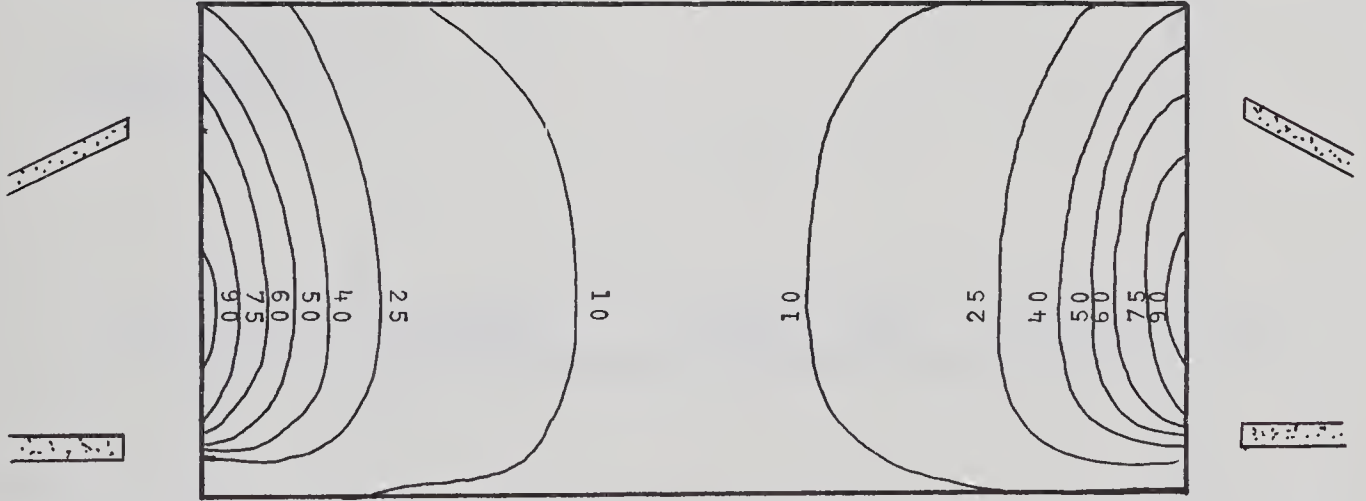




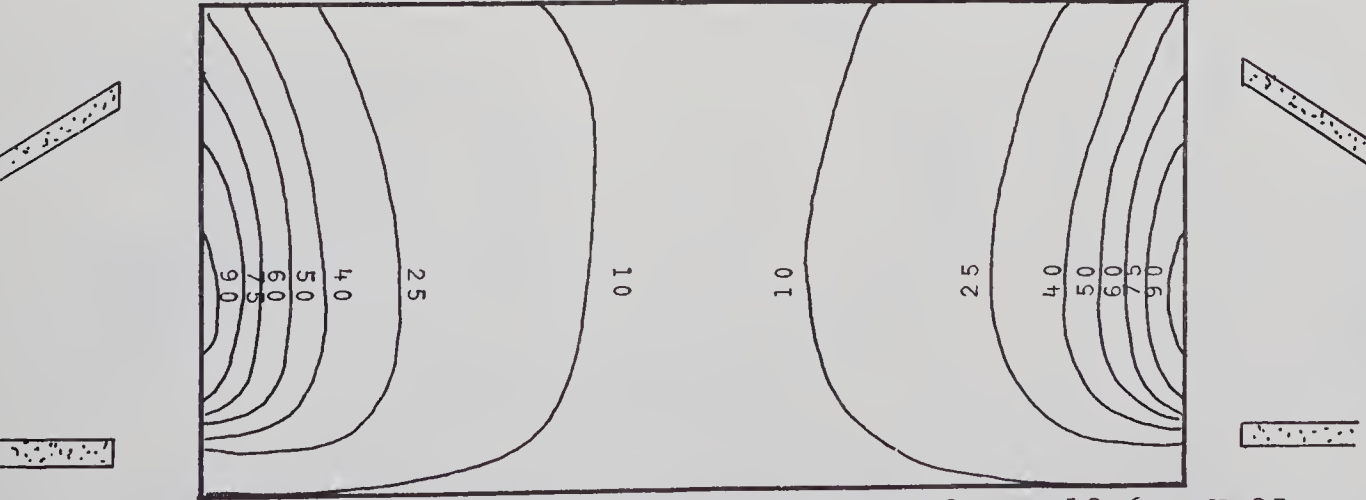
MODEL RECTANGULAR 0° - SUM 80 KEV H<sub>2</sub>O 19.6cm X 25cm



MODEL RECTANGULAR 30° - SUM 80 KEV H<sub>2</sub>O 19.6cm X 25cm



MODEL RECTANGULAR 45° - SUM 80 KEV H<sub>2</sub>O 19.6cm X 25cm



MODEL RECTANGULAR 60° - SUM 80 KEV H<sub>2</sub>O 19.6cm X 25cm

FIGURE 26



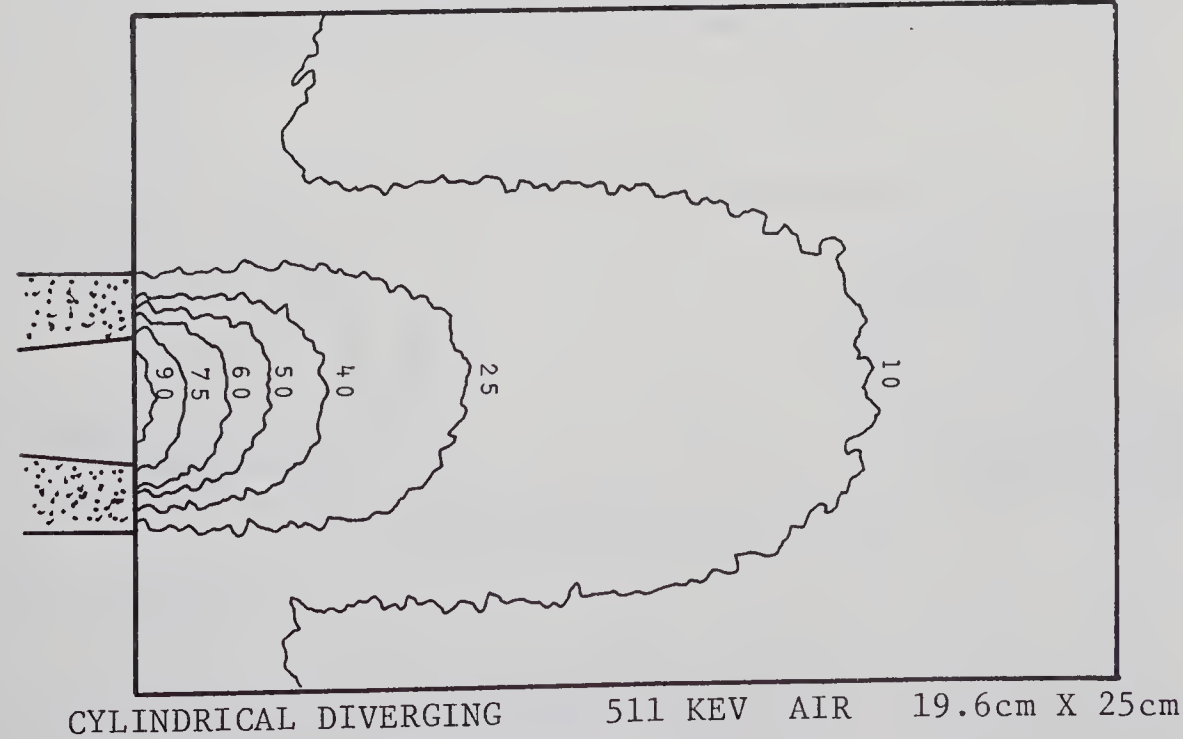
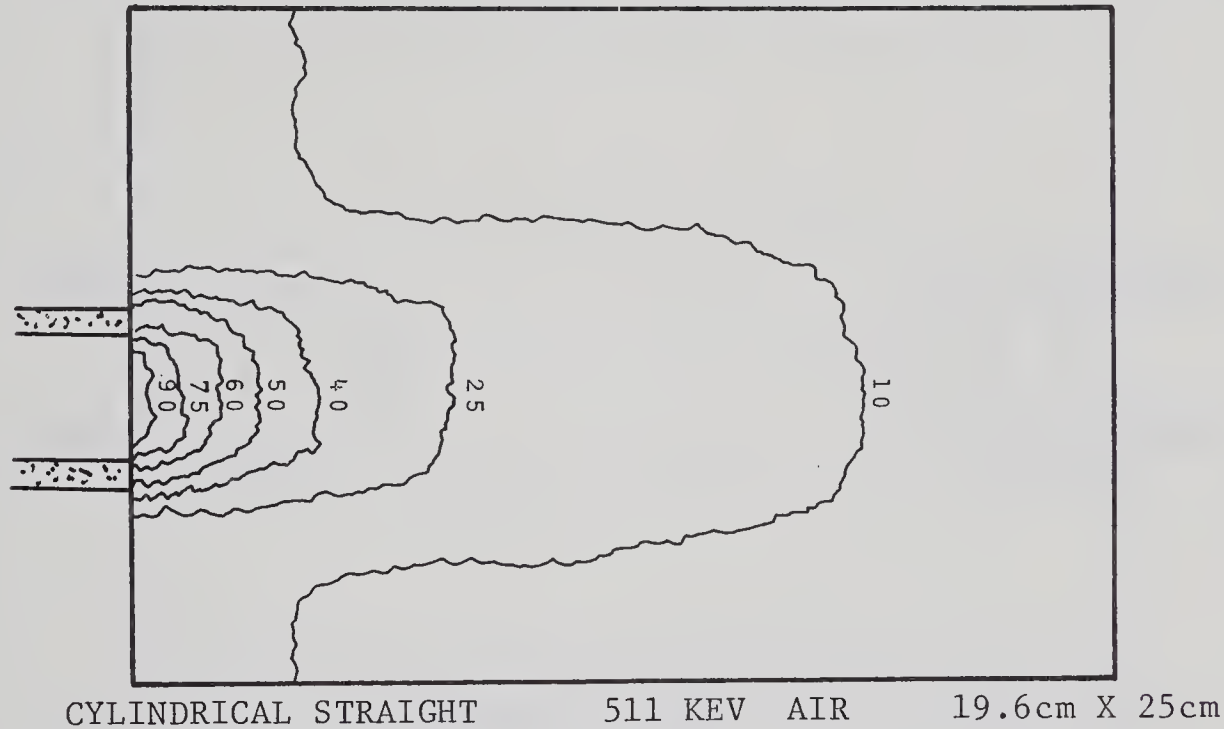
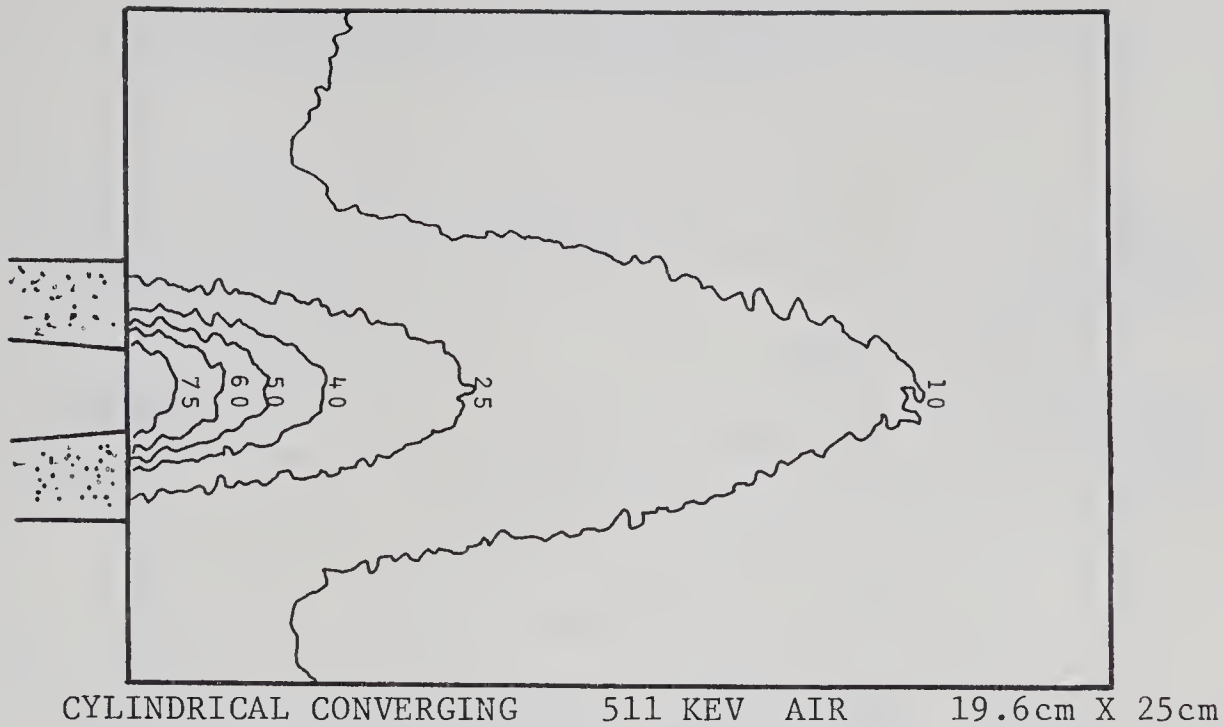
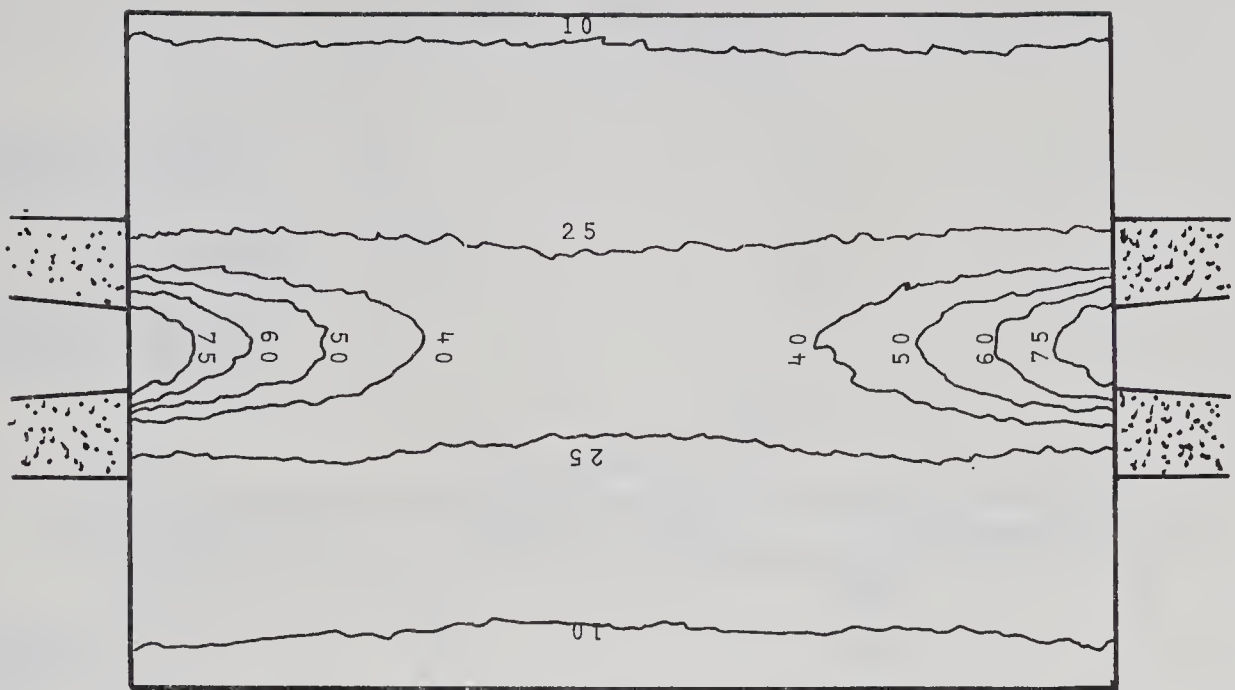
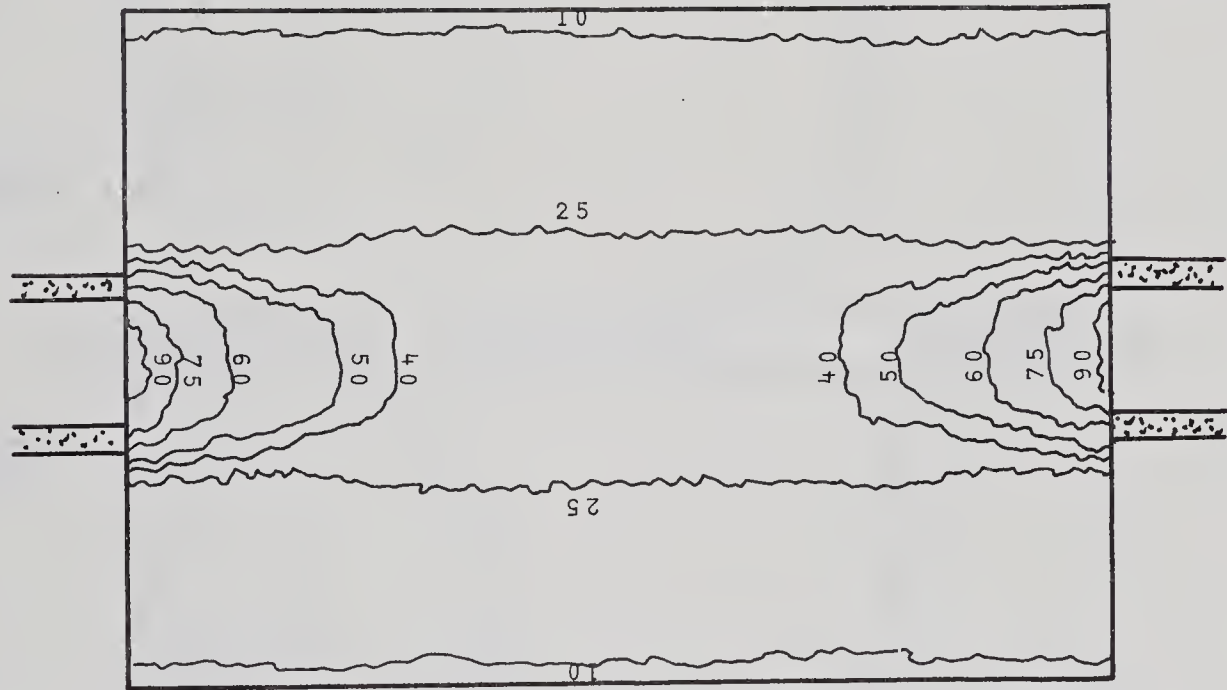


FIGURE 27

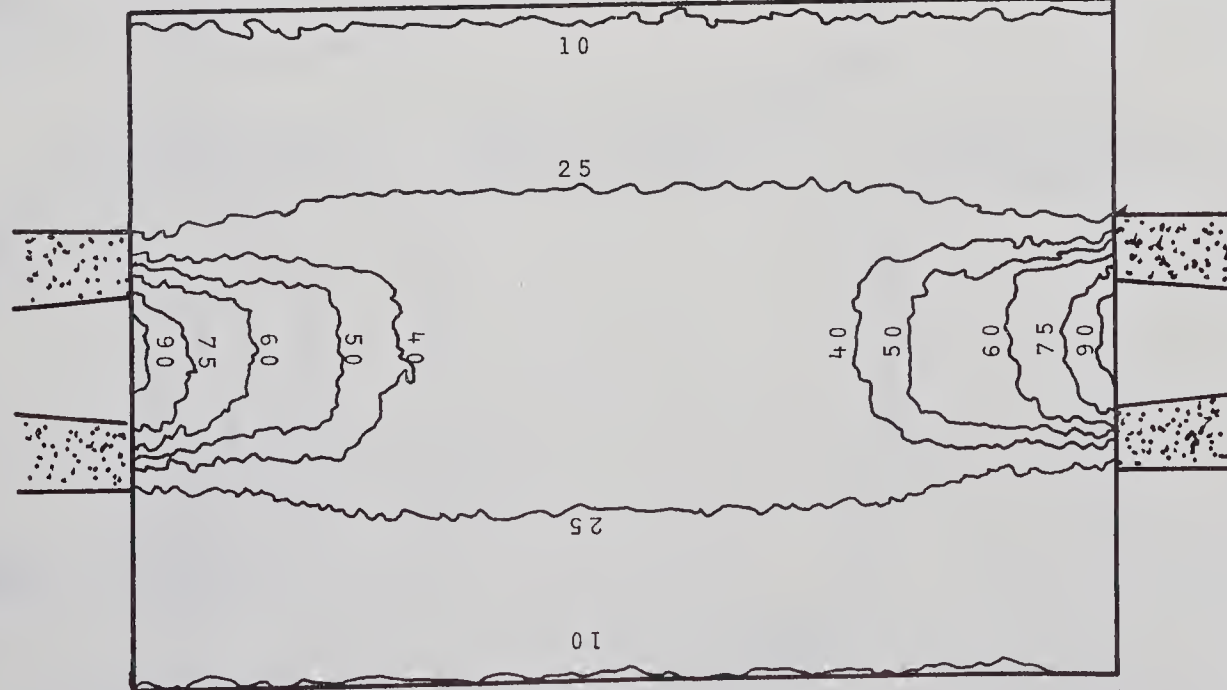




CYLINDRICAL CONVERGING-SUM 511 KEV AIR 19.6cm X 25cm



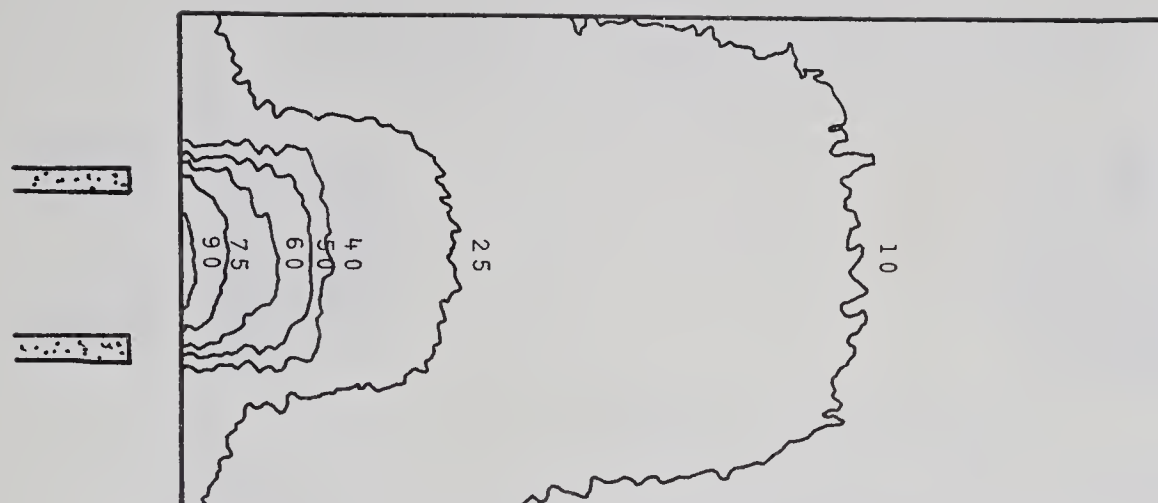
CYLINDRICAL STRAIGHT-SUM 511 KEV AIR 19.6cm X 25cm



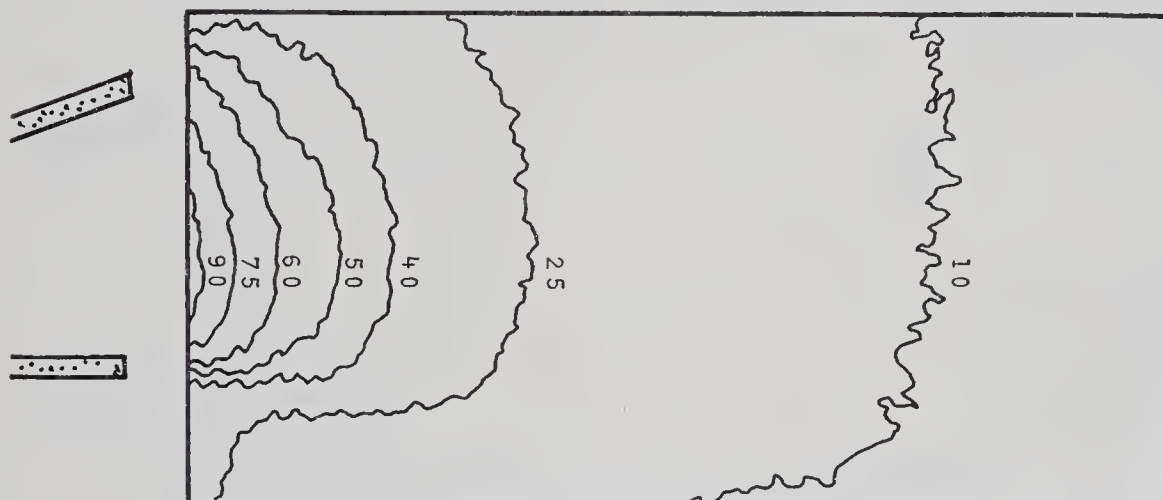
CYLINDRICAL DIVERGING-SUM 511 KEV AIR 19.6cm X 25cm

FIGURE 28

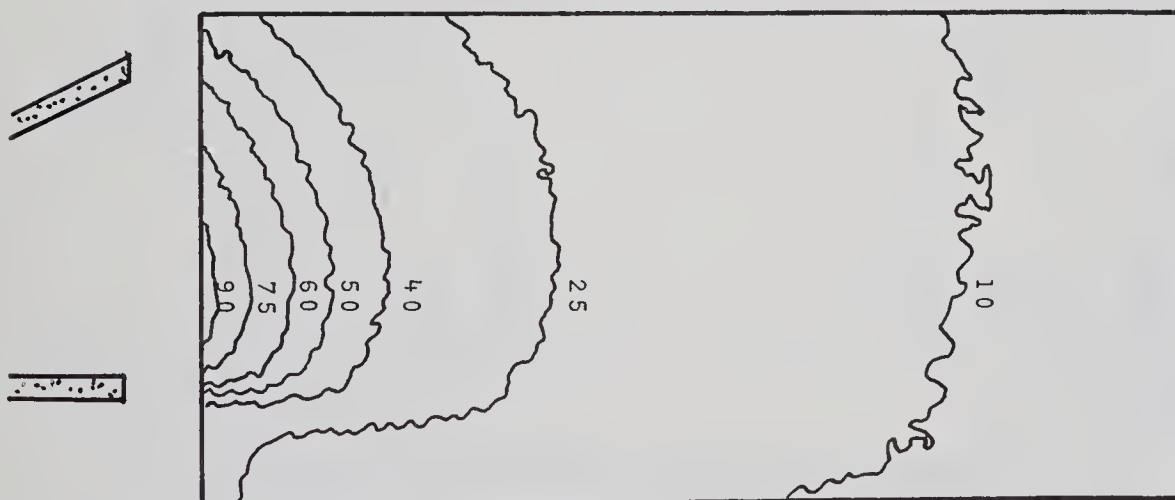




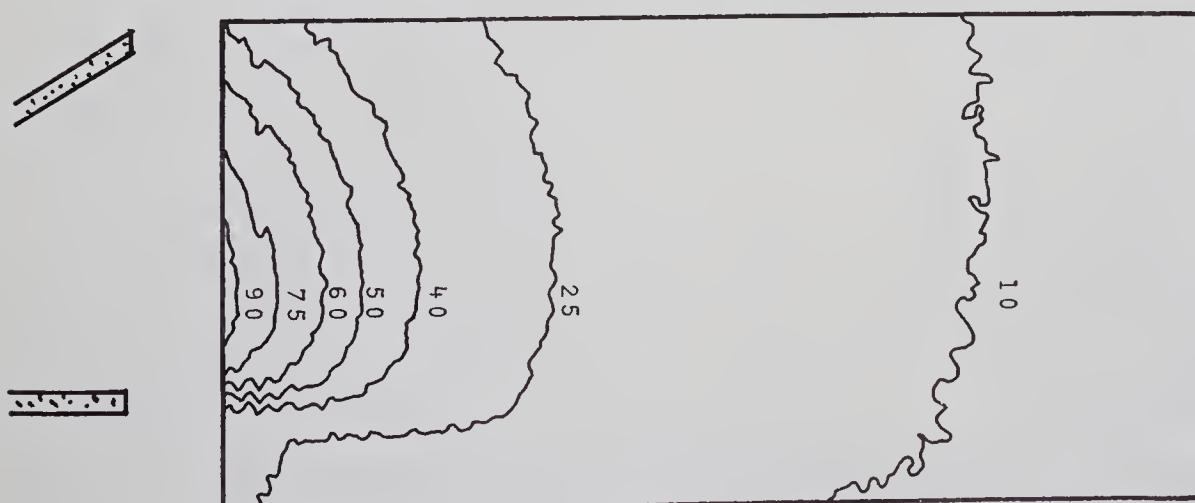
RECTANGULAR 0° 511 KEV AIR 19.6cm X 25cm



RECTANGULAR 30° 511 KEV AIR 19.6cm X 25cm



RECTANGULAR 45° 511 KEV AIR 19.6cm X 25cm



RECTANGULAR 60° 511 KEV AIR 19.6cm X 25cm

FIGURE 29





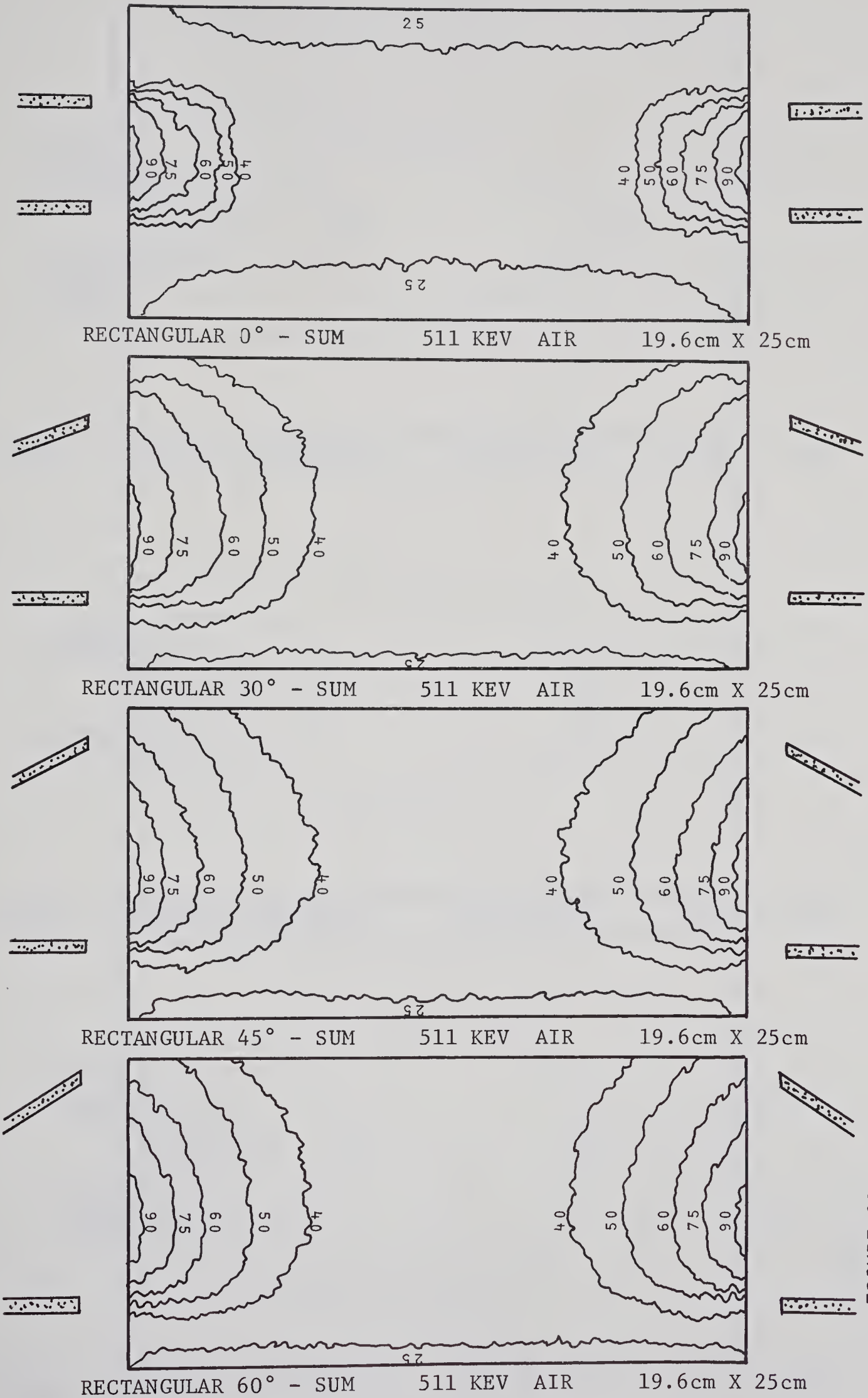


FIGURE 30



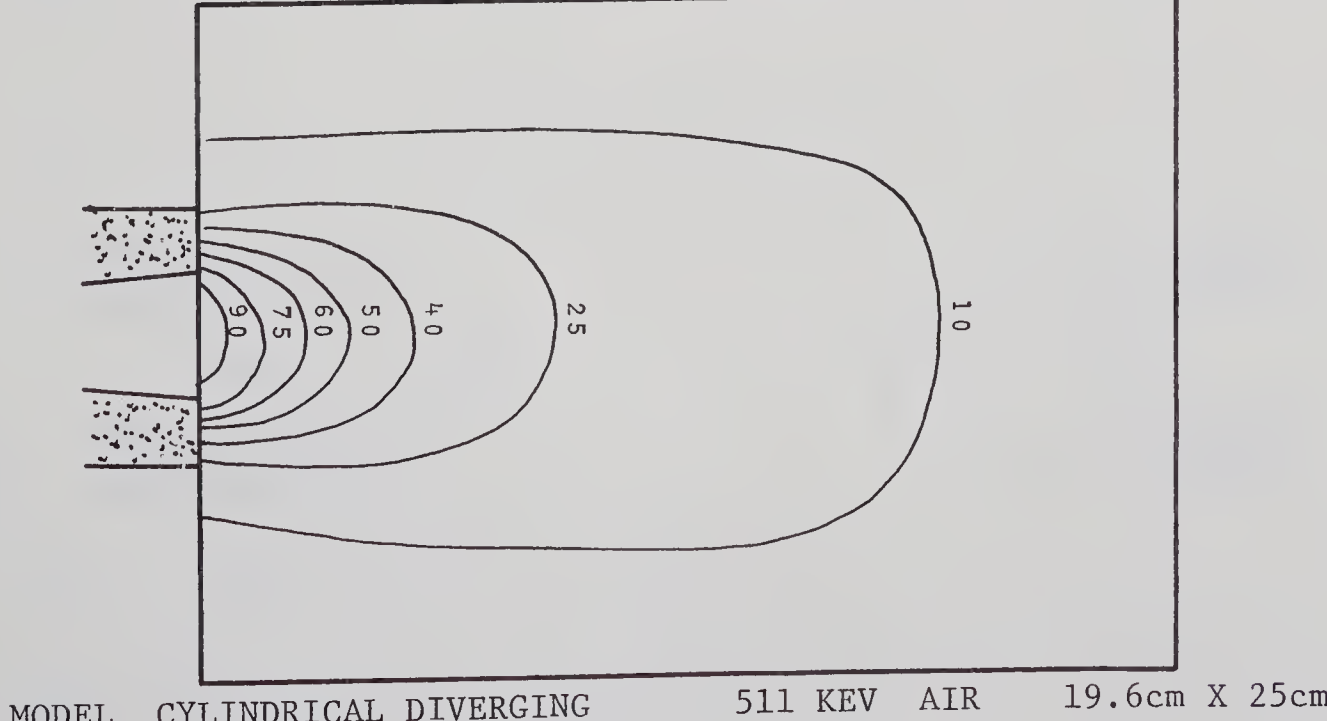
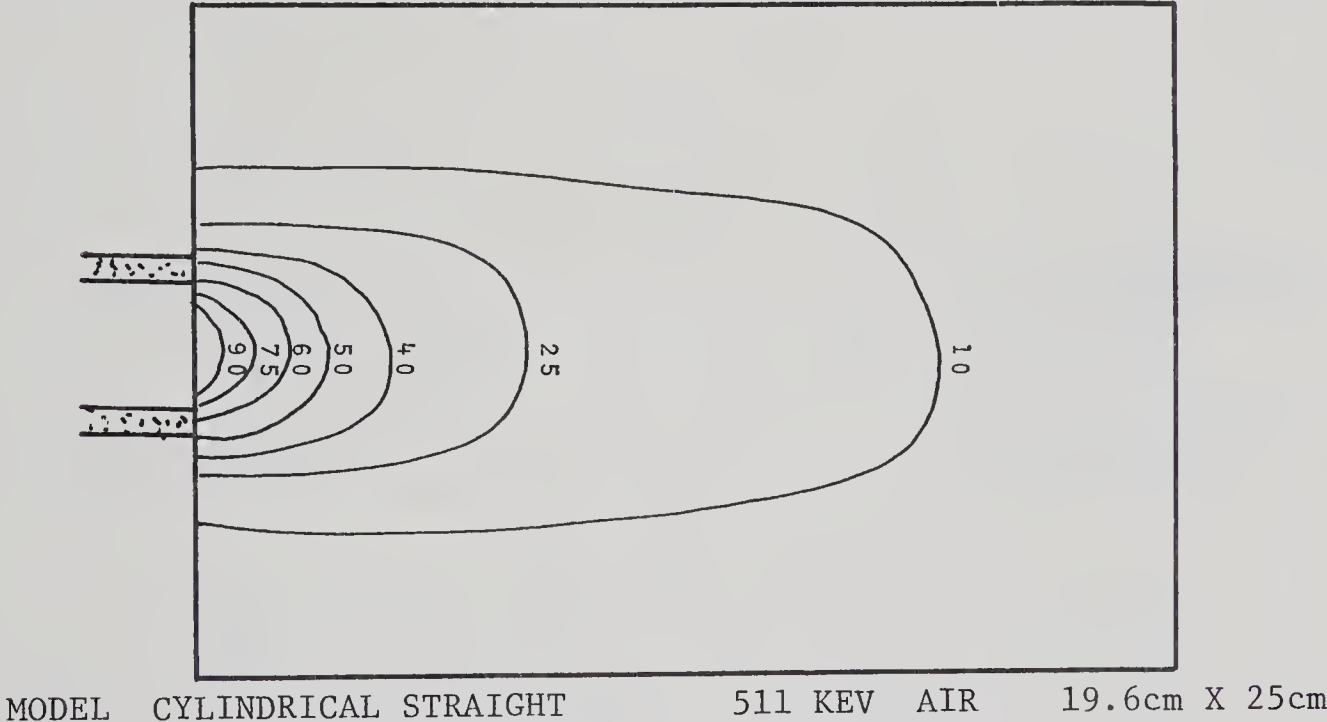
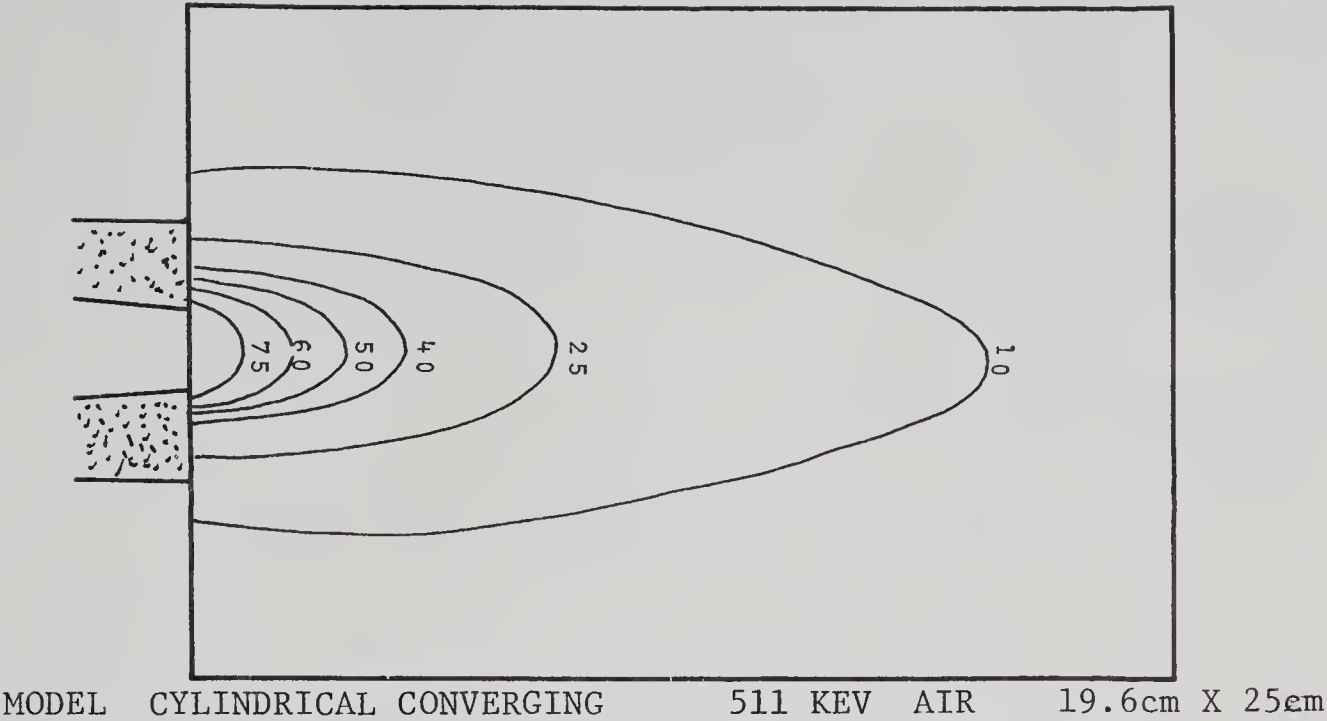
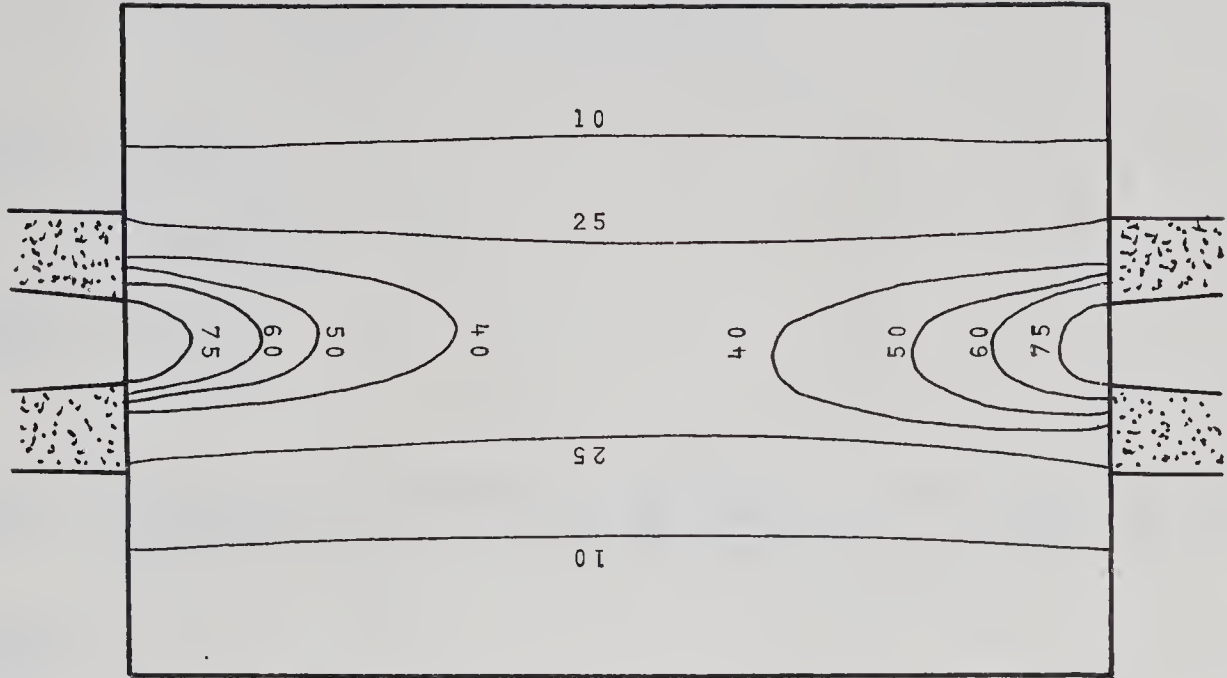
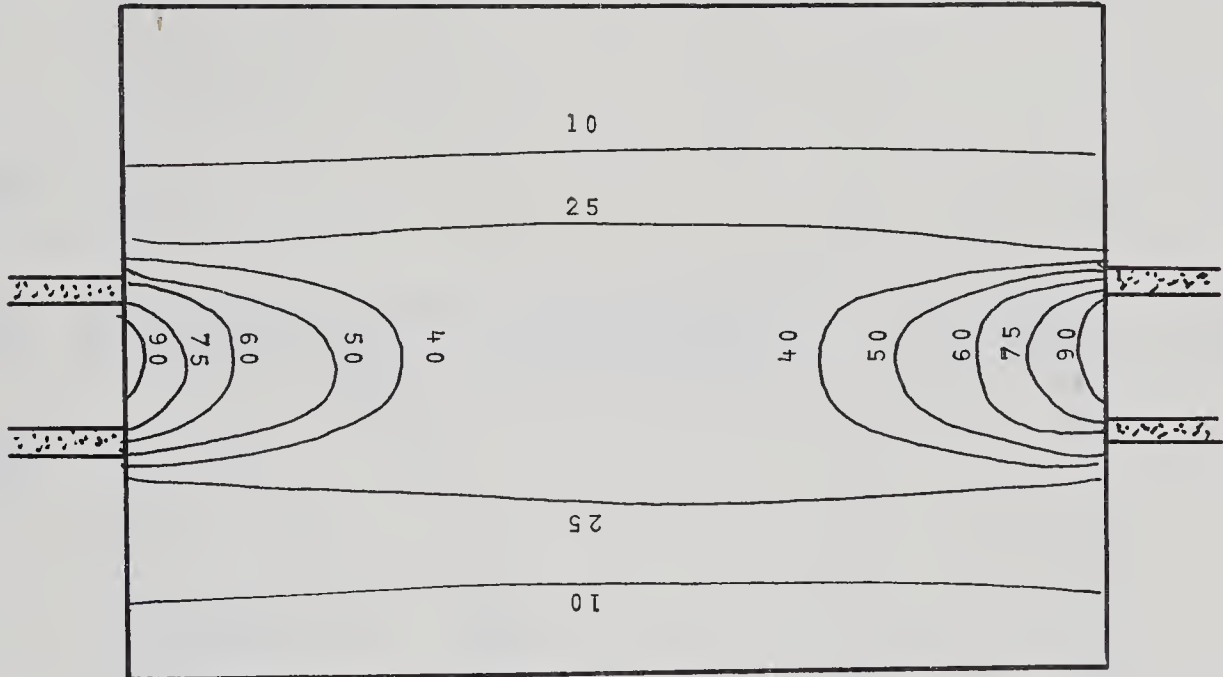


FIGURE 31

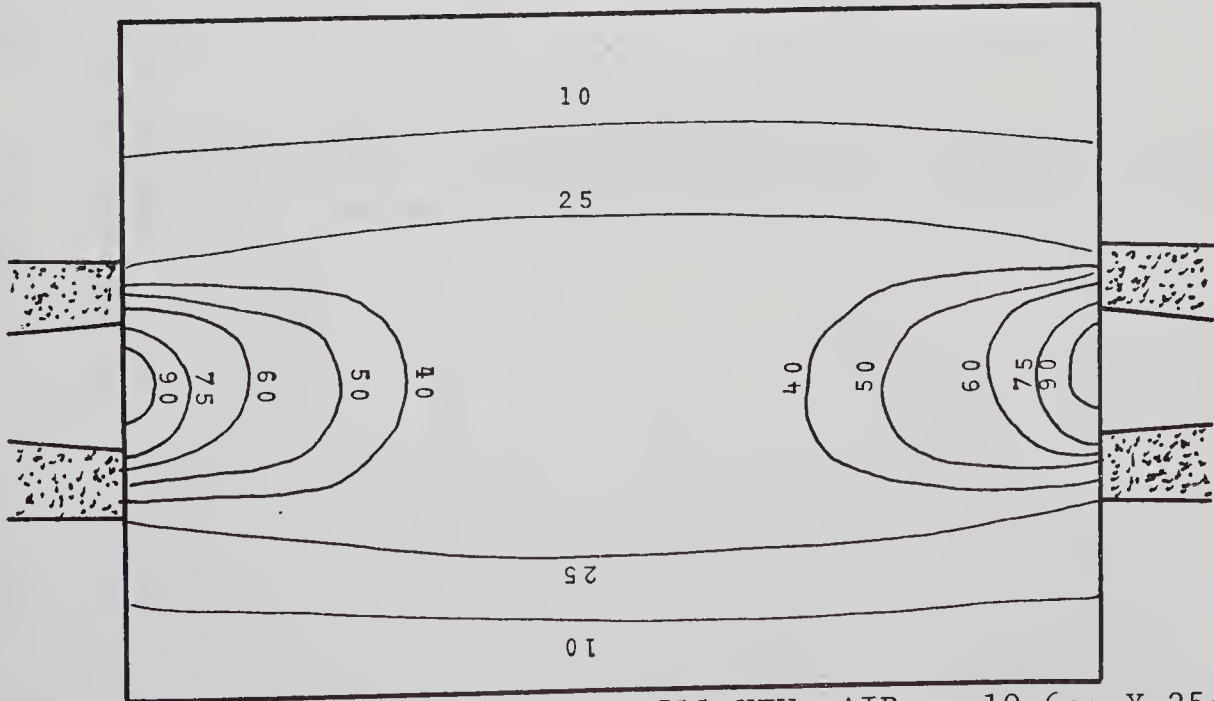




MODEL CYLINDRICAL CONVERGING-SUM 511 KEV AIR 19.6cm X 25cm



MODEL CYLINDRICAL STRAIGHT-SUM 511 KEV AIR 19.6cm X 25cm



MODEL CYLINDRICAL DIVERGING-SUM 511 KEV AIR 19.6cm X 25cm

FIGURE 32



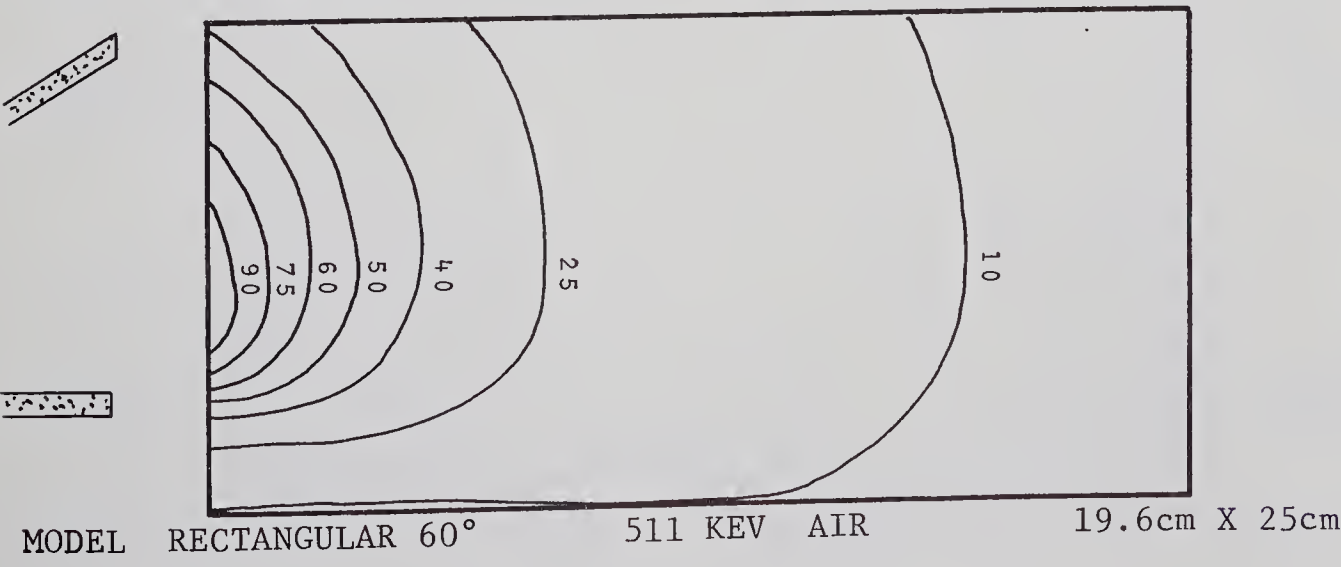
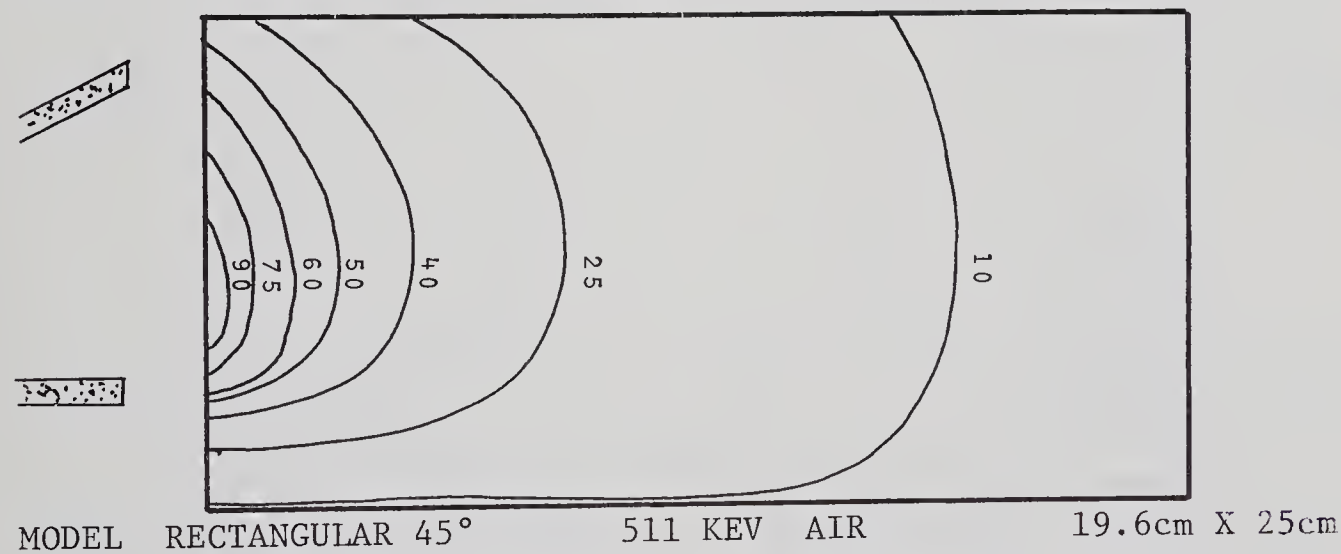
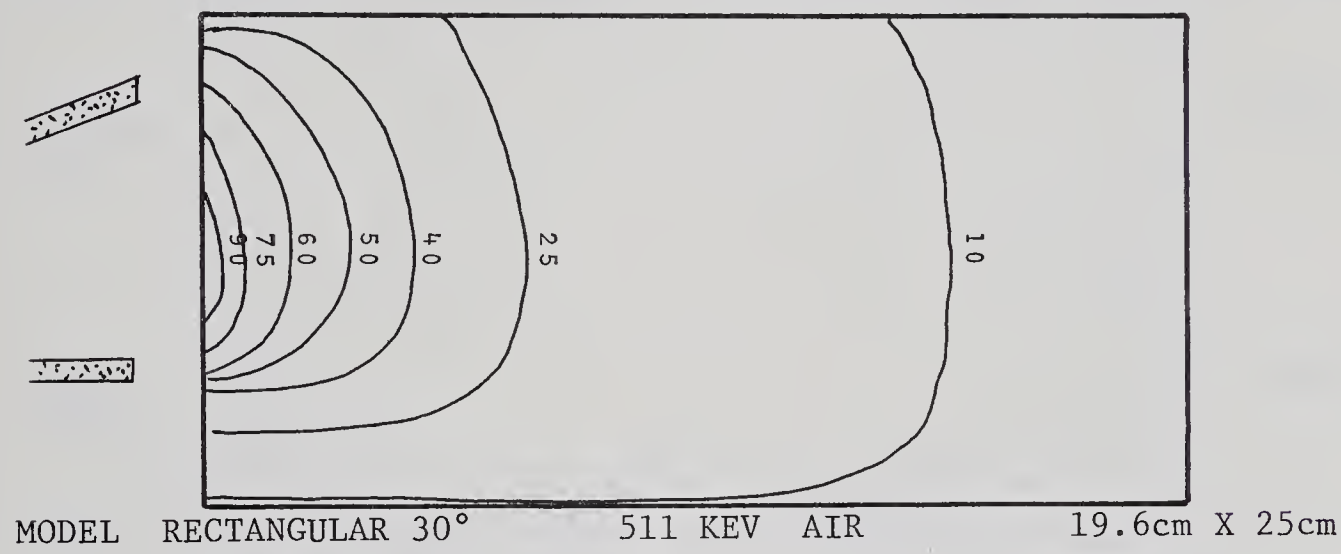
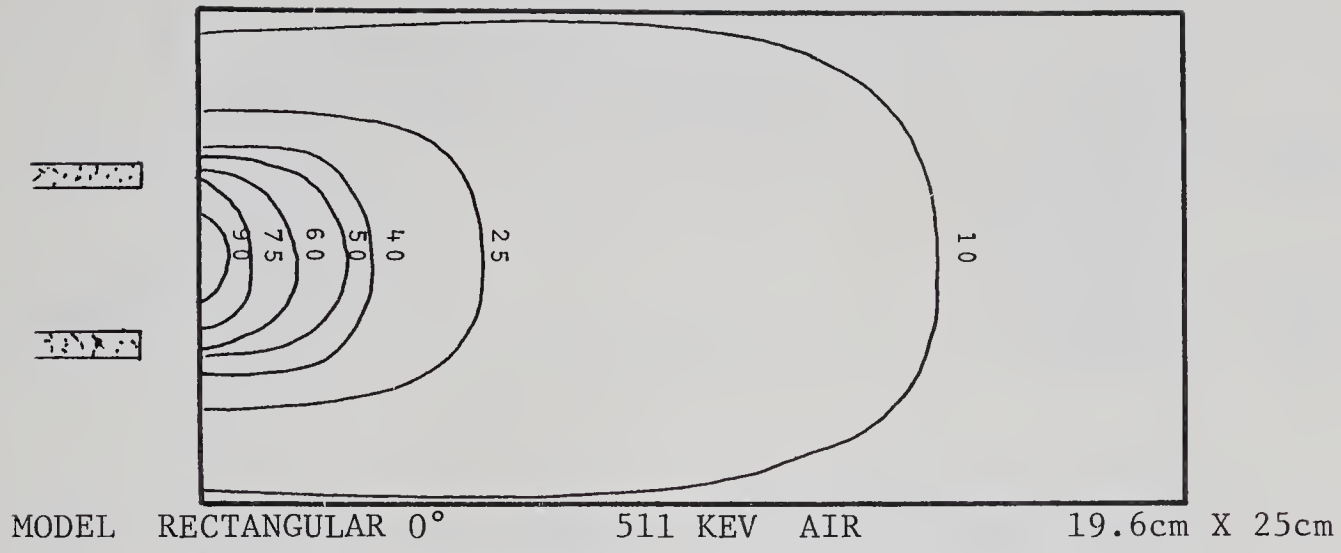
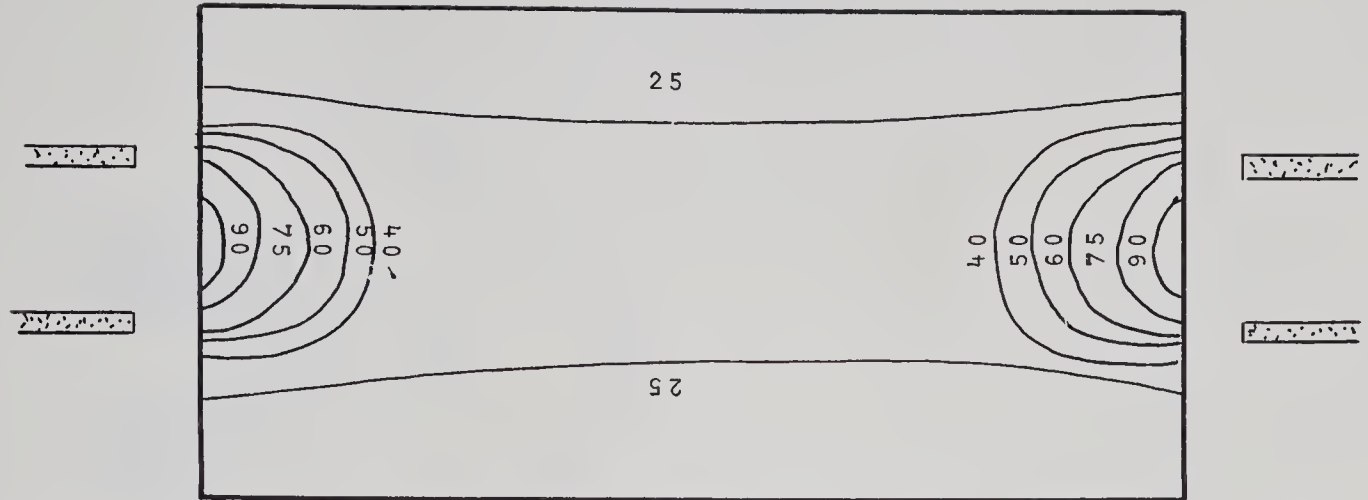


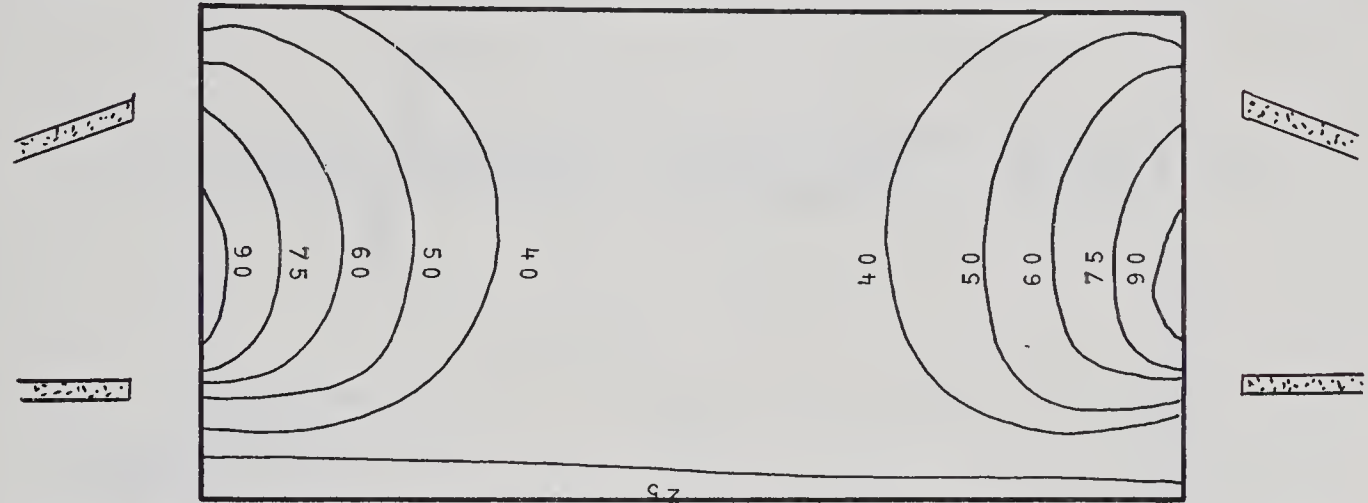
FIGURE 33



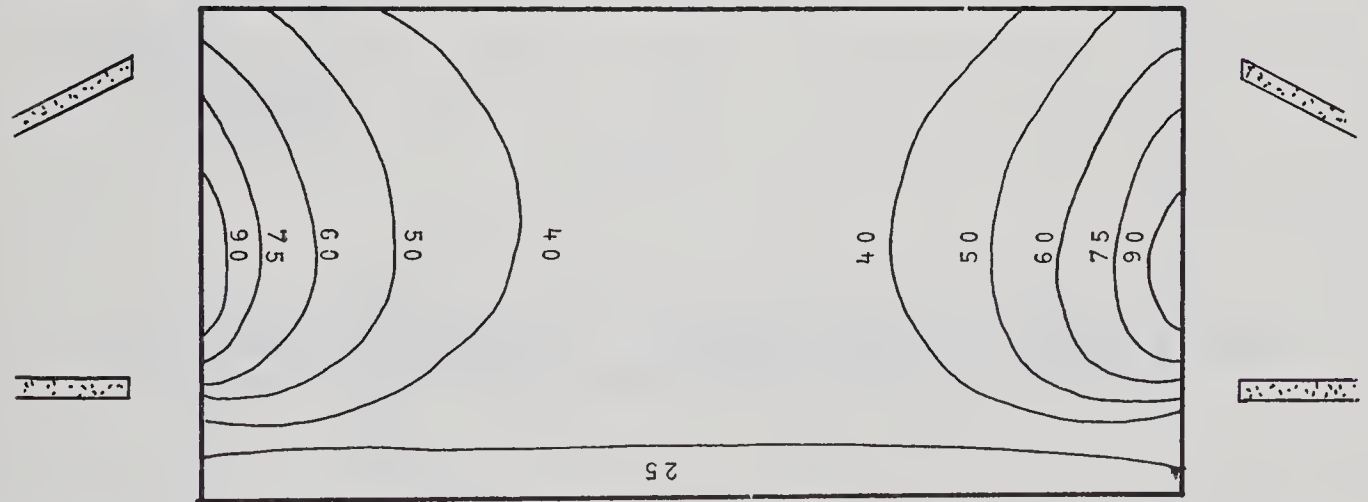




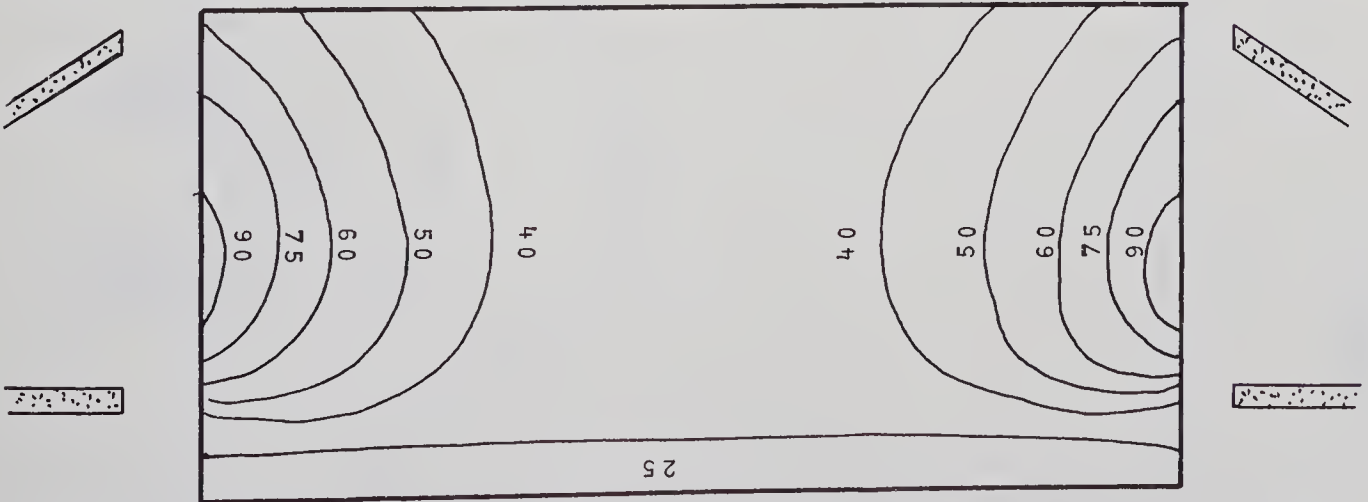
MODEL RECTANGULAR 0° - SUM 511 KEV AIR 19.6cm X 25cm



MODEL RECTANGULAR 30° - SUM 511 KEV AIR 19.6cm X 25cm



MODEL RECTANGULAR 45° - SUM 511 KEV AIR 19.6cm X 25cm



MODEL RECTANGULAR 60° - SUM 511 KEV AIR 19.6cm X 25cm

FIGURE 34



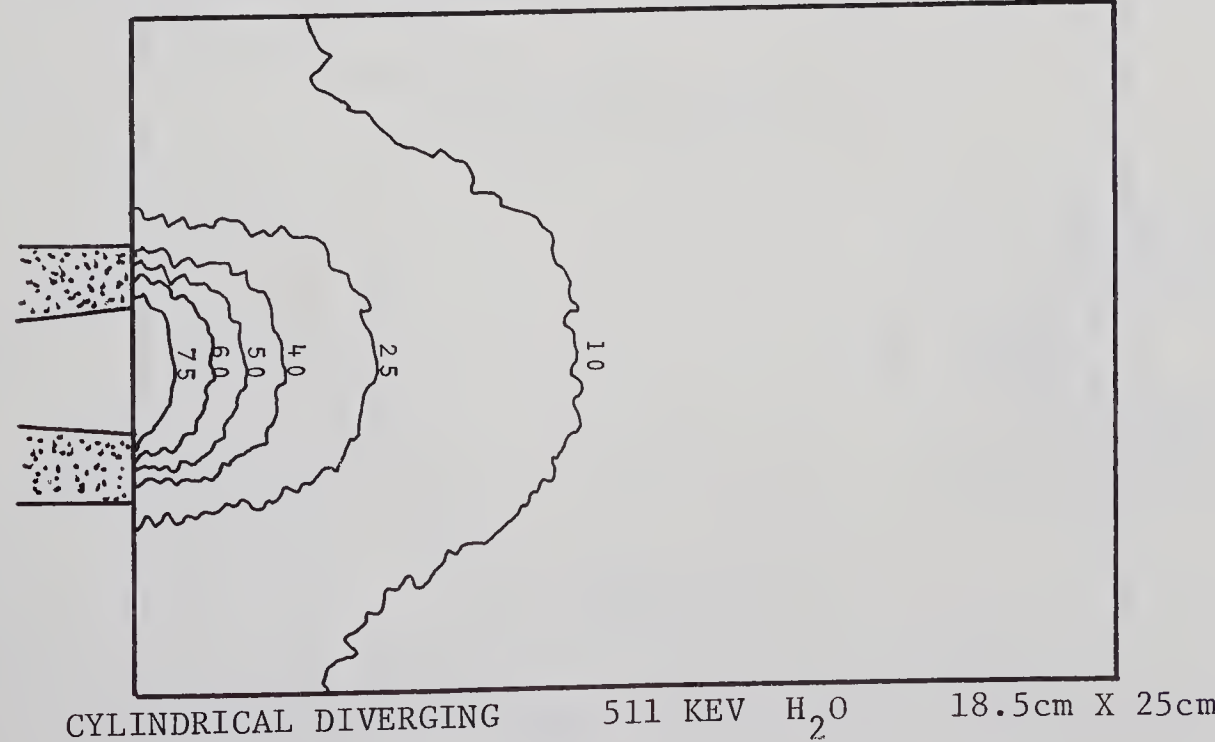
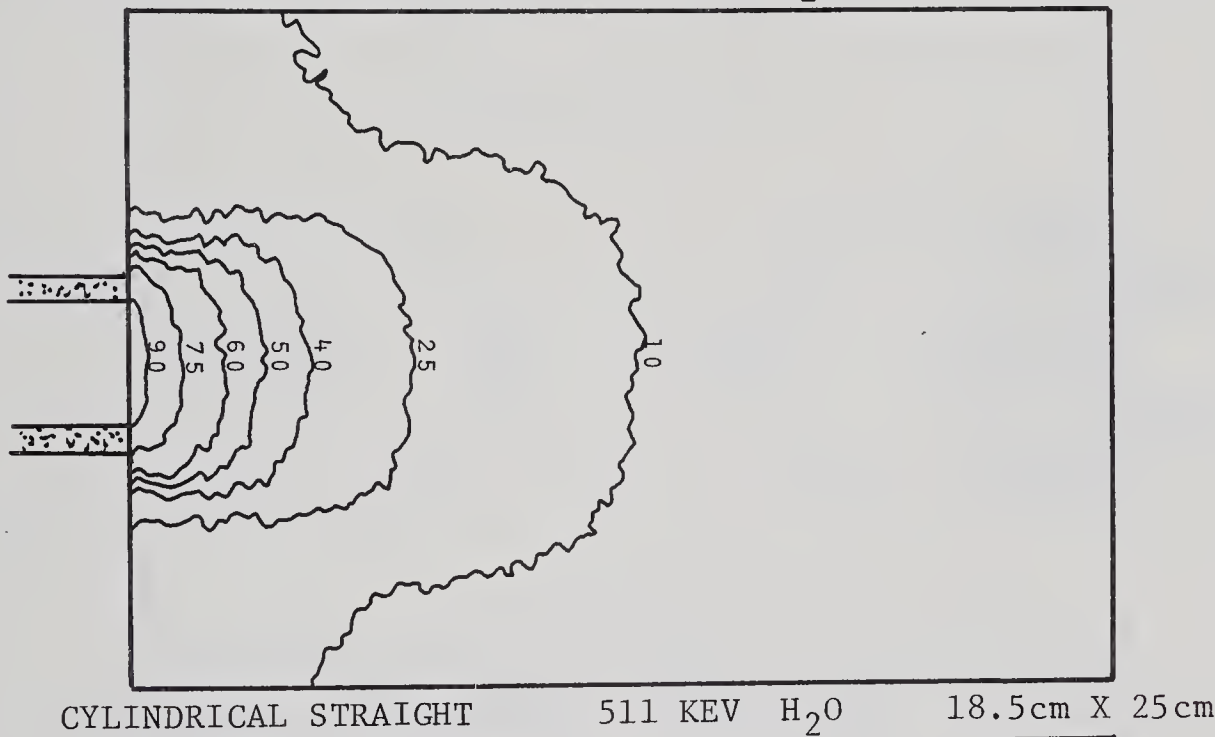
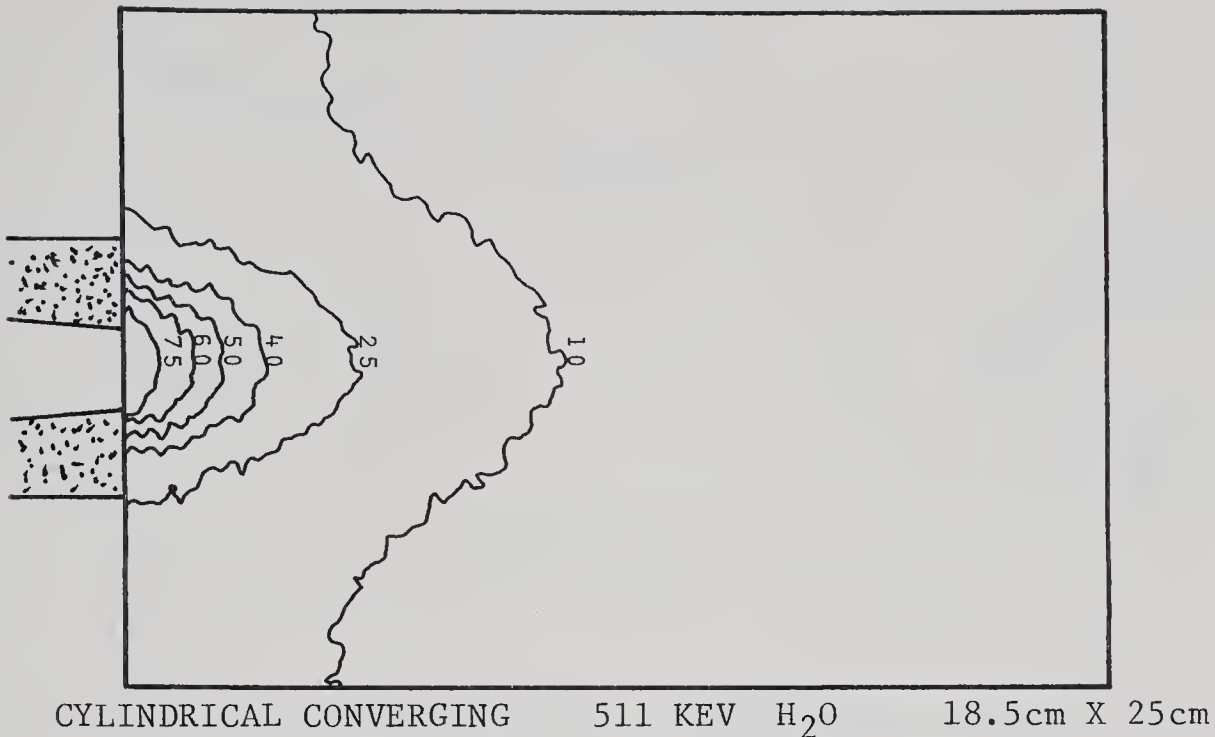
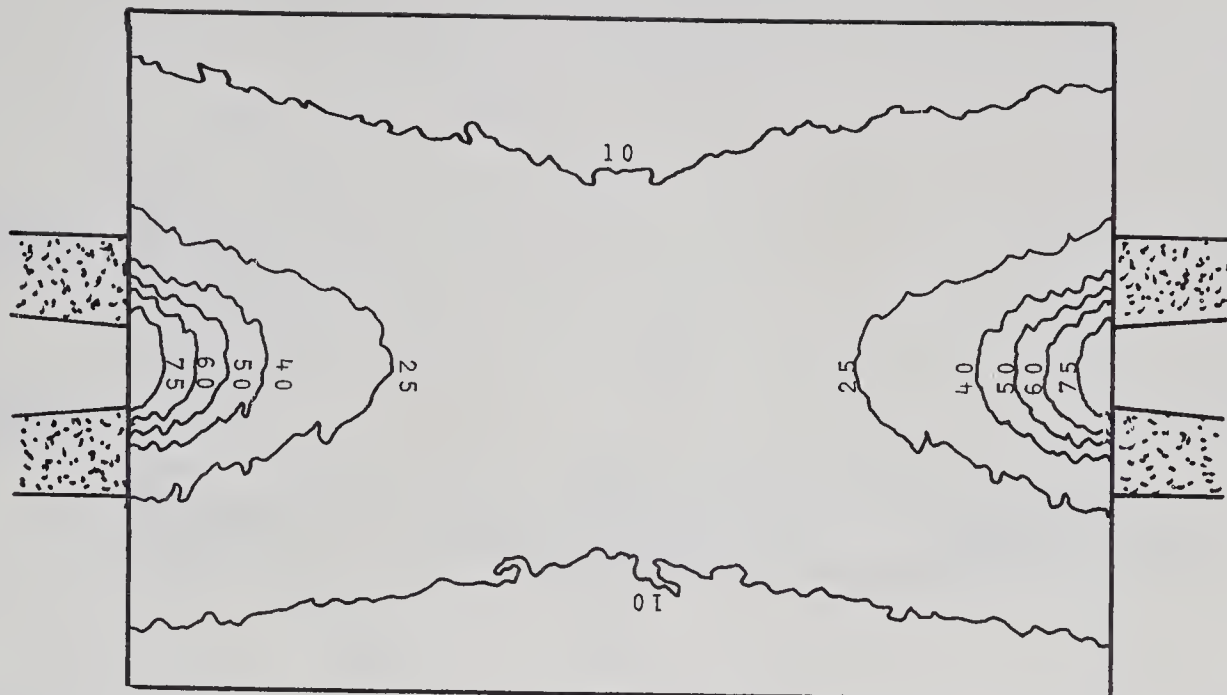
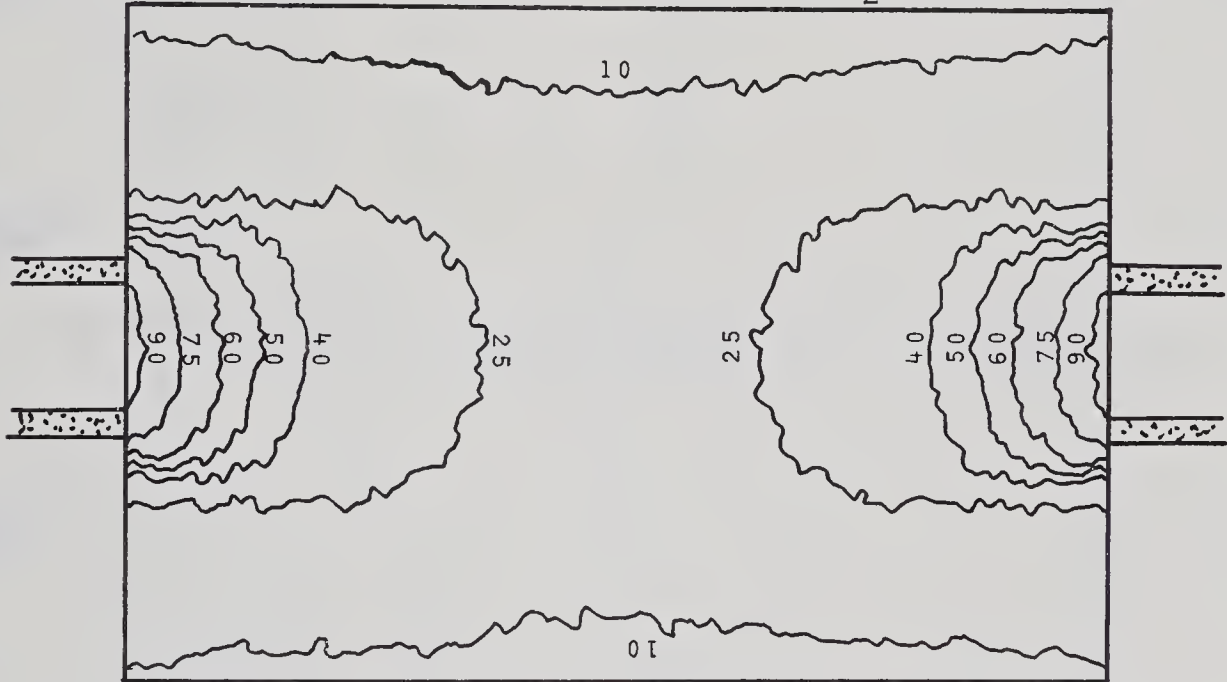


FIGURE 35

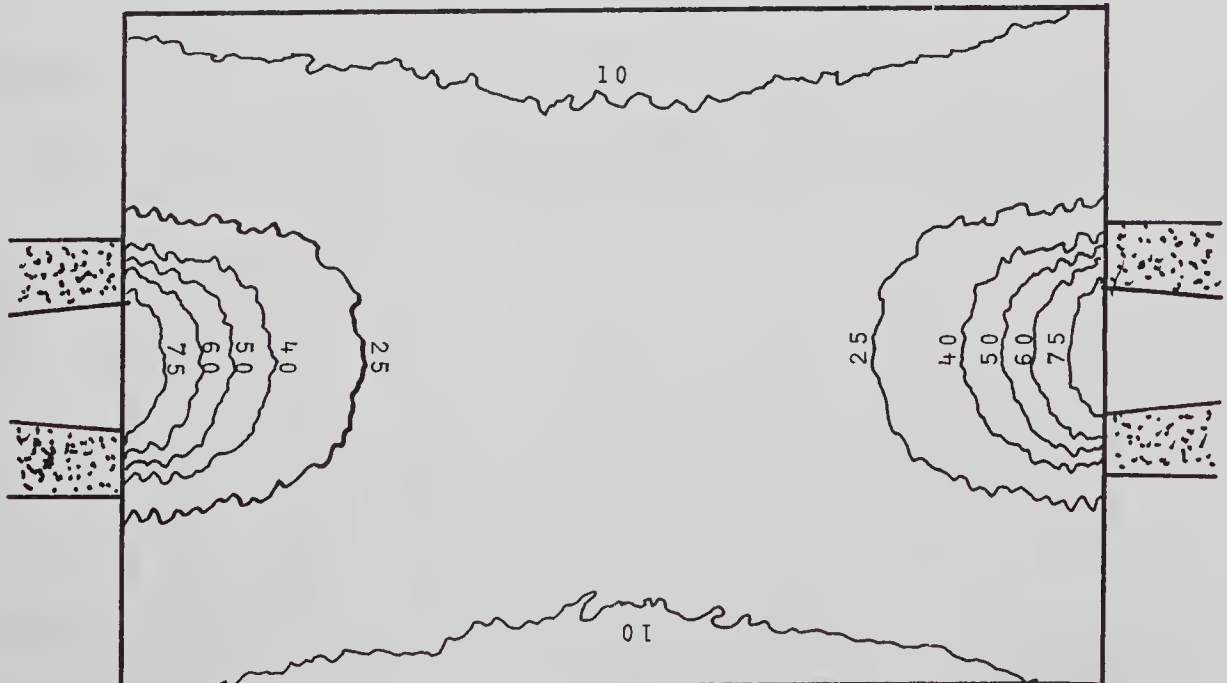




CYLINDRICAL CONVERGING-SUM 511 KEV H<sub>2</sub>O 18.5cm X 25cm



CYLINDRICAL STRAIGHT-SUM 511 KEV H<sub>2</sub>O 18.5cm X 25cm



CYLINDRICAL DIVERGING-SUM 511 KEV H<sub>2</sub>O 18.5cm X 25cm

FIGURE 36



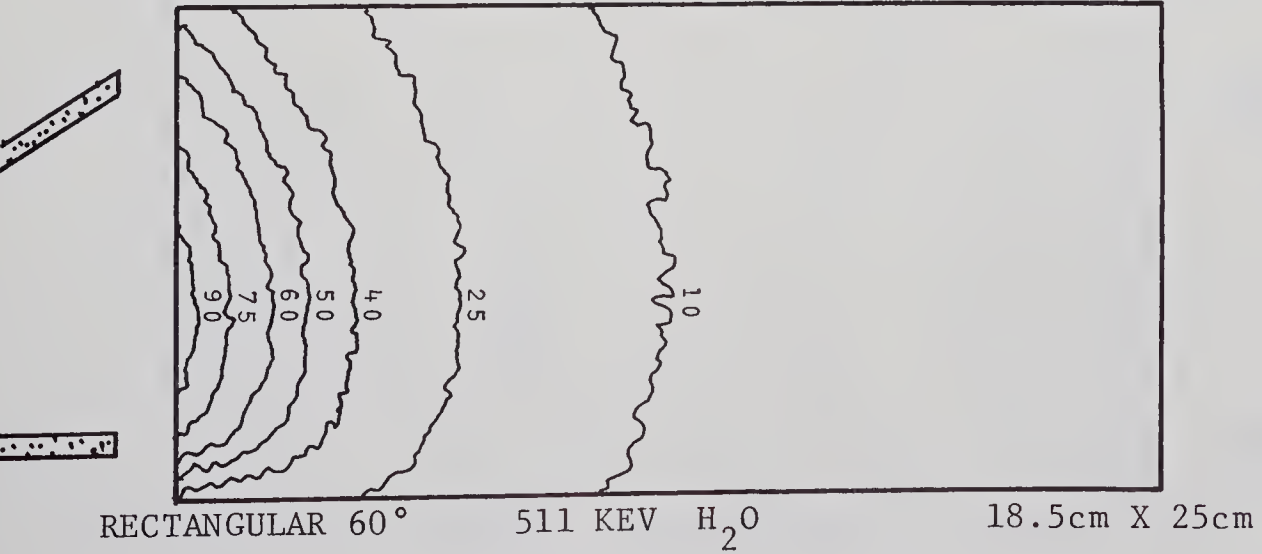
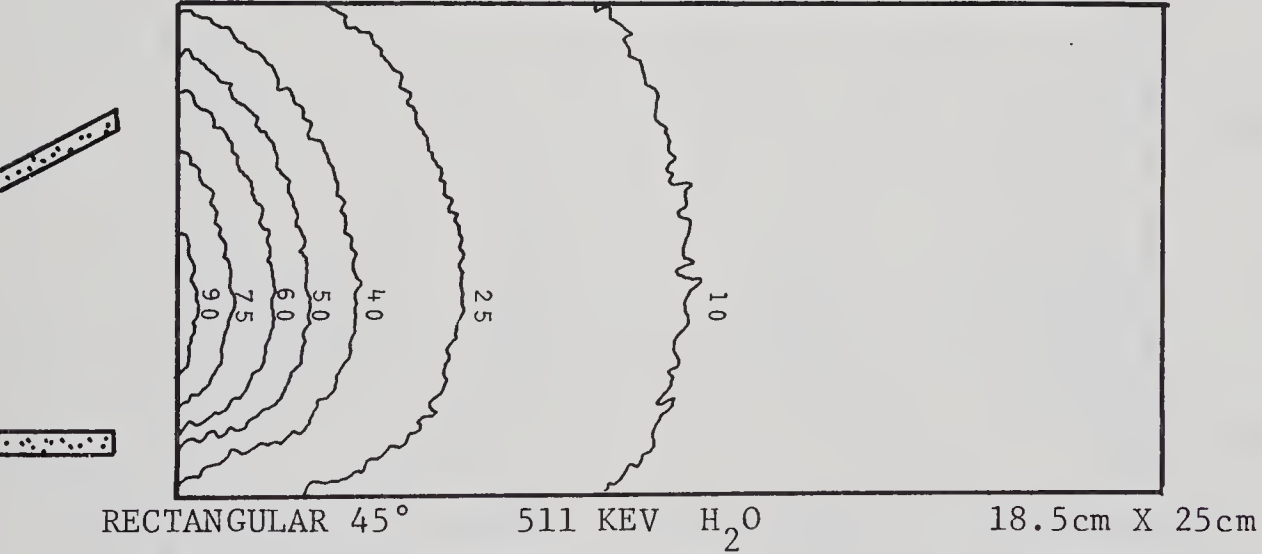
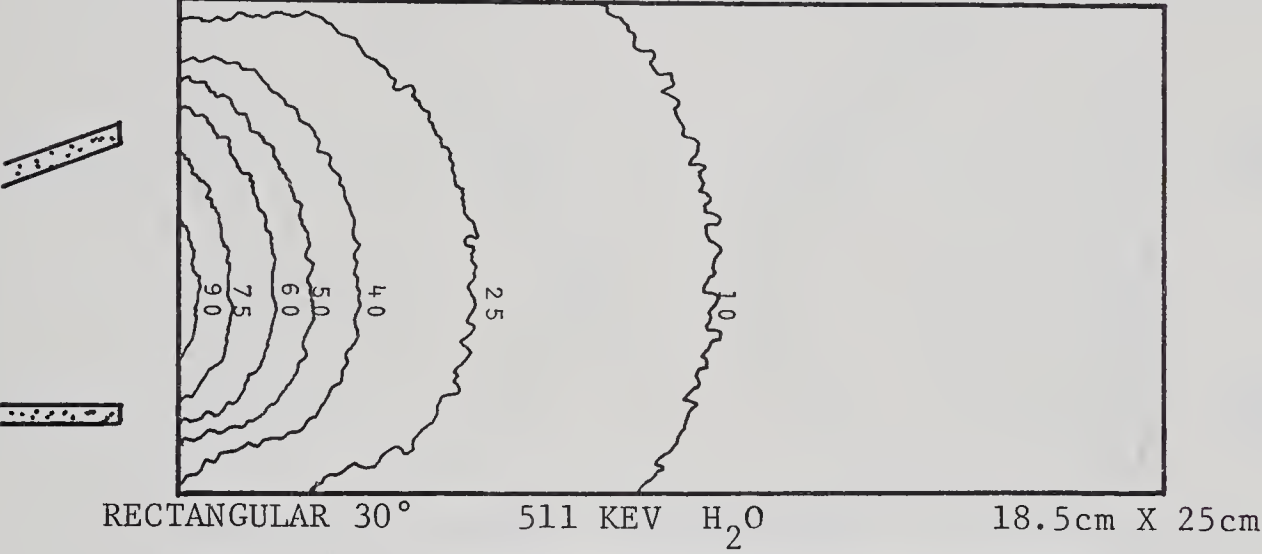
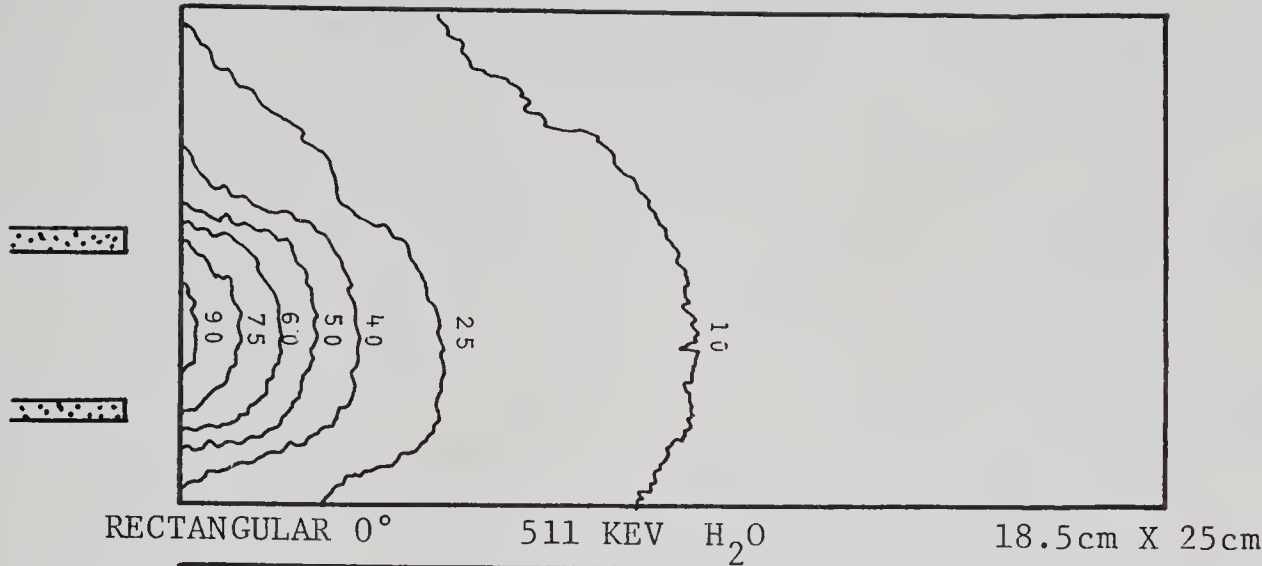


FIGURE 37





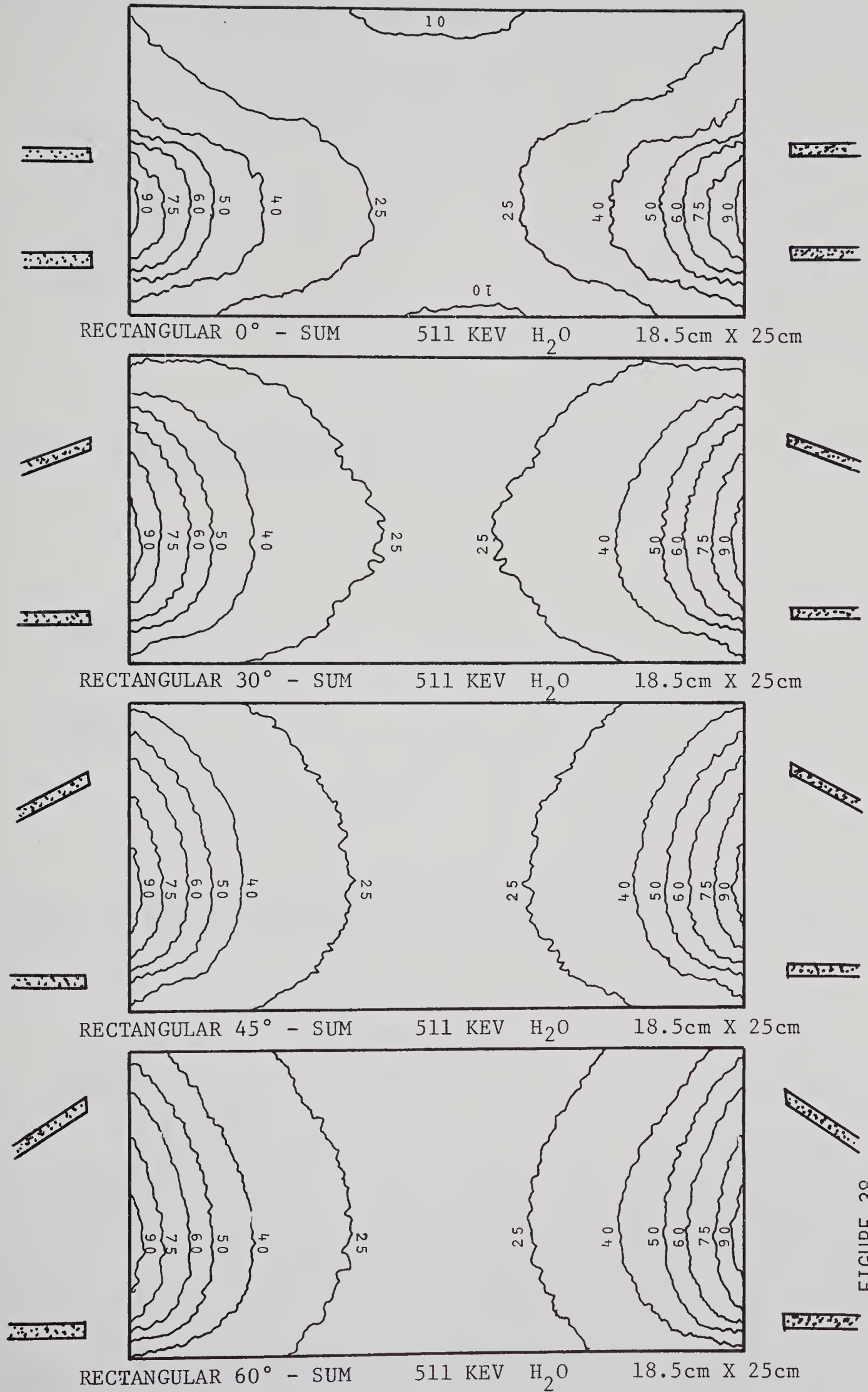
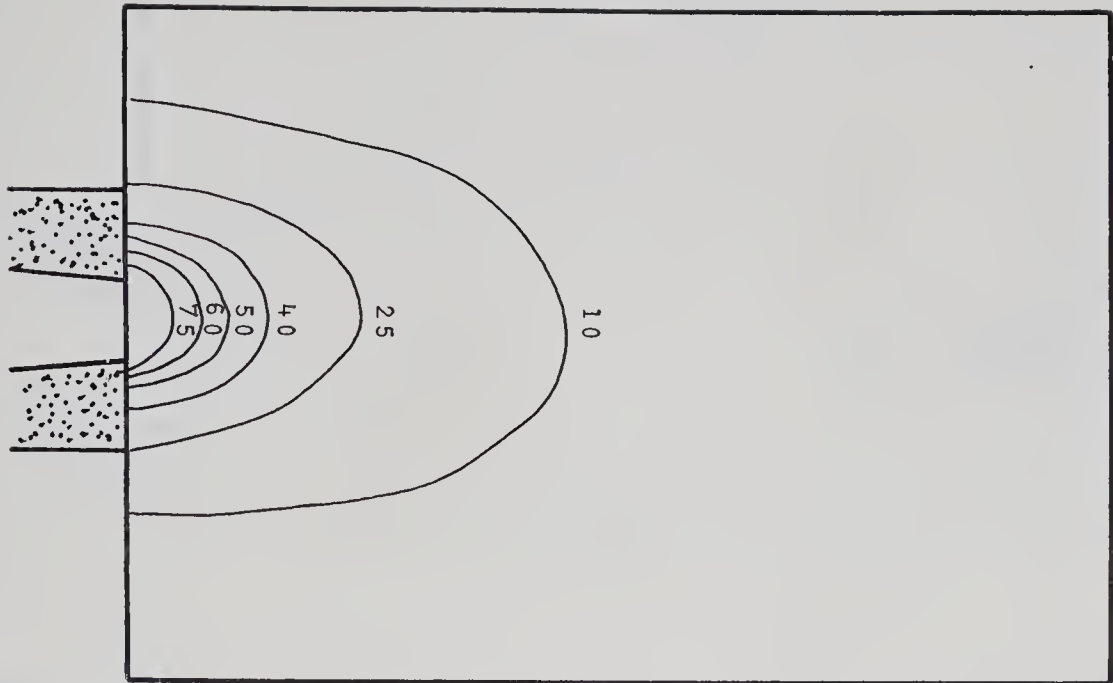
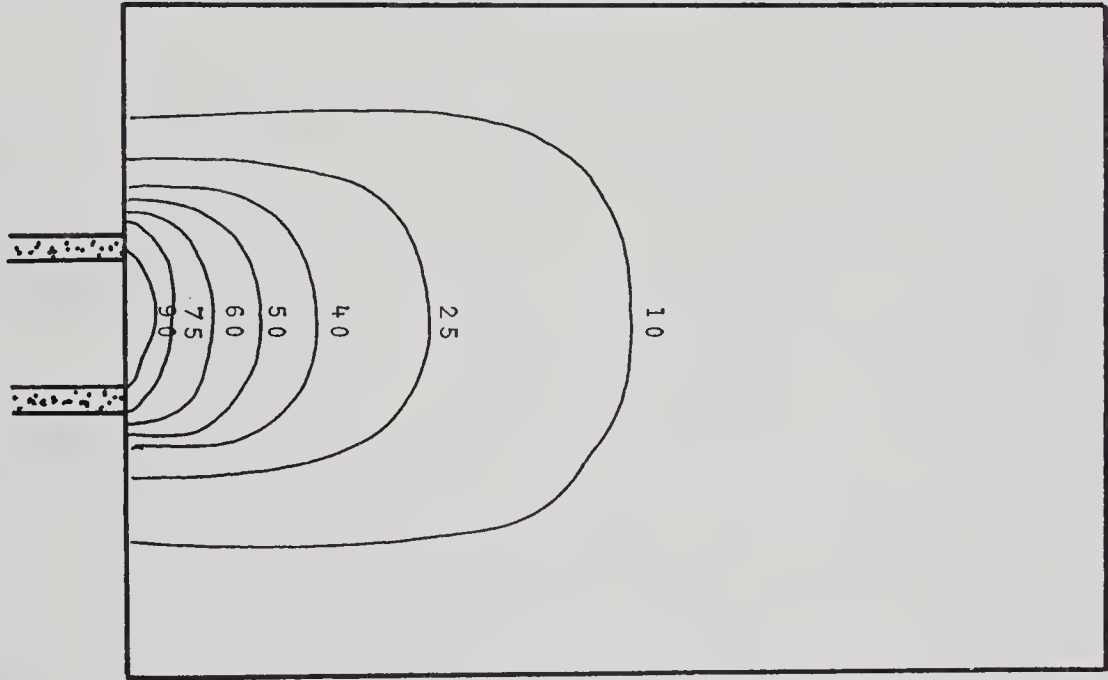


FIGURE 38

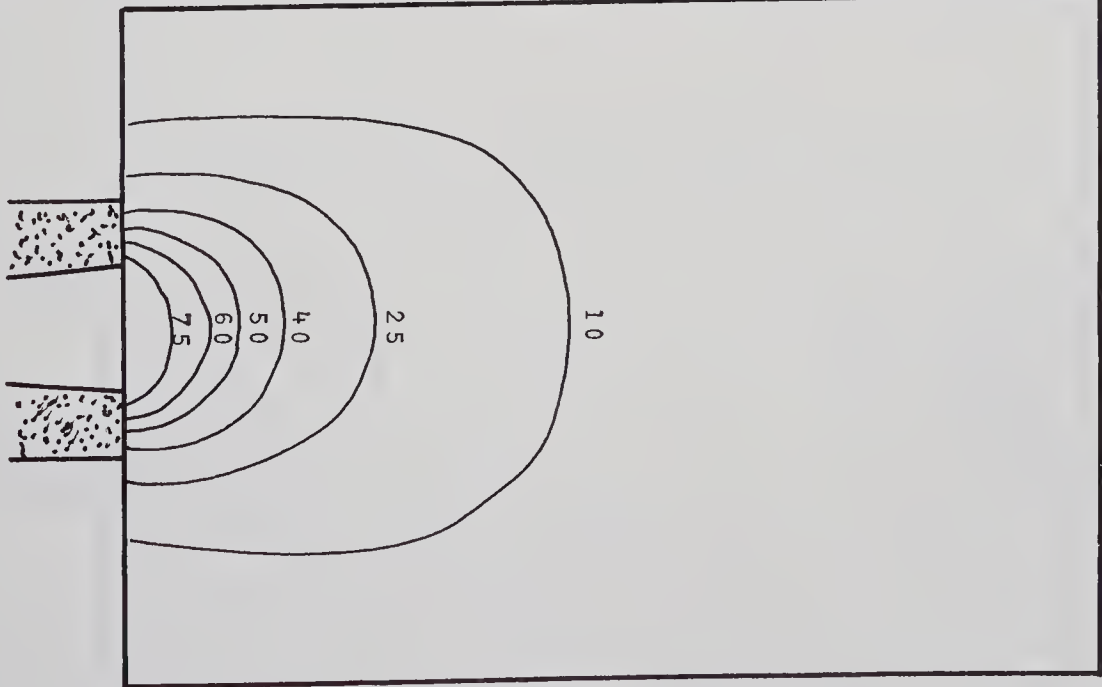




MODEL CYLINDRICAL CONVERGING      511 KEV    $H_2O$    18.5cm X 25cm



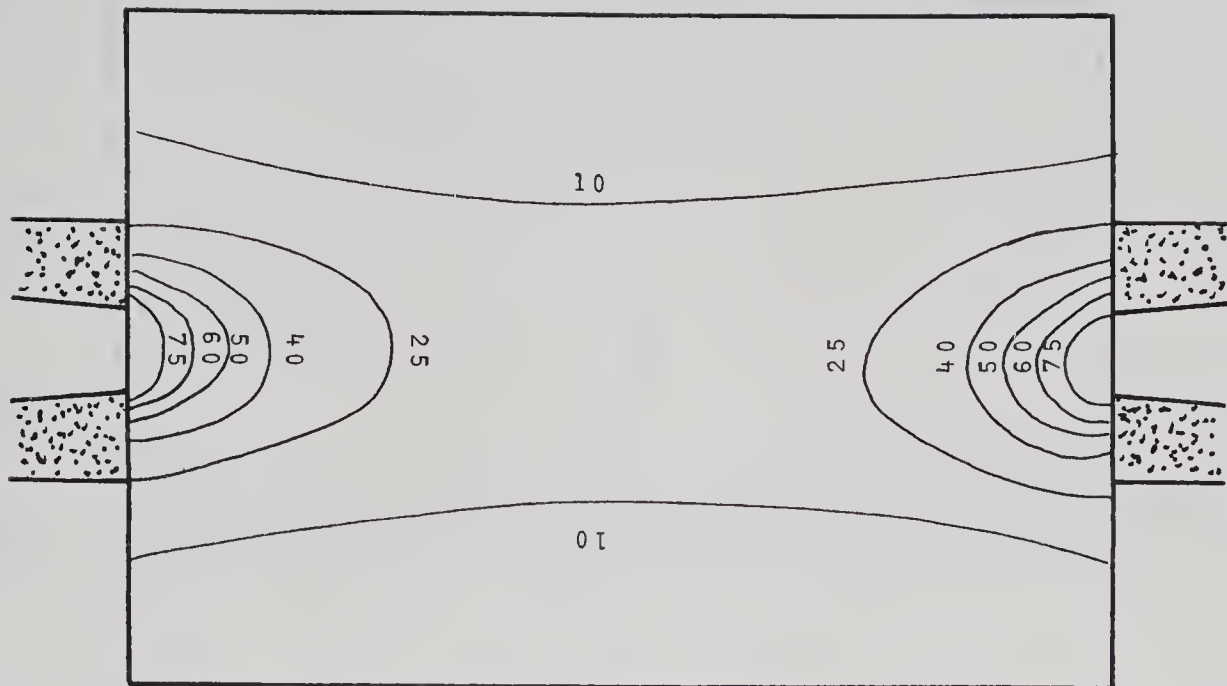
MODEL CYLINDRICAL STRAIGHT      511 KEV    $H_2O$    18.5cm X 25cm



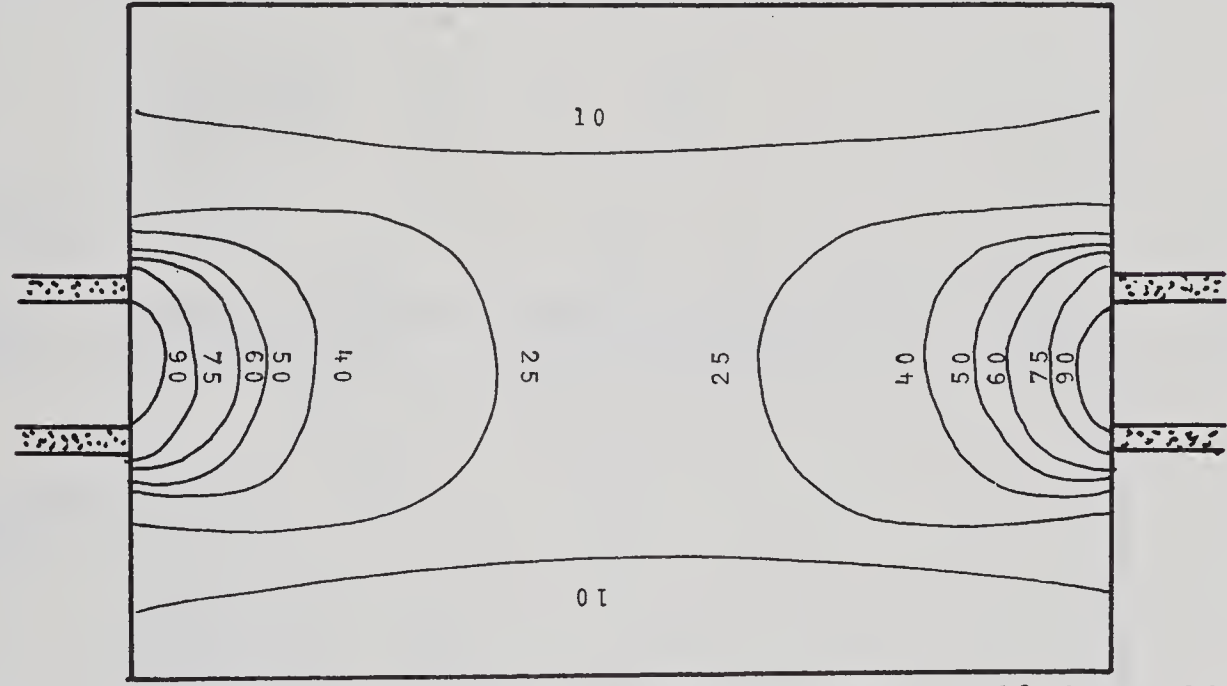
MODEL CYLINDRICAL DIVERGING      511 KEV    $H_2O$    18.5cm X 25cm

FIGURE 39

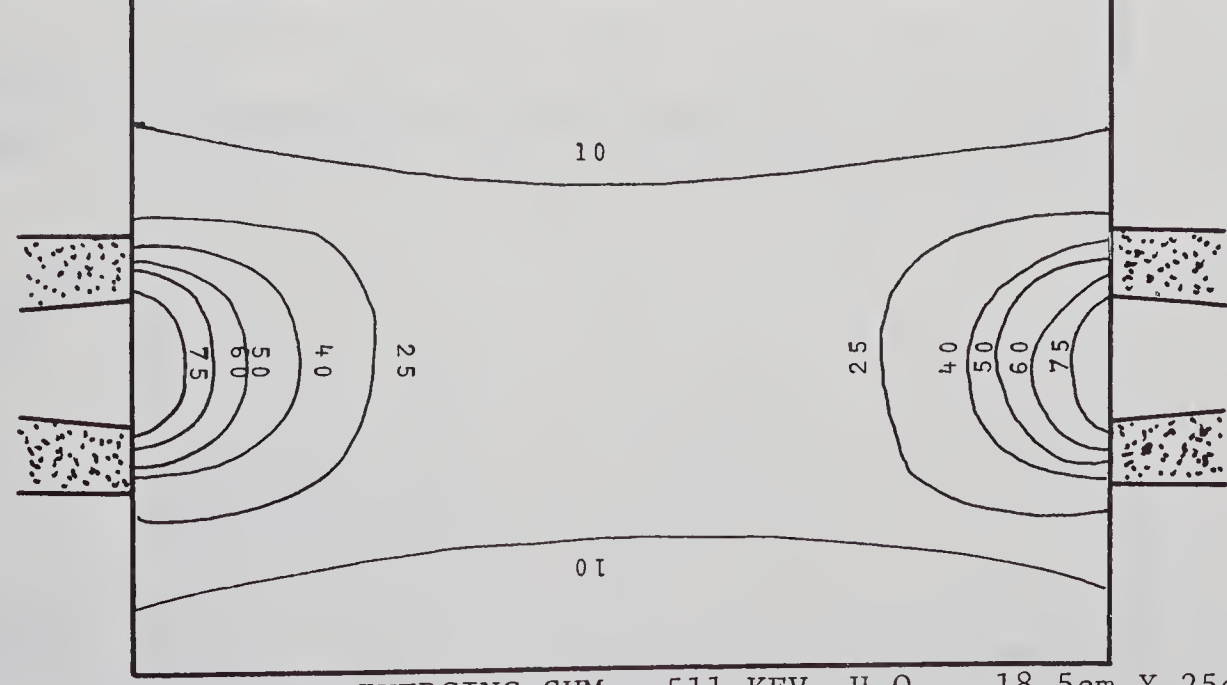




MODEL CYLINDRICAL CONVERGING-SUM 511 KEV  $H_2O$  18.5cm X 25cm



MODEL CYLINDRICAL STRAIGHT-SUM 511 KEV  $H_2O$  18.5cm X 25cm



MODEL CYLINDRICAL DIVERGING-SUM 511 KEV  $H_2O$  18.5cm X 25cm

FIGURE 40



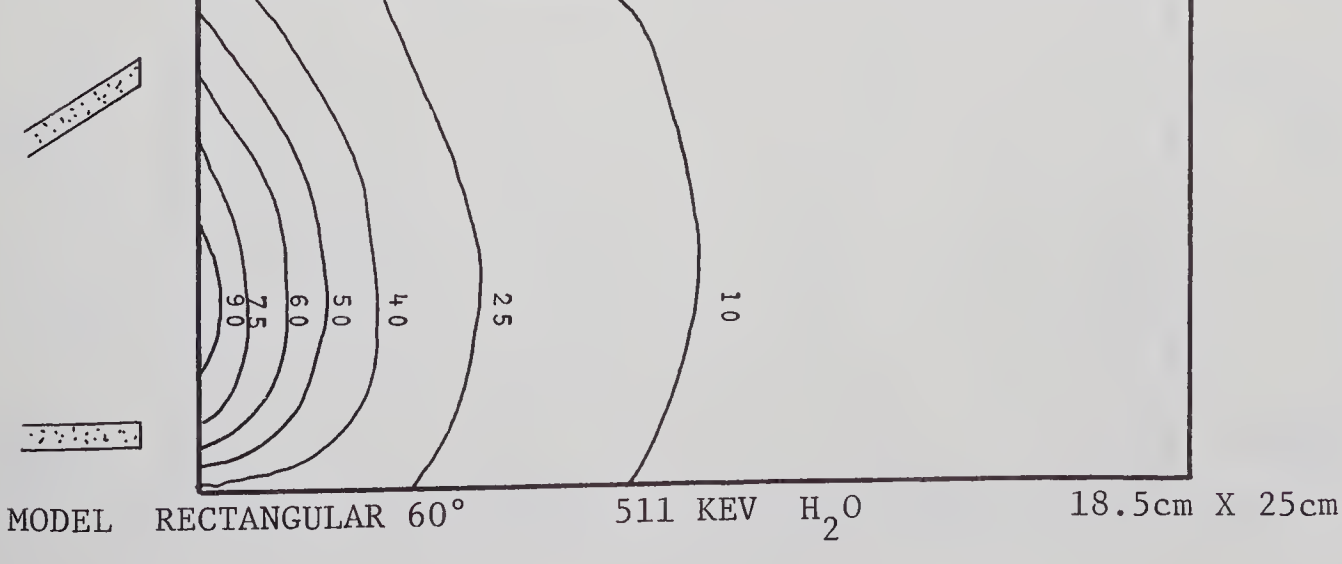
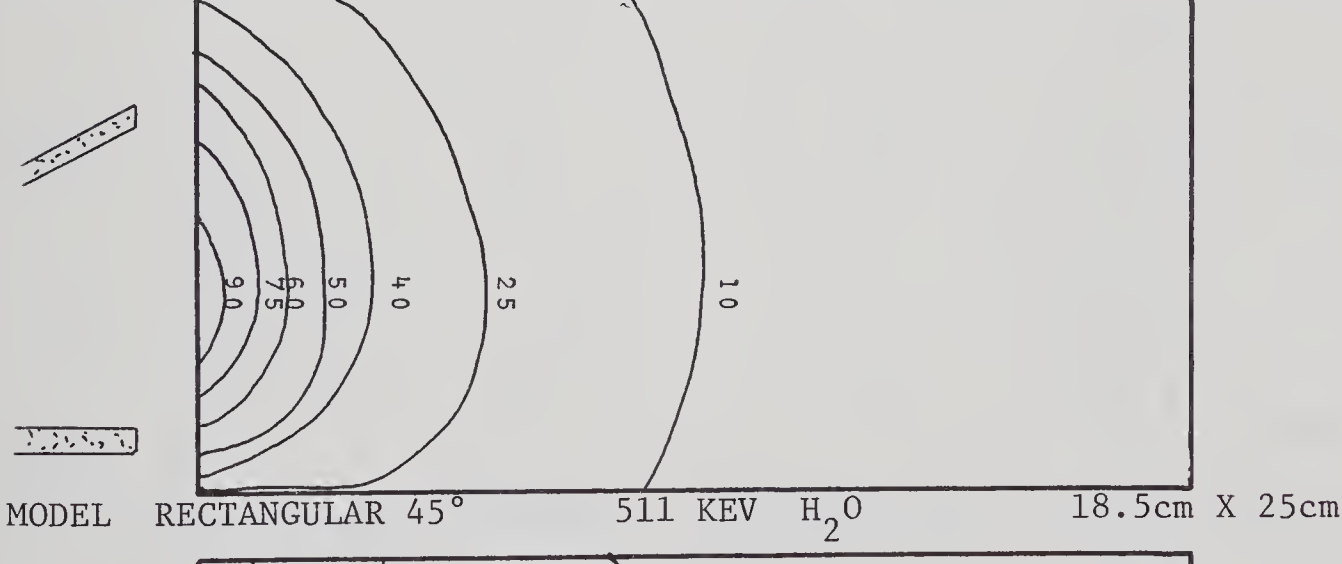
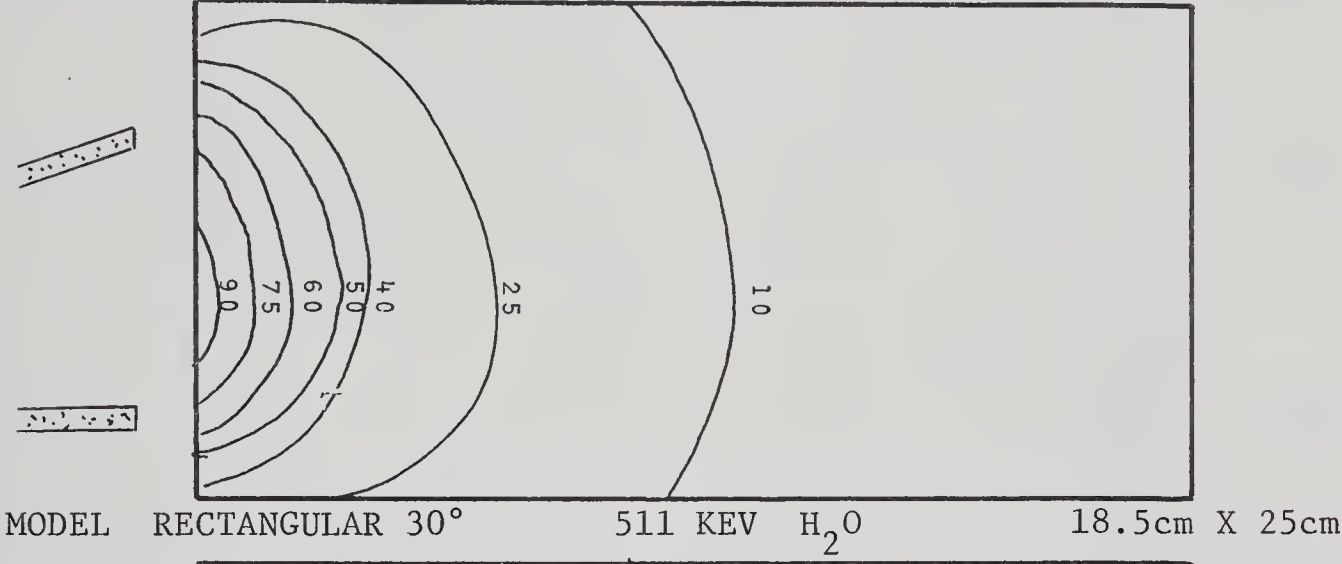
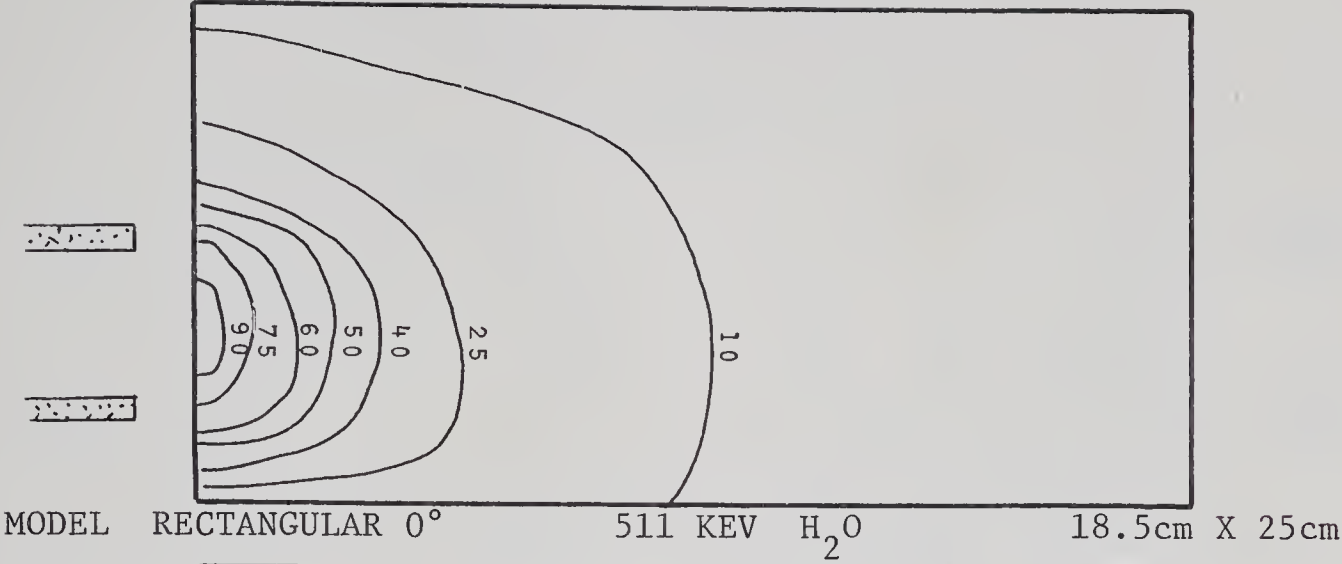


FIGURE 41





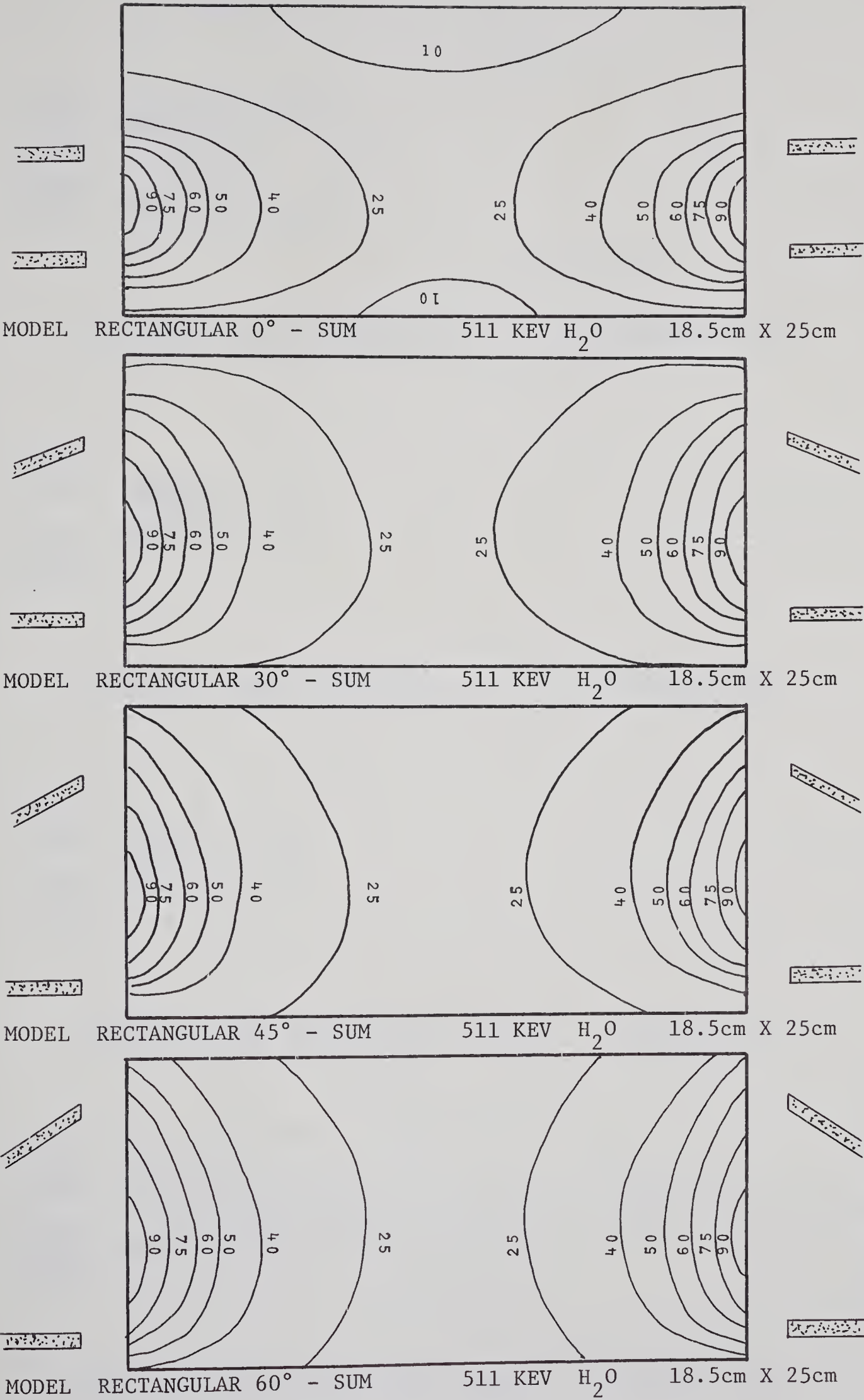


FIGURE 42



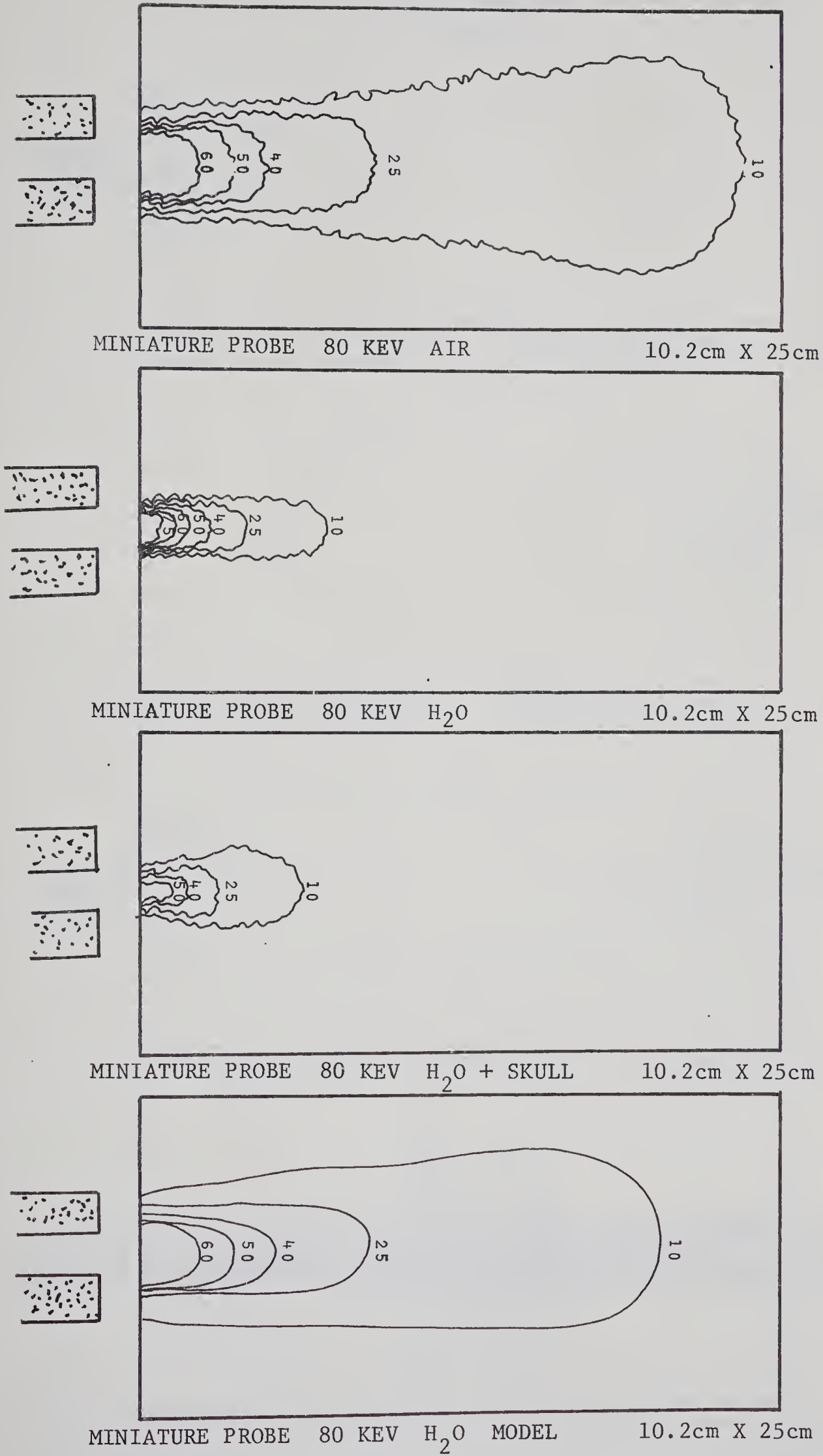
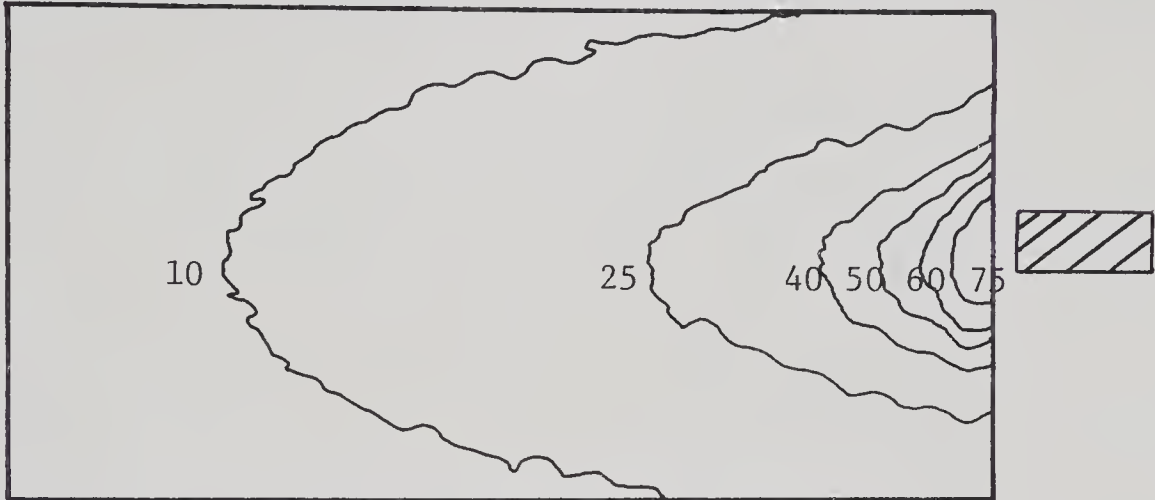


FIGURE 43

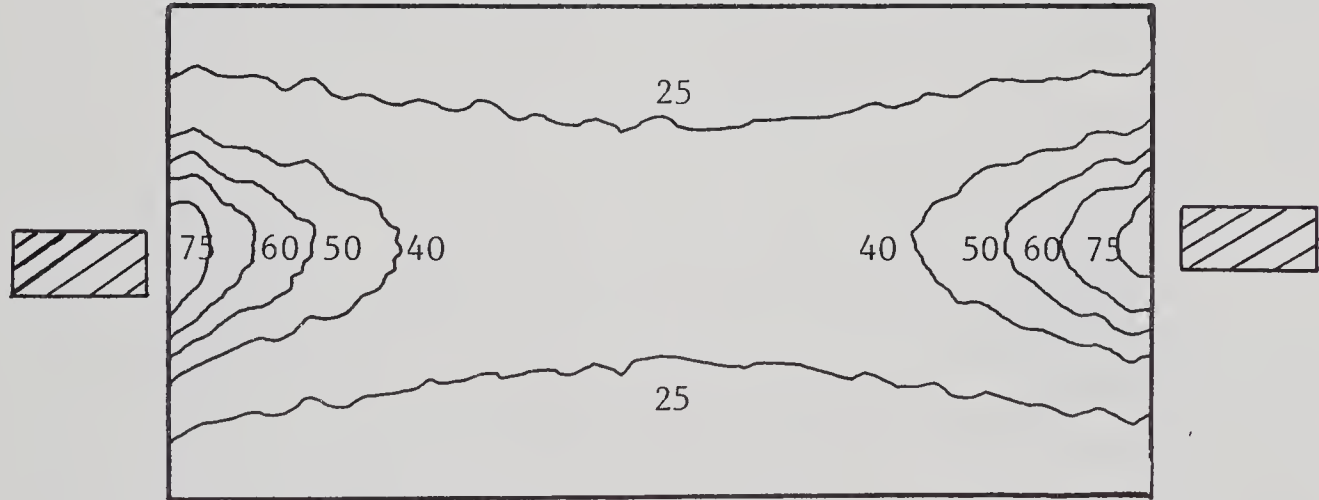




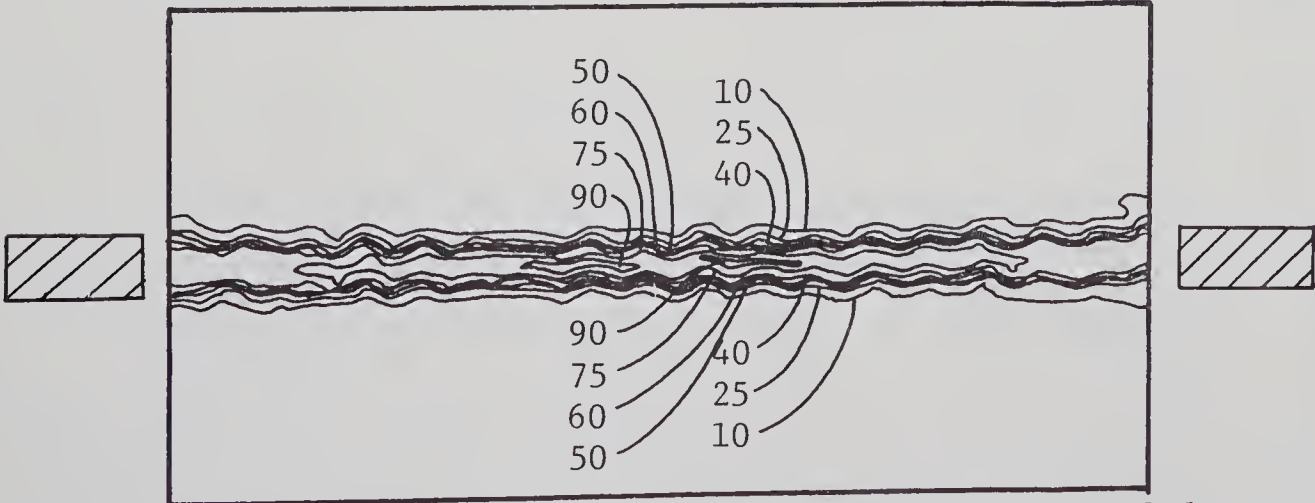
POSITRON SCAN - DETECTOR 1 - 511 KEV-AIR-19.8cm X 9.1cm



POSITRON SCAN - DETECTOR 2 - 511 KEV-AIR-19.8cm X 9.1cm



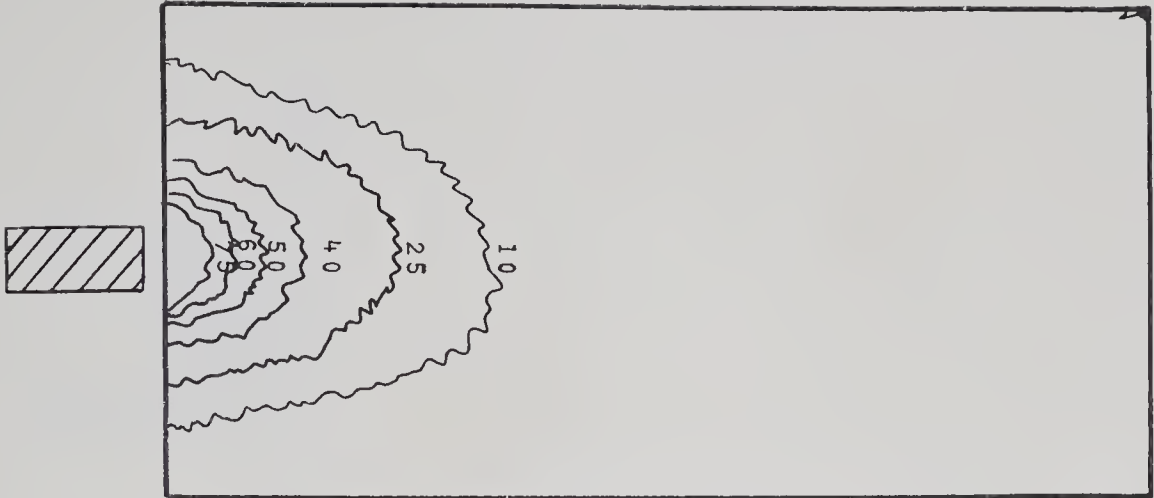
POSITRON SCAN - SUM - 511 KEV AIR 19.8cm X 9.1cm



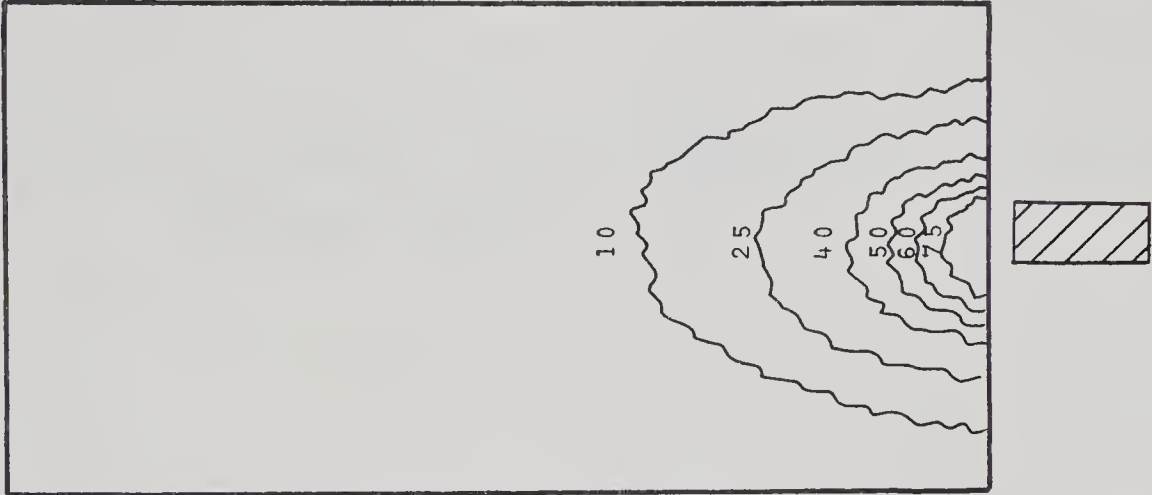
POSITRON SCAN - COINCIDENCE - 511 KEV AIR 19.8cm X 9.1cm

FIGURE 44

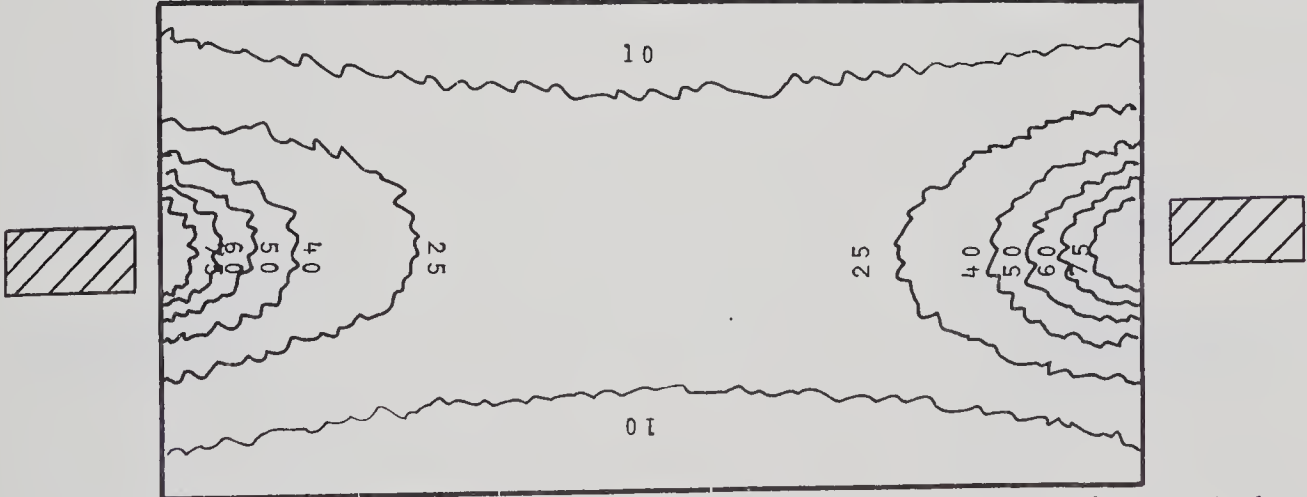




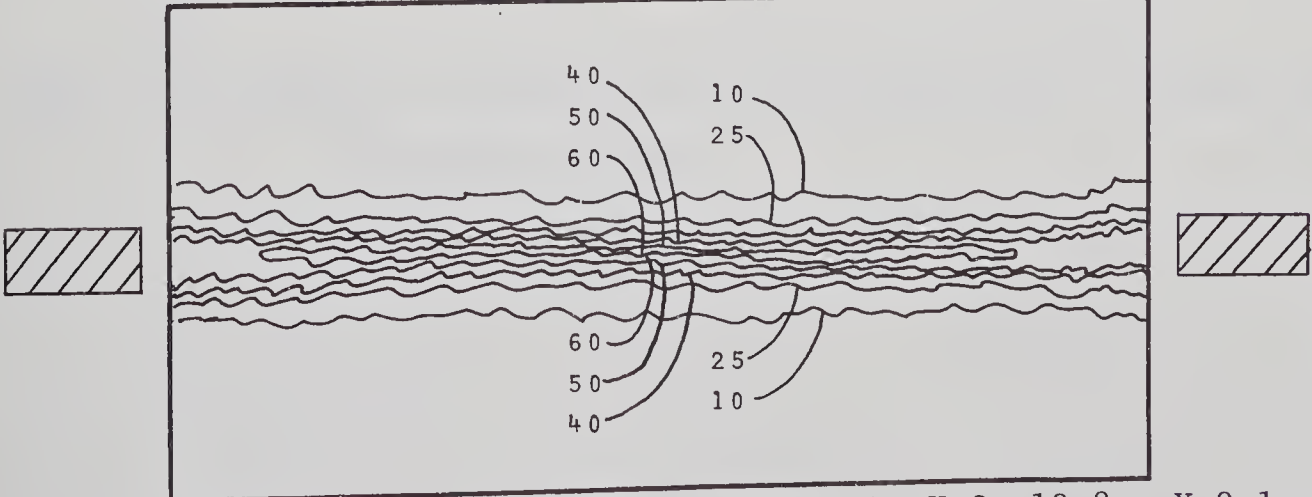
POSITRON SCAN - DETECTOR 1 - 511 KEV -H<sub>2</sub>O- 19.8cm X 9.1cm



POSITRON SCAN - DETECTOR 2 - 511 KEV -H<sub>2</sub>O- 19.8cm X 9.1cm



POSITRON SCAN - SUM - 511 KEV H<sub>2</sub>O 19.8cm X 9.1cm

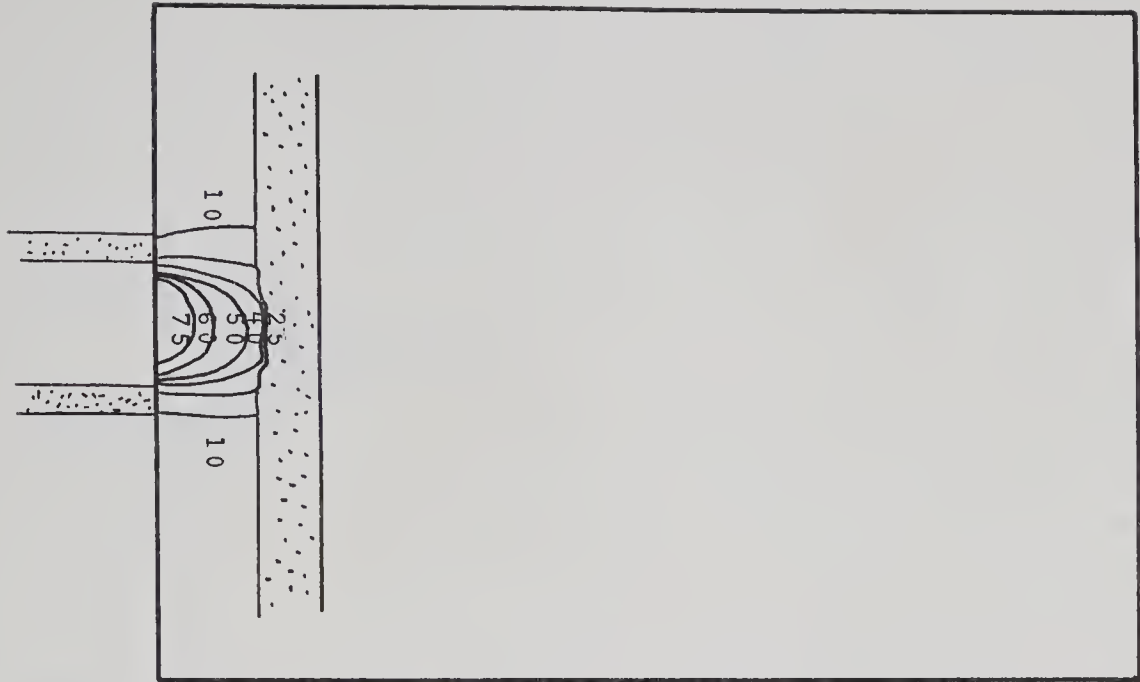


POSITRON SCAN - COINCIDENCE - 511 KEV -H<sub>2</sub>O- 19.8cm X 9.1cm

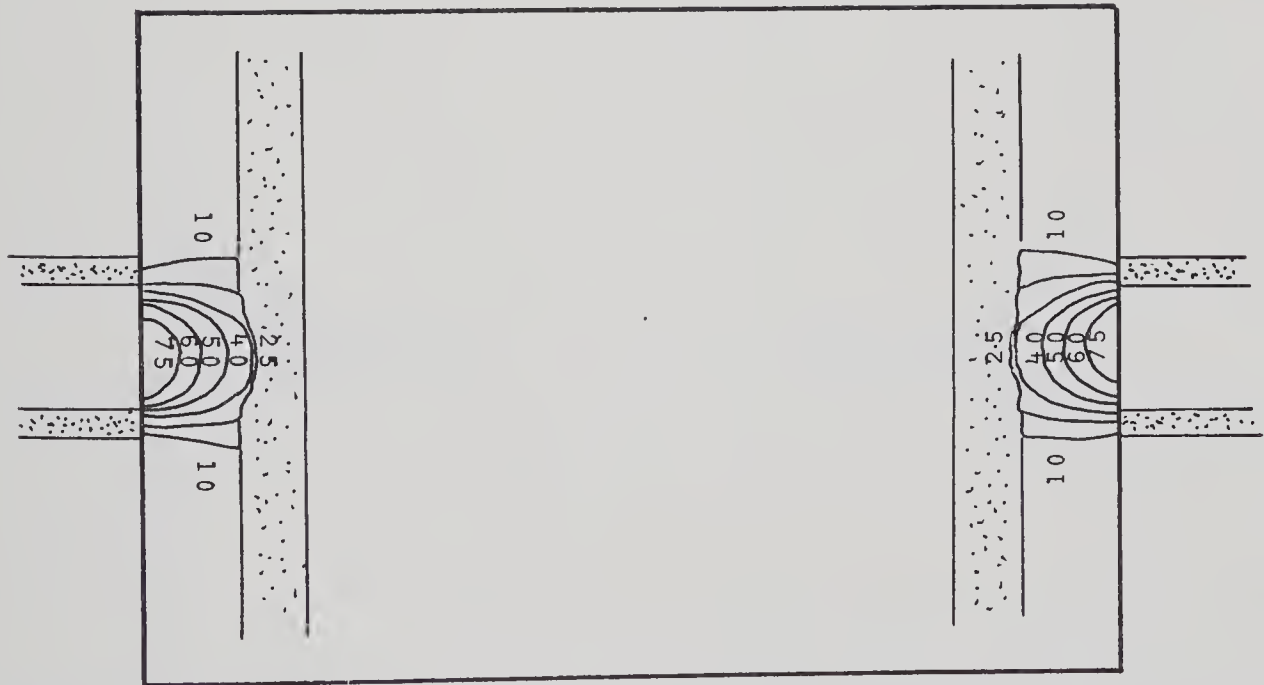
FIGURE 45







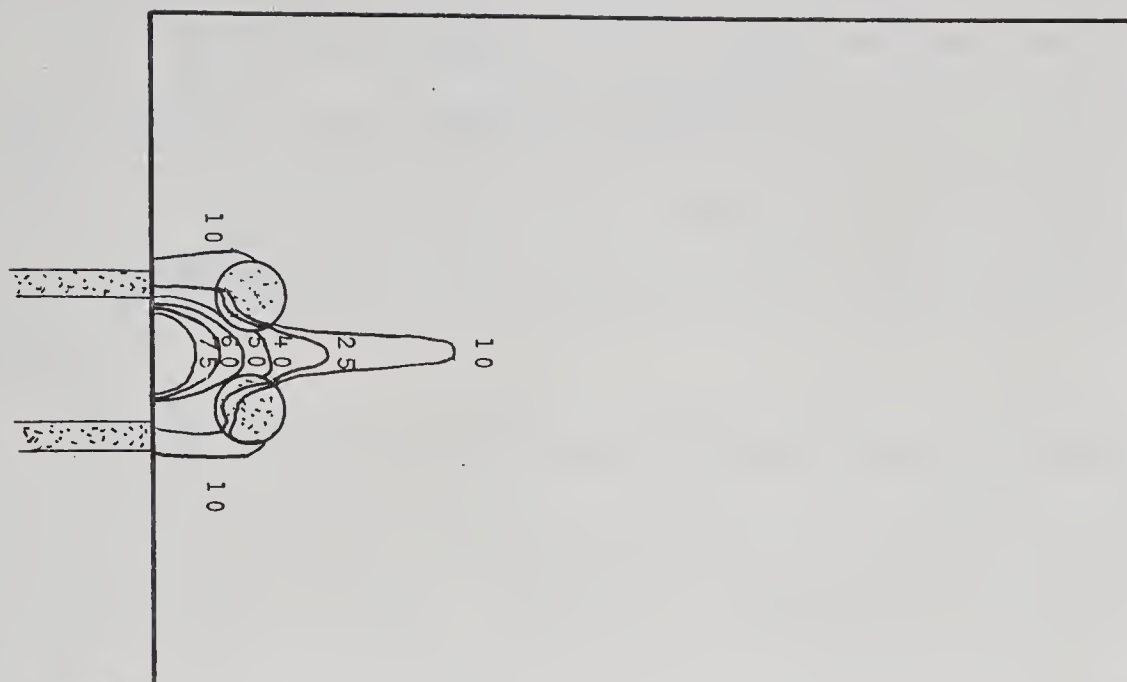
MODEL CYLINDRICAL STRAIGHT 80 KEV TISSUE+1 RIB 19.6cm X 25cm  
TRANSVERSE SECTION



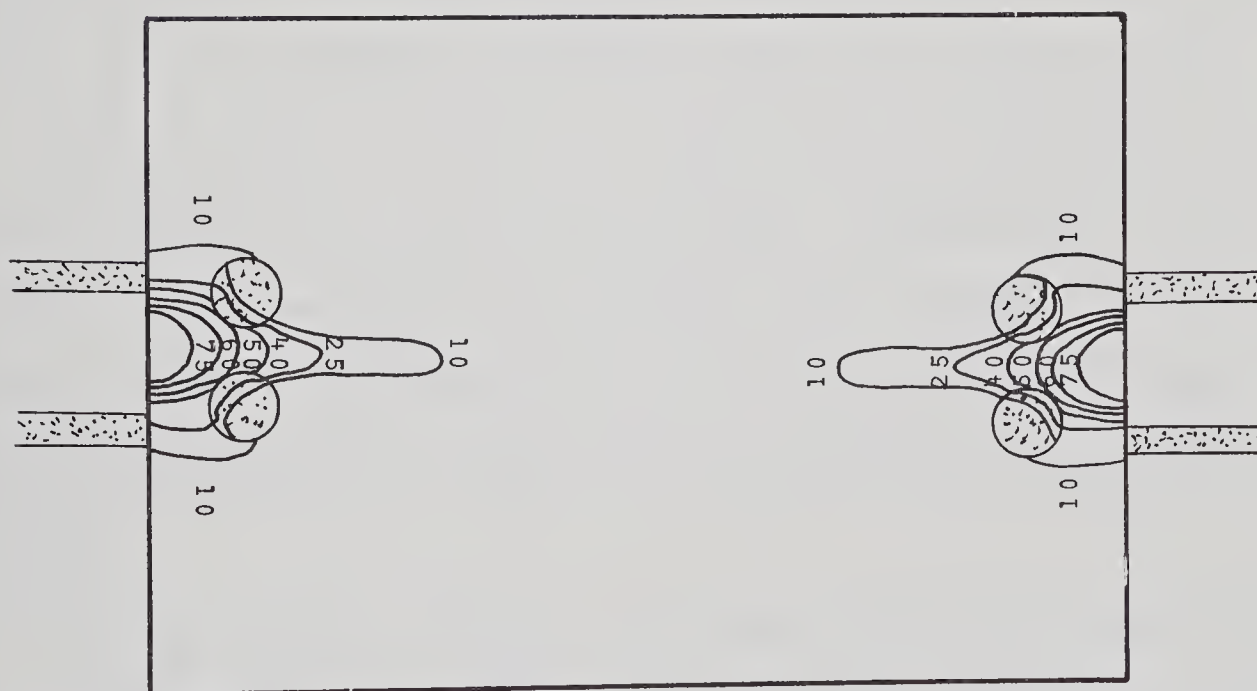
MODEL CYLINDRICAL STRAIGHT-SUM 80 KEV TISSUE+1 RIB 19.6cm X 25cm  
TRANSVERSE SECTION

FIGURE 46





MODEL CYLINDRICAL STRAIGHT 80 KEV TISSUE+2 RIB 19.6cm X 25cm  
SAGITTAL SECTION



MODEL CYLINDRICAL STRAIGHT-SUM 80 KEV TISSUE+2 RIB 19.6cm X 25cm  
SAGITTAL SECTION

FIGURE 47



#### 4.4 Comparison of Collimators

In comparing collimators, it is apparent that the cylindrical straight collimator has response lines which are fairly flat, i.e. uniform with depth. The enhancement of this parameter is desired in the PFSS, but a flatter field response can be obtained with diverging or rectangular collimators.

The cylindrical converging collimator has the highest spatial resolution of all the large collimators tested, as can be seen by the narrowness of the response lines. However, a high spatial resolution is not required in the PFSS and consequently this particular collimator is not considered with respect to lung function studies. Possible applications of this type of collimator could be in regional studies of smaller organs such as the kidney or thyroid. Spatial resolution could be made equal to that of the miniature detection system, shown in Figure 43 but the sensitivity would be larger for the converging collimator, due to the larger crystal.

The cylindrical diverging collimator yielded fairly uniform iso-response lines for all source-medium-detector configurations. While this is a desired characteristic for the PFSS, a major drawback in this type of collimator is the circular field-of-view. With this field-of-view, certain regions of the lungs are not "seen" by the detectors; consequently, analysis is complete.

The rectangular straight collimator yielded the flattest isoresponse lines. If the height of the collimator is increased from the height of the measured collimator (7.6 cm), the response lines would become flatter still. The field-of-view of this collimator is given by equation (B.15) in Appendix B and is rectangular, with the corners slightly rounded off. It is this type of collimator that can view the complete lung, with minimal overlap.

In the higher energy scans, using  $^{22}\text{Na}$  (Figures 27 and 29), the



"flareout" at the ends is due to collimator penetration due to improper shielding of the crystal at the back of the collimator and should be disregarded.

For tapered rectangular collimators, only diverging collimators were tested as a large field-of-view in the PFSS is desired and this cannot be achieved readily with converging collimators. Three taper angles were measured:  $30^{\circ}$ ,  $45^{\circ}$ , and  $60^{\circ}$  to the normal. Although the diverging rectangular collimators give slightly better flat field response, particularly for the  $30^{\circ}$  diverging collimator, the field lines eventually curve at the ends. This end curvature arises since the collimator no longer limits the crystal, and a distance squared dependence results. This effect becomes more prominent with larger taper angle. The "flareout" at the ends, (evident in some of the scans), is again due to improper crystal shielding and should be disregarded.

With variation in depth the "tightest" and most uniform iso-response lines were obtained for the positron coincidence scans, which involved no physical collimation. The reasons for this excellent field-of-view are two-fold. First, positron annihilation results in two gamma rays travelling in directions  $180^{\circ}$  apart. In order for a coincidence event to be detected, the annihilation event is constrained to occur in the geometrical space of the cylinder formed between the two crystals, which therefore makes the field-of-view distance-independent. Second, since the annihilation radiation is of a reasonably high energy (551 keV), the attenuation in tissue is not as depth-dependent as for 80 keV gamma rays. However, the major problem in using positron emitters for clinical work is that most have short half-lives and must be accelerator produced. Also, the radiation dose to the patient is usually larger than for 'single photon' radioisotopes since large amounts of activity must be





used in order to obtain significant numbers of coincidence events.

For overall comparisons, in comparing source energy, it is apparent that the higher energy scans (551 keV) have deeper equi-valued isocount response lines than the 80 keV scans for the same geometries. This of course is due to the greater attenuation of the lower energy gamma rays by the medium they traverse.

In comparing source media, a higher density medium (water as compared to air) moved the isocount curves closer to the crystal face, making the depth response shallower. This again is due to the higher linear attenuation coefficient for the denser medium which emphasizes attenuation as a function of path length.

Water or tissue also scatters gamma rays more than air and this is evident from the scans made in water since the isocount curves are much broader than the corresponding scans made in air. The broadening results from scattering which allows the crystal to detect gamma rays whose path direction would not normally have been through the crystal.

The high energy scans are also slightly broader than their low energy counterparts. This effect results from edge penetration of the collimator. Edge penetration occurs for gamma rays from just outside the geometrical field-of-view of the collimator, and is more prominent in a brass collimator than in a lead collimator.

All the collimators yielded roughly the same depth response for any particular energy, with the 50% isoresponse line lying between 8 and 10 cm from the collimator face for 80 keV gamma rays in air and 5 and 7 cm in water.

The major differences between the several scans is the field-of-view, which is reflected in the broadness of the isocount curves. The field-of-view, which was discussed in Chapter 2, is dependent mainly on collimator geometry. Bearing in mind that neither the smallest field-of-view nor the largest is necessarily the best field-of-view for any particular application,



the cylindrical converging collimator gave the narrowest field-of-view among the collimators, with the cylindrical diverging and rectangular diverging collimators having the broadest values. The isocount contours for any one scan also reflect the widening of the field-of-view with increasing distance from the collimator face. This can be seen by comparing a 50% response contour with a 75% contour and noting that the 50% contour, which lies deeper, is also wider than the 75% response line.

The modelling scans, prefixed with an M in the diagrams, simulate the experimental results quite well. The major differences seen arise from gamma ray scattering in the experimental studies which was not accounted for in the simulations. However, these effects were not large enough to create significant alterations in the isocount profiles. Of particular interest are scans MR1 and MR2 which simulate lung geometry that could not be measured experimentally. Scan MR1 has one rib, 1.25 cm diameter, across the middle of the detector field of view; while scan MR2 assumes two ribs lie in the field of view, both 1.25 cm in diameter. The scans show the amount of radioactivity that is incident on the crystal as a function of crystal position (vector  $A_j$  defined previously). This vector,  $\sum_i A_{ij}$ , which is the total amount of activity that reaches detector point j, is not a useful parameter in a single collimator counting system, since the photomultiplier attached to the crystal cannot differentiate spatial events inside the crystal. However, it is useful in an imaging system employing a multihole collimator.  $\sum_i A_{ij}$  would then be the amount of activity that is imaged in position j on the crystal face. By comparing simulated images from known source distributions to experimental images, reasonable estimations of the unknown source distributions can be obtained.



## CHAPTER FIVE

### SUMMARY AND CONCLUSION

It was the purpose of this study to investigate gamma-ray collimator characteristics with specific aims of defining and of simplifying collimator design procedures for various clinical measurement situations. The particular clinical situation considered in this study is the measurement of regional pulmonary function using an inert, diffusible radioactive gas ( $^{133}\text{Xe}$ ). Specific goals of the optimization process are:

- (i) to provide a well defined, non-overlapping field-of-view between detectors,
- (ii) to obtain maximum sensitivity for this field-of view , and
- (iii) to produce a uniform, or iso-sensitive counting field at a distance from the collimator face.

As discussed in Chapter 4, all collimators tested yield roughly the same sensitivity with depth in any one medium. In comparing the response of the rectangular straight collimator to the responses of the cylindrical straight and diverging collimators for  $^{133}\text{Xe}$  in water, it can be seen that the straight rectangular collimator provides the broadest field response. Also, since the field-of-view of a rectangular collimator is rectangular, this type of collimator on the PFSS will view the complete lung and not just cylindrical sections as in the current system. Field-of-view overlap can also be more easily minimized using rectangular collimators.

As an optimum condition in the PFSS, a field-of-view width of 8 cm is desired at a distance 13 cm from the collimator face. The field-of-view is also required to include the chest from the sternum to the side of the rib cage, a distance of approximately 18 cm. In considering the results of this study, the ideal collimator for





optimizing these several parameters would be a tapered rectangular collimator. The crystal end dimensions should be square, having sides equal to the diameter of the crystal. The face end dimensions should be a width equal to the crystal diameter; the face end length 7.6 cm. The overall length of this collimator should be 12.7 cm and only the side distal to the sternum should be tapered. This collimator will have good sensitivity and collimators of this type used in the PFSS will view the complete lung with minimal overlap between detectors.

As an additional concluding remark, the modelling programs used in this work may be utilized in testing characteristics of potential collimators. Using the programs, since collimator specifications can be varied easily and quickly, corresponding field responses for different configurations can be determined analytically without the need of fabrication and testing.





## BIBLIOGRAPHY

1. T.R. Overton, L.W. Friedenbergl, B.J. Sproule and D. Fenna,  
Phys. Med. Bio. 18 p 246 1973
2. B. Cassen and L. Curtis, UCLA Report No. 130 1951
3. B. Cassen, L. Curtis and C. Reed, Nucleonics 6(6) p 78 1950
4. H.W. Anger, Rev. Sci. Instr. 29 p 27 1958
5. R.N. Beck, J. Nucl. Med. 2 p 314 1961
6. P.V. Harper, R.N. Beck, D.B. Charleston and K.A. Lathrop,  
Nucleonics 22(1) p 50 1964
7. M.A. Bender, Medical Radioisotope Scanning, Vol. 1, Vienna,  
IAEA, p 391 1964
8. R.N. Beck, Medical Radioisotope Scanning, Vol. 1, Vienna,  
IAEA, p 211 1964
9. K.A. Lathrop, P.V. Harper, A. Gottschalk, R.N. Beck, G.M. Hinn,  
P. Finston and R.D. Cohen, J. Nucl. Med. 8 p 283 1967
10. R.N. Beck, D.B. Charleston, P. Eidelberg and P.V. Harper  
J. Nucl. Med. 8 p 1 1967
11. H.O. Anger, Fundamental Problems in Scanning, A. Gottschalk  
and R.N. Beck (eds.), Charles C. Thomas, Springfield, Ill.  
p 195 1968
12. R.P. Parker, E.M. Gunnerson, J.L. Wankling and R.A. Ellis,  
Medical Radioisotope Scintigraphy, Vol. 1, Vienna, IAEA,  
p 71 1969
13. R.N. Beck, L.T. Zimmer, D.B. Charleston and P.B. Hoffer,  
IEEE Trans. Nucl. Sci. NS-18(3) p 3 1972



14. L. Kaufman, G.A. Armantrout, D.C. Camp, J.H. McQuaid and S.P. Swierkowski, Proceedings of the IEEE Nuclear Science Symposium, 1973
15. P.A. Schlosser, D.W. Miller, M.S. Gerber, R.F. Redmond, J.W. Harpster, W.J. Collis and W.W. Hunter Jr., Proceedings of the IEEE Nuclear Science Symposium, 1973
16. J.F. Detko, Medical Radioisotope Scintigraphy, Vol. 1, Vienna, IAEA, p 241 1973
17. R.H. Jones, R.P. Grenier and D.C. Sabiston Jr., Medical Radioisotope Scintigraphy, Vol. 1, Vienna, IAEA, p 299 1973
18. G.L. Brownell, C.A. Burnham, B. Hoop Jr. and H. Kazemi, Medical Radioisotope Scintigraphy, Vol. 1, Vienna, IAEA, p 313 1973
19. D.E. Kuhl, R.Q. Edwards, A.R. Ricci and M. Reivich, Medical Radioisotope Scintigraphy, Vol. 1, Vienna, IAEA, p 347 1973
20. J. Ambrose and G. Hounsfield, Br. J. Radiol. 46 p 148 1973
21. C.A. Mistretta, M.G. Ort, M.P. Siedband, J.R. Cameron and A.B. Crummy, Proceedings of the IEEE Nuclear Science Symposium 1973
22. P.B. Hoffer, W.B. Jones, R.B. Crawford, R.N. Beck and A. Gottschalk, J. Radiol. 90(2) p 342 1968
23. J.A. Patton, A.B. Brill and R.E. Johnston, Semiconductor Detectors in the Future of Nuclear Medicine, P.B. Hoffer, R.N. Beck and A. Gottschalk (eds.), New York, The Society of Nuclear Medicine p 258 1971
24. A.B. Brill, J.A. Patton, R. Price and C.V.F. Kosik, Medical Radioisotope Scintigraphy, Vol. 1, Vienna, IAEA, p 217 1973
25. W.L. Rogers, K.S. Han, L.W. Jones and W.H. Beierwaltes, J. Nucl. Med. 13(8) p 612 1972



26. H.H. Barrett, J. Nucl. Med. 13(6) p 612 1972
27. H.H. Barrett, G.D. DeMeester, D.T. Wilson and M.H. Farmelant,  
Medical Radioisotope Scintigraphy, Vol. 1, Vienna, IAEA,  
p 269 1973
28. K.R. Corey, P. Kenny, E. Greenberg, A. Pazianos, O.E. Pearson  
and J.S. Laughlin, Am. J. Roentgenol. Radium Therapy Nucl.  
Med. 85 p 955 1961
29. C.C. Harris, P.R. Bell, J.E. Francis Jr., M.M. Satterfield,  
J.C. Jordan and J.P. Murray, Progress in Medical Radioisotope  
Scanning, R.M. Kriseley, G.A. Andrews and C.C. Harris (eds.)  
TID-7673 p 25 USAEC, Washington D.C. 1963
30. P.J. Kenny, Sem. Nucl. Med. 3(3) p 259 1973
31. R.N. Beck, IEEE Trans. Nucl. Sci., Vol. NS-21(2) p 15 1974
32. B. Cassen, L. Curtis, C. Reed and R. Libby, Nucleonics 9 p 46 1951
33. G.L. Brownell, Int. J. App. Rad. and Isotopes 3 p 181 1958
34. A. Brookman and T.J. Baur, J. Nucl. Med 14 p 21 1973
35. H.O. Anger, Nature 170 p 200 1952
36. J.R. Mallard, Progress in Nuclear Medicine, Vol. 1, p 1  
Karger, Basel and University Park Press, Baltimore 1972
37. W.V. Mayneord, Brit. J. Radiol. suppl.(2) 1950
38. R.P. Gardner and K. Verghese, Nucl. Inst. Methods 93 p 163 1971
39. A. Keith, The Mechanism of Respiration in Man: Further Advances  
in Physiology, Edward Arnold & Co., London, 1909
40. J.D. Janiec, M.Sc. Thesis, Naval Postgraduate School, Monterey,  
California, 1973
41. A.B. Otis, W.O. Fenn and H. Rahn, J. Appl. Physiol. 2 p 592 1950



42. K. von Neergaard, A. Geo. Exp. Med. 66 p 373 1929
43. A.H. Cromer, Physics for the Life Sciences, McGraw-Hill, New York, 1974
44. V.B. Mountcastle, Medical Physiology, Vol. 1, p. 611, The C.V. Mosby Co., St. Louis, 1968
45. F.F. Kao, An Introduction to Respiratory Physiology, Excerpta Medica, Amsterdam, 1972
46. B.L. Holmon and J.F. Lindeman, Regional Pulmonary Function in Health and Disease in Progress in Nuclear Medicine, Vol. 3, E.J. Potchen and V.R. McCready (eds.), University Park Press, Baltimore 1973
47. G.J. Hine, Instrumentation in Nuclear Medicine, Vol. 1, Academic Press, New York, 1967
48. A. Gottschalk and R.N. Beck (eds.), Fundamental Problems in Scanning, Charles C. Thomas, Illinois, 1968
49. E.H. Quimby, S. Feitelberg and W. Gross (eds.), Radioactive Nuclides in Medicine and Biology, Lea & Febiger, Philadelphia, 1970
50. J.B. West, Ventilation/Blood Flow and Gas Exchange, Blackwell Scientific Publications, Oxford, 1965
51. J.F. Perkins, Respiration, Encyclopaedia Britannica, Chicago, 1961
52. A.C. Guyton, Textbook of Medical Physiology, W.B. Saunders Company, Philadelphia, 1971
53. J.H. Knowles, S.K. Hong and H. Rahn, J. Appl. Physiol. 14 p 525, 1959
54. J. Mead, Physiol. Rev. 41, p 281, 1961
55. J. Mead, J. Appl. Physiol. 15 p 325, 1960





## APPENDIX A

### The Physics of the Lung

A continuous and adequate supply of oxygen is a fundamental requirement for the metabolism of all mammalian cells. In addition, a means is needed to remove unwanted metabolic by-products of these cells - principally carbon dioxide. The organ which meets these requirements is the lung.

Until recently the lung could only be studied "in vivo" by making measurements at the mouth, or by bronchspirometry in which the patient must be anesthetized in order to study individual lung lobes. Nuclear medicine has been important in furthering our knowledge of regional lung function at the lower anatomical scale and this Appendix will discuss some of the physical processes involved.

#### A.1 Mechanics of Respiration

##### A.1.1 Expansion and Contraction

The lung itself is passive and has no musculature except for some smooth muscle in the airways and blood vessels. Its main purpose is to bring blood and air very close together to enable gas exchange. This it does via the alveolar membrane, which is of the order of one micron in thickness and has a total surface area for both lungs in the normal male adult of about 70 square meters.

The act of breathing depends upon the fact that the thoracic cavity is a closed compartment and the lung contained in it is open to the exterior via the trachea. (The basic anatomy of



the lung is shown in Figure 48). Thus, when the total volume of the cavity increases, negative pressure (with respect to atmospheric) in the cavity causes air to be drawn inward through the trachea; when the volume decreases, the pleural pressure goes toward atmospheric and lung volume decreases (Figure 49). The lung is therefore able to "breathe" by periodic expansions and contractions of the thoracic cavity brought about by intermittent contractions of the respiratory muscles and passive recoil of the elastic lungs.

The enlargement of the thorax during quiet breathing is brought about primarily by diaphragmatic contraction and by movements of the ribs, sternum, and vertebrae. As the intercostal muscles contract the ribs move upwards bringing the plane of the ribs nearer to a perpendicular with the vertebral column, thus increasing the thoracic volume.

The most important inspiratory muscle is the diaphragm, which serves as a "piston" in a thoracic "cylinder". It is dome shaped, due partly to negative intrathoracic pressure and partly to positive intra-abdominal pressure which produce approximately 10 Newtons of force acting over its surface. Its direction of movement is vertical, with a surface area of approximately 250 square centimeters. A descent therefore of 1 centimeter increases thoracic volume by about 250 cc. As this is an increase in volume in the cavity at a constant temperature, Boyle's law dictates that the pressure must decrease, which forces the lungs to expand thus drawing in air from the airways. This process is reversed as the diaphragm makes its regulated ascent. The excursion of the dome averages 1.25 cm during normal breathing ( 39 ).



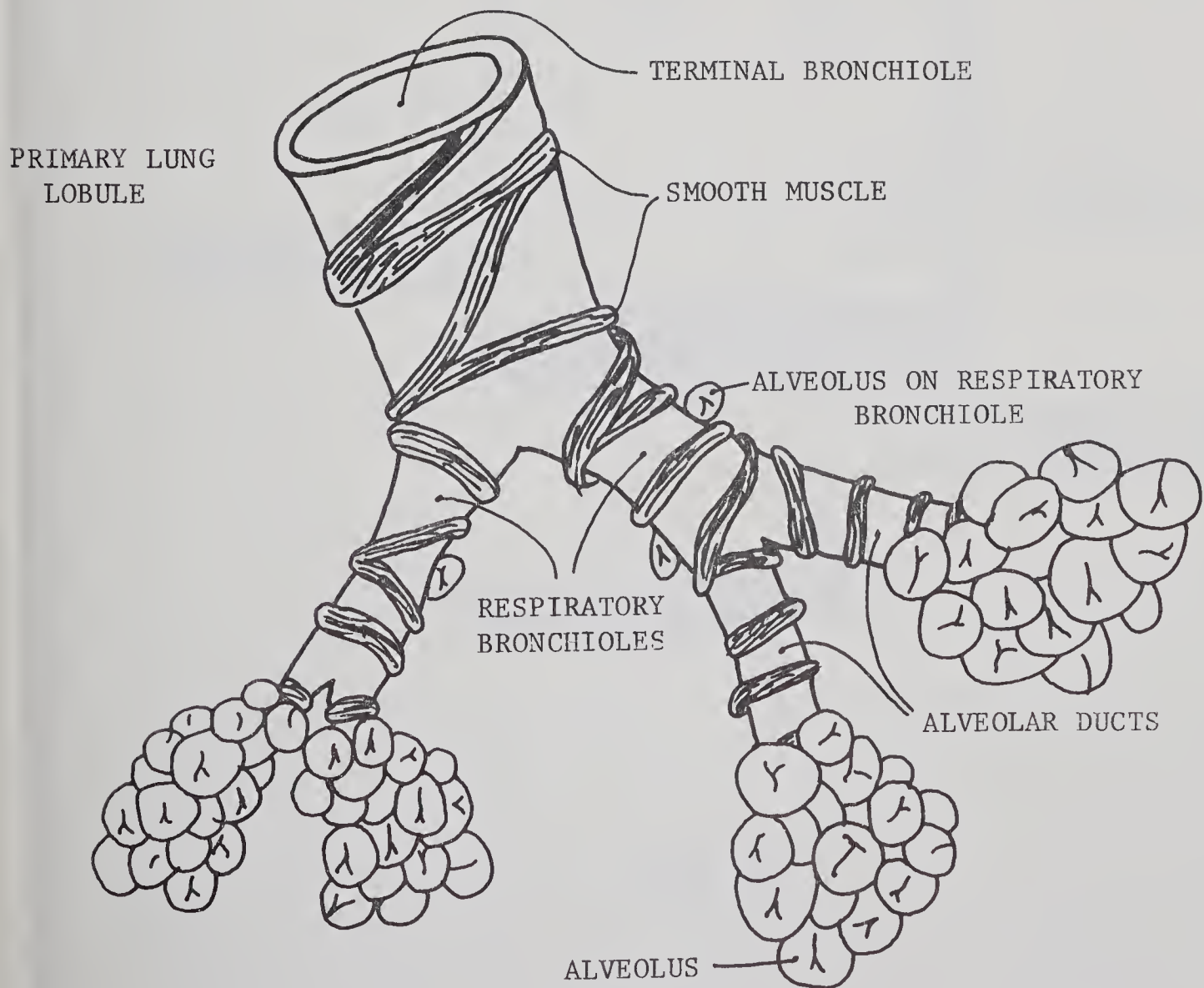
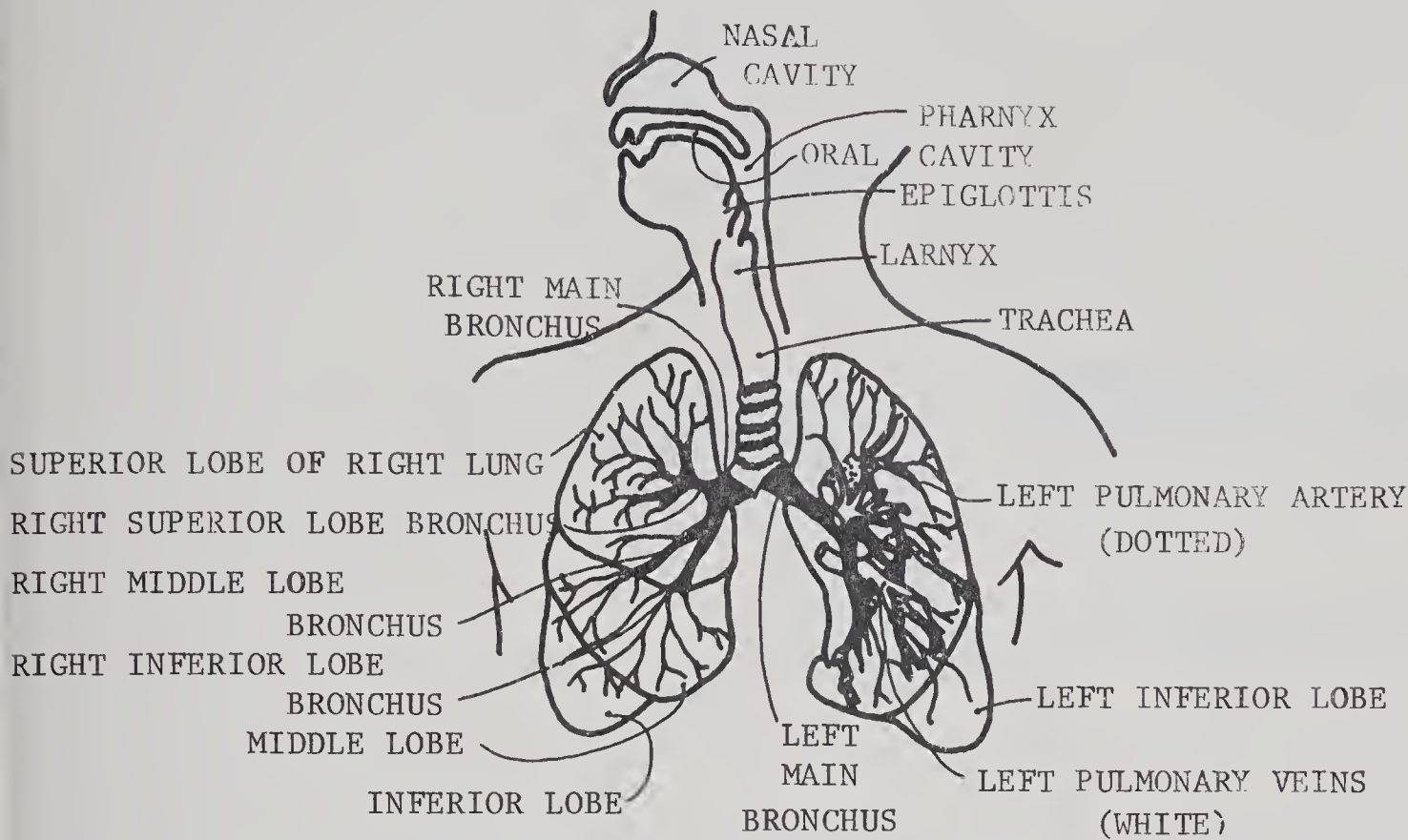


FIGURE 48





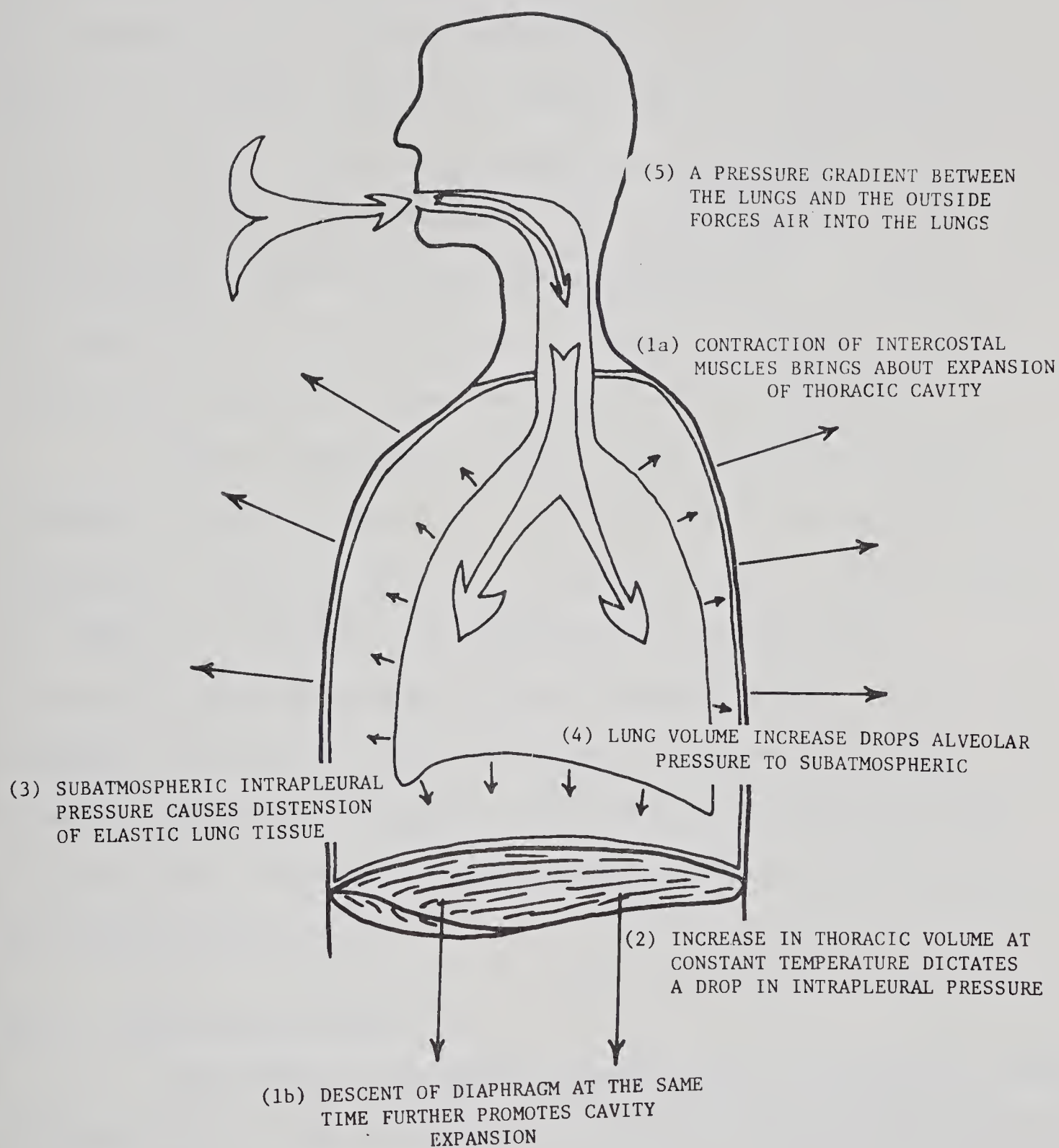


FIGURE 49





### A.1.2 Respiratory Pressure - The Lung Pump

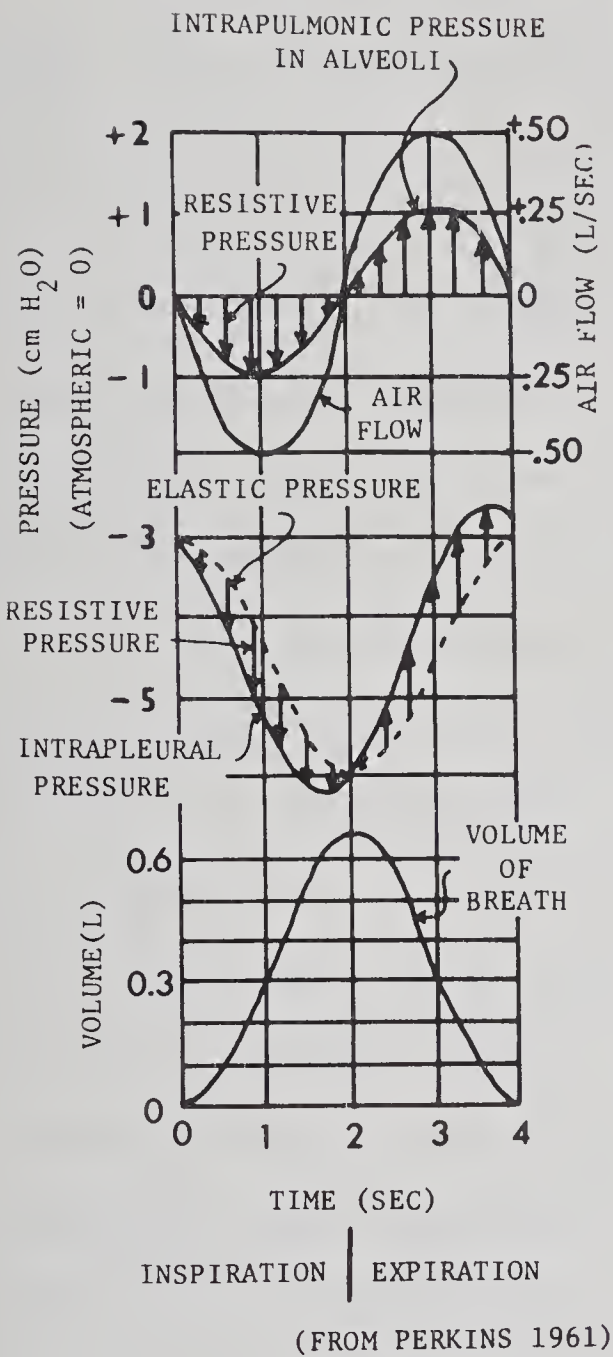
As the ribs expand at the start of an inspiration, the intrathoracic pressure is reduced to about -5mmHg subatmospheric. This negative pressure in turn affects the intrapulmonary pressure which is the pressure existing in the air passages and the alveoli within the lungs. During normal breathing, intrapulmonary pressure within the alveoli ranges from about -3mmHg subatmospheric during inspiration to atmospheric at the end of inspiration, to +3mmHg at the beginning of expiration and finally back to atmospheric pressure at the end of expiration, thus completing one cycle (Figure 50).

Normal intrapulmonic pressure fluctuations can be greatly exceeded by vigorous contraction of the inspiratory and expiratory muscles while breath holding with the glottis closed. Values as high as -90mmHg and +110mmHg can be produced, but to prevent acute circulatory depression the safe range of maxima are about -20 to +30mmHg. The reason for this circulatory depression is that the veins are thin-walled collapsible tubes, and if the outside pressure is greater than the inside driving pressure, the tube will collapse and flow will stop ( 40 ).

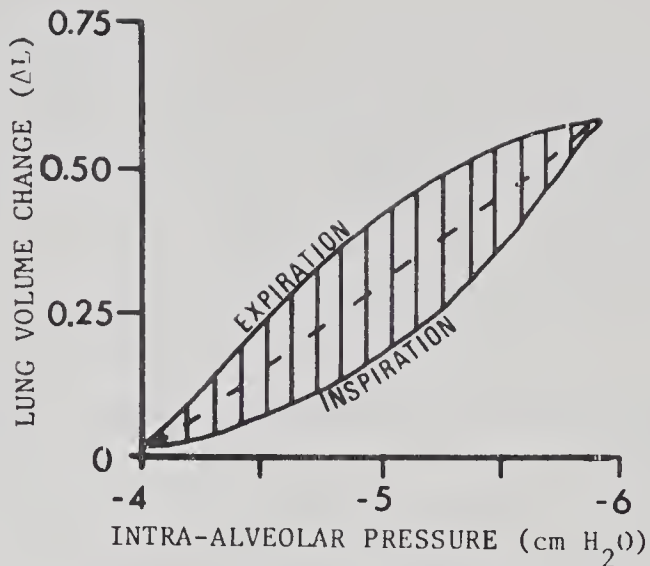
### A.1.3 Compliance and Work

Ventilation of the alveoli requires that the respiratory muscles overcome several types of resistance. The work done by these muscles can be estimated by multiplying the mean force of muscular contraction by the mean distance of muscle movement. These measurements can be made using miniature isometric strain gauges and microelectrodes implanted in the muscles. However, for the lung, a much easier and accepted way is to express the work



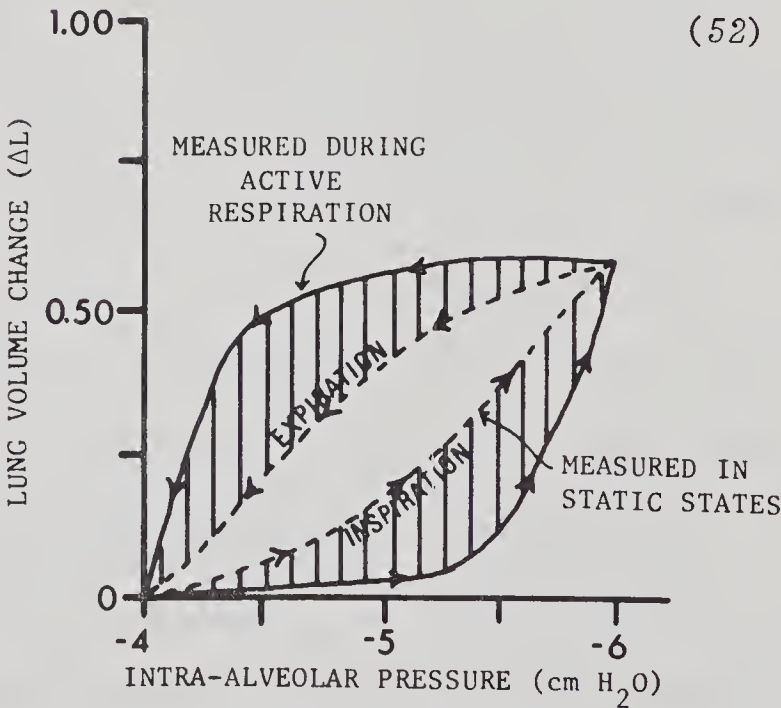


(51)



COMPLIANCE DIAGRAM OF THE LUNGS ALONE. THE SHADED AREA REPRESENTS  $\int P dv$ , THE WORK REQUIRED TO OVERCOME NONELASTIC TISSUE RESISTANCE. THE DOTTED LINE REPRESENTS THE COMPLIANCE. (FROM GUYTON 1971)

(52)



THE OUTER LOOP IS THE PRESSURE-VOLUME RECORDED CONTINUOUSLY DURING A CYCLE OF RESPIRATION WHILE THE INNER LOOP IS THE ABOVE STATIC COMPLIANCE DIAGRAM. THE SHADED AREA REPRESENTS THE INCREASED WORK NEEDED TO OVERCOME AIRWAYS RESISTANCE. (FROM GUYTON 1971)

(52)

FIGURE 50



done in terms of pressure change ( $\Delta P$ ) times volume change ( $\Delta V$ ), both of which can be measured using either an intraesophageal balloon or a less traumatic body plethysmograph ( 41 ).

A graph of lung volume change verses intrapleural pressure change gives a compliance diagram (Figure 50). Compliance is the ability of the lungs to be expanded. It is defined as the ratio of volume change to pressure change and can be either a static or dynamic phenomenon. The lungs alone, when removed from the chest, are roughly twice as distensible as the lungs and thorax together because the thoracic cage itself must also be stretched in normal breathing, which is an energy drain on the respiratory muscles.

The overall mechanical energy expended by the respiratory muscles is used up in three main ways: 1) Elastic work is the work required to stretch the elastic tissues of the lungs and thorax and can be calculated from compliance diagrams, 2) inertial work is related to the force needed to set tissues such as the liver, diaphragm and chest wall in motion. (However, this is significant only at high rates of ventilation and is negligible in normal breathing), and 3) work done to overcome airway resistance is that energy expended in moving the respiratory gases through the airways. As can be seen from Figure 50 airway resistance accounts for a major portion of the available energy. It will be discussed in greater detail in the following section.

The total work, therefore, can be determined and has been found to range in normal subjects between 0.2-0.4 Joules/breath. The mechanical efficiency of this breathing is defined as the respiratory work done per unit of oxygen required for the work, or

$$\frac{\text{work per liter}}{\text{O}_2 \text{ cost per liter.}}$$





This efficiency is about 8% in normals and depends upon the frequency and depth of breathing.

#### A.1.4 Surface Tension and Elastic Recoil

The elasticity of the lung is not due solely to its elastic fibers. Of equal importance for elastic recoil is the surfactant that covers all lung alveoli. In 1929 von Neergaard inflated the lungs of anaesthetized cats and measured deflation pressures ( 42 ). He used both gas and physiologic liquids to distend the lungs and found that the pressure required to maintain any given lung volume with fluid, under static conditions, was less than half that required to maintain the same volume of an air filled lung. Von Neergaard deduced that there must be a liquid-air interface on the alveoli which tends to retract the alveoli, thus contributing to the lung recoil. Filling the lung with liquid would eliminate the fluid-gas interface and its recoil force.

Using Laplace's Law,

$$P = \frac{2\gamma}{r} \quad (A.1)$$

and approximating the alveolus as a sphere, the pressure (P) is related to the surface tension ( $\gamma$ ) and the radius (r) of the "bubble". Assuming that the alveolar film exerts a surface tension of 50 dynes/cm which is equal to that of plasma, it has been calculated that the recoil pressure of the lung is roughly  $2 \times 10^4$  dynes/cm<sup>2</sup> or about 20 cm H<sub>2</sub>O for a fully inflated lung.

This is verified experimentally but it is almost an order of magnitude too large at normal or low lung volumes. The implication is that the surface tension of the alveoli must be 5 - 10 dynes/cm instead





of 50 dynes/cm. This, however, could only occur if the alveolar membrane was lined with something that reduced the surface tension. This indeed is the case as the walls of the alveoli secrete a material with a high dipalmitoyl lecithin concentration which reduces the surface tension by a factor as great as 15. The surfactant's ability to reduce surface tension depends upon its concentration. Therefore, when the alveolus is deflated, the concentration (per unit surface area) is high and the surface tension is very low, so that the alveolus is expanded without difficulty. However, as it expands, the concentration of the surfactant decreases and the surface tension increases, until a point of equilibrium is reached at maximum expansion. Upon exhaling the increased surface tension helps to collapse the alveolus and expel the air from it.

Consider for example that during inhalation the radius of an alveolus expands from about  $0.5 \times 10^{-2}$  to  $1.0 \times 10^{-2}$  cm ( 43 ). Assuming a surface tension of 50 dynes/cm, the pressure differences required to inflate an alveolus would be:

$$P_i - P_o = \frac{2\gamma}{r} \quad (\text{A.2})$$

$$= 2 \times 10^4 \text{ dynes/cm}^2 = 15 \text{ mmHg}$$

This means that the gauge pressure  $P_o$  outside the alveolus would have to be 15 mmHg less than the pressure  $P_i = -3$  mmHg inside it. Thus  $P_o$  would be -18 mmHg. However, the intrapleural pressure is only about -4 mmHg, so that the pressure difference is only about 1 mmHg, or 15 times less than would be required. Pulmonary surfactant overcomes this difficulty.



Besides reducing muscular effort in inflating the lungs, pulmonary surfactant helps to stabilize the alveolar gas bubbles and keep them from collapsing. Alveoli vary in size throughout the lungs, some having radii 3-4 times that of others. Laplace's Law shows that if the surface tension was equal for bubbles of differing radii, the smaller bubbles would collapse and the larger ones would overexpand. The lung therefore, would consist of one hyperinflated alveolus, with all other alveoli being collapsed. That this is not the case is due solely to the surfactant. A collapsed alveolus without a coating of surfactant would behave like a bubble being formed on the end of a straw (Figure 51). The alveolar pressure would have to increase to relatively high levels before the alveolus would "pop" open. Thereafter, less pressure would be required to expand the alveolus to a higher volume.

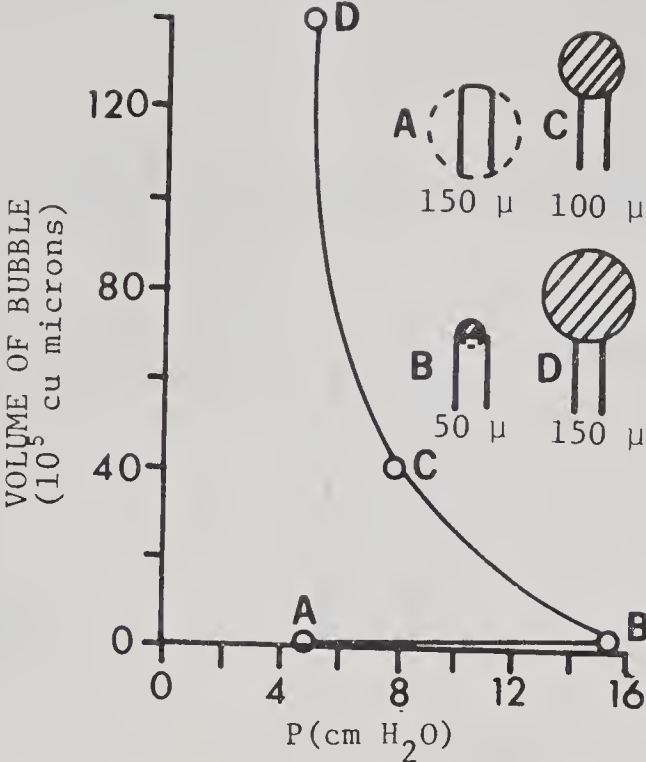
Table A-1 shows the elastic properties of the chest wall and lungs. It is apparent from this table that the lungs seek a lower volume even at residual volume (20% of lung capacity) while the chest wall has an expanding tendency until the lungs are inflated to approximately 50% vital capacity. Lung volume greater than 50% vital capacity results in the chest wall recoiling inward rather than outward as it does below 50% vital capacity.

## A.2 Flow Dynamics

### A.2.1 Volumes and Capacities

The basic nomenclature of pulmonary function is given in Figure 52. Physiologically, the main bronchi, bronchioles, and terminal bronchioles, which do not play a part in actual gas exchange, can be classified as airways. The respiratory bronchioles and the alveoli





PRESSURE-VOLUME CURVE OF A BUBBLE BLOWN AT THE END OF A GLASS TUBE.

(FROM COMROE 1974) (56)

FIGURE 51

TABLE A-1 (FROM KNOWLES, HONG, AND RAHN; 1959)

(53)

% of Vital Capacity	Recoil (Relaxation) Pressure of Lungs + Thoracic Cage (Torr)	Recoil Pressure of Lungs Alone (Torr)	Recoil Pressure of Thoracic Cage Alone (Torr)
20	-8	1.8	-9.8
40	4	5.0	-1.0
60	14	8.9	4.1
80	21	13.3	7.7
100	30	21.0	9.0



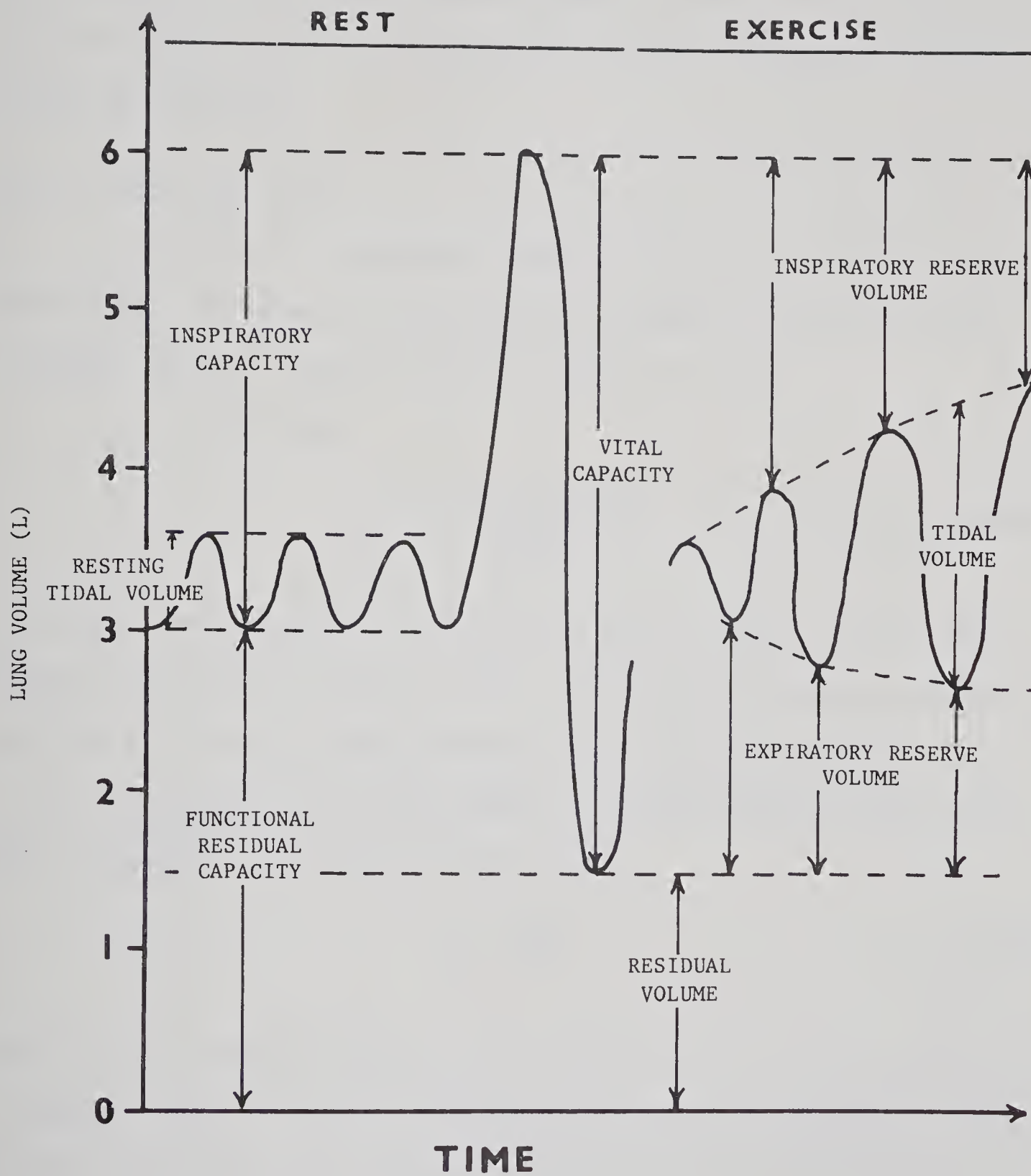


FIGURE 52





on the other hand, may be considered the basic lung units involved with oxygen transfer to the blood cells. There are therefore two main areas of the lung, one involved with gas transport, and the other with gas exchange. Making the assumption that all units are basically the same, the whole organ can be depicted as shown in Figure 53. Typical values are included.

### A.2.2 Rates and Flows

As outlined previously, the total force exerted by respiratory muscles must overcome several types of resistance in ventilating the pulmonary alveoli. The main one is airways resistance.

In fluid flow,

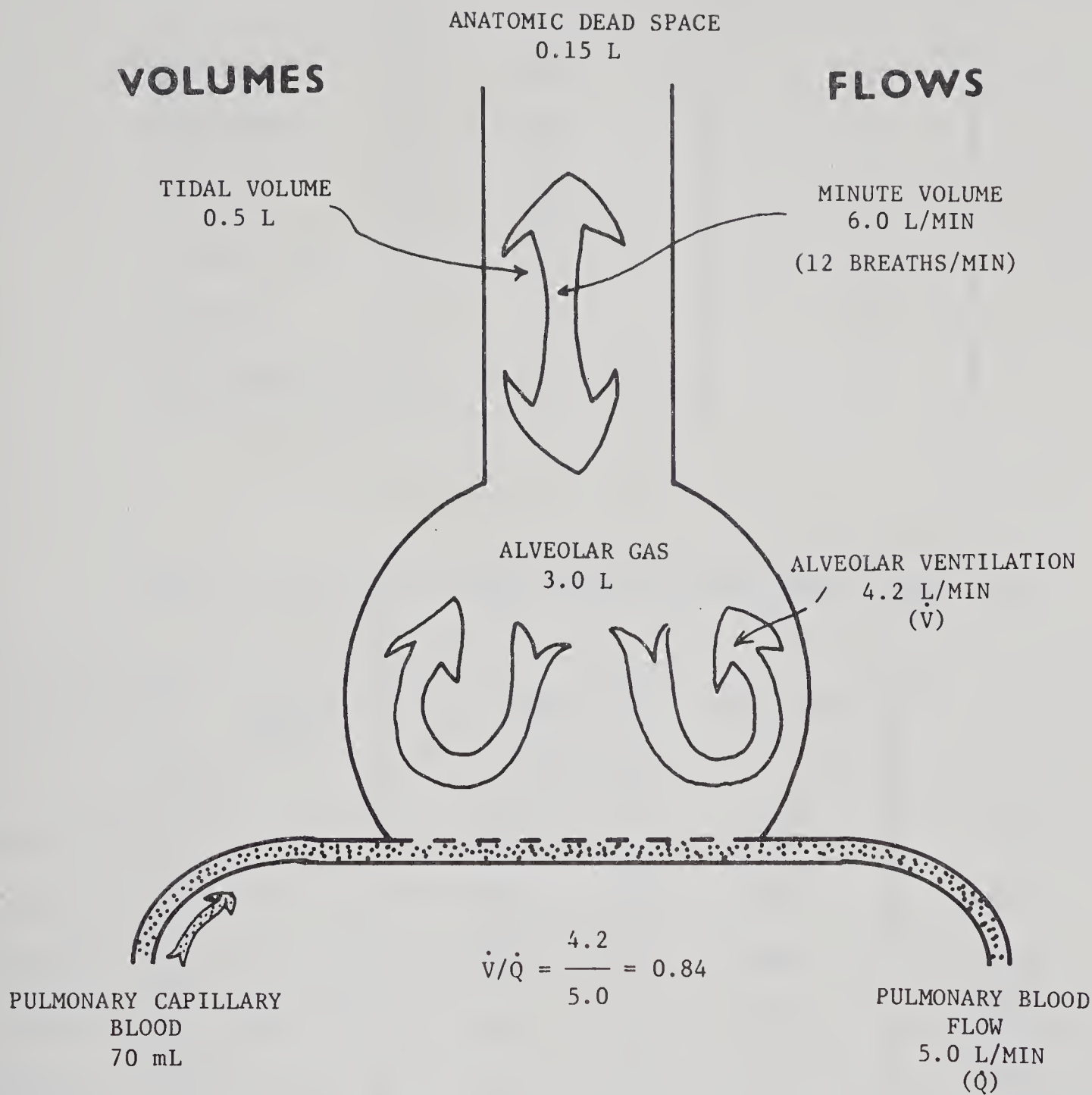
$$R = \frac{\text{Driving pressure}}{\text{Flow}} \quad (\text{A.3})$$

where  $R$  is the resistance to flow in the tube or tubes. In the lung however, there are two types of flow, laminar and turbulent, and each requires a different driving pressure. The first step therefore, is to determine what type of flow exists at various levels in the system. This can be done using the Reynolds' number,

$$R_N = \frac{\bar{r}\bar{v}\rho}{\eta} \quad (\text{A.4})$$

The flow of a fluid of density  $\rho$  and viscosity  $\eta$  at an average speed of  $\bar{v}$  through a tube of radius  $r$  is laminar as long as the Reynolds' number is less than 1000. Note that both the viscosity and the density of the gas in question are important. Table A-2 lists both of these parameters for gases involved in respiration. Table A-3 gives the calculated Reynolds' number at various sites in the respiratory tract. The velocity of air flow in the alveoli is generally thought to be small enough to be negligible.





NUMBERS ARE TYPICAL VALUES ONLY AND THERE IS CONSIDERABLE VARIATION. NOTE THAT NORMAL RATIO OF VENTILATION TO BLOOD FLOW IS  $\sim 1$

FIGURE 53



TABLE A-2 (TAKEN FROM KAO, F.F. 1972) (45)

GAS	$\eta$ (POISE $\times 10^{-6}$ )	$\rho$ (g/ML $\times 10^{-3}$ ) at Atmospheric
OXYGEN	214	126
NITROGEN	184	110
CO <sub>2</sub>	156	173
WATER VAPOR	103	70.8
HELIUM	203	15.6
RESPIRED AIR	180	112

TABLE A-3 REYNOLD'S NUMBER (ADAPTED FROM MEAD, 1961) (54)

LOCATION	RADIUS (MM)	$\dot{V} = 6$ L/MIN	$\dot{V} = 60$ L/MIN	$\dot{V} = 200$ L/MIN
NASAL CANAL	2.5	200	2000	6000
PHARNYX	6	400	4000	12000
GLOTTIS	4	800	8000	24000
TRACHEA	10.5	625	6250	18500
BRONCHI	8.5	455	4550	13650
	4.5	350	3500	10500
	3	285	2850	8550
	2	95	950	2850
	0.5	17.5	175	525



Where the gas flow is laminar, Poiseuille's Law states that:

$$\Delta P = \dot{V} \frac{8\ell\eta}{\pi r^4} = \dot{V} R_L \quad (\text{A.5})$$

which relates the volume flow per unit time ( $\dot{V}$ ) to the pressure gradient  $\Delta P$  in a tube of length  $\ell$  and radius  $r$ ,  $\eta$  being the viscosity. It is seen

$$R_L = \frac{8\ell\eta}{\pi r^4} \quad (\text{A.6})$$

where  $R_L$  is the resistance to laminar flow.

Where the flow is turbulent,

$$\Delta P = \dot{V}^2 \frac{k\ell\rho}{\pi^2 r^5} = \dot{V}^2 R_T \quad (\text{A.7})$$

$\rho$  being the density of the gas and  $k$  a constant relating to frictional effects between the gas and the wall. Here,

$$R_T = \frac{k\ell\rho}{\pi^2 r^5} \quad (\text{A.8})$$

where  $R_T$  is the resistance to turbulent flow. Note that  $R_L$  depends mainly on the gas viscosity, while  $R_T$  depends primarily on gas density.

In smooth, straight tubes, turbulent flow occurs only at high velocities which are present in the main bronchi and trachea. The flow rates in the smaller anatomical levels are very low because the total airflow is divided among hundreds of thousands of tubes and the total cross-sectional area of these tubes is very large leading to very low flow velocity. However, eddy formation may occur at each branching of the tracheobronchial tree and the pressure required for eddy flow is approximately the same as for turbulent flow. Turbulence or eddy





formation at low rates is particularly apt to occur when there are irregularities in the tubes. In the respiratory system airflow is both laminar and turbulent with eddy formation. Rohrer's equation combines these influences and the flow pressure relationship for this "impure" physiologic state is

$$\Delta P = R_L \dot{V} + R_T \dot{V}^2 \quad (\text{A.9})$$

Figure 54 shows an experimental determination of this equation. The slope of the curve at any point gives the resistance to flow at that particular pressure and flow rate.

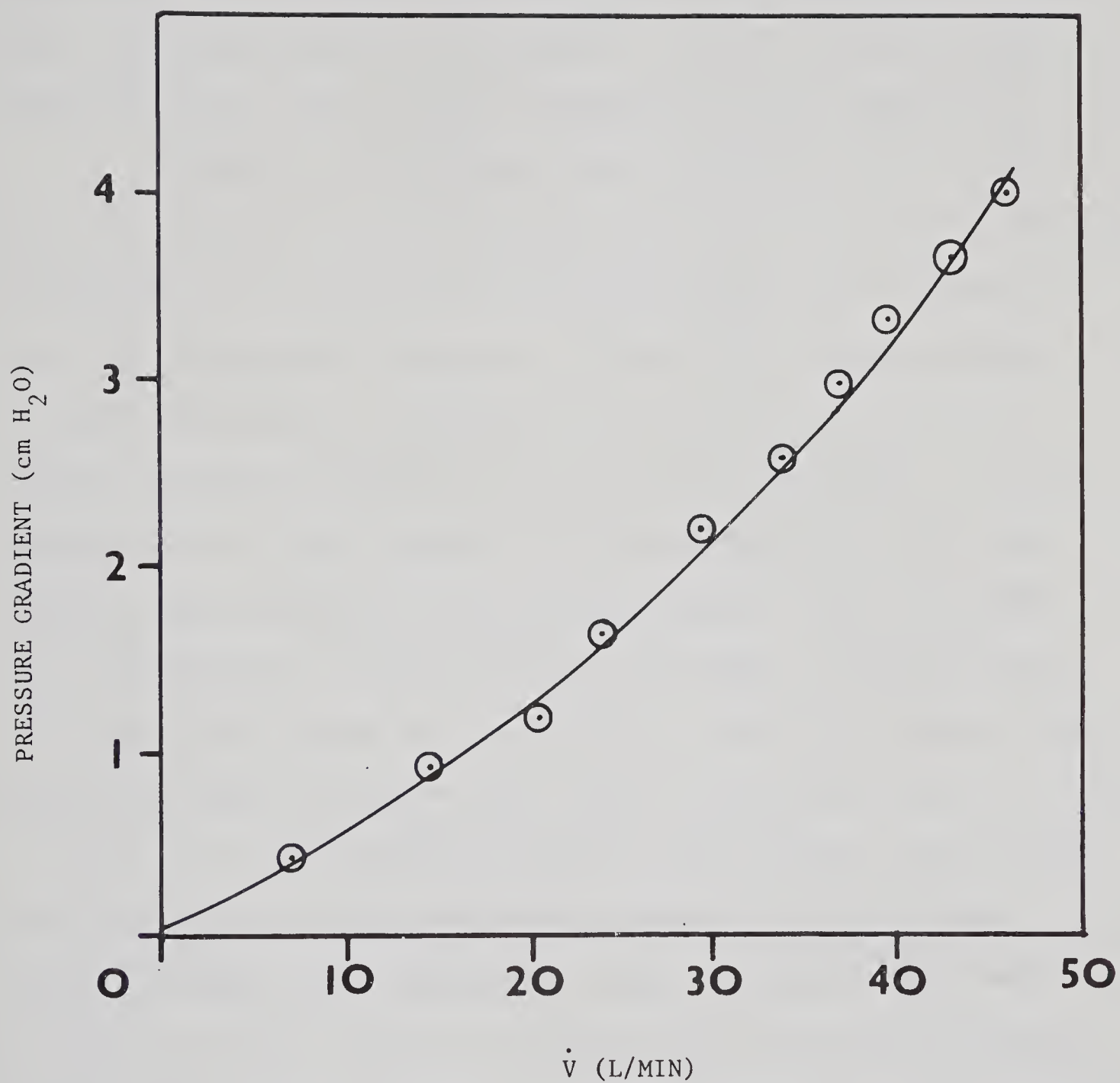
### A.3 The Lung and Gas Exchange

#### A.3.1 The Pressures

Only a few of the cells of human tissues could survive extended direct exposure to the partial pressures of gases present in the earth's atmosphere ( 44 ). Oxygen at sea level pressures is distinctly toxic, and so the pulmonary structure evolved in man has had to provide a portable gaseous environment. This is the environment found in the alveoli and is considerably different from that of the ambient atmosphere.

In respiratory gas exchange, the separate behaviours of the various gases must be considered, since their physiologic roles are also different from each other. This state goes well with Dalton's law, which enables the partial pressures of each gas to be treated distinctly. The partial pressure of a gas is of extreme importance both in the physical dynamics of pulmonary - blood - tissue gas exchange and in the participation of the gas in the chemical processes of metabolism.





THE FLOW-PRESSURE CURVE OF THE RESPIRATORY SYSTEM. THE EXPERIMENTAL DATA POINTS LIE CLOSEST TO THE CURVE WITH EQUATION:

$$P(\text{cm H}_2\text{O}) = 0.0417 \dot{V} + 0.0009 \dot{V}^2$$

(FROM MEAD 1960) (55)

FIGURE 54



The two main gases involved in respiration are oxygen and carbon dioxide. Oxygen supplies energy needed by the body's cells for their metabolic processes and carbon dioxide is the by-product of tissue metabolism. In addition, there is the "inert" fraction of the atmosphere, consisting primarily of nitrogen, but also including trace amounts of argon, xenon, krypton, hydrogen and helium (Table A-4).

Movement of the individual gas molecules by the time they reach the alveoli is largely Brownian, but because of pressure gradients, mass-movement occurs by diffusion from the higher partial pressure of gas to the lower partial pressure. At this level, each gas behaves to a good approximation according to the ideal gas law and can be treated completely by application of the kinetic hypothesis. It is in this way that the lung functions, bringing blood and air very close together, separated only by the alveolar membrane. With an alveolar  $PO_2$  of 100 mmHg and a venous blood  $PO_2$  of 40 mmHg, a driving pressure of 60 mmHg forces oxygen into the blood where most of it combines with hemoglobin (Table A-5, Figure 55). Figure 55 shows that very little time is required for equilibration of alveolar with pulmonary capillary  $PO_2$ . This equilibration occurs even during exercise when the pulmonary capillary transit time is decreased. Figure 55 shows how this rapid equilibration can be upset by alteration in the diffusion properties of the alveolocapillary membrane. Increased thickness of this membrane increases the time required for equilibration. If the defect is severe enough the systemic arterial blood will be incompletely oxygenated. Conversely, a venous blood  $PCO_2$  of roughly 46 mmHg and alveolar  $PCO_2$  of 40 mmHg results in a  $PCO_2$  gradient favorable for elimination of carbon dioxide from the body.



TABLE A-4 GASEOUS COMPOSITION OF THE ATMOSPHERE  
(FROM MOUNTCASTLE, 1968) (44)

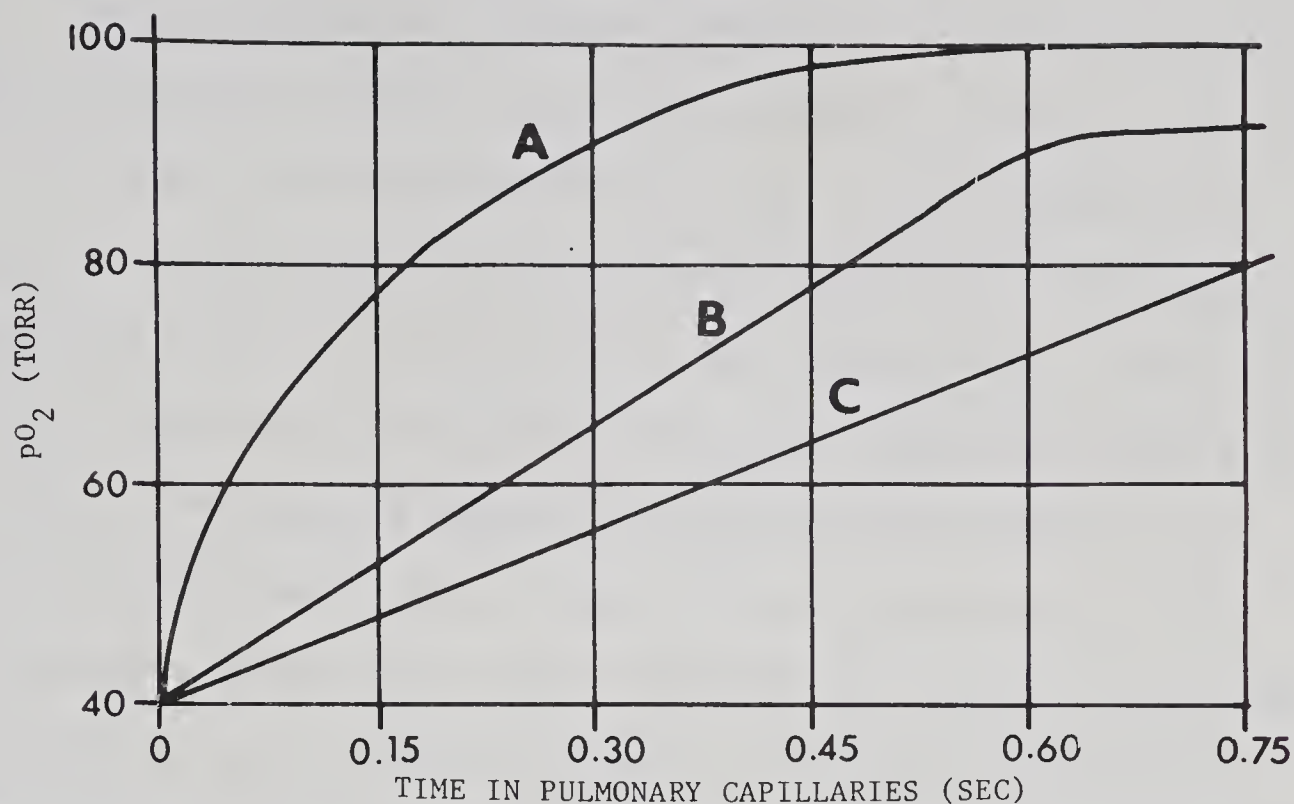
ELEMENT	% IN DRY AIR
NITROGEN	78.09
OXYGEN	20.94
ARGON	0.93
CARBON DIOXIDE	0.03
NEON	0.002
HELIUM	0.0005
KRYPTON	0.00001
HYDROGEN	0.00005
XENON	0.000008

TABLE A-5 PARTIAL PRESSURES OF RESPIRATORY GASES (mmHg)  
(FROM MOUNTCASTLE, 1968) (44)

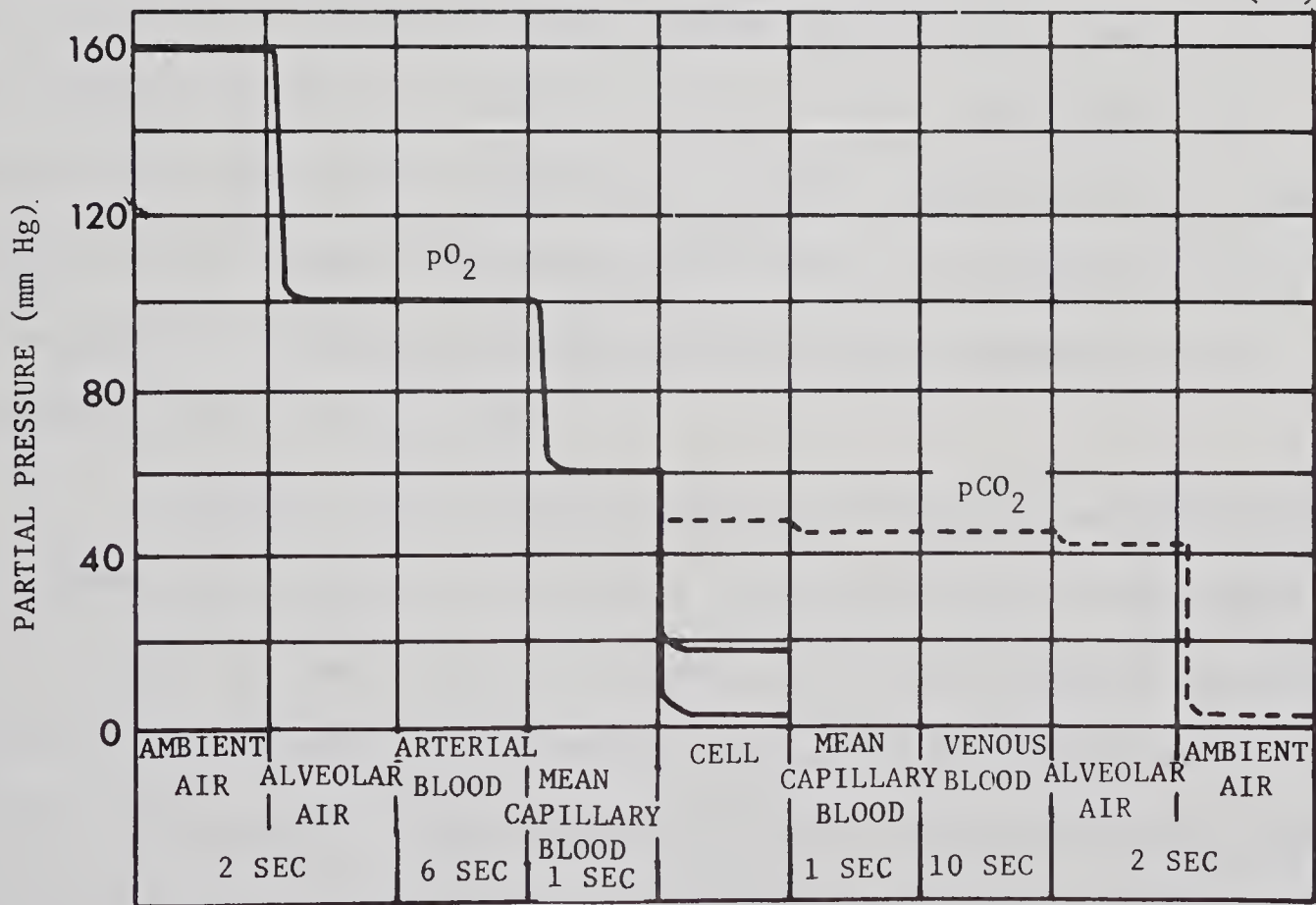
GAS	AMBIENT AIR	TRACHEAL AIR	EXPIRED AIR	ALVEOLAR AIR	ARTERIAL BLOOD	MIXED VENOUS BLOOD	TISSUES
O <sub>2</sub>	158.0	149.0	116	100	95	40	≤40
CO <sub>2</sub>	0.3	0.3	32	40	40	46	≥46
H <sub>2</sub> O	5.7	47.0	47	47	47	47	47
N <sub>2</sub>	596.0	563.7	565	573	573	573	573
TOTALS	760	760	760	760	755	706	≤706







IN NORMAL BREATHING (A) ALVEOLAR  $pO_2$  EQUILIBRIUM IS REACHED WELL WITHIN THE TIME THAT THE BLOOD REMAINS IN THE CAPILLARIES. CURVE B REPRESENTS A MODERATE ALVEOLOCAPILLARY BLOCK AND CURVE C A SEVERE CASE OF DIFFUSION IMPAIRMENT. EXERCISE SHORTENS THE TIME BY AS MUCH AS 2/3 BUT NOTE THAT AT 0.25 SEC THE  $pO_2$  OF A IS ALREADY AS HIGH AS 90 mmHg. (ADAPTED FROM COMROE 1974) (56)<sup>2</sup>



CHANGES IN  $pO_2$  AND  $pCO_2$  ALONG RESPIRATORY TRACK. (MOUNTCASTLE 1968) (44)

FIGURE 55



### A.3.2 Diffusion and the Alveolar Membrane

Diffusion is a very important physiologic process in the body because, in the end, it alone governs the transport of oxygen from the lungs and thereby to the mitochondria of cells. The diffusion of  $O_2$  and  $CO_2$  that is essential to pulmonary gas exchange takes place between gas and tissue - that is between gaseous and liquid phases. Thus the solubility of the gas in the liquid now becomes important. Henry's Law states that the volume of a fairly insoluble gas that dissolves in a liquid at a given temperature is almost directly proportional to the partial pressure of that gas. Since the diffusion rate of a gas within a liquid depends on its pressure gradient, the greater the solubility of a gas, the more rapid will be its rate of diffusion. The relative solubilities of  $CO_2$  and  $O_2$  in water are nearly 25 to 1 which explains why  $CO_2$  diffuses far more rapidly between alveoli and capillary blood, even though the pressure gradient for  $O_2$  is much higher than  $CO_2$ . However, the ability of hemoglobin to combine chemically with  $O_2$  and release  $CO_2$  is a factor of greater importance in the diffusibility of these gases, but detailed consideration of these phenomena is not within the scope of this work.

Alveolar walls can be as thin as 0.2 micron, and calculations have shown that diffusion of gas in a normal alveolus is 80% complete in 0.002 sec, if the diffusion distance is 0.5 mm. However, there are several diseases which can cause the alveolocapillary membranes to thicken dramatically (alveolocapillary block). These give good evidence to the importance of the length of the diffusion path as discussed above.

It is also obvious that the area of the diffusing surface is important, for the body must not only maintain a highly inflexible rate



of oxygen transport, but a stringently governed volume of oxygen uptake as well. Certain diseases can destroy alveolar walls, decreasing the area from its normal average of 70 square meters.

In addition to these problems, blood - gas mixing is also important. There are capillaries in the lung that do not perfuse ventilated alveoli, and the deoxygenated blood in them is sent through the body a second time. This lowers the percentage of oxygenated hemoglobin, which, in turn, decreases the oxygen supply to the metabolizing tissues.

In summary, mechanics, flow dynamics, diffusion and physiologic and anatomic dead space all contribute to the broader category of pulmonary ventilation. The matching of ventilation with blood flow determines, to a large extent, the degree to which the peripheral tissues will be oxygenated. By using radioactive materials and appropriate methodologies, scintillation detectors positioned over the chest can provide information about the distributions of ventilation. The detector is therefore very important in the assessment of general lung performance, and any improvements in it may allow more accurate diagnosis of lung impairments.



## APPENDIX B

### Collimator Field-of-View Derivations

For single hole collimators, the index of spatial resolution refers to the diameter or length of the field-of-view. The field-of-view may be defined as the area exposed to the crystal, geometrically limited by the collimator, at any distance from the collimator face. This appendix details the calculations for field-of-view perimeters and areas, for both cylindrical and rectangular collimators of variable dimensions.

#### B.1 Cylindrical Collimators

For cylindrical collimators (Figure 56) the diameter of the field-of-view, at a distance  $s$  from the collimator face is given by:

$$d = 2r_2 + \frac{2s}{h} (r_2 + r_1) \quad (\text{B.1})$$

where  $r_1$  and  $r_2$  are the radii of the collimator ends at the crystal and at the face respectively, and  $h$  is the collimator length. Note that (B.1) is valid for all  $r_1$  and  $r_2$  whether the collimator is converging, diverging, or straight.

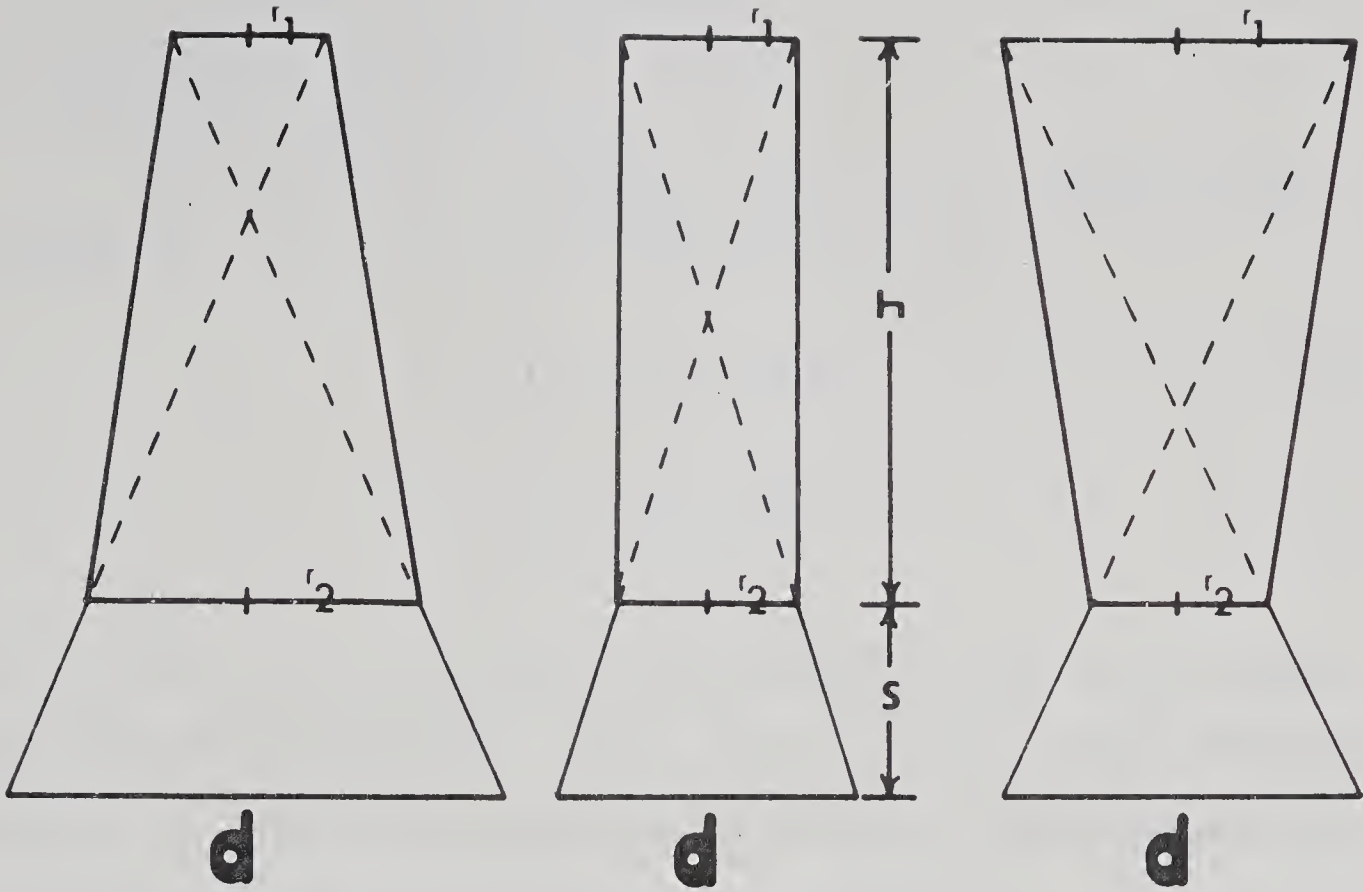
The area seen by this collimator at a distance  $s$  is:

$$A_G = \pi r_2^2 \left( \frac{s(r_1 + r_2)}{hr_2} + 1 \right)^2 \quad (\text{B.2})$$

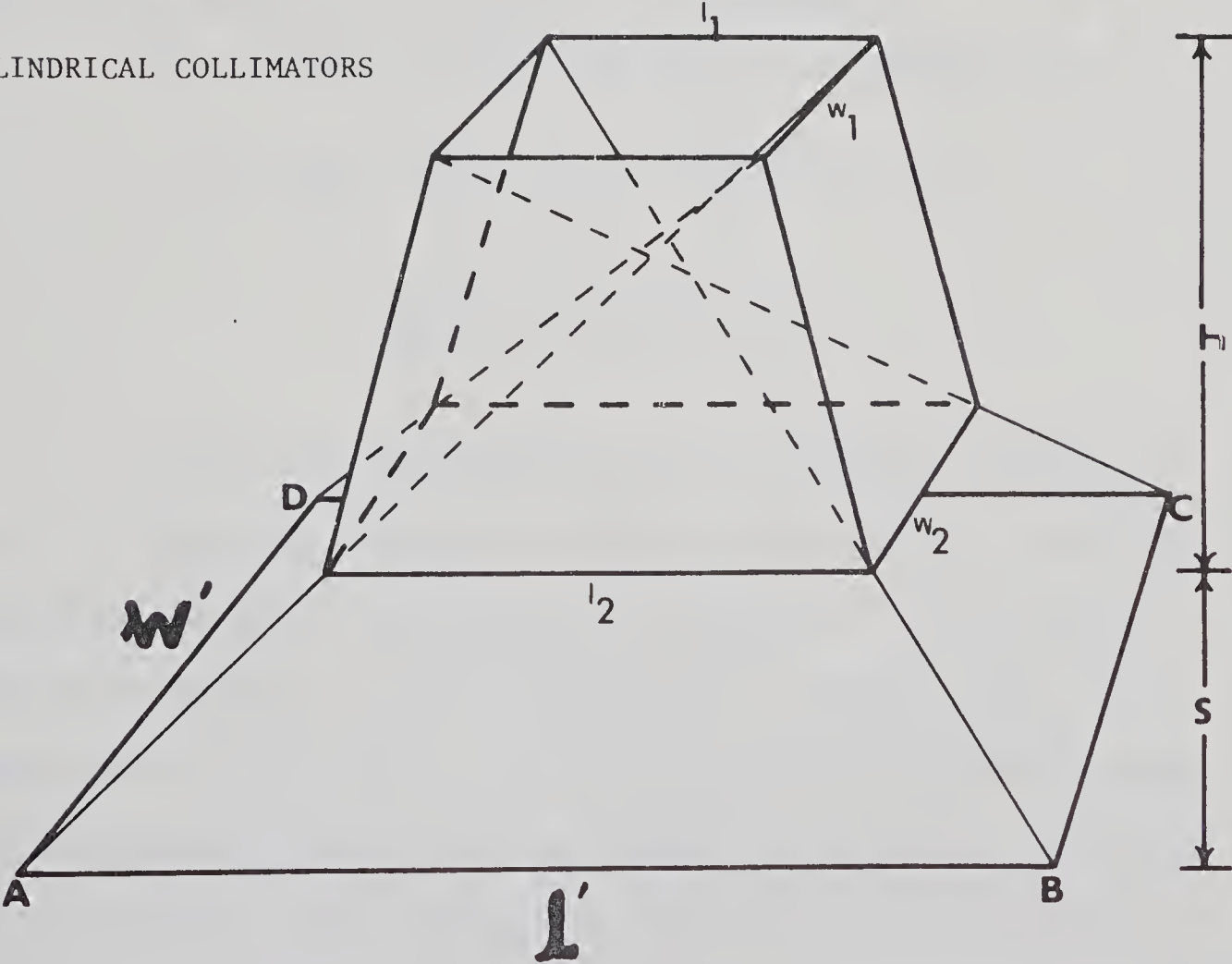








CYLINDRICAL COLLIMATORS



RECTANGULAR COLLIMATORS

FIGURE 56



$A_C$  directly relates to the plane sensitivity of the detector, as can be deduced from equation (2.11).

## B.2 Rectangular Collimators

For rectangular collimators (Figure 56) the length of the field-of-view ( $\ell'$ ) and the width ( $w'$ ) are given by:

$$\ell' = \ell_2 + \frac{s}{h} (\ell_2 + \ell_1) \quad (\text{B.3})$$

$$w' = w_2 + \frac{s}{h} (w_2 + w_1) \quad (\text{B.4})$$

where  $\ell_1$  and  $\ell_2$  are the lengths of the collimator ends at the crystal and at the face respectively, and  $w_1$  and  $w_2$  are the corresponding widths. Although not evident from Figure 56, the perimeter ABCD includes the rays from diagonally far corners of the collimator.

The area seen by this collimator at a distance  $s$  is:

$$\begin{aligned} A_R = \ell_2 w_2 + \frac{s \ell_2}{h} (w_2 + w_1) + \frac{s w_2}{h} (\ell_2 + \ell_1) \\ + \frac{s^2}{h^2} (\ell_2 + \ell_1) (w_2 + w_1) \end{aligned} \quad (\text{B.5})$$

In most cases, single detector crystals are cylindrical, with a circular cross-section. Equation (B.5), however, assumes the crystal to have a rectangular cross-section. If a circular crystal is placed in a square collimator of cross-sectional side length equal to  $2R$ , where  $R$  is the radius of the inscribed crystal, then the field-of-view area can no longer be described by equation (B.5). Instead, a more complicated expression is derived for the locus of points on a plane a distance  $s$  away from the face of the collimator that describes the perimeter of the field-of-view. From



Figure 57, if the crystal face lies in the  $z = 0$  plane in normal 3-space centered on  $x = x_C$ ,  $y = y_C$ , and if any point on the perimeter of the crystal face is denoted by  $P_D (x_D, y_D, z_D)$  then all such points  $P_D$  satisfy:

$$\begin{aligned} (x_D - x_C)^2 + (y_D - y_C)^2 &= R^2 \\ z_D &= 0 \end{aligned} \tag{B.6}$$

The line joining a point  $P_D$  to any point  $P_S$  with coordinates  $x_S, y_S, z_S$  is described parametrically by:

$$\begin{aligned} x &= x_D + (x_S - x_D)t \\ y &= y_D + (y_S - y_D)t \\ z &= z_D + (z_S - z_D)t \end{aligned} \tag{B.7}$$

Now, if the collimator length is  $h$ , (Figure 57) and  $P_S$  lies on edge A, its coordinates satisfy  $x_1 \leq x_S \leq x_2$ ,  $y_S = y_2$ ,  $z_S = h$ . Using equation (B.7), the line  $P_S P_D$  is therefore described by:

$$\begin{aligned} x &= [(1 - \alpha)x_1 + \alpha x_2]t + (1 - t)x_D, \quad 0 \leq \alpha \leq 1 \\ y &= y_2 t + (1 - t)y_D \\ z &= ht \end{aligned} \tag{B.8}$$

In the plane  $z = s + h$ ,  $t = \frac{s + h}{h}$ , and equations (B.8) become:

$$\begin{aligned} x &= [(1 - \alpha)x_1 + \alpha x_2] \left( \frac{s + h}{h} \right) - \frac{s}{h} x_D, \quad 0 \leq \alpha \leq 1 \\ y &= y_2 \left( \frac{s + h}{h} \right) - \frac{s}{h} y_D \\ z &= s + h \end{aligned} \tag{B.9}$$



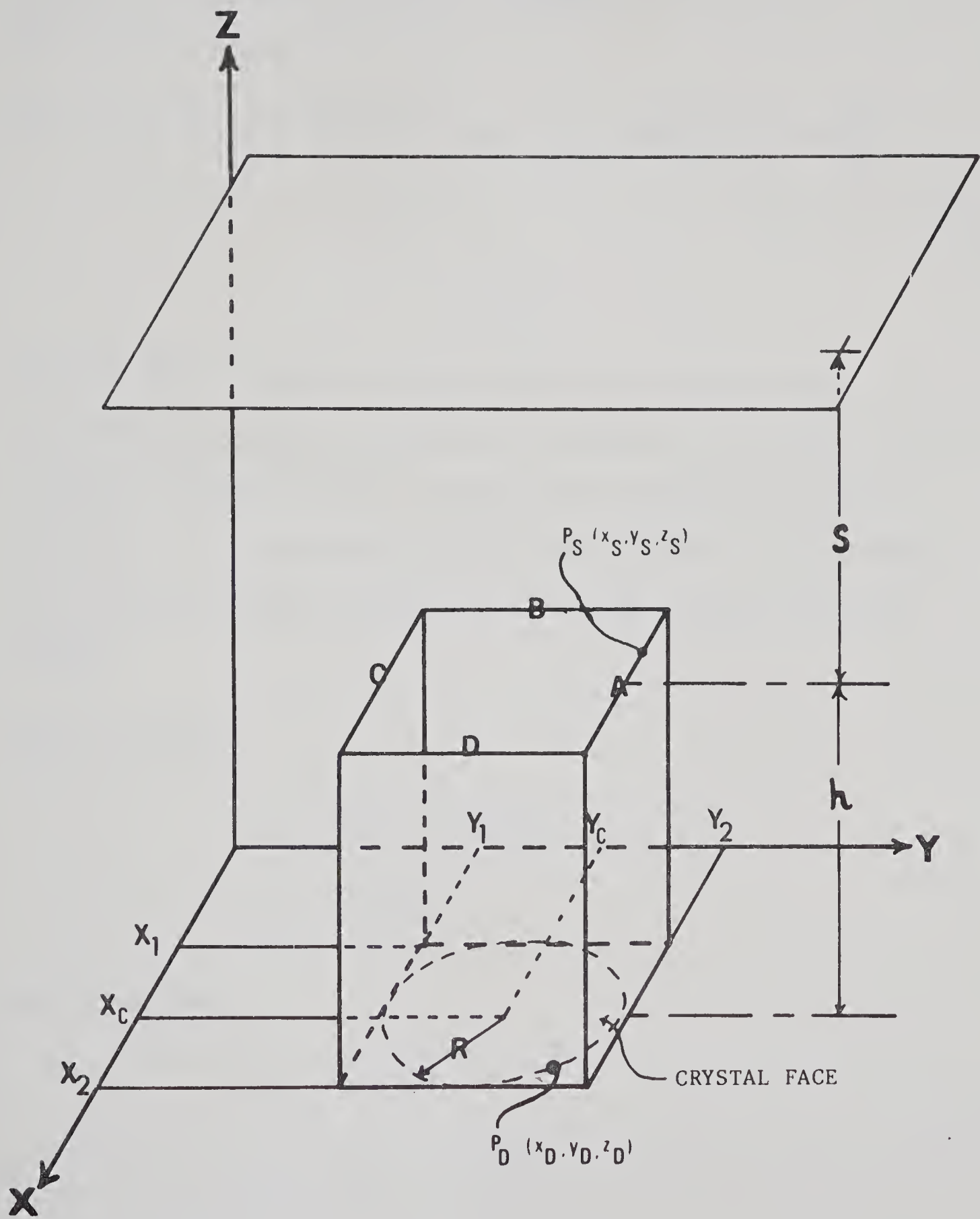


FIGURE 57





The point  $(x_D, y_D, z_D)$  obviously satisfies equation (B.6), as it lies on the circle. Thus  $x_D$ ,  $y_D$ , and  $z_D$  may be eliminated using (B.6) and (B.9), to yield an expression relating  $x, y$  to  $x_C, y_C$ . This expression is:

$$\{x - [x_C + R(2\alpha - 1)\frac{(s + h)}{h}]\}^2 + \{y - [y_C + R\frac{(s + h)}{h}]\}^2 = R^2\frac{s^2}{h^2}$$

$$0 \leq \alpha \leq 1 \quad (\text{B.10})$$

$$z = s + h$$

Equation (B.10) therefore defines the perimeter of the field-of-view of the crystal area over one edge of the collimator, in a plane a distance  $s$  from the collimator face. The other three edges may be treated similarly, and corresponding fields-of-view defined. In all cases, the expressions define circles with radius  $R\frac{s}{h}$ , but with differing centers:

Edge A; Centres:

$$x = x_C + R(2\alpha - 1)\frac{(s + h)}{h}, \quad 0 \leq \alpha \leq 1$$

$$y = y_C + R\frac{(s + h)}{h}$$
(B.11)

Edge B; Centres:

$$x = x_C - R\frac{(s + h)}{h}$$

$$y = y_C + R(2\alpha - 1)\frac{(s + h)}{h}, \quad 0 \leq \alpha \leq 1$$
(B.12)



Edge C; Centres:

$$\begin{aligned} x &= x_C + R(2\alpha - 1)\left(\frac{s + h}{h}\right), \quad 0 \leq \alpha \leq 1 \\ y &= y_C - R\left(\frac{s + h}{h}\right) \end{aligned} \quad (\text{B.13})$$

Edge D; Centres:

$$\begin{aligned} x &= x_C + R\left(\frac{s + h}{h}\right) \\ y &= y_C + R(2\alpha - 1)\left(\frac{s + h}{h}\right), \quad 0 \leq \alpha \leq 1 \end{aligned} \quad (\text{B.14})$$

Figure 58 shows the field-of-view at various distances  $s$  from the collimator face as calculated from these equations. As can be seen, imposing the constraint that the crystal is circular rounds the corners off in the field-of-view response described by equation (B.5), and decreases the area viewed. The area is given by:

$$A_R' = A_R - (4 - \pi)R^2 \frac{s^2}{h^2} \quad (\text{B.15})$$

where  $A_R$  is defined in (B.5) and  $\ell_1 = \ell_2 = w_1 = w_2 = 2R$ .



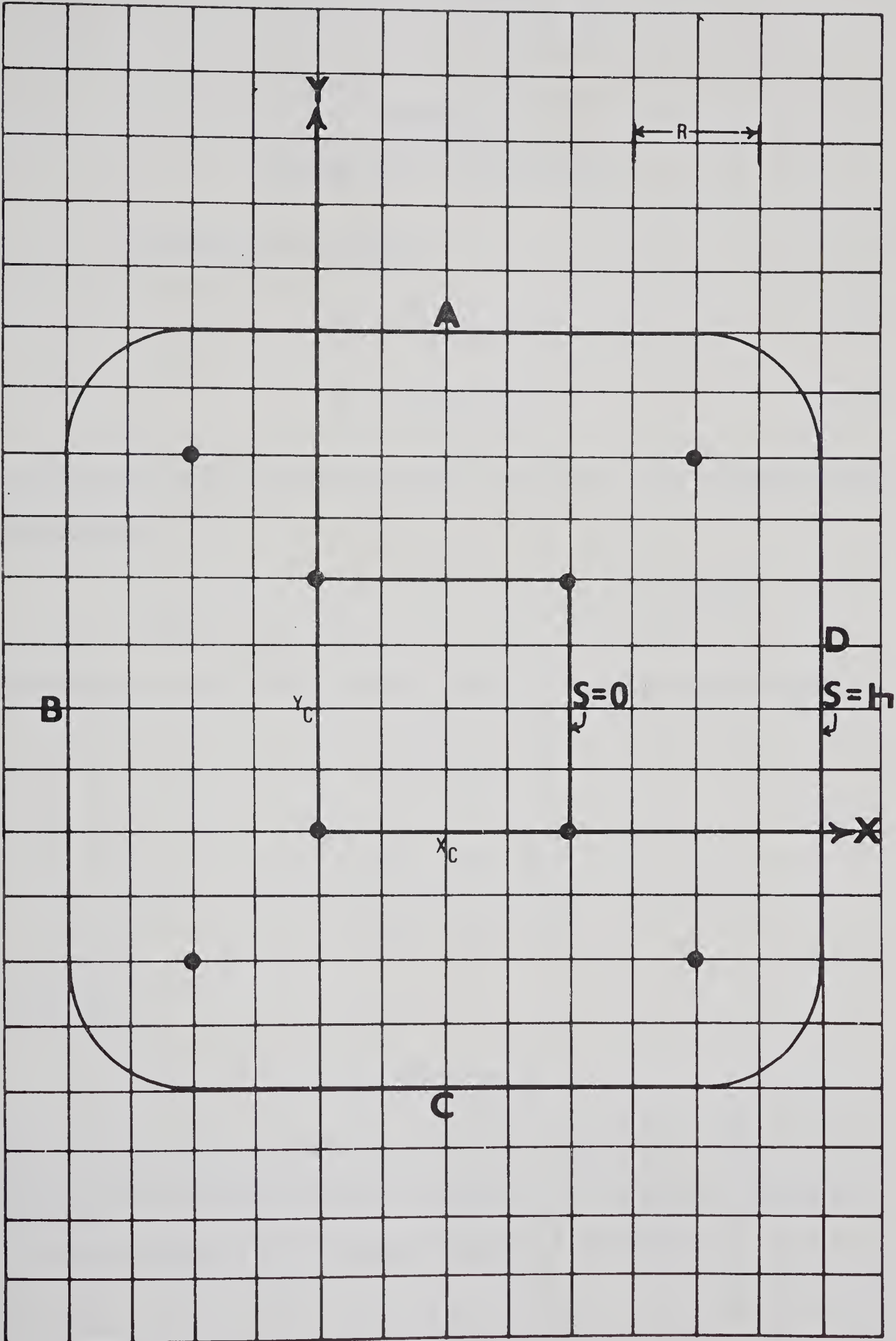


FIGURE 58



## APPENDIX C

### Mathematics of Ray-Tracing

Assuming any two points,

$$P_D = (x_D, y_D, z_D) \quad (C.1)$$

$$P_S = (x_S, y_S, z_S) \quad (C.2)$$

on the detector grid and source grid respectively, the distance between these points is

$$D_{DS} = [(x_S - x_D)^2 + (y_S - y_D)^2 + (z_S - z_D)^2]^{1/2}$$

The equation of the line joining  $P_D$  and  $P_S$  is given parametrically by:

$$\begin{aligned} x &= x_D + (x_S - x_D)t \\ y &= y_D + (y_S - y_D)t \\ z &= z_D + (z_S - z_D)t \end{aligned} \quad (C.3)$$

The point

$$P_A = (x_A, y_A, z_A)$$

on the skin surface through which the line  $P_D P_S$  passes must be found.

Assuming that the skin surface is parallel to the detector plane and lies in the plane  $z = z_A$ , the coordinates of  $P_A$  become:





$$\begin{aligned}
 x_A &= x_D + (x_S - x_D) \frac{(z_A - z_D)}{(z_S - z_D)} \\
 y_A &= y_D + (y_S - y_D) \frac{(z_A - z_D)}{(z_S - z_D)} \\
 z_A &= z_A
 \end{aligned} \tag{C.4}$$

The distance  $D_{SA}$  between  $P_S$  and  $P_A$ ,

$$D_{SA} = [(x_S - x_A)^2 + (y_S - y_A)^2 + (z_S - z_A)^2]^{1/2}$$

is the length of tissue absorber through which the gamma ray must pass. Neglecting collimation, the remaining length,  $D_{DS} - D_{SA}$  is the length of air absorber which the gamma-ray must also traverse.

The crystal will be surrounded by a collimator, and edge penetration effects must be taken into account. In cross section, the collimator will be a height  $h$  above the crystal face. Whether it is a tapered or straight cylindrical, or tapered or straight rectangular collimator, its geometry may be defined analytically. Then, intersection points of the line  $P_D P_S$  with the collimator can be found and the distance through collimator material determined and hence the attenuation calculated.

### C.1 Cylindrical Straight Collimator

Figure 59 shows a section of the collimator of length  $h$  above the detector grid, whose axis passes through the point  $(x_1, y_1, z_D)$  and whose inner and outer radii are  $R_i$  and  $R_o$  respectively. The surface of this collimator can thus be described by the equations:

$$(x - x_1)^2 + (y - y_1)^2 = R_i^2 \tag{C.5}$$



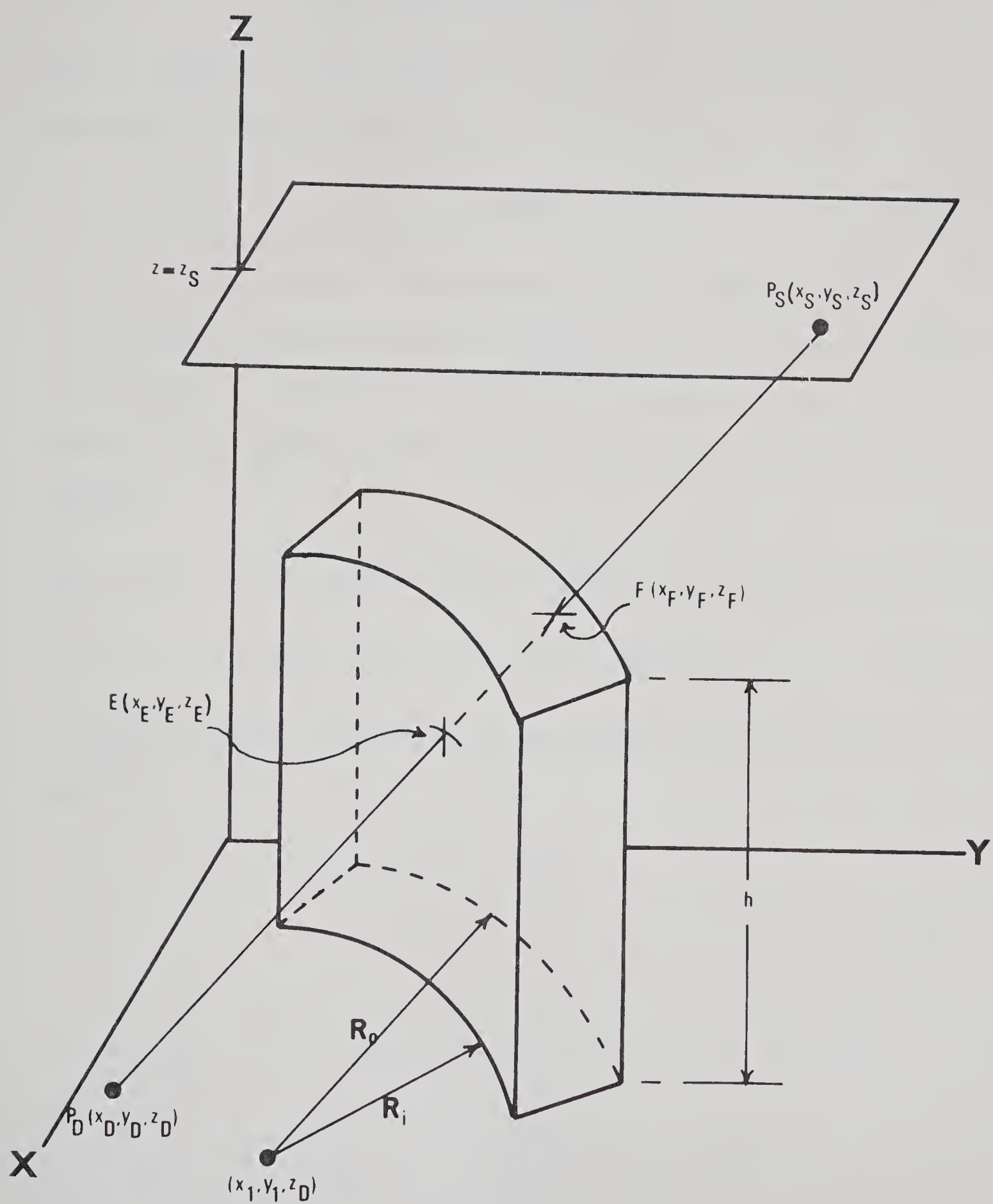


FIGURE 59



for the inside and

$$(x - x_1)^2 + (y - y_1)^2 = R_o^2 \quad (C.6)$$

for the outside. In both cases, the z-coordinate is restricted to the length of the collimator, i.e.

$$0 \leq z \leq h \quad (C.7)$$

$R_o - R_i$  is the collimator thickness and  $h$  is its length. Consider the two points  $P_D$  and  $P_S$  given by (C.1) and (C.2). The line that joins these points is characterized by the set of equations (C.3). By solving (C.3) and (C.5) simultaneously, a quadratic equation for  $t$  is derived:

$$\begin{aligned} & [(y_S - y_D)^2 + (x_S - x_D)^2]t^2 + 2[(y_D - y_1)(y_S - y_D) + (x_D - x_1)(x_S - x_D)]t \\ & + [(y_D - y_1)^2 + (x_D - x_1)^2 - R_i^2] = 0 \end{aligned} \quad (C.8)$$

By substituting for the differences that appear in (C.8), it may be simplified. Let

$$\begin{aligned} \alpha &= x_S - x_D \\ \beta &= y_S - y_D \\ \gamma &= z_S - z_D \end{aligned} \quad (C.9)$$

and

$$\begin{aligned} A &= x_D - x_1 \\ B &= y_D - y_1 \\ C &= z_D - z_1 \end{aligned} \quad (C.10)$$



Then (C.8) is solved for  $t$ , and gives:

$$t_E = \frac{-(A\alpha + B\beta)}{\alpha^2 + \beta^2} \pm \frac{[R_i^2(\alpha^2 + \beta^2) - (A\beta - B\alpha)^2]^{1/2}}{\alpha^2 + \beta^2}$$

Using this value of  $t$ , equations (C.3) become uniquely defined.

$t$  must be chosen so that the  $z$  intercept is greater than zero. Since  $P_D$  will always be inside the cylinder and on  $z = z_D$ , there will always be only one positive  $z$  intercept (assuming  $z_D$  will normally be zero).

The point so defined (E), will be the point of entry of the line  $P_S P_D$  into the collimator. The exit point (F) may be determined in an exactly similar fashion, and is characterized by  $t_F$ :

$$t_F = \frac{-(A\alpha + B\beta)}{\alpha^2 + \beta^2} \pm \frac{[R_o^2(\alpha^2 + \beta^2) - (A\beta - B\alpha)^2]^{1/2}}{\alpha^2 + \beta^2} \quad (C.11)$$

From Figure 60, there are three possible ways in which  $P_D P_S$  will intersect the collimator.

Case (1) If  $E(x_E, y_E, z_E)$  has  $z_E > h$  then there will be no penetration through the collimator.

Case (2) If  $z_E < h$  and the exit point  $F(x_F, y_F, z_F)$  which is uniquely defined by substituting (C.11) into (C.3) has  $z_F > h$ , then the ray  $P_D P_S$  passes through the top face of the collimator and the new coordinates of F will be given from (C.4) as:

$$\begin{aligned} x_F &= x_D + (x_S - x_D) \frac{(h - z_D)}{(z_S - z_D)} \\ y_F &= y_D + (y_S - y_D) \frac{(h - z_D)}{(z_S - z_D)} \end{aligned} \quad (C.12)$$





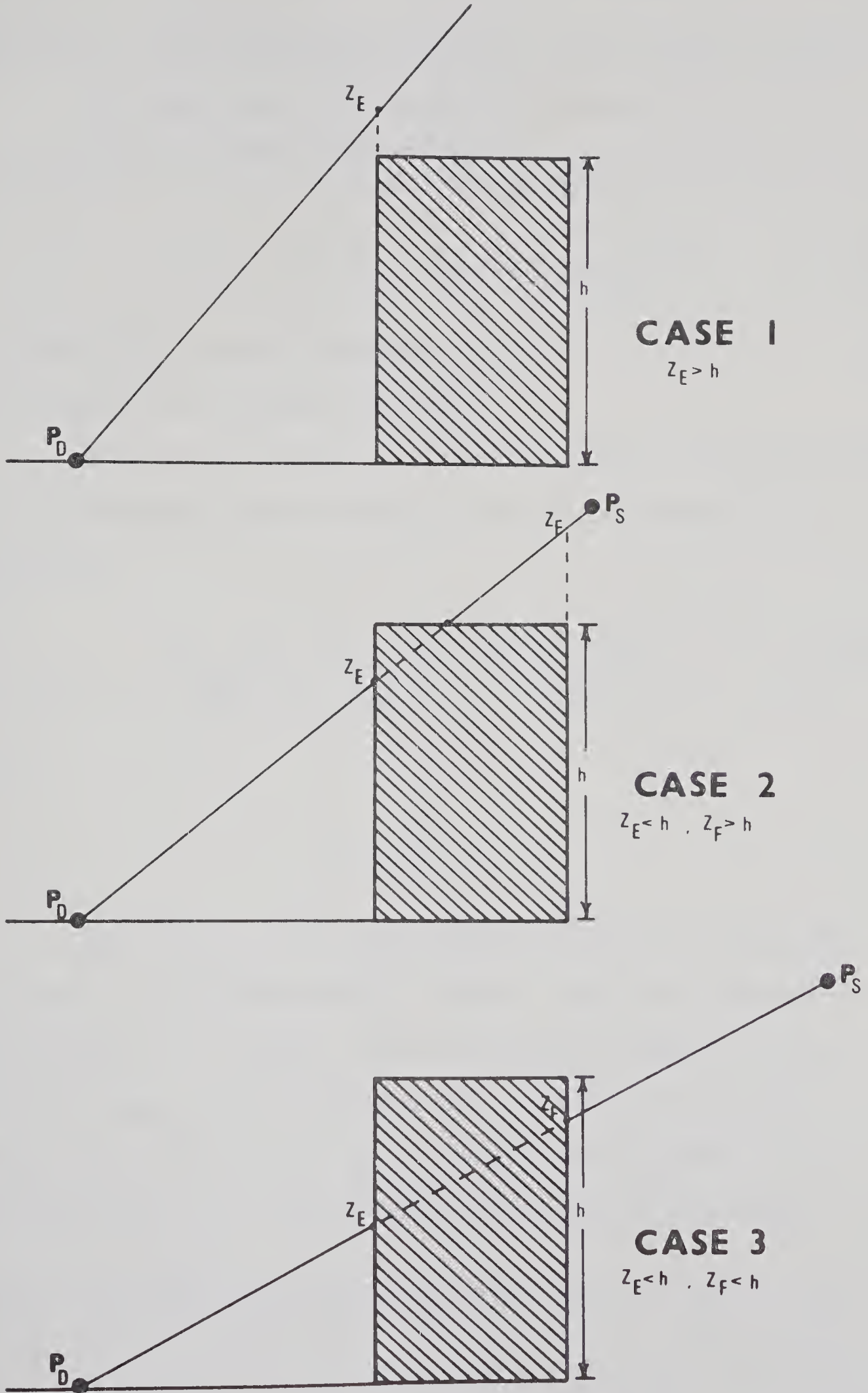


FIGURE 60



$$z_F = h$$

Case (3) If  $z_F$  and  $z_E$  are both less than  $h$ , the ray passes through the outer side of the collimator, and equations (C.3) and (C.11) are used to determine  $F$ .

For either one of the last two cases, the absorber thickness will be

$$\tau = [(x_F - x_E)^2 + (y_F - y_E)^2 + (z_F - z_E)^2]^{1/2} \quad (C.13)$$

## C.2 Cylindrical Tapered Collimators

### C.2.1 Cylindrical Diverging Collimator

Knowing the equation of a conic in 3-space, the inside surface of the cylindrical tapered diverging collimator in Figure 61 can be described by:

$$\frac{(x - x_1)^2}{R^2} + \frac{(y - y_1)^2}{R^2} = \frac{(z + D - h)^2}{D^2} \quad (C.14)$$

where

$$D = R \tan \phi.$$

The line  $P_D P_S$  will again intersect the conic at one point only, using the same constraints as before. Since the outside of the collimator is a cylinder, the outer surface is given by (C.6). The finite length of the collimator ( $h$ ) constrains  $z$  as in (C.7). Solving (C.3) and (C.14) for  $t$ , and using the substitutions (C.9) and (C.10) where  $z_1 = h - D$ , a quadratic equation in  $t$  is formed:

$$[\alpha^2 + \beta^2 - \frac{R^2}{D^2} \gamma^2] t^2 + 2[A\alpha + B\beta - \frac{R^2}{D^2} C\gamma] t + [A^2 + B^2 - \frac{R^2}{D^2} C^2] = 0$$



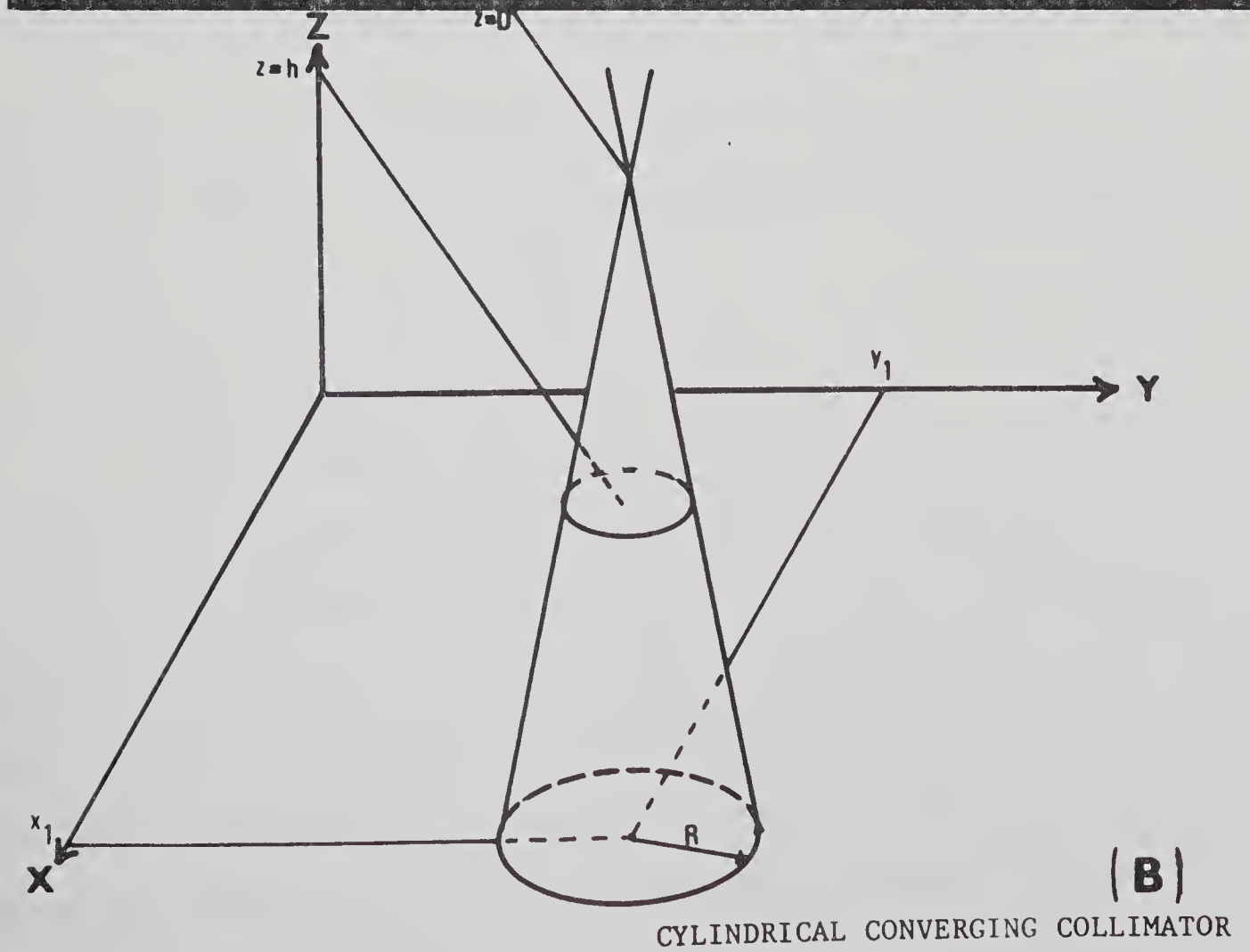
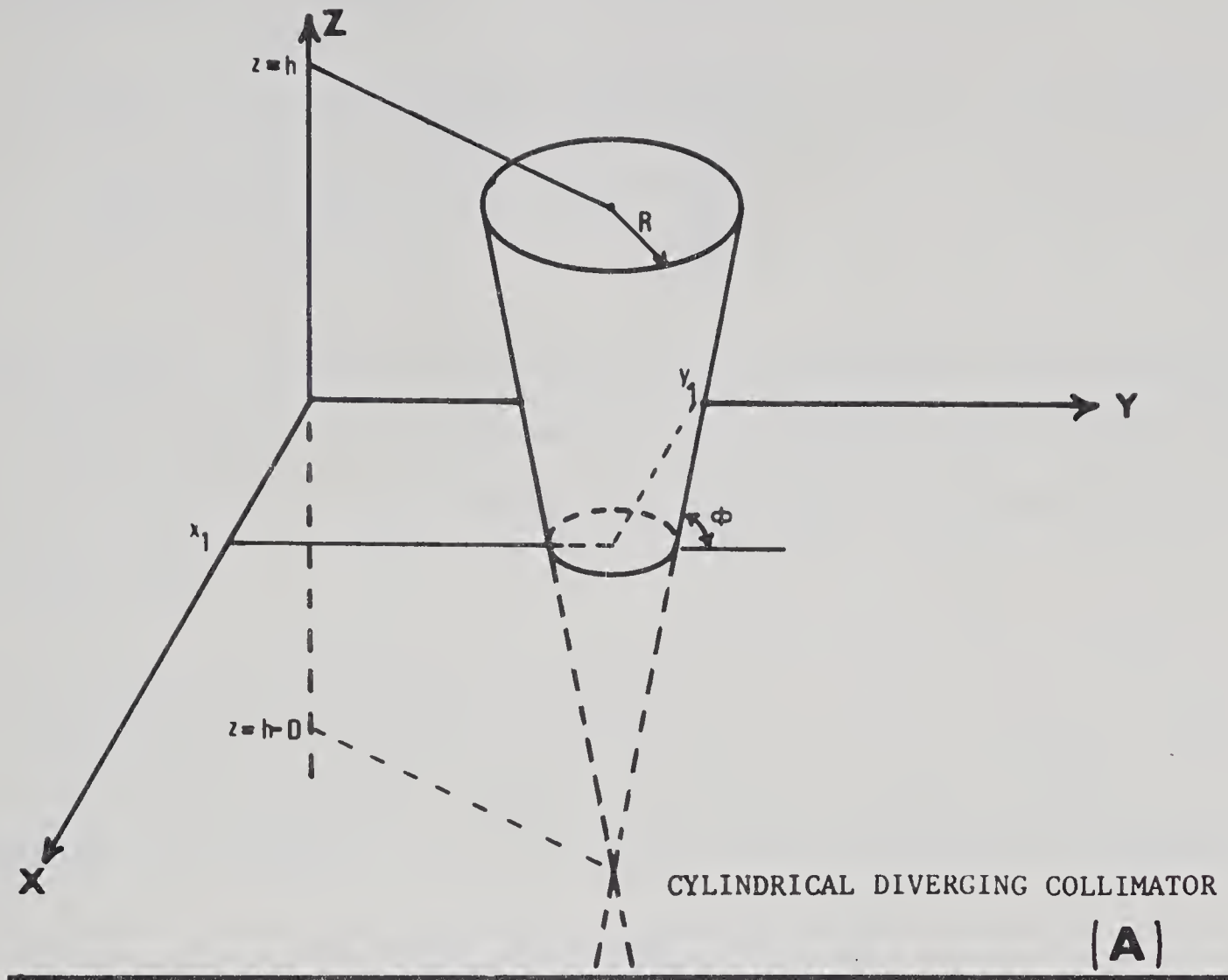


FIGURE 61



The solution for  $t$  becomes:

$$t_E = \frac{-(A\alpha + B\beta - \frac{R^2 C\gamma}{D^2}) \pm \left[ \frac{R^2 (A\gamma - C\alpha)^2}{D^2} + \frac{R^2 (B\gamma - C\beta)^2}{D^2} - (A\beta - B\alpha)^2 \right]^{1/2}}{\alpha^2 + \beta^2 - \frac{R^2 \gamma^2}{D^2}}$$

$t$  must again be chosen so that  $z_E$  from (C.3) is positive. The value for  $t$  for the exit point F will be given by (C.12) for Case (2). For Case (3), F will be given by (C.11). The absorber thickness  $\tau$  is given by (C.13) for both cases.

### C.2.2 Cylindrical Converging Collimator

For a cylindrical tapered converging collimator, from Figure 61, the equation of the conic describing the inside face will be:

$$\frac{(x - x_1)^2}{R^2} + \frac{(y - y_1)^2}{R^2} = \frac{(z - D)^2}{D^2}$$

The solution to the intersection points will be the same as for the diverging collimator except that instead of  $z_1 = h - D$ , one needs to substitute  $z_1 = D$ .

### C.3 Straight Rectangular Collimator

For a straight rectangular collimator, the sides are described by equations of planes, all parallel to the  $z$  axis (Figure 62). If all the planes are considered to be infinite, the analysis becomes simpler. However, any line,  $P_D P_S$ , can then intersect all the planes. In order to avoid this, the proper side of the collimator involved in penetration can first be determined by certain selection rules. In Figure 62, looking down on the  $x$ - $y$  plane, the collimator can be divided into four quadrants. If the point  $P_S$  given by (C.2) is projected onto the  $z = z_D$  plane, (which will normally be the  $z = 0$  plane),





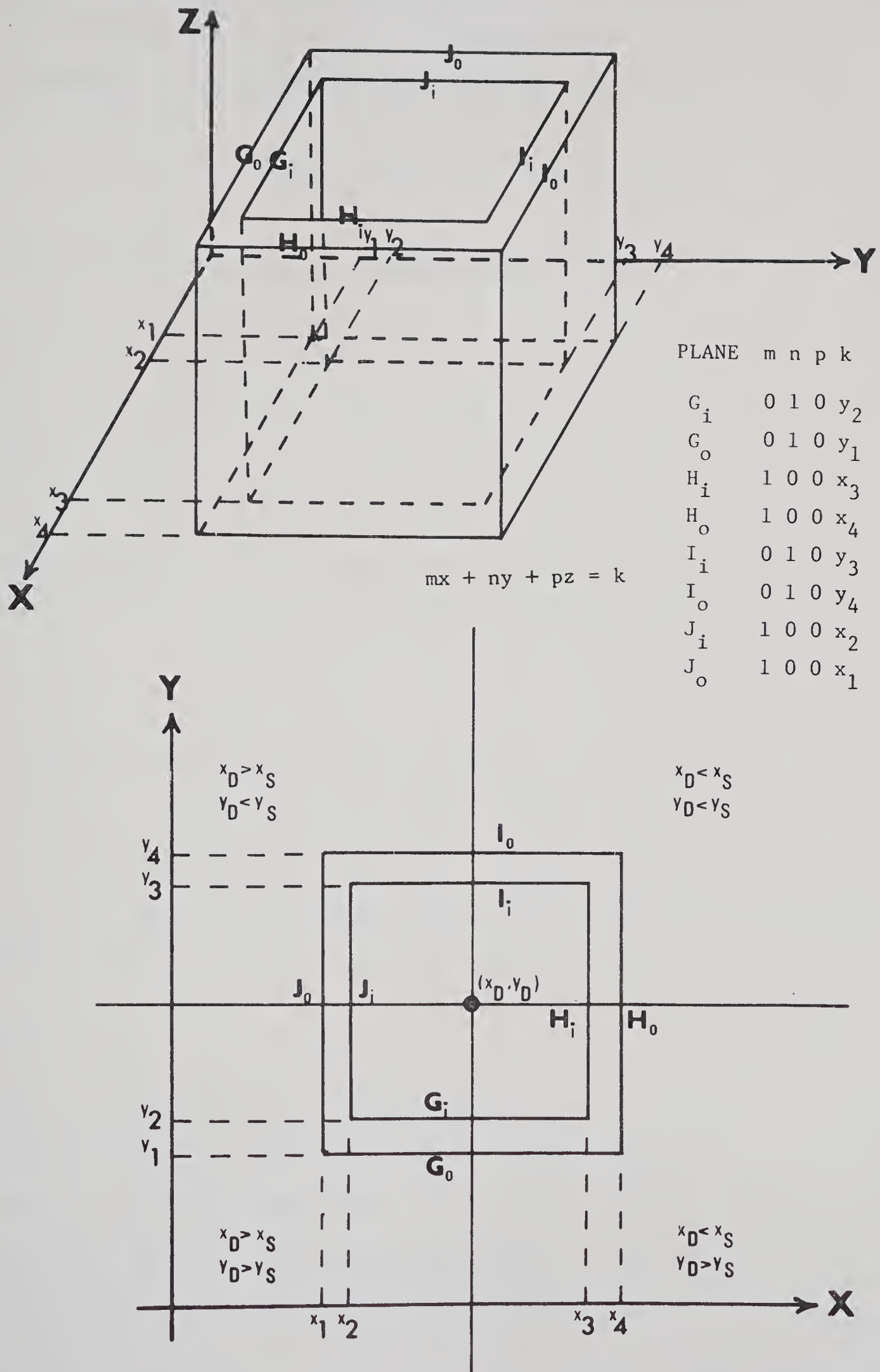


FIGURE 62



the  $z$  coordinates of the points  $P_D$  and  $P_S$  are equal and can be ignored. The equations for  $x$  and  $y$  in (C.3) can be solved simultaneously, eliminating  $t$ , to give  $x$  in terms of  $y$ , or vice versa:

$$(y - y_D)(x_D - x_S) = (x - x_D)(y_D - y_S)$$

If  $x_D \neq x_S$  and  $y_D \neq y_S$ , four possibilities exist:

Case (A)  $x_D > x_S, y_D > y_S$

Possible sides involved:  $J_i, J_o, G_i, G_o$

$$\text{Side } J_i: (y_D - y_2)(x_D - x_S) \geq (x_D - x_2)(y_D - y_S)$$

$$\text{Side } G_i: (y_D - y_2)(x_D - x_S) \leq (x_D - x_2)(y_D - y_S)$$

$$\text{Side } J_o: (y_D - y_1)(x_D - x_S) \geq (x_D - x_1)(y_D - y_S)$$

$$\text{Side } G_o: (y_D - y_1)(x_D - x_S) \leq (x_D - x_1)(y_D - y_S)$$

Case (B)  $x_D > x_S, y_D < y_S$

Possible sides involved:  $I_i, I_o, J_i, J_o$

$$\text{Side } I_i: (y_3 - y_D)(x_D - x_S) \leq (x_D - x_2)(y_S - y_D)$$

$$\text{Side } J_i: (y_3 - y_D)(x_D - x_S) \geq (x_D - x_2)(y_S - y_D)$$

$$\text{Side } I_o: (y_4 - y_D)(x_D - x_S) \leq (x_D - x_1)(y_S - y_D)$$

$$\text{Side } J_o: (y_4 - y_D)(x_D - x_S) \geq (x_D - x_1)(y_S - y_D)$$

Case (C)  $x_D < x_S, y_D > y_S$

Possible sides involved:  $G_i, G_o, H_i, H_o$

$$\text{Side } G_i: (y_D - y_2)(x_S - x_D) \leq (x_3 - x_D)(y_D - y_S)$$

$$\text{Side } H_i: (y_D - y_2)(x_S - x_D) \geq (x_3 - x_D)(y_D - y_S)$$

$$\text{Side } G_o: (y_D - y_1)(x_S - x_D) \leq (x_4 - x_D)(y_D - y_S)$$

$$\text{Side } H_o: (y_D - y_1)(x_S - x_D) \geq (x_4 - x_D)(y_D - y_S)$$



Case (D)  $x_D < x_S, y_D < y_S$

Possible sides involved:  $H_i, H_o, I_i, I_o$

Side  $H_i$ :  $(y_3 - y_D)(x_S - x_D) \geq (x_3 - x_D)(y_S - y_D)$

Side  $I_i$ :  $(y_3 - y_D)(x_S - x_D) \leq (x_3 - x_D)(y_S - y_D)$

Side  $H_o$ :  $(y_4 - y_D)(x_S - x_D) \geq (x_4 - x_D)(y_S - y_D)$

Side  $I_o$ :  $(y_4 - y_D)(x_S - x_D) \leq (x_4 - x_D)(y_S - y_D)$

In every case, only one outside plane and one inside plane will satisfy the conditions. In all four cases, if the left hand side equals the right hand side, then the projection intersects the corner of the rectangle.

Other cases:

$x_D = x_S, y_D > y_S \Rightarrow$  sides  $G_i$  and  $G_o$

$x_D = x_S, y_D < y_S \Rightarrow$  sides  $I_i$  and  $I_o$

$x_D > x_S, y_D = y_S \Rightarrow$  sides  $J_i$  and  $J_o$

$x_D < x_S, y_D = y_S \Rightarrow$  sides  $H_i$  and  $H_o$

$x_D = x_S, y_D = y_S \Rightarrow$  no penetration factor possible.

Once the penetration sides have been determined, since any plane can be described by

$$mx + ny + pz = k \quad (C.15)$$

where the values of  $m, n, p, k$  are given in Figure 62 for each of the planes, then the value of  $t$  from (C.3) will be

$$t = \frac{k - mx_D - ny_D - pz_D}{m(x_S - x_D) + n(y_S - y_D) + p(z_S - z_D)} \quad (C.16)$$



The entry and exit points E and F will then be given by (C.3) for Case (3), where an inside wall will be used for E and an outside wall for F. For Case (2), if  $z_E < h$  and  $z_F > h$ , the point F will have coordinates given by (C.12). The absorber thickness  $\tau$  is given by (C.13)

#### C.4 Tapered Rectangular Collimators

The last case to be considered is that of a tapered diverging rectangular collimator. Normally, only two opposing sides will be angled, the other two opposing sides being left parallel to the  $z$  axis (Figure 63). The problem of choosing the proper intersection planes still exists, but the method of selection is different since the equations of the tapered planes are more complicated.  $t$  can be determined from (C.16) for both  $H_i$  and  $J_i$ , and the corresponding values of  $(x_E, y_E, z_E)$  calculated from (C.3). If, for example, the  $z_E$  value of plane  $H_i$  is negative, assuming  $z_D = 0$ , the plane  $J_i$  must be used. On the other hand, if the  $z_E$  value of plane  $J_i$  is negative, the plane  $H_i$  must be used. One of the intersection points must be positive, while the other is constrained to be negative. After one of the two planes has been chosen, its corresponding  $y_E$  value is checked to see that the condition

$$y_2 \leq y_E \leq y_3 \quad (C.17)$$

holds. If this is not the case, then no penetration of the tapered planes is possible. If (C.17) is true, a final check is made to see whether  $z_E < h$ . If this constraint also holds, then the entry point E has been found. If  $z_E > h$ , no penetration of the collimator occurs (Case (1)). Assuming an entry point has been found on  $H_i$  or  $J_i$ ,





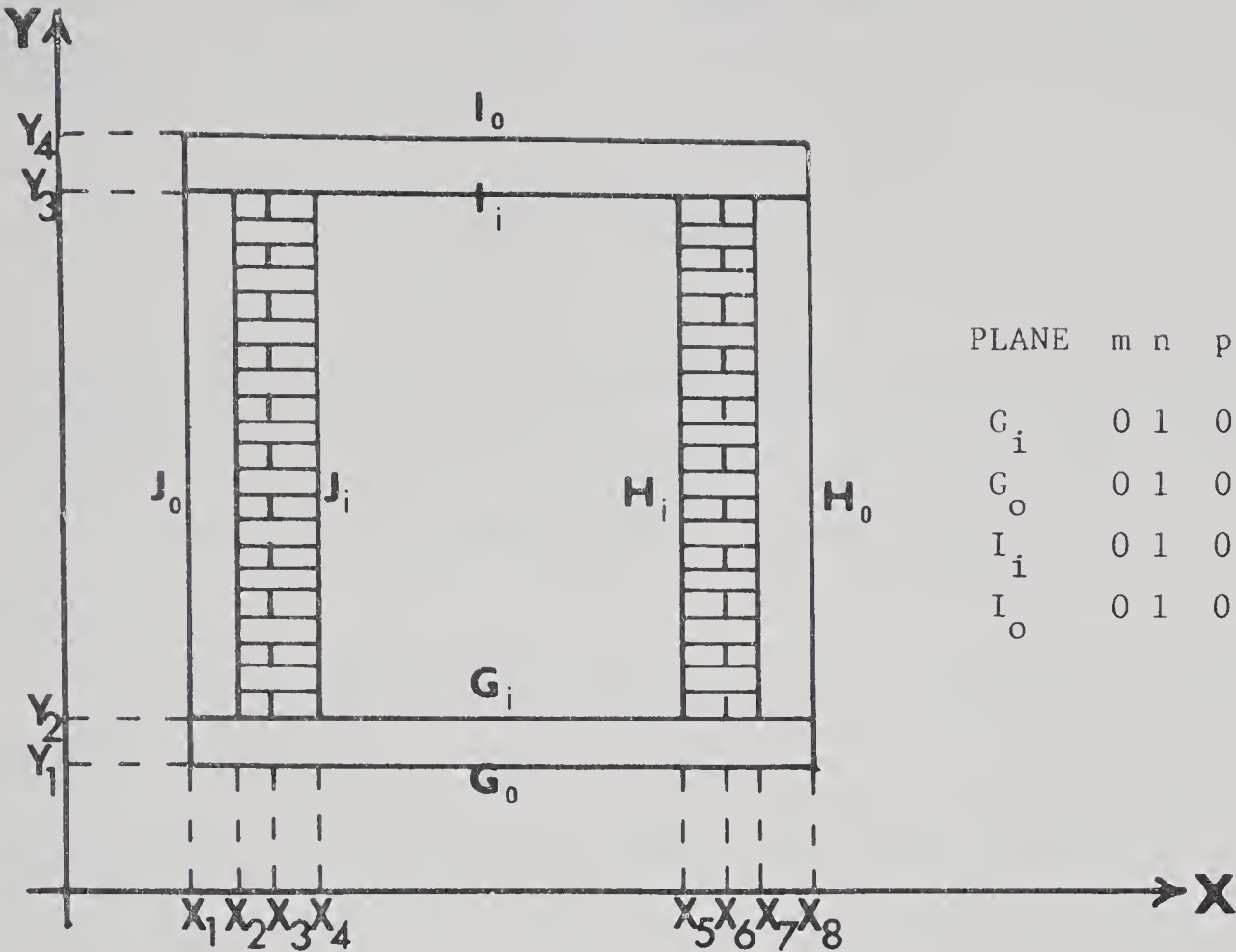
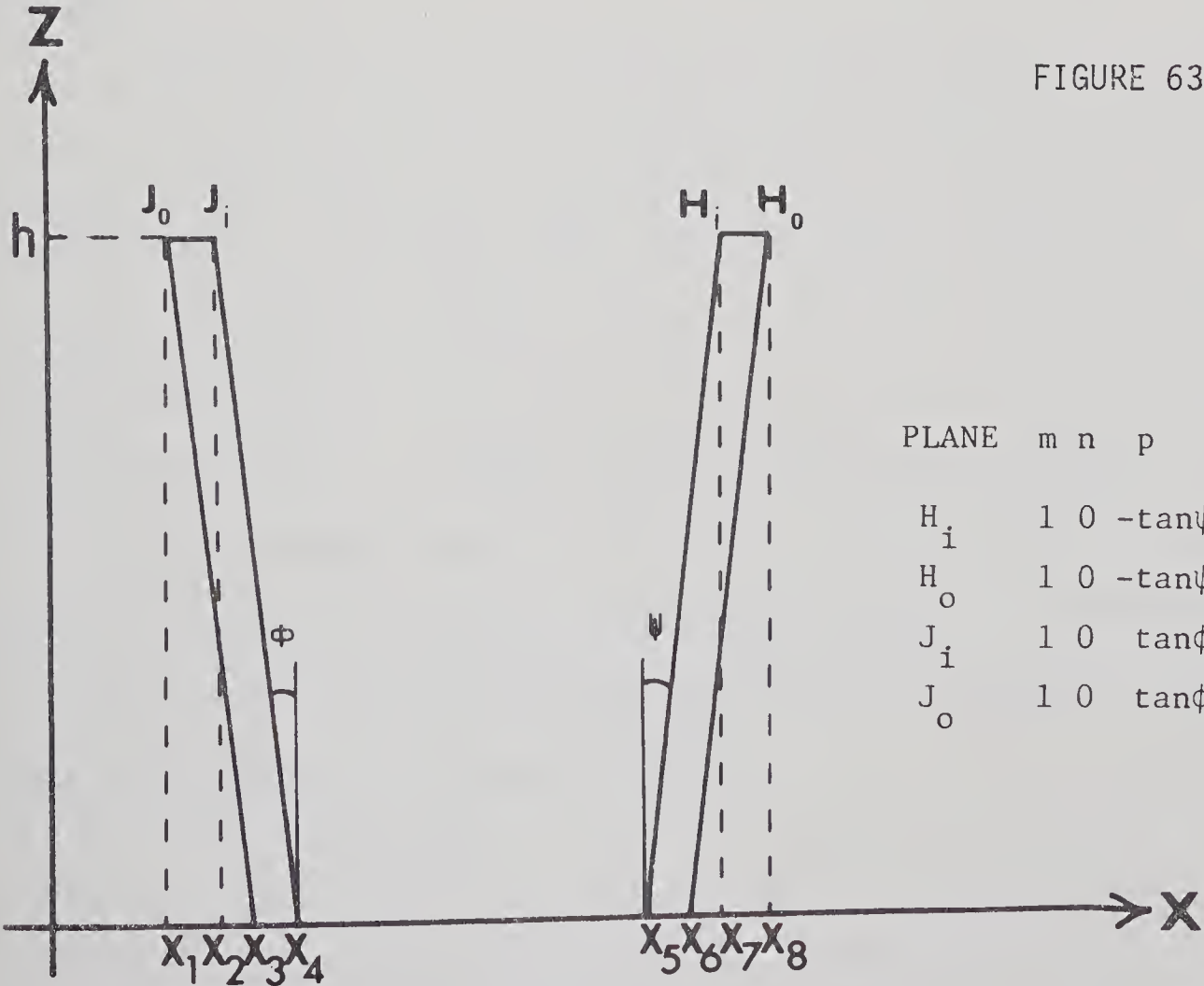


FIGURE 63





then  $t$  is calculated for  $H_O$  or  $J_O$  respectively, and  $(x_F, y_F, z_F)$  determined. The condition

$$y_1 \leq y_F \leq y_4 \quad (C.18)$$

is checked for validity. If it holds, then  $z_F$  for the outer plane is compared with  $h$ . For Case (2),  $F$  is given by (C.12), and for Case (3), the value of  $t$  for the outer plane is inserted into (C.3) to yield  $(x_F, y_F, z_F)$ .

When (C.18) does not hold for  $y_F$  but an entry point  $E$  exists on  $H_i$  or  $J_i$  then the ray must pass through  $G_O$  or  $I_O$  respectively. A simple test  $y_D > y_S$  or  $y_D < y_S$ , determines if the plane is  $G_O$  or  $I_O$  respectively. Once this is done,  $t$  for  $G_O$  or  $I_O$  can be found from (C.16) and the exit point  $F$  determined from (C.3). Again if  $z_F > h$ ,  $F$  is given by (C.12).

If (C.17) is not true, then the ray must pass through either  $G_i$  or  $I_i$ . Again,  $y_D > y_S$  or  $y_D < y_S$  determines if the plane is  $G_i$  or  $I_i$ , respectively. The entry point  $E$  on the plane is then found. If  $z_E > h$ , no penetration occurs. If  $z_E < h$ , the entry point  $E$  on the inside plane is found.  $t$  is calculated for  $H_O$  or  $J_O$ , whichever applies, and (C.18) is tested. The same procedure as before determines if one of these outer tapered planes is involved. If not, then  $G_O$  or  $I_O$ , whichever applies, is used and  $t$  calculated for one of these and  $F$  found.  $F$  is determined from either Case (2) or Case (3). Finally,  $\tau$ , the attenuation distance, is given by (C.13).



## APPENDIX D

## Solid Angle Derivations

The solid angle subtended by a circular disk at an off-axis point may be determined by replacing the disk by an equal area, right polygon with total number of sides  $n$ , where  $n$  is even (38), (Figure 64).

It has been shown (38) that the total solid angle for the  $n$ -sided polygon for any  $s$ ,  $R$ , and  $\rho$ , is

$$\Omega(s, R, \rho) = 2 \sum_{r=1}^{\frac{(n-2)}{2}} (E_r - F_r) \quad (D.1)$$

where

$$E_r = \arctan \frac{s(x_{r+1}^2 + y_r^2 - 2m_r x_r y_r + m_r^2 x_r^2 + s^2 + m_r^2 x_{r+1}^2 + 2m_r x_{r+1} y_r - 2m_r^2 x_{r+1} x_r)^{1/2}}{m_r (s^2 + x_{r+1}^2 x_r^2 - x_{r+1} y_r)} \quad (D.2)$$

$$F_r = \arctan \frac{s(x_r^2 + y_r^2 + s^2)^{1/2}}{m_r (x_r^2 + s^2) - x_r y_r} \quad (D.3)$$

where

$$m_r = \tan \left[ (n - 4r) \frac{\pi}{2n} \right], \quad 1 \leq r \leq \frac{(n-2)}{2} \quad (D.4)$$

$$y_r = \frac{1/2 p \sin \left[ (2(r-1) \frac{\pi}{n}) \right]}{\sin (\pi/n)}, \quad 1 \leq r \leq \frac{n}{2} \quad (D.5)$$

$$p = 2R \left[ \left( \frac{\pi}{n} \right) \tan \left( \frac{\pi}{n} \right) \right]^{1/2} \quad (D.6)$$



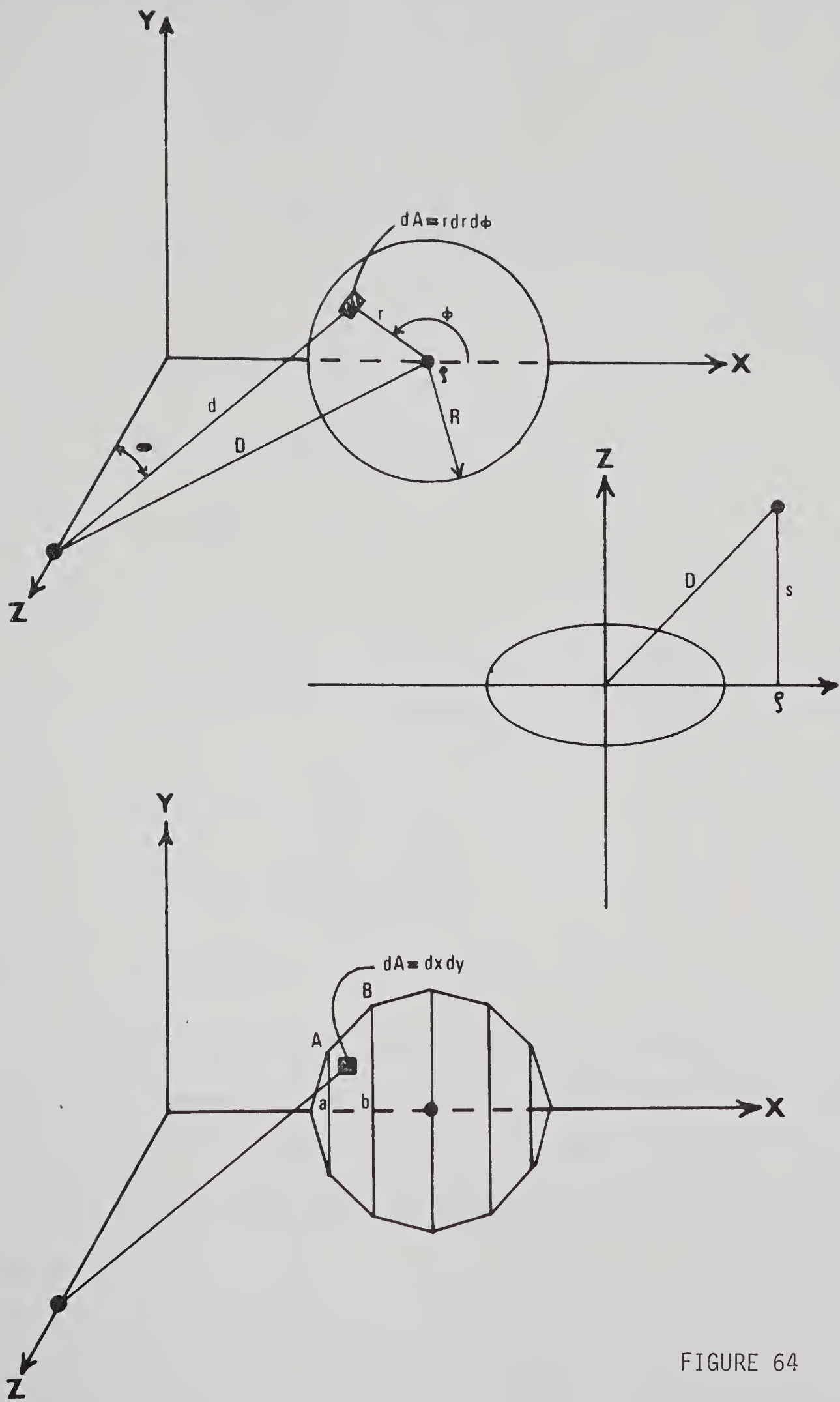


FIGURE 64





$$x_r = \rho - d_r, \quad 1 \leq r \leq \frac{n}{2} \quad (\text{D.7})$$

$$\rho = (D^2 - s^2)^{1/2} \quad (\text{D.8})$$

for  $\frac{n}{2}$  even:

$$d_r = \frac{1}{2}p + \frac{p \sin\left(\frac{\pi}{4} - \frac{\pi r}{n}\right) \sin\left(\frac{\pi r}{n} + \frac{\pi}{4} - \frac{\pi}{n}\right)}{\sin(\pi/n)}, \quad 1 \leq r \leq \frac{(n-4)}{4} \quad (\text{D.9})$$

$$d_r = \frac{1}{2}p, \quad r = \frac{n}{4} \quad (\text{D.10})$$

$$d_r = -d_\ell, \quad \left(\frac{n+4}{4}\right) \leq r \leq \frac{n}{2} \quad (\text{D.11})$$

where  $\ell = \left(\frac{n+2}{2}\right) - r \quad (\text{D.12})$

for  $\frac{n}{2}$  odd:

$$d_r = \frac{p \sin\left(\frac{\pi}{4} - \frac{\pi}{2n} + \frac{\pi r}{n}\right) \sin\left(\frac{\pi}{4} + \frac{\pi}{2n} - \frac{\pi r}{n}\right)}{\sin(\pi/n)}, \quad 1 \leq r \leq \frac{(n-2)}{4} \quad (\text{D.13})$$

$$d_r = 0, \quad r = \frac{(n+2)}{4} \quad (\text{D.14})$$

$$d_r = -d_\ell, \quad \left(\frac{n+6}{4}\right) \leq r \leq \frac{n}{2} \quad (\text{D.15})$$

where  $\ell = \left(\frac{n+2}{2}\right) - r \quad (\text{D.16})$

It was found that a 36 sided polygon was necessary to give 0.1% accuracy whereas for a 1.0% accuracy, it was sufficient to use a 20 sided polygon. This however was only required for  $s/D \leq 0.1$  and  $0.1 \leq R/D \leq 2$ . For other cases the number of sides could be greatly reduced.



# APPENDIX E

## COMPUTER PROGRAMS

### RASTER SCANNER DATA ANALYSIS PROGRAM

```

REAL RDATA(10000)
INTEGER ENDPT(1000),DEFT(200),L(200),NDEFT(200)
REAL A(10000),AR(10000),AS(10000),CVAL(20)
INTEGER EOS,EOS1(20),POSS,FINAL,PART1,PART2,IOP(5)
DIMENSION FORM(10)
REWIND 2

```

#### DATA INPUT FROM MAGNETIC TAPE

```

WRITE(6,124)
READ(5,100) FORM
DO 1 J=1,100
READ(2,FORM,END=3,FRR=200) A,RDATA(J),AB
IF(A.NE.0.0) GOTO 2
GOTO 1
2 RDATA(1)=RDATA(J)
ENDPT(1)=J
WRITE(6,115) RDATA(1),ENDPT(1)
GOTO 3
1 CONTINUE
3 KK=0
WRITE(6,127)
READ(5,115) XI
IF(XI.NE.0.0) XI=2.1962E-6
K=2
KK1=1
KK2=0
IKJ=0

```

#### CHECKS FOR AND STORES END-OF-SCAN POINTS

```

DO 4 J=K,10000
READ(2,FORM,END=5,FRR=201) A,RDATA(J),AB
IF(RDATA(J).GT.10.0*RDATA(J-1)) RDATA(1)=RDATA(J)/100.0
RDATA(J)=RDATA(J)*EXP(XI*10.0*(J-1))
GOTO 8
5 K=J
KK=KK+1
IF(KK.GE.7) GOTO 6

```



```

201  K=J
      GOTO 7
      8  IF(AB) 10,10,11
11    IKJ=IKJ+1
      EOS1(IKJ)=J
10    IF(A) 4,4,9
      9  KK1=KK1+1
      ENDPT(KK1)=J
      IF(ENDPT(KK1)-ENDPT(KK1-1).NE.1) GOTO 4
      KK2=KK2+1
      DEFT(KK2)=ENDPT(KK1-1)
      WRITE(6,110) DEFT(KK2)
4     CONTINUE
7     CONTINUE
      GOTO 17

```

C  
C  
C  
C ALL RECORDS HAVE BEEN READ IN, DECAY CORRECTED, AND THE SUMS OF  
C DET. 1 & DET. 2 HAVE ALSO BEEN RECORDED IN RQATS. K IS THE  
C ADDRESS OF THE TOTAL NO. OF RECORDS.

FINDS INITIAL SCAN LENGTHS

```

C      KD=KK2-1
      DO 12 J=1,KD
      L(J)=DEFT(J+1)-DEFT(J)
      IF(I(J).GE.55) GOTO 12
      L(J)=L(J-1)
12     CONTINUE

```

FINDS MINIMUM SCAN LENGTH

```

        IK=1
63      ISCAN=L(IK)
        IK2=IK+1
        M2=0
        DO 13 J=IK2,KD
          IF(ISCAN-L(J).EQ. 0) M2=M2+1
13      CONTINUE
        IF(M2.GT.10) GOTO 64
        IK=IK+1
        IF(IK.EQ.(KD-1)) GOTO 65
        GOTO 63
65      WRITE(6,120)
        READ(5,117) M2
64      LMIN=ISCAN

```



```

WRITE(6,104) LMIN
LENGTH=LMIN-2
WRITE(6,105) LENGTH
WRITE(6,122)
DO 14 J=1,IKJ
WRITE(6,110) EOS1(J)
14 CONTINUE
WRITE(6,123)
READ(5,110) EOS

C
C
C
C RDATA1 IS NORMALIZED WRT ITS LARGEST MEMBER
C I.E. MAXIMUM = 1.0
C
C
C
C
XM1=0.0
DO 32 J=1,K
XM1=AMAX1(XM1,RDATA1(J))
32 CONTINUE
WRITE(6,126) XM1
DO 33 J=1,K
RDATA1(J)=RDATA1(J)/XM1
33 CONTINUE

C
C
C
C ENSURES ALL ENDPOINTS ARE MARKED & STORED IN NDEFT(I)
C
C
C
I=1
DO 36 J=1,KD
I1=2
IPAR=DEFT(J+1)-(DEFT(J)+LMIN)+3
IF(IPAR.LE.0) GOTO 60
GOTO (37,37,37,37,37), IPAR
39 PART1=(DEFT(J+1)-DEFT(J))*1.0/I1 +0.5
PART2=PART1-LMIN+3
IF(PART2.GT.0) GOTO 61
IPT=J
GOTO 62
61 GOTO(38,38,38,38,38), PART2
I1=I1 + 1
GOTO 39
37 NDEFT(I)=DEFT(J)
GOTO 40
38 NDEFT(I)=DEFT(J)
I=I+1
41 NDEFT(I)=DEFT(J)+PART1
DEFT(J)=NDEFT(I)
IF(I1.EQ.2) GOTO 40
I1=I1-1
I=I+1
GOTO 41
60 DEFT(J+1)=DEFT(J)
GOTO 36
40 I=I+1
36 CONTINUE
NDEFT(I)=DEFT(KK2)

```









```

71  J1=0
    J2=1
72  DO 300 J=1,LENGTH
    NINB=(NT-N)*J1 + N*J2
    DO 301 JJ=1,NINB
    IS=J+LENGTH*(JJ-1)
    AS(IS)=A1(IS)
301  CONTINUE
    NINM1=(NT-N+1)*J1 + (N+1)*J2
    NINM2=N*J1 + (NT-N)*J2
    DO 303 JJ=NINM1,NINM2
    IS=J+LENGTH*(JJ-1)
    AS(IS)=(A1(IS)+AR(IS))*(J1*1.0)
303  CONTINUE
    NIN=(N+1)*J1 + (NT-N+1)*J2
    DO 304 JJ=NIN,NT
    IS=J+LENGTH*(JJ-1)
    AS(IS)=AR(IS)
304  CONTINUE
300  CONTINUE
    WRITE(6,111)
    READ(5,115) XSIZE,YSIZE

C
C
C
C      SETTING  PARAMETERS FOR PLOT
C
C
C
C
CALL PLOTS
CALL PLOT(0.0,1.0,-3)
M=LENGTH
NC=7
CVAL(1)=0.1
CVAL(2)=0.25
CVAL(3)=0.4
CVAL(4)=0.5
CVAL(5)=0.6
CVAL(6)=0.75
CVAL(7)=0.9
IOP(1)=1
IOP(2)=1
IOP(3)=0
IOP(4)=1
IOP(5)=15
CALL MAPY(XSIZE,YSIZE,A1,M,NT,CVAL,NC,IOP)
CALL PLOT(0.0,1.0,-3)
CALL MAPY(XSIZE,YSIZE,AS,M,NT,CVAL,NC,IOP)
999 CALL PLOT(24.0,0.0,999)
    WRITE(6,121) LENGTH,NT,LENGTH,N
    STOP
100  FORMAT(' ',10A4)
200  WRITE(6,101) J
101  FORMAT(' ','THERE HAS BEEN AN ERROR IN READING THE ',I4,' ;H RECOR
2D')
103  FORMAT(' ',10X,I4,' RECORDS HAVE BEEN READ IN')

```



```

104  FORMAT(' ',10X,13,' HAS BEEN DETERMINED AS THE MINIMUM SCAN LENGT
2H')
105  FORMAT(' ',10X,13,' HAS BEEN DETERMINED AS THE SCAN LENGTH IN THE
2 X DIRECTION')
106  FORMAT(' ',10X,'THERE ARE ',14,' RECORDS IN THIS SCAN'////////)
110  FORMAT(' ',14)
111  FORMAT(' ','THE PLOTTING IS NOW BEING INITIALIZED ','
2' ENTER X BY Y PLOT DIMENSIONS <INCHES>')
112  FORMAT('0','NO.OF CONTOURS DESIRED? <12>')
113  FORMAT(' ',12)
114  FORMAT('0','VALUE OF CONTOUR NO. ',12,' ?')
115  FORMAT(' ',3G8.3)
116  FORMAT('0','MINIMUM NO. OF POINTS PER CONTOUR DESIRED? <13>')
117  FORMAT(' ',13)
62  WRITE(6,118) IPT
118  FORMAT('0','SCAN ENDPOINT ANOMAIY AROUND RECORD',15)
120  FORMAT('0','SCAN LENGTH CANNOT BE DETERMINED - PLEASE ENTER IT:',
2'<13>')
121  FORMAT('0','THE PLOT SIZE IS ',13,' BY ',13,' - X BY Y'/
2'THE SCAN SIZE IS ',13,' BY ',13,' - X BY Y')
122  FORMAT('0','THE FOLLOWING ARE THE POSSIBLE END-OF-SCAN PTS.:')
123  FORMAT('0','ENTER CORRECT END-OF-SCAN FROM'/
2'ONE OF THE ABOVE : <14>')
124  FORMAT('0','ENTER DATA INPUT FORMAT')
125  FORMAT('0','ENTER DETECTOR SEPARATION IN INCHES')
126  FORMAT('0','THE MAXIMUM COUNT IS',F8.0)
127  FORMAT('0','XENON SOURCE - ENTER 1.0 , POSITRON SOURCE - 0.0')
STOP
END

```



CYLINDRICAL COLLIMATOR MODELLING  
PROGRAM

FTN

```

PROGRAM CLMOD
DIMENSION XIBON(9),XFBON(9),YBONE(9),ZBONE(9),RBONE(9),DR(50)
INTEGER LU(5),DATE(9),TAPE,ISR(100),IDR(50),IT1(5),IT2(5)
REAL MUAIR,MUTIS,MUBON,MUCOL
DATA ILU/1/,TAPE/9/,DR/130*0.0/
CALL RMPAR(LU)
IF(LU.GT.0) ILU=LU

```

ADDRESSES	MEANING	UNITS
CRR	CRYSTAL RADIUS	CM
H	COLLIMATOR HEIGHT	CM
R1	CYL. COLL. CRYSTAL END RADIUS	CM
R2	CYL. COLL. FACE END RADIUS	CM
T	COLLIMATOR THICKNESS	CM
TSCFS	TISSUE SURFACE-CRYSTAL FACE SEP.	CM
SY1,SY1,SZ1		
SX2,SY2,SZ2	SOURCE PLANE CORNER	
SX3,SY3,SZ3	COORDINATES	CM
SX4,SY4,SZ4		
NB	NUMBER OF ATTENUATING BONES	-
XIBON(I)	INITIAL X COORDINATE OF BONE I	CM
XFBON(I)	FINAL X COORDINATE OF BONE I	CM
YBONE(I)	INITIAL Y COORDINATE OF BONE I	CM
ZBONE(I)	INITIAL Z COORDINATE OF BONE I	CM
RBONE(I)	RADIUS OF BONE I	CM
MUAIR	AIR LINEAR ATTENUATION COEFF.	CM-1
MUTIS	TISSUE LINEAR ATTENUATION COEFF.	CM-1
MUBON	BONE LINEAR ATTENUATION COEFF.	CM-1
MUCOL	COLL. MATERIAL LINEAR ATTEN. COEFF.	CM-1
SIGMA	SOURCE ACTIVITY PER UNIT GRID	PHOTONS/TIME/SQ. CM
GREN	GAMMA RAY ENERGY	KEV

INPUT OF INITIAL MODEL PARAMETERS

```

WRITE(ILU,90)
READ(ILU,*) ISCN
WRITE(ILU,91)
READ(ILU,92) (DATE(I),I=1,9)
WRITE(6,93) ISCN,(DATE(I),I=1,9)
WRITE(ILU,100)
READ(ILU,*) CRR
WRITE(6,200) CRR
WRITE(6,201)
WRITE(ILU,103)
READ(ILU,*) H,R1,R2,R0
WRITE(6,2031) H,R1,R2
T=R0-R2
WRITE(6,2032) T
2 WRITE(ILU,106)

```





```

READ(ILU,*) SX1,SY1,SZ1
WRITE(6,206) SX1,SY1,SZ1
WRITE(ILU,107)
READ(ILU,*) SX2,SY2,SZ2
WRITE(6,207) SX2,SY2,SZ2
WRITE(ILU,108)
READ(ILU,*) SX3,SY3,SZ3
WRITE(6,208) SX3,SY3,SZ3
WRITE(ILU,109)
READ(ILU,*) SX4,SY4,SZ4
WRITE(6,209) SX4,SY4,SZ4
WRITE(ILU,105)
READ(ILU,*) TSCFS
WRITE(6,205) TSCFS
WRITE(ILU,110)
READ(ILU,*) NB
IF(NB,EQ,0) GOTO 3
WRITE(6,210) NB
WRITE(ILU,111)
DO 4 I=1,NB
WRITE(ILU,112) I
READ(ILU,*) XIBON(I),XFBON(I),YBONE(I),ZBONE(I),RBONE(I)
WRITE(6,212) I,XIBON(I),XFBON(I),YBONE(I),ZBONE(I),RBONE(I)
4 CONTINUE
GOTO 5
3 WRITE(6,211)
5 WRITE(ILU,1040)
WRITE(ILU,1041)
READ(ILU,*) MUAIR
WRITE(ILU,1042)
READ(ILU,*) MUTIS
WRITE(ILU,1043)
READ(ILU,*) MUBON
WRITE(ILU,1044)
READ(ILU,*) MUCOL
WRITE(6,2040)
WRITE(6,2041) MUAIR
WRITE(6,2042) MUTIS
WRITE(6,2043) MUBON
WRITE(6,2044) MUCOL
WRITE(ILU,114)
READ(ILU,*) SIGMA
WRITE(6,214) SIGMA
WRITE(ILU,115)
READ(ILU,*) GREN
WRITE(6,215) GREN
WRITE(6,250)

```

C  
C  
C

```

90 FORMAT(1X,"ENTER SCAN NUMBER:  ")
91 FORMAT(1X,"ENTER DATE:  ")
92 FORMAT(9A2)
100 FORMAT(1X,"CRYSTAL RADIUS? (CM):  ")
1019 FORMAT(1X,"ENTER COLLIMATOR HEIGHT (CM):  ")
103 FORMAT(1X,"ENTER HEIGHT, CRYSTAL END RADIUS , FACE END",
2" RADIUS AND OUTSIDE RADIUS"/" OF COLLIMATOR IN THAT ORDER",
3" (CM):  ")
1040 FORMAT(1X,"LINEAR ATTENUATION COEFFICIENTS USED (CM-1):")
1041 FORMAT(1X,"AIR:  ")

```



```

1042 FORMAT(1X,"TISSUE:  ")
1043 FORMAT(1X,"BONE:  ")
1044 FORMAT(1X,"COLLIMATOR MATERIAL:  ")
105  FORMAT(1X,"TISSUE SURFACE - CRYSTAL FACE SEPARATION? (CM):  ")
106  FORMAT(1X,"X,Y,Z COORDINATES OF SOURCE PLANE PT. P1? (CM):  ")
107  FORMAT(1X,"P2?:  ")
108  FORMAT(1X,"P3?:  ")
109  FORMAT(1X,"P4?:  ")
110  FORMAT(1X,"NO. OF CYLINDRICAL BONES DESIRED, PARALLEL TO",
2" X AXIS BETWEEN SOURCE"/" AND CRYSTAL?:  ")
111  FORMAT(1X,"ENTER INITIAL AND FINAL X VALUES; INITIAL",
2" Y AND Z VALUES; AND THE RADIUS  FOR EACH BONE (CM): ")
112  FORMAT(1X,"BONE # ",I1,"":  ")
113  FORMAT(1X,"ENTER LINEAR ATTENUATION COEFFICIENT OF BONE",
2" FOR DESIRED"/" GAMMA RAY ENERGY (CM-1):  ")
114  FORMAT(1X,"SOURCE ACTIVITY PER UNIT GRID (PHOTONS/UNIT TIME)",
2":  ")
115  FORMAT(1X,"GAMMA RAY ENERGY OF SOURCE PLANE? (KEV):  ")

```

C  
C

```

93  FORMAT("1",10X,"SCAN # ",I3,20X,9A2,5(/1X))
200  FORMAT("0","THE CRYSTAL RADIUS IS ",F6.3," CM")
2011 FORMAT("0","THE COLLIMATOR SHAPE IS CYLINDRICAL")
2031 FORMAT("0","COLLIMATOR HEIGHT:",F6.3," CM;"," CRYSTAL",
2" END RADIUS:",F6.3," CM;"/" FACE END RADIUS:",F6.3,
3" CM")
2032 FORMAT("0","THE FACE END THICKNESS OF THE COLLIMATOR IS ",
2F6.2," CM")
2040 FORMAT("0","LINEAR ATTENUATION COEFFICIENTS USED"
2," (CM-1):")
2041 FORMAT(1X,26X,"AIR: ",F9.6)
2042 FORMAT(1X,23X,"TISSUE: ",F9.6)
2043 FORMAT(1X,25X,"BONE: ",F9.6)
2044 FORMAT(1X,10X,"COLLIMATOR MATERIAL: ",F9.6)
205  FORMAT("0","TISSUE SURFACE - CRYSTAL FACE SEPARATION: ",
2F6.3," CM")
206  FORMAT("0","X,Y,Z COORDINATES OF SOURCE PLANE PT. P1: ",
23F8.3," (CM)")
207  FORMAT(1X,38X,"P2: ",3F8.3," (CM)")
208  FORMAT(1X,38X,"P3: ",3F8.3," (CM)")
209  FORMAT(1X,38X,"P4: ",3F8.3," (CM)")
210  FORMAT("0","THERE ARE",I2," BONES BETWEEN SOURCE AND",
2" CRYSTAL TO ACT AS ABSORBERS AND SCATTERERS")
211  FORMAT("0","THERE ARE NO BONE ABSORBERS USED IN THIS",
2" SIMULATION")
212  FORMAT(1X," BONE #",I1," XI:",F7.3," XF:",F7.3,
2" YI:",F7.3," ZI:",F7.3," RADIUS:",F7.3," (CM)")
214  FORMAT("0","SOURCE ACTIVITY PER UNIT GRID AREA USED:",
2F10.1," PHOTONS/UNIT TIME")
215  FORMAT("0","SOURCE GAMMA RAY ENERGY USED:",F8.2," KEV")
250  FORMAT("1"," ")
251  FORMAT("0","EXECUTION STARTED AT: ",I3," HRS ",I3," MINS ",
2I3," SECS"/1X,10X,"STOPPED AT: ",I3," HRS ",I3," MINS ",
3I3," SECS")
300  FORMAT(/)
301  FORMAT(1X,I6)
500  FORMAT(I5)
501  FORMAT(1X,6F8.3)

```

C  
C



# INITIALIZING DETECTOR POINT PARAMETERS

```

CALL EXEC(11,IT1)
INC=CRR/0.2 + 0.5
INU=5.0*INC/13.0 + 0.5
XINC=INC*1.0/2.0
IINC=INC/2
XINU=INU*1.0/2.0
IINU=INU/2
IF(XINC.LE.IINC) INC=INC+1
IF(XINU.LE.IINU) INU=INU+1

```

```

ICRXI=INC/2
ICRYI=INU/2
DZ=0.0
XC=100.0
YC=100.0

```

## INITIALIZING SOURCE POINT PARAMETERS

```

NTL=(SQRT((SX2-SX1)**2+(SY2-SY1)**2+
2(SZ2-SZ1)**2))/0.5 + 0.5
NTW=(SQRT((SX3-SX2)**2+(SY3-SY2)**2+
2(SZ3-SZ2)**2))/1.0 + 0.5
NKL=NTL+1
NKW=NTW+1

```

```

DO 9 KW=1,NKW
TW=(KW-1)*1.0/NTW*1.0
X1=SX1+(SX4-SX1)*TW
Y1=SY1+(SY4-SY1)*TW
Z1=SZ1+(SZ4-SZ1)*TW
X2=SX2+(SX3-SX2)*TW
Y2=SY2+(SY3-SY2)*TW
Z2=SZ2+(SZ3-SZ2)*TW
IS=0

```

```

DO 10 KL=1,NKL
TL=(KL-1)*1.0/NTL*1.0
SX=X1+(X2-X1)*TL
SY=Y1+(Y2-Y1)*TL
SZ=Z1+(Z2-Z1)*TL

```

```

RHO=SQRT((SX-XC)**2+(SY-YC)**2)
CALL SOL(CRR,SZ,RHO,36,SOLAN)
WRITE(6,501) SOLAN
IS=IS+1

```

```

J=-1
JJ=1
SR=0.0
JD=0
WT=0.0

```





C  
C  
C        MAIN CONTROLLING SEGMENT

DO 50 IX=1,INC  
DX=(-ICRXI + (IX-1))\*0.4 + 100.0  
IF(JJ,GE,INC) GOTO 7  
J=J+1  
II=(ICRYI+J)\*2 + 1  
IF(II,LE,INC) GOTO 6  
JJ=JJ+1

C  
7    J=J-1  
     II=II-2  
6    DO 8 IY=1,II  
     DY=(-(ICRYI+J) + (IY-1))\*0.4 + 100.0  
     JD=JD+1

C  
     A=DX-XC  
     B=DY-YC  
     ALP=SX-DX  
     BET=SY-DY  
     GAM=SZ-DZ

C  
     W=GAM/(ALP\*\*2+BET\*\*2+GAM\*\*2)\*\*1.5  
     WT=W+WT  
     U=W\*SULAN\*SIGMA

C  
     IF(NB,EQ,0) GOTO 40  
     BONAT=0.0  
     XBONT=0.0  
     DO 41 JB=1,NB  
     BR=DY-YBONE(JB)  
     BC=DZ-ZBONE(JB)  
     RB=RBONE(1)  
     CALL BTH(RB,BB,BC,BET,GAM,BONTH)  
     BONAT=EXP(-MUBON\*BONTH) + BONAT  
     XBONT=XBONT+BONTH

41    CONTINUE  
     GOTO 42

40    BONAT=1.0  
     XBONT=0.0

42    CALL TTH(TSCFS,DX,DY,DZ,SX,SY,SZ,ALP,BET,GAM,TISTH,XBONT)  
     WRITE(6,2042) TISTH  
     TISAT=EXP(-MUTIS\*TISTH)  
     GOTO 11

16    COLAT=EXP(-MUCOL\*COLTH)  
     WRITE(6,2044) COLTH  
     CALL ATH(ALP,BET,GAM,AIRTH,TISTH,BONTH,COLTH)  
     AIRAT=EXP(-MUAIR\*AIRTH)  
     WRITE(6,2041) AIRTH  
     GOTO 12

11    IF(R2-R1) 13,14,15  
13    CALL CCTH(DX,DY,DZ,SX,SY,SZ,A,B,C,ALP,BET,GAM,T,R1,R2,H,COLTH)  
     GOTO 16  
14    CALL CSTH(DX,DY,DZ,SX,SY,SZ,A,B,C,ALP,BET,GAM,T,R1,R2,H,COLTH)  
     GOTO 16  
15    CALL CDTH(DX,DY,DZ,SX,SY,SZ,A,B,C,ALP,BET,GAM,T,R1,R2,H,COLTH)  
     GOTO 16  
12    AFIN=Q\*BONAT\*TISAT\*COLAT\*AIRAT  
     DR(JD)=AFIN + DR(JD)





```
SR=AFIN + SR
```

```
C
```

```
8 CONTINUE
50 CONTINUE
```

```
C
```

```
C
```

```
C
```

```
SUM OVER INDIVIDUAL MATRIX INDICES AND DUMP
ON PAPER TAPE
```

```
IF(JD,GT,50) STOP
```

```
DO 17 JX=1,JD
```

```
IDR(JX)=OR(JX)/WT
```

```
17 CONTINUE
```

```
ISR(IS)=SR/WT
```

```
C
```

```
IF(ISR(IS).LE.,0) GOTO 10
```

```
WRITE(6,301) ISR(IS)
```

```
C
```

```
10 CONTINUE
```

```
WRITE(4,500) (ISR(III),III=1,NKL)
```

```
9 CONTINUE
```

```
C
```

```
WRITE(4,500) (IDR(III),III=1,JD)
```

```
CALL EXEC(3,1004B)
```

```
CALL EXEC(11,IT2)
```

```
C
```

```
WRITE(6,251) IT1(4),IT1(3),IT1(2),IT2(4),IT2(3),IT2(2)
```

```
WRITE(6,300)
```

```
STOP
```

```
END
```

```
C
```

```
C
```

```
C
```

```
C
```

```
C
```

```
SOLID ANGLE SUBROUTINE
```

```
SUBROUTINE SOL(R,H,RHO,NC,SOLAN)
```

```
DIMENSION E(90),F(90),G(90),D(90),EM(90),
2Y(90),X(90)
```

```
N=NC
```

```
PI=3.1415926
```

```
N2=(N-2)/2
```

```
XN=N
```

```
N4=N/4
```

```
N6=(N+6)/4
```

```
N444=(N+4)/4
```

```
B0=SIN(PI/XN)
```

```
N21=N2+1
```

```
N24=(N-2)/4
```

```
N44=(N-4)/4
```

```
N241=N24+1
```

```
SRR=(PI/XN)*(B0/COS(PI/XN))
```

```
IF(SRR.LT.,0.,0) STOP1
```

```
XP=2.*R*SQR(SRR)
```

```
C
```

```
DETERMINE IF N/2 IS ODD OR EVEN
```

```
XN2=N/4
```

```
XNN=XN-4.*XN2
```

```
IF(XNN)20,10,20
```

```
C
```

```
ODD,EVEN,ODD
```

```
C
```

```
CALCULATION OF D(IR) IF N/2 EVEN
```

```
10 DO 13 IR=1,N44
```

```
XIR=IR
```

```
13 D(IR)=XP/2.,0+XP*SIN(PI/4.,0-PI*XIR/XN)*
```



```

2 SIN(PI*XIR/XN+PI/4,0-PI/XN)/BO
D(N4)=XP/2,0
DO 14 IR=N444,N21
IRR=(N+2)/2-IR
14 D(IR)=-D(IRR)
GO TO 30
C CALCULATION OF D(IR) IF N/2 ODD
20 DO 21 IR=1,N24
XIR=IR
21 D(IR)=XP*SIN(PI/4,0-PI/(2,0*XN)+PI*XIR/XN)*
2 SIN(PI/4,0-PI/(2,0*XN)+PI*XIR/XN)/BO
D(N241)=0,0
DO 22 IR=N6,N21
IRR=(N+2)/2-IR
22 D(IR)=-D(IRR)
30 CONTINUE
DO 31 IR=1,N2
XIR=IR
31 EM(IR)=SIN(((XN-4,0*XIR)*PI)/(2,0*XN))/
2 COS(((XN-4,0*XIR)*PI)/(2,0*XN))
DO 35 IR=1,N2
XIR=IR
35 Y(IR)=(XP/2,0)*SIN((2,0*XIR-1,0)*PI/XN)/BO
DO 39 IR=1,N21
39 X(IR)=RHO-D(IR)
DO 41 IR=1,N2
TOP=H*SQR(X(IR)**2+Y(IR)**2+H**2)
BOT=EM(IR)*(X(IR)**2+H**2)-X(IR)*Y(IR)
F(IR)=ATAN(TOP/BOT)
IF(F(IR))50,41,41
50 F(IR)=F(IR)+PI
41 CONTINUE
DO 45 IR=1,N2
SRR=X(IR+1)**2+Y(IR)**2-2,0*EM(IR)*
2 X(IR)*Y(IR)+(EM(IR)**2)*(X(IR)**2)+H*H+
3 (EM(IR)**2)*(X(IR+1)**2)+2,0*EM(IR)*X(IR+1)*
4 Y(IR)-2,0*(EM(IR)**2)*X(IR+1)*X(IR)
IF(SRR.LT.0,0) STOP2
TOP=H*SQR(SRR)
BOT=EM(IR)*(H*H+X(IR+1)*X(IR))-X(IR+1)*Y(IR)
E(IR)=ATAN(TOP/BOT)
IF(E(IR))51,45,45
51 E(IR)=E(IR)+PI
45 CONTINUE
DO 42 IR=1,N2
42 G(IR)=E(IR)-F(IR)
SOLAN=0,0
DO 43 IR=1,N2
43 SOLAN=SOLAN+2,0*G(IR)
RETURN
END
C
C
C BONE THICKNESS SUBROUTINE
C
SUBROUTINE BTH(RB,BB,BC,BET,GAM,BONTH)
TEST=(RB**2)*(BET**2+GAM**2)-(BET*BC-GAM*BB)**2
IF(TEST) 1,1,2
1 BONTH=0,0

```



```

RETURN
2 BONT=2.0*SQRT(TEST)/(BET**2+GAM**2)
RETURN
END

```

# TISSUE THICKNESS SUBROUTINE

```

SUBROUTINE TTH(TSCFS,DX,DY,DZ,SX,SY,SZ,ALP,BET,GAM,TISTH,XBONT)
IF(TSCFS.LT.SZ) GOTO 1
TISTH=0.0
RETURN
1 AX=DX+ALP*(TSCFS-DZ)/GAM
  AY=DY+BET*(TSCFS-DZ)/GAM
  SRR=((SX-AX)**2+(SY-AY)**2+(SZ-TSCFS)**2)
  TISTH=SQRT(SRR)-XBONT
100 FORMAT(1X,E10.6)
RETURN
END

```

# CYLINDRICAL CONVERGING COLLIMATOR SUBROUTINE

```

SUBROUTINE CCTH(DX,DY,DZ,SX,SY,SZ,A,B,C,ALP,BET,GAM,T,R1,R2,H,
2COLTH)
RD=R2+1
R=((R1-R2)/H)**2
D=H*R1/(R1-R2)
C=-D
ENUM1=-A*ALP-B*BET+R*C*GAM
SRR=R*(A*GAM-C*ALP)**2+R*(B*GAM-C*BET)**2-(A*BET-B*ALP)**2
IF(SRR.LT.0.0) STOP4
ENUM2=SQRT(SRR)
EDEN=ALP**2+BET**2-R*(GAM**2)

TEPL=(ENUM1+ENUM2)/EDEN
TEMI=(ENUM1-ENUM2)/EDEN
WRITE(6,100) DX,DY,DZ,SX,SY,SZ
WRITE(6,100) A,B,C,ALP,BET,GAM
WRITE(6,100) R,D,ENUM1,ENUM2,EDEN,SRR,TEPL,TEMI
100 FORMAT(1X,10F8.3)
EZ=DZ+GAM*TEPL
IF(EZ) 1,1,2
1 EZ=DZ+GAM*TEMI
7 IF(EZ-H) 5,6,6

2 EZ2=DZ+GAM*TEMI
  IF(EZ2) 7,7,3
3 IF(EZ2-EZ) 4,7,7
4 EZ=EZ2
  GOTO 7
6 COLTH=0.0
RETURN

5 TEPAR=(EZ-DZ)/GAM
  EX=DX+ALP*TEPAR

```



LY=DY+BET\*TEPAR

FNUM1=-(A\*ALP+B\*BET)  
 SRR=RD\*\*2\*(ALP\*\*2+BET\*\*2)-(A\*BET-B\*ALP)\*\*2  
 IF(SRR,LT,0,0) STOP5  
 FNUM2=SQRT(SRR)  
 FDEN=ALP\*\*2+BET\*\*2

IF(FDEN,EN,0,0) GOTO 13  
 TFPL=(FNUM1+FNUM2)/FDEN  
 TFM1=(FNUM1-FNUM2)/FDEN  
 FZ=DZ+GAM\*TFPL

IF(FZ) 10,10,12  
 10 FZ=DZ+GAM\*TFM1  
 12 IF(FZ=H) 11,13,13

11 TFPAR=(FZ-DZ)/GAM

FX=DX+ALP\*TFPAR  
 FY=DY+BET\*TFPAR  
 GOTO 14

13 FX=DX+ALP\*(H-DZ)/GAM  
 FY=DY+BET\*(H-DZ)/GAM  
 FZ=H

14 COLTH=SQRT((FX-EX)\*\*2+(FY-EY)\*\*2+(FZ-EZ)\*\*2)  
 RETURN  
 END

# CYLINDRICAL STRAIGHT COLLIMATOR SUBROUTINE

SUBROUTINE CSTH(DX,DY,DZ,SX,SY,SZ,A,B,C,ALP,BET,GAM,T,R1,R2,H,  
 2COLTH)

R=R1  
 C=0,0  
 XNUM1=-(A\*ALP+B\*BET)  
 DEN=ALP\*\*2+BET\*\*2  
 IF(DEN,EN,0,0) GOTO 6  
 1 SRR=R\*\*2\*(ALP\*\*2+BET\*\*2)-(A\*BET-B\*ALP)\*\*2  
 IF(SRR,LT,0,0) STOP3  
 XNUM2=SQRT(SRR)

TPL=(XNUM1+XNUM2)/DEN  
 TMI=(XNUM1-XNUM2)/DEN  
 WRITE(6,100) R,XNUM1,XNUM2,DEN,SRR,TPL,TMI  
 100 FORMAT(1X,10F8.3)

IF(R-R1) 2,2,3  
 2 EZ=DZ+GAM\*TPL  
 IF(EZ) 4,4,5  
 4 EZ=DZ+GAM\*TMI  
 5 IF(EZ=H) 7,6,6  
 6 COLTH=0,0  
 RETURN







```

7  TEPAR=(EZ-DZ)/GAM
   EX=DX+ALP*TEPAR
   EY=DY+BET*TEPAR
   R=R1+T
   GOTO 1

```

```

3  FZ=DZ+GAM*TPL
   IF(FZ) 8,8,9
8  FZ=DZ+GAM*TM1
9  IF(FZ-H) 10,11,11

```

```

10 TEPAR=(FZ-DZ)/GAM
   FX=DX+ALP*TEPAR
   FY=DY+BET*TEPAR
   GOTO 12

```

```

11 FX=DX+ALP*(H-DZ)/GAM
   FY=DY+BET*(H-DZ)/GAM
   FZ=H

```

```

12 COLTH=SQRT((FX-EX)**2+(FY-EY)**2+(FZ-EZ)**2)
   RETURN
   END

```

# CYLINDRICAL DIVERGING COLLIMATOR SUBROUTINE

```

SUBROUTINE CDTH(DX,DY,DZ,SX,SY,SZ,A,B,C,ALP,BET,GAM,T,R1,R2,H,
2COLTH)

```

```

   RO=R2+T
   R=((R2-R1)/H)**2
   D=H*R2/(R2-R1)
   C=D-H

```

```

   ENUM1=-(A*ALP+B*BET-R*C/GAM)
   SRR=R*(A*GAM-C*ALP)**2+R*(B*GAM-C*BET)**2
2-(A*BET-B*ALP)**2
   IF(SRR,LT.0.0) STOP6
   ENUM2=SQRT(SRR)
   EDEN=ALP**2+BET**2-R*GAM**2

```

```

   TEPL=(ENUM1+ENUM2)/EDEN
   TEMI=(ENUM1-ENUM2)/EDEN

```

```

   EZ=DZ+GAM*TEPL
   IF(EZ) 1,1,2
1  EZ=DZ+GAM*TEMI
   IF(EZ) 6,6,2
6  COLTH=0.0
   RETURN

```

```

2  IF(EZ-H) 3,6,6

```

```

3  TEPAR=(EZ-DZ)/GAM
   EX=DX+ALP*TEPAR
   EY=DY+BET*TEPAR

```



```

FNUM1=- (A*ALP+B*BET)
SRR=RD**2*(ALP**2+BET**2)-(A*BET-B*ALP)**2
IF(SRR.LT.0.0) STOP7
FNUM2=SQRT(SRR)
FDEN=ALP**2+BET**2

```

```

C
TFPL=(FNUM1+FNUM2)/FDEN
TFMI=(FNUM1-FNUM2)/FDEN

```

```

FZ=DZ+GAM*TFPL

```

```

IF(FZ) 10,10,12

```

```

10 FZ=DZ+GAM*TFMI

```

```

C
12 IF(FZ-H) 11,13,13

```

```

11 TFPAR=(FZ-DZ)/GAM

```

```

C
FX=DX+ALP*TFPAR

```

```

FY=DY+BET*TFPAR

```

```

GOTO 14

```

```

C
13 FX=DX+ALP*(H-DZ)/GAM

```

```

FY=DY+BET*(H-DZ)/GAM

```

```

FZ=H

```

```

C
14 COLTH=SQRT((FX-EX)**2+(FY-EY)**2+(FZ-EZ)**2)

```

```

RETURN

```

```

END

```

# AIR THICKNESS SUBROUTINE

```

SUBROUTINE ATH(ALP,BET,GAM,AIRTH,TISTH,BONTH,COLTH)

```

```

DIS=SQRT(ALP**2+BET**2+GAM**2)

```

```

AIRTH=DIS-TISTH-BONTH-COLTH

```

```

RETURN

```

```

END

```

```

END$

```



## RECTANGULAR COLLIMATOR MODELLING

## PROGRAM

FTN

```

PROGRAM RCMOD
DIMENSION XIBON(9),XFBON(9),YBONE(9),ZBONE(9),RBONE(9),DR(50)
INTEGER LU(5),DATE(9),TAPE,ISR(100),IDR(50),IT1(5),IT2(5)
REAL L1,L2,MGI,NGI,KGI,MHI,NHI,KHI,MJI,NJI,KJI,MII,NII,KII
REAL MGO,NGO,KGO,MHO,NHO,KHO,MIO,NIO,KIO,MJO,NJO,KJO
REAL MUAIR,MUTIS,MUBON,MUCOL
COMMON DX,DY,DZ,SX,SY,SZ,A,B,C,ALP,BET,GAM,T,R1,R2,H,RB,TSCFS
COMMON CULTH,AIRTH,TISTH,BONTH,MGI,NGI,PGI,KGI,MGO,NGO,PGO,KGO
COMMON MHI,NHI,PHI,KHI,MHO,NHO,PHO,KHO,MII,NII,PII,KII,MIO,NIO
COMMON PIO,KIO,MJI,NJI,PJI,KJI,MJO,NJO,PJO,KJO,XBONT,BB,BC
DATA ILU/1/,TAPE/9/,DR/130*0.0/
CALL RMPAR(LU)
IF(LU.GT.0) ILU=LU

```

ADDRESSES	MEANING	UNITS
CRR	CRYSTAL RADIUS	CM
H	COLLIMATOR HEIGHT	CM
L1	REC. COLL. CRYSTAL END LENGTH	CM
W1	REC. COLL. CRYSTAL END WIDTH	CM
L2	REC. COLL. FACE END LENGTH	CM
W2	REC. COLL. FACE END WIDTH	CM
T	COLLIMATOR THICKNESS	CM
TSCFS	TISSUE SURFACE-CRYSTAL FACE SEP.	CM
SX1,SY1,SZ1	SOURCE PLANE CORNER COORDINATES	CM
SX2,SY2,SZ2		
SX3,SY3,SZ3		
SX4,SY4,SZ4		
MGI,NGI,PGI,KGI	RECTANGULAR COLLIMATOR PLANE PARAMETERS	CM
MHI,NHI,PHI,KHI		
MII,NII,PII,KII		
MJI,NJI,PJI,KJI		
MGO,NGO,PGO,KGO		
MHO,NHO,PHO,KHO		
MIO,NIO,PIO,KIO		
MJO,NJO,PJO,KJO		
NB	NUMBER OF ATTENUATING BONES	-
XIBON(I)	INITIAL X COORDINATE OF BONE I	CM
XFBON(I)	FINAL X COORDINATE OF BONE I	CM
YBONE(I)	INITIAL Y COORDINATE OF BONE I	CM
ZBONE(I)	INITIAL Z COORDINATE OF BONE I	CM
RBONE(I)	RADIUS OF BONE I	CM
MUAIR	AIR LINEAR ATTENUATION COEFF.	CM-1
MUTIS	TISSUE LINEAR ATTENUATION COEFF.	CM-1
MUBON	BONE LINEAR ATTENUATION COEFF.	CM-1
MUCOL	COLL. MATERIAL LINEAR ATTEN. COEFF.	CM-1
SIGMA	SOURCE ACTIVITY PER UNIT GRID	PHOTONS/TIME/SQ.CM
GREN	GAMMA RAY ENERGY	KEV



C  
C  
C

# INPUT OF INITIAL MODEL PARAMETERS

```

WRITE(ILU,90)
READ(ILU,*) ISCN
WRITE(ILU,91)
READ(ILU,92) (DATE(I),I=1,9)
WRITE(6,93) ISCN,(DATE(I),I=1,9)
WRITE(ILU,100)
READ(ILU,*) CRR
WRITE(6,200) CRR
WRITE(6,2012)
WRITE(ILU,1019)
READ(ILU,*) H
WRITE(ILU,1020)
READ(ILU,*) MGI,NGI,PGI,KGI
WRITE(ILU,1021)
READ(ILU,*) MHI,NHI,PHI,KHI
WRITE(ILU,1022)
READ(ILU,*) MII,NII,PII,KII
WRITE(ILU,1023)
READ(ILU,*) MJI,NJI,PJI,KJI
WRITE(ILU,1024)
READ(ILU,*) MGO,NGO,PGO,KGO
WRITE(ILU,1021)
READ(ILU,*) MHO,NHO,PHO,KHO
WRITE(ILU,1022)
READ(ILU,*) MIO,NIO,PIO,KIO
WRITE(ILU,1023)
READ(ILU,*) MJU,NJU,PJU,KJU
WRITE(6,2021)
WRITE(6,2022) MGI,NGI,PGI,KGI,MHI,NHI,PHI,KHI,
2MII,NII,PII,KII,MJI,NJI,PJI,KJI
WRITE(6,2023)
WRITE(6,2022) MGO,NGO,PGO,KGO,MHO,NHO,PHO,KHO,MIO,NIO,PIO,KIO
2,MJU,NJU,PJU,KJU
L1=ABS(KHI-KJI)
L2=L1 + ABS(H*(PJI-PHI))
W1=ABS(KII-KGI)
W2=W1
T=ABS(KGI-KGO)
WRITE(6,2024) H,L1,W1,L2,W2
WRITE(6,2032) T
WRITE(ILU,106)
READ(ILU,*) SX1,SY1,SZ1
WRITE(6,206) SX1,SY1,SZ1
WRITE(ILU,107)
READ(ILU,*) SX2,SY2,SZ2
WRITE(6,207) SX2,SY2,SZ2
WRITE(ILU,108)
READ(ILU,*) SX3,SY3,SZ3
WRITE(6,208) SX3,SY3,SZ3
WRITE(ILU,109)
READ(ILU,*) SX4,SY4,SZ4
WRITE(6,209) SX4,SY4,SZ4
WRITE(ILU,105)
READ(ILU,*) TSCFS
WRITE(6,205) TSCFS
WRITE(ILU,110)
READ(ILU,*) NB

```







```

IF(NB, EQ, 0) GOTO 3
WRITE(6, 210) NB
WRITE(1LU, 111)
DO 4 I=1, NB
WRITE(1LU, 112) I
READ(1LU, *) XIBON(I), XFBON(I), YBONE(I), ZBONE(I), RBONE(I)
WRITE(6, 212) I, XIBON(I), XFBON(I), YBONE(I), ZBONE(I), RBONE(I)
4 CONTINUE
GOTO 5
3 WRITE(6, 211)
5 WRITE(1LU, 1040)
WRITE(1LU, 1041)
READ(1LU, *) MUAIR
WRITE(1LU, 1042)
READ(1LU, *) MUTIS
WRITE(1LU, 1043)
READ(1LU, *) MUBON
WRITE(1LU, 1044)
READ(1LU, *) MUCOL
WRITE(6, 2040)
WRITE(6, 2041) MUAIR
WRITE(6, 2042) MUTIS
WRITE(6, 2043) MUBON
WRITE(6, 2044) MUCOL
WRITE(1LU, 114)
READ(1LU, *) SIGMA
WRITE(6, 214) SIGMA
WRITE(1LU, 115)
READ(1LU, *) GREN
WRITE(6, 215) GREN
WRITE(6, 250)

```

C  
C  
C

```

90 FORMAT(1X, "ENTER SCAN NUMBER:  ")
91 FORMAT(1X, "ENTER DATE:  ")
92 FORMAT(9A2)
100 FORMAT(1X, "CRYSTAL RADIUS? (CM):  ")
1019 FORMAT(1X, "ENTER COLLIMATOR HEIGHT (CM):  ")
1020 FORMAT(1X, "ENTER COORDINATES OF RECTANGULAR PLANES - ", (/1X),
2" INSIDE PLANES: M N P K", (/1X), 7X,
3" PLANE G:  ")
1021 FORMAT(1X, 7X, "PLANE H:  ")
1022 FORMAT(1X, 7X, "PLANE I:  ")
1023 FORMAT(1X, 7X, "PLANE J:  ")
1024 FORMAT(1X, " OUTSIDE PLANES: M N P K", (/1X), 7X,
2" PLANE G:  ")
1040 FORMAT(1X, "LINEAR ATTENUATION COEFFICIENTS USED (CM-1):")
1041 FORMAT(1X, "AIR:  ")
1042 FORMAT(1X, "TISSUE:  ")
1043 FORMAT(1X, "BONE:  ")
1044 FORMAT(1X, "COLLIMATOR MATERIAL:  ")
105 FORMAT(1X, "TISSUE SURFACE - CRYSTAL FACE SEPARATION? (CM):  ")
106 FORMAT(1X, "X, Y, Z COORDINATES OF SOURCE PLANE PT. P1? (CM):  ")
107 FORMAT(1X, "P2?:  ")
108 FORMAT(1X, "P3?:  ")
109 FORMAT(1X, "P4?:  ")
110 FORMAT(1X, "NO. OF CYLINDRICAL BONES DESIRED, PARALLEL TO",
2" X AXIS BETWEEN SOURCE/" AND CRYSTAL?:  ")
111 FORMAT(1X, "ENTER INITIAL AND FINAL X VALUES; INITIAL",

```



```

2" Y AND Z VALUES; AND THE RADIUS   FOR EACH BONE (CM): ")
112  FORMAT(1X,"BONE # ",I1," :  ←")
113  FORMAT(1X,"ENTER LINEAR ATTENUATION COEFFICIENT OF BONE",
2" FOR DESIRED"/" GAMMA RAY ENERGY (CM-1):  ←")
114  FORMAT(1X,"SOURCE ACTIVITY PER UNIT GRID (PHOTONS/UNIT TIME)",
2" :  ←")
115  FORMAT(1X,"GAMMA RAY ENERGY OF SOURCE PLANE? (KEV):  ←")
C
C
93  FORMAT("1",10X,"SCAN # ",I3,20X,9A2,5(/1X))
200  FORMAT("0","THE CRYSTAL RADIUS IS ",F6.3," CM")
2012 FORMAT("0","THE COLLIMATOR SHAPE IS RECTANGULAR")
2021 FORMAT("0","RECTANGULAR COLLIMATOR PLANE COORDINATES:",
22(/1X),10X,"INSIDE PLANES:   M           N           P           K")
2022 FORMAT("0",22X,"G: ",4(F6.2,2X),/1X,22X,"H: "4(F6.2,2X),
2/1X,22X,"I: ",4(F6.2,2X),/1X,22X,"J: "4(F6.2,2X))
2023 FORMAT("0",9X,"OUTSIDE PLANES:   M           N           P           K")
2024 FORMAT("0","COLLIMATOR HEIGHT:",F6.3," CM;"," CRYSTAL",
2" END LENGTH:",F6.3," CM;"," WIDTH:",F6.3," CM;"/,
3" FACE END LENGTH:",F6.3," CM;"," WIDTH:",F6.3," CM")
2032 FORMAT("0","THE FACE END THICKNESS OF THE COLLIMATOR IS ",
2F6.2," CM")
2040 FORMAT("0","LINEAR ATTENUATION COEFFICIENTS USED"
2," (CM-1):")
2041 FORMAT(1X,26X,"AIR: ",F9.6)
2042 FORMAT(1X,23X,"TISSUE: ",F9.6)
2043 FORMAT(1X,25X,"BONE: ",F9.6)
2044 FORMAT(1X,10X,"COLLIMATOR MATERIAL: ",F9.6)
205  FORMAT("0","TISSUE SURFACE - CRYSTAL FACE SEPARATION: ",
2F6.3," CM")
206  FORMAT("0","X,Y,Z COORDINATES OF SOURCE PLANE PT. P1: ",
23F8.3," (CM)")
207  FORMAT(1X,38X,"P2: ",3F8.3," (CM)")
208  FORMAT(1X,38X,"P3: ",3F8.3," (CM)")
209  FORMAT(1X,38X,"P4: ",3F8.3," (CM)")
210  FORMAT("0","THERE ARE",I2," BONES BETWEEN SOURCE AND",
2" CRYSTAL TO ACT AS ABSORBERS AND SCATTERERS")
211  FORMAT("0","THERE ARE NO BONE ABSORBERS USED IN THIS",
2" SIMULATION")
212  FORMAT(1X," BONE #",I1," XI:",F7.3," XF:",F7.3,
2" YI:",F7.3," ZI:",F7.3," RADIUS:",F7.3," (CM)")
214  FORMAT("0","SOURCE ACTIVITY PER UNIT GRID AREA USED:",
2F10.1," PHOTONS/UNIT TIME")
215  FORMAT("0","SOURCE GAMMA RAY ENERGY USED:",F8.2," KEV")
250  FORMAT("1"," ")
251  FORMAT("0","EXECUTION STARTED AT: ",I3," HRS ",I3," MINS ",
213," SECS"/1X,10X,"STOPPED AT: ",I3," HRS ",I3," MINS ",
313," SECS")
300  FORMAT(/)
301  FORMAT(1X,I6)
500  FORMAT(I5)

```

INITIALIZING DETECTOR POINT PARAMETERS

```

CALL EXEC(11,IT1)
INC=CRK/0.2 + 0.5
INU=0.0*INC/13.0 + 0.5

```



```

XINC=INC*1.0/2.0
IINC=INC/2
XINU=INU*1.0/2.0
IINU=INU/2
IF(XINC.LE.IINC) INC=INC+1
IF(XINU.LE.IINU) INO=INO+1

```

```

ICRXI=INC/2
ICRYI=INO/2
OZ=0.0
ZC=0.0
XC=100.0
YC=100.0

```

# INITIALIZING SOURCE POINT PARAMETERS

```

NTL=(SQRT((SX2-SX1)**2+(SY2-SY1)**2+
2(SZ2-SZ1)**2))/0.5 + 0.5
NTW=(SQRT((SX3-SX2)**2+(SY3-SY2)**2+
2(SZ3-SZ2)**2))/1.0 + 0.5
NKL=NTL+1
NKW=NTW+1

```

```

DO 9 KW=1,NKW
TW=(KW-1)*1.0/NTW*1.0
X1=SX1+(SX4-SX1)*TW
Y1=SY1+(SY4-SY1)*TW
Z1=SZ1+(SZ4-SZ1)*TW
X2=SX2+(SX3-SX2)*TW
Y2=SY2+(SY3-SY2)*TW
Z2=SZ2+(SZ3-SZ2)*TW
IS=0

```

```

DO 10 KL=1,NKL
TL=(KL-1)*1.0/NTL*1.0
SX=X1+(X2-X1)*TL
SY=Y1+(Y2-Y1)*TL
SZ=Z1+(Z2-Z1)*TL

```

```

RHO=SQRT((SX-XC)**2+(SY-YC)**2)
CALL SOL(CRR,SZ,RHO,36,SOLAN)
IS=IS+1

```

```

J=-1
JJ=1
SP=0.0
JD=0
WT=0.0

```

# MAIN CONTROLLING SEGMENT

```

DO 50 IX=1,INC
DX=(-ICRXI + (IX-1))*0.4 + 100.0
IF(JJ.GE.INO) GOTO 7
J=J+1

```





```

II=(ICRYI+J)*2 + 1
IF(II,LE,INC) GOTO 6
JJ=JJ+1

```

```

7 J=J-1
II=II-2
8 DO 8 IY=1,II
DY=(-(ICRYI+J) + (IY-1))*0.4 + 100.0
JD=JD+1

```

```

A=DX-XC
B=DY-YC
C=DZ-ZC
ALP=SX-DX
BET=SY-DY
GAM=SZ-DZ

```

```

K=GAM/(ALP**2+BET**2+GAM**2)**1.5
WT=K+WT
Q=W*SOLAN*SIGNA

```

```

IF(NB,EQ,0) GOTO 40
BONAT=0.0
XBUNT=0.0
DO 41 JB=1,NB
BR=DY-YBONE(JB)
BC=DZ-ZBONE(JB)
RB=RBONE(1)
CALL BTH
BONAT=EXP(-MUBON*BUNTH) + BONAT
XBUNT=XBUNT+BUNTH
41 CONTINUE
GOTO 42
40 BONAT=1.0
XBUNT=0.0
42 CALL TTH
TISAT=EXP(-MUTIS*TISTH)
CALL RTH
COLAT=EXP(-MUCOL*COLTH)
CALL ATH
AIRAT=EXP(-MUAIR*AIRTH)
AFIN=Q*BONAT*TISAT*COLAT*AIRAT
DR(JD)=AFIN + DR(JD)
SR=AFIN + SR

```

```

8 CONTINUE
50 CONTINUE

```

```

SUM OVER INDIVIDUAL MATRIX INDICES AND DUMP
ON PAPER TAPE

```

```

IF(JD.GT.50) STOP
DO 17 JX=1,JD
IDR(JX)=DR(JX)/WT
17 CONTINUE
ISR(IS)=SR/WT

```

```

IF(ISR(IS).LE.0) GOTO 10
WRITE(6,301) ISR(IS)

```





```

10 CONTINUE
  WRITE(4,500) (ISR(III),III=1,NKL)
9 CONTINUE

```

```

  WRITE(4,500) (IDR(III),III=1,JD)
  CALL EXEC(3,1004B)
  CALL EXEC(11,IT2)

```

```

  WRITE(6,251) IT1(4),IT1(3),IT1(2),IT2(4),IT2(3),IT2(2)
  WRITE(6,300)
  STOP
  END

```

# SOLID ANGLE SUBROUTINE

```

SUBROUTINE SOL(R,H,RHO,NC,SOLAN)
  DIMENSION E(90),F(90),G(90),D(90),EM(90),
  2Y(90),X(90)

```

```

  N=NC
  PI=3.1415926
  N2=(N-2)/2
  XN=N
  N4=N/4
  N6=(N+6)/4
  N44=(N+4)/4
  B0=SIN(PI/XN)
  N21=N2+1
  N24=(N-2)/4
  N44=(N-4)/4
  N241=N24+1
  SRR=(PI/XN)*(B0/COS(PI/XN))
  IF(SRR.LT.0.0) STOP1
  XP=2.*R*SQRT(SRR)

```

```

  DETERMINE IF N/2 IS ODD OR EVEN

```

```

  XN2=N/4
  XNN=XN-4.*XN2
  IF(XNN)20,10,20

```

```

  ODD,EVEN,ODD

```

```

  CALCULATION OF D(IR) IF N/2 EVEN

```

```

10 DO 13 IR=1,N44
  XIR=IR

```

```

13 D(IR)=XP/2.*XP*SIN(PI/4.*N-PI*XIR/XN)*
  2SIN(PI*XIR/XN+PI/4.*N-PI/XN)/B0
  D(N4)=XP/2.*

```

```

  DO 14 IR=N44,N21

```

```

  IPR=(N+2)/2-IR

```

```

14 D(IR)=-D(IPR)

```

```

  GO TO 30

```

```

  CALCULATION OF D(IR) IF N/2 ODD

```

```

20 DO 21 IR=1,N24
  XIR=IR

```

```

21 D(IR)=XP*SIN(PI/4.*N-PI/(2.*XN)+PI*XIR/XN)*
  2SIN(PI/4.*N-PI/(2.*XN)+PI*XIR/XN)/B0
  D(N241)=0.0

```

```

  DO 22 IR=N6,N21

```

```

  IPR=(N+2)/2-IR

```

```

22 D(IR)=-D(IPR)

```

```

30 CONTINUE

```



```

      DO 31 IR=1,N2
      XIR=IR
31  EM(IR)=SIN(((XN-4.0*XIR)*PI)/(2.0*XN))/
      2COS(((XN-4.0*XIR)*PI)/(2.0*XN))
      DO 35 IR=1,N2
      XIR=IR
35  Y(IR)=(XP/2.0)*SIN((2.0*XIR-1.0)*PI/XN)/BO
      DO 39 IR=1,N21
39  X(IR)=RHU-D(IR)
      DO 41 IR=1,N2
      TOP=H*SQRT(X(IR)**2+Y(IR)**2+H**2)
      BOT=EM(IR)*(X(IR)**2+H**2)-X(IR)*Y(IR)
      F(IR)=ATAN(TOP/BOT)
      IF(F(IR))50,41,41
50  F(IR)=F(IR)+PI
41  CONTINUE
      DO 45 IR=1,N2
      SRR=X(IR+1)**2+Y(IR)**2-2.0*EM(IR)*
      2X(IR)*Y(IR)+(EM(IR)**2)*(X(IR)**2)+H*H+
      3(EM(IR)**2)*(X(IR+1)**2)+2.0*EM(IR)*X(IR+1)*
      4Y(IR)-2.0*(EM(IR)**2)*X(IR+1)*X(IR)
      IF(SRR.LT.0.0) STOP2
      TOP=H*SQRT(SRR)
      BOT=EM(IR)*(H*H+X(IR+1)*X(IR))-X(IR+1)*Y(IR)
      E(IR)=ATAN(TOP/BOT)
      IF(E(IR))51,45,45
51  E(IR)=E(IR)+PI
45  CONTINUE
      DO 42 IR=1,N2
42  G(IR)=E(IR)-F(IR)
      SOLAN=0.0
      DO 43 IR=1,N2
43  SOLAN=SOLAN+2.0*G(IR)
      RETURN
      END

```

# BONE THICKNESS SUBROUTINE

```

SUBROUTINE BTH
REAL L1,L2,MGI,NGI,KGI,MHI,NHI,KHI,MII,NII,KII,MJI,NJI,KJI
REAL MGO,NGO,KGO,MHO,NHO,KHO,MIO,NIO,KIO,MJJO,NJO,KJO
REAL MUAIR,MUTIS,MUBON,MUCOL
COMMON DX,DY,DZ,SX,SY,SZ,A,B,C,ALP,BET,GAM,T,R1,R2,H,RB,TSCFS
COMMON COLTH,AIRTH,TISTH,BONTH,MGI,NGI,PGI,KGI,MGO,NGO,PGO,KGO
COMMON MHI,NHI,PHI,KHI,MHO,NHO,PHO,KHO,MII,NII,PII,KII,MIO,NIO
COMMON PIO,KIO,MJI,NJI,PJI,KJI,MJO,NJO,PJO,KJO,XBONT,BB,BC
TEST=(RB**2)*(BET**2+GAM**2)-(BET*BC-GAM*BB)**2
IF(TEST) 1,1,2
1  BONTH=0.0
  RETURN
2  BONTH=2.0*SQRT(TEST)/(BET**2+GAM**2)
  RETURN
END

```

# TISSUE THICKNESS SUBROUTINE



## SUBROUTINE TTH

```

REAL L1,L2,MGI,NGI,KGI,MHI,NHI,KHI,MII,NII,KII,MJI,NJI,KJI
REAL MGO,NGO,KGO,MHO,NHO,KHO,MIO,NIO,KIO,MJJO,NJO,KJO
REAL MUAIR,MUTIS,MUBON,MUCOL
COMMON DX,DY,DZ,SX,SY,SZ,A,B,C,ALP,BET,GAM,T,R1,R2,H,RB,TSCFS
COMMON COLTH,AIRTH,TISTH,BONTH,MGI,NGI,PGI,KGI,MGO,NGO,PGO,KGO
COMMON MHI,NHI,PHI,KHI,MHO,NHO,PHO,KHO,MII,NII,PII,KII,MIO,NIO
COMMON PIO,KIO,MJI,NJI,PJI,KJI,MJO,NJO,PJO,KJO,XBONT,BB,BC
IF(TSCFS.LT.SZ) GOTO 1
TISTH=0.0
RETURN
1 AX=DX+ALP*(TSCFS-DZ)/GAM
  AY=DY+BET*(TSCFS-DZ)/GAM
  SPR=((SX-AX)**2+(SY-AY)**2+(SZ-TSCFS)**2)
  TISTH=SQRT(SPR)-XBONT
100 FORMAT(1X,E10.6)
  RETURN
END

```

## RECTANGULAR COLLIMATOR SUBROUTINE

## SUBROUTINE RTH

```

REAL L1,L2,MGI,NGI,KGI,MHI,NHI,KHI,MII,NII,KII,MJI,NJI,KJI
REAL MGO,NGO,KGO,MHO,NHO,KHO,MIO,NIO,KIO,MJO,NJO,KJO
COMMON DX,DY,DZ,SX,SY,SZ,A,B,C,ALP,BET,GAM,T,R1,R2,H
COMMON COLTH,AIRTH,TISTH,BONTH,MGI,NGI,PGI,KGI,MGO,NGO,PGO,KGO
COMMON MHI,NHI,PHI,KHI,MHO,NHO,PHO,KHO,MII,NII,PII,KII,MIO,NIO
COMMON PIO,KIO,MJI,NJI,PJI,KJI,MJO,NJO,PJO,KJO,TSCFS
DEN=MHI*ALP+NHI*BET+PHI*GAM
IF(DEN.EQ.0.0) GOTO 1
THI=(KHI-MHI*DX-NHI*DY-PHI*DZ)/DEN

EZH=DZ+GAM*THI
IF(EZH) 1,1,2
1 DEN=MJI*ALP+NJI*BET+PJI*GAM
  IF(DEN.EQ.0.0) GOTO 6
  TJI=(KJI-MJI*DX-NJI*DY-PJI*DZ)/DEN
  EZJ=DZ+GAM*TJI
  IF(EZJ) 6,6,3

2 DEN=MJI*ALP+NJI*BET+PJI*GAM
  IF(DEN.EQ.0.0) GOTO 4
  TJI=(KJI-MJI*DX-NJI*DY-PJI*DZ)/DEN
  EZJ=DZ+GAM*TJI
  IF(EZJ) 4,4,5
5 IF(EZJ-EZH) 3,3,4
3 TEPAR=(EZJ-DZ)/GAM
  I=1
  GOTO 10
4 TEPAR=(EZH-DZ)/GAM
  I=2
  GOTO 10

10 EY=DY+BET*TEPAR

IF(Y2.LE.EY.AND.EY.LE.Y3) GOTO 11
GOTO 6

```





```

11  EZ=DZ+GAM*TEPAR
    IF (EZ=H) 12,60,60
C
60  COLTH=0.0
    RETURN
12  EX=DX+ALP*TEPAR
C
    IF (I=1) 13,13,14
13  DEN=MJO*ALP+NJO*BET+PJO*GAM
    IF (DEN.EQ.0.0) GOTO 21
    TJO=(KJO-MJO*DX-NJO*DY-PJO*DZ)/DEN
    FY=DY+BET*TJO
    GOTO 16
C
14  DEN=MH0*ALP+NH0*BET+PH0*GAM
    IF (DEN.EQ.0.0) GOTO 21
    TH0=(KH0-MH0*DX-NH0*DY-PH0*DZ)/DEN
    FY=DY+BET*TH0
C
16  IF (Y1.LE.FY.AND.FY.LE.Y4) GOTO 17
    GOTO 18
17  FZ=DZ+GAM*(FY-DY)/BET
    IF (FZ=H) 19,21,21
21  FX=DX+ALP*(H-DZ)/GAM
    FY=DY+BET*(H-DZ)/GAM
    FZ=H
    GOTO 20
19  FX=DX+ALP*(FY-DY)/BET
    GOTO 20
C
18  IF (DY=SY) 22,22,23
22  DEN=MIO*ALP+NIO*BET+PIO*GAM
    IF (DEN.EQ.0.0) GOTO 21
    TIO=(KIO-MIO*DX-NIO*DY-PIO*DZ)/DEN
    FZ=DZ+GAM*TIO
    IF (FZ=H) 24,21,21
24  FX=DX+ALP*TIO
    FY=DY+BET*TIO
    GOTO 20
C
23  DEN=IGO*ALP+NGO*BET+PGO*GAM
    IF (DEN.EQ.0.0) GOTO 21
    TGO=(KGO-IGO*DX-NGO*DY-PGO*DZ)/DEN
    FZ=DZ+GAM*TGO
    IF (FZ=H) 25,21,21
25  FX=DX+ALP*TGO
    FY=DY+BET*TGO
    GOTO 20
C
6  IF (DY=SY) 30,30,31
30  DEN=MII*ALP+NII*BET+PII*GAM
    IF (DEN.EQ.0.0) GOTO 60
    TII=(KII-MII*DX-NII*DY-PII*DZ)/DEN
    EZ=DZ+GAM*TII
    IF (EZ=H) 32,60,60
32  EX=DX+ALP*TII
    EY=DY+BET*TII
    IF (ALP) 13,13,14
C
31  DEN=NGI*ALP+NGI*BET+PGI*GAM

```





```

IF(DEN.EQ.0.0) GOTO 60
TGI=(KGI-MGI*DX-NGI*DY-PGI*DZ)/DEN
EZ=DZ+GAM*TGI
IF(EZ=H) 33,60,60
33 EX=DX+ALP*TGI
EY=DY+BET*TGI
IF(ALP) 13,13,14

```

```

24 COLTH=SQRT((FX-EX)**2+(FY-EY)**2+(FZ-EZ)**2)
RETURN
END

```

# AIR THICKNESS SUBROUTINE

```

SUBROUTINE AJH
REAL L1,L2,MGI,NGI,KGI,MHI,NHI,KHI,MII,NII,KII,MJI,NJI,KJI
REAL MGO,NGO,KGO,MHO,NHO,KHO,MIO,NIO,KIO,MJJO,NJO,KJO
REAL MUAIR,MUTIS,MUBON,MUCOL
COMMON DX,DY,DZ,SX,SY,SZ,A,B,C,ALP,BET,GAM,T,R1,R2,H,RB,TSCFS
COMMON COLTH,AIRTH,TISTH,BONTH,MGI,NGI,PGI,KGI,MGO,NGO,PGO,KGO
COMMON MHI,NHI,PHI,KHI,MHO,NHO,PHO,KHO,MII,NII,PII,KII,MIO,NIO
COMMON PIO,KIO,MJI,NJI,PJI,KJI,MJO,NJO,PJO,KJO,XBONT,BB,BC
DIS=SQRT(ALP**2+BET**2+GAM**2)
AIRTH=DIS-TISTH-BONTH-COLTH
RETURN
END
ENDb

```













**B30141**